

154560169



This is to certify that the  
dissertation entitled

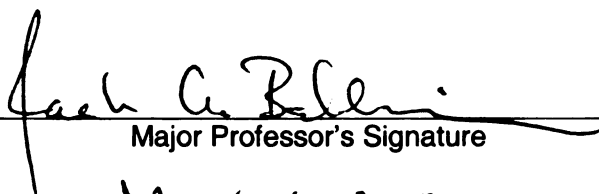
An Abundance Study of IC 418 Using High Resolution, Signal-  
to-Noise Emission Spectra

presented by

Brian David Sharpee

has been accepted towards fulfillment  
of the requirements for the

Ph.D. degree in Astrophysics

  
Major Professor's Signature

March 6, 2003

Date

**PLACE IN RETURN BOX** to remove this checkout from your record.  
**TO AVOID FINES** return on or before date due.  
**MAY BE RECALLED** with earlier due date if requested.

DATE DUE	DATE DUE	DATE DUE

AN ABUNDANCE STUDY OF IC 418 USING HIGH  
RESOLUTION, SIGNAL-TO-NOISE EMISSION SPECTRA

By

Brian David Sharpee

A DISSERTATION

Submitted to  
Michigan State University  
in partial fulfillment of the requirements  
for the degree of

DOCTOR OF PHILOSOPHY

Department of Physics and Astronomy

2003



## ABSTRACT

### AN ABUNDANCE STUDY OF IC 418 USING HIGH RESOLUTION, SIGNAL-TO-NOISE EMISSION SPECTRA

By

Brian David Sharpee

An on-going problem in astrophysics involves the large and varying disagreement between abundances measurements made in planetary nebulae (PNe), determined from the strengths of emission lines arising from the same source ion, but excited by differing mechanisms (recombination and collisional excitation) in planetary nebulae (PNe).

We investigate the extent of this problem in IC 418, a PN chosen for its great surface brightness and perceived visually uncomplicated geometry, through the use of high resolution ( $R \approx 30000 = 10 \text{ km sec}^{-1}$  at  $6500\text{\AA}$ ) echelle emission spectroscopy in the optical regime ( $3500\text{-}9850\text{\AA}$ ). These observations allow us to construct the most detailed list of atomic emission lines ever compiled for IC 418, and among the most detailed from among all PNe. Ionic abundances are calculated from the fluxes of numerous weak ( $1 \times 10^{-5} \text{ H}\beta$ ) atomic emission lines from the ions of C,N,O, and Ne, using the most recent and accurate atomic transition information presently available. The high resolution of these spectra provides well-defined line profiles, which, coupled

with the perceived simplicity of the object's expansion velocity distribution, allows us to better determine where in the nebula lines are formed, and where the ions that produce them are concentrated. Evidence for "non-conventional" line excitation mechanisms, such as continuum fluorescence from the ground state or enhanced dielectronic recombination, is sought in the profile morphologies and relative line strengths. Non-conventional excitation processes may influence the strengths of lines enough to significantly alter abundances calculated from them.

Our calculations show that recombination line-derived abundances exceed those derived from collisionally excited lines, for those ions for which we observed lines of both types:  $O^+$ ,  $O^{+2}$ , and  $Ne^{+2}$  by real and varying amounts. We find that both continuum fluorescence and dielectronic recombination excites numerous lines in IC 418, but that there is no evidence in our data that either process is responsible for the observed overabundances in all recombination lines as opposed to their collisionally excited counterparts. The calculated levels of temperature fluctuations in the zones in which these ion reside are dubious, and significantly exceed model predicted values. In summary, no satisfactory, single universally applicable answer to the abundance discrepancy problem shown to exist by us in IC 418, is revealed by our observations.

We developed several new techniques to analyze these data. Of particular interest is EMILI (Emission Line Identifier), a public-domain program that utilizes a comprehensive atomic transition list and a set of simple tests and criteria, to quickly provide its user with a list of rank ordered IDs for unidentified emission lines found in deep, high resolution spectra. Presented here are the results of applying EMILI to the identification of weak emission lines in the spectra of IC 418 and other PNe.

*To Tanya*

## ACKNOWLEDGMENTS

It is said that the journey of a thousand miles begins with a single step. I am most grateful to my advisor, Professor Jack Baldwin, for guiding my first steps down that road, then provisioning me for the long haul. When the road forked along the way I was glad for the presence of my guidance committee: Professors Robert Williams, Eugene Capriotti, James Linnemann, and Hendrik Schatz who provided caring and sound advice. Thanks also to Professors Horace Smith and Peter van Hoof for providing me essential tools for completing this thesis.

I cannot forgot the many folks who shared the road with me, my fellow grads and travelers: Andrew Schnepf, Chris Hanley, Barton Pritzl, Robert Slater, Wayne and Marguerite Tonjes, Jason and Viki Grenya, Zach Constan, James Armstrong, Alexander Volya, Michael Davis, Dali Georgobiani, Regner Trampedach, Aaron Lacluyze, Karen Kinemuchi, Mark Watry, all in PA 318, and later BMPS 3245/3248/3265.

To those there where the road began: my parents, Jerry and Boni Sharpee, thanks for your never-ending encouragement and faith in me. Finally, this thesis would not have been possible without the compassion and caring of my wife, Tatyana Sharpee, who has always kept me steering in the right direction!

# TABLE OF CONTENTS

<b>LIST OF TABLES</b>	<b>ix</b>
<b>List of Figures</b>	<b>xi</b>
<b>1 Introduction</b>	<b>1</b>
1.1 The Emission Line Spectra of PNe . . . . .	3
1.2 Abundance Determinations . . . . .	7
1.3 Nature and History of Abundance Discrepancies . . . . .	11
1.4 Proposed Solutions . . . . .	12
1.5 IC 418 . . . . .	18
1.6 Goals . . . . .	21
<b>2 Observations and Reductions</b>	<b>23</b>
2.1 Observations . . . . .	23
2.2 Reductions . . . . .	28
2.3 Error Analysis . . . . .	44
2.3.1 Internal Agreement . . . . .	44
2.3.2 Systemic Disagreements Between Spectra . . . . .	48
2.3.3 Obtaining a Total Error Estimate for Final Line Values . . . . .	51
2.4 Comparisons With Other Spectra . . . . .	61
<b>3 A Semi-Automated Emission Line Identifier - EMILI</b>	<b>65</b>
3.1 Introduction . . . . .	65
3.2 Overview . . . . .	66
3.3 Modeling the Nebula . . . . .	69
3.3.1 Velocity Structure Modeling . . . . .	70
3.3.2 Abundances . . . . .	72
3.4 Template Flux . . . . .	78
3.5 Multiplet Check . . . . .	83
3.6 Ranking the Transitions . . . . .	88
3.7 Output . . . . .	88
3.8 Application to Other Spectra . . . . .	93
3.9 Application to Current Dataset . . . . .	95
3.10 Future Directions of the Code . . . . .	99
3.11 Conclusions . . . . .	102
<b>4 Results</b>	<b>104</b>
4.1 Plasma Diagnostics . . . . .	104

4.1.1	Temperature and Density Diagnostics . . . . .	104
4.1.2	Balmer Jump Temperature . . . . .	110
4.2	Abundances . . . . .	113
4.2.1	Ionic Abundances from Collisionally Excited Lines . . . . .	113
4.2.2	Ionic Abundances from Recombination Lines . . . . .	120
4.2.3	Ne <sup>+2</sup> /H <sup>+</sup> . . . . .	158
4.2.4	Other Ions . . . . .	160
4.2.5	Comparative Ionic Abundances . . . . .	161
4.3	Sources of Abundance Discrepancy . . . . .	163
4.3.1	Continuum Fluorescence . . . . .	163
4.3.2	Enhanced Dielectronic Recombination . . . . .	180
4.3.3	Temperature Fluctuations . . . . .	187
<b>5</b>	<b>Conclusions</b>	<b>194</b>
	<b>APPENDICES</b>	<b>206</b>
<b>A</b>	<b>Mechanics of Data Reduction Steps</b>	<b>207</b>
A.1	Bias Correction and Image Trimming . . . . .	207
A.2	Flat Fielding . . . . .	208
A.3	Scattered Light and Sky Background Corrections . . . . .	211
<b>B</b>	<b>RDGEN</b>	<b>213</b>
B.1	Inputs . . . . .	213
B.2	Method . . . . .	214
B.3	Operation . . . . .	218
B.4	Code Benefits and Limitations . . . . .	223
<b>C</b>	<b>Profile Fitter</b>	<b>225</b>
C.1	Introduction . . . . .	225
C.2	Method . . . . .	226
C.3	Operation . . . . .	232
C.4	Benefits and Limitations of the Code . . . . .	238
C.5	Future Work . . . . .	241
<b>D</b>	<b>EMILI User's Manual</b>	<b>242</b>
D.1	Introduction and Purpose . . . . .	242
D.2	User Inputs . . . . .	243
D.2.1	Input Line List . . . . .	244
D.2.2	Matched Line List . . . . .	245
D.2.3	Abundance Table . . . . .	250
D.2.4	Command/Parameter List . . . . .	251
D.3	Installing and Running the Code . . . . .	256
D.4	The EMILI Process . . . . .	258
D.5	Outputs . . . . .	261
D.5.1	Full Output List . . . . .	261

D.5.2	Sample Line Identification . . . . .	264
D.5.3	Summary List . . . . .	268
D.5.4	Reader . . . . .	269
D.6	Future Improvements . . . . .	271
D.7	Contact Information . . . . .	272
<b>E</b>	<b>IC 418 Line List</b>	<b>273</b>
	<b>Bibliography</b>	<b>305</b>

## LIST OF TABLES

2.1	Observing journal for IC 418 observations. . . . .	26
2.2	Effective total integration times of co-added object spectra (in hours). .	34
2.3	Lines saturated in the <i>long</i> spectra. . . . .	38
2.4	Observed versus laboratory wavelengths for Balmer and Paschen lines. .	41
2.5	Reddening parameters . . . . .	43
2.6	Statistics of matched line measurements within blue, intermediate, and red set-ups, and in their overlap regions . . . . .	47
2.7	Wavelengths of strong lines, and ionization potentials of their parent ions.	54
2.8	Estimated wavelength uncertainty budget for each line, depending upon it's S/N and final wavelength. The numbers $N$ indicate the numbers of lines which were used to calculate the error within the particular S/N or wavelength bin. . . . .	57
2.9	Comparisons lines ( $I_{H\beta} = 100$ ). . . . .	62
2.10	Relative flux in line ratios . . . . .	64
3.1	The ionization potential energy bins and signature lines used to calculate the ICF values . . . . .	69
3.2	The IDI assignment breakdown for a putative IDs for a given unidentified line. A lower IDI value means a better ID in general. . . . .	89
3.3	Manual IDs versus EMILI IDs for emission lines in the Orion Nebula as observed by Baldwin et al. (2000). The second column lists the number of times within each EMILI rank, that a particular manual line identifications matched the EMILI identification of that rank for that line. The bottom row without a rank entry indicates the number of lines for which the manual ID was not ranked by EMILI, or for which the transition was not present in the EMILI transition database. The third column shows the percentage of all 388 lines that fall in each category. . . . .	94
3.4	The same as Table 3.3 for the spectrum of the PN NGC 7009 by Walsh et al. (2001). . . . .	94
3.5	The same as Table 3.3 for the spectrum of IC 418 as observed by HAF. These statistics include only lines assigned single distinct IDs by HAF.	94



3.6	Numbers and percentage of EMILI IDs chosen as final IDs for each EMILI IDI rank, out of the total number of IDs used from EMILI. The average, minnum, and maximum IDI values among IDs chosen within each rank are also listed. These numbers includes all transitions from lines thought to be blends, or which otherwise had multiple EMILI selected for them. “Total” equals the total number of EMILI IDs selected, not the number of individual emission lines. . . . .	97
4.1	References for Atomic Data for Collisionally Excited Lines. . . . .	105
4.2	Plasma Diagnostics and Their Uncertainties for IC 418. . . . .	106
4.3	Ionic abundances from collisionally excited lines . . . . .	117
4.4	References for atomic data for recombination excited lines. . . . .	122
4.5	Temperatures used for recombination line abundance calculations. . . .	123
4.6	Recombination line $\text{He}^+/\text{H}^+$ abundances. . . . .	125
4.7	Recombination line $\text{C}^{+2}/\text{H}^+$ abundances. . . . .	131
4.8	High excitation C II recombination lines. . . . .	132
4.9	Recombination line $\text{N}^+/\text{H}^+$ abundances. . . . .	134
4.10	Recombination line $\text{N}^{+2}/\text{H}^+$ abundances. . . . .	139
4.12	Recombination line $\text{O}^+/\text{H}^+$ abundances. . . . .	146
4.13	Recombination line $\text{O}^{+2}/\text{H}^+$ abundances. . . . .	151
4.15	Recombination line $\text{Ne}^{+2}/\text{H}^+$ abundances. . . . .	159
4.16	Comparative ionic abundances for IC 418 from collisional/recombination lines, in units such that $\log(\text{H}^+)=12.0$ , for present and other surveys. . . . .	162
4.17	Measured IC 418 expansion velocity from line profiles. . . . .	170
4.18	C II dielectronic lines. . . . .	181
4.19	N II dielectronic lines. . . . .	182
4.20	O II dielectronic lines and abundances. . . . .	183
4.21	Temperature fluctuation $t^2$ and $T_o$ values and corrected abundances, $\text{N}^{+i}/\text{H}^+$ , using different Balmer jump temperatures $T_e(\text{H}^+)$ and Model value of $t^2 = 0.005$ . . . . .	190
C.1	Legend for entries in final column of the profile fitter output. . . . .	239
D.1	The ionization energy bins used to determine ICF values and velocity corrections to the observed line as a function of putative ID ion’s ionization energy. . . . .	246
D.2	The lines specifically used to calculate the ICF values, and their defaults in each bin. . . . .	246
D.3	For each observed unidentified line, all putative IDs are ranked, by defining a “score” or IDI value for each transition. The IDI is awarded on the basis of the putative ID meeting the main criteria listed below. A lower score generally means a better ID. . . . .	262
E.1	IC 418 Line List . . . . .	278

## LIST OF FIGURES

2.1	Approximate slit position with respect to an HST image of IC 418 (Ciardullo et al. 1999). The width of the slit is 1" and the length shown here corresponds to the 11.9" long decker employed in the blue and intermediate set-ups. . . . .	24
2.2	An excerpt from a typical 2-D <i>intermediate</i> spectrum. Each roughly horizontal dark strip is an echelle order, with wavelength increasing from left to right within an order, and from top to bottom across adjacent orders. Nebular and night sky emission lines, represented as "blobs" and more narrow strips respectively, can be seen superimposed within the orders. Atmospheric absorption bands appear as "bright" bands within an order (see 7 orders from the bottom). Scattered light objects and ghosts (objects between and intruding into orders) can also be seen. Flares emanated from the bright saturated lines of H $\alpha$ and the flanking [N II] doublet $\lambda\lambda 6538, 6584\text{\AA}$ at the rough center right of the image. Cosmic rays appear as small pin prick strikes across the entire spectrum. . . . .	27
2.3	Segment from the co-added blue 1-D flux calibrated spectra. Numerous weak emission lines can be seen. Steps for reducing 2-D spectra to 1-D spectra are given in the text. . . . .	28
2.4	A blown-up portion of the 2-D blue spectrum, showing emission lines of differing profile morphology depending upon the ionization energy of the line's parentage. The "central cavity" in the [N I] lines is created by the differential expansion of the nebula, its ionization stratification, and the effect of looking through the nebula to intercept the same spherically expanding shell. At the center of the slit, most of the expansion velocity is in the direction of the observer, leading to a larger Doppler shift in the line profile, whereas at the edges, the expansion velocity is more perpendicular to the line of sight, hence the "donut" shape of the lines on the 2-D spectrum. The dashed lines show the extraction windows over which the order was summed at each column in the CCD. . . . .	29

2.5	A comparison between the extracted spectrum, calibrated with the fit to the sensitivity function used to calibrate the nebular spectra, and a tabulated low resolution spectrum (Humay et al. 1994) for the flux standard star $\xi^2$ Cet (HR 718). The smooth curve is the tabulated spectrum, whereas the somewhat more broken curve is the flux calibrated spectrum. Over most of the orders the two spectra nearly overlap, typically to better than 5%. There is some deviation on the edges of orders as indicated by the “spikes” sticking out above the smooth curve. . . . .	33
2.6	A portion of the full slit blue spectrum extracted from the order shown in Figure 2.4. This demonstrates the differing profile morphologies exhibited by lines whose parents ions are of different ionization potentials. Higher ionization lines, such as [Ar III] $\lambda 5191.8\text{\AA}$ on the left have more Gaussian-like profiles, while low ionization lines, such as the [N I] doublet on the right have double peaked Gaussian-like profiles, as influenced by the differential expansion velocity of the nebula exceeding the thermally generated width of the line. . . . .	37
2.7	A portion of the 2-D red spectrum which depicts an obvious night sky emission line near the center of the image. Note that it fills the entire slit rather than just the portion superimposed on the nebula, as the adjacent nebular line does. Both lines sit on the wing of the broad nebular emission line blend of O I $\lambda 8446\text{\AA}$ on the left edge of the picture. From Osterbock et al. (1996) the night sky line is most likely 6-2 P2(3.5) $\lambda 8452.250\text{\AA}$ , a vibration-rotational transition of the terrestrial OH molecule, and has a FWHM of $\approx 9 \text{ km s}^{-1}$ which is the instrumental resolution. The adjacent nebular line we believe is He I $\lambda 8451.158$ . . . . .	39
2.8	The absolute value of the wavelength difference (in $\text{km sec}^{-1}$ ) between the reddest and bluest measures ( $\Delta \lambda_{\text{m}} \equiv \text{reddest} - \text{bluest}$ ) among those used to compute the final line wavelength values, versus the minimum S/N among all the measures. Similarly, the ratio of the reddest to bluest measurements’ fluxes (Flux Ratio $\equiv \text{reddest/bluest}$ ). . . . .	46
2.9	Flux and Wavelength Agreement as a Function of Wavelength in Blue, Intermediate, and Red Spectra. . . . .	49
2.10	Statistics of Multiple Line Measurements in the Intermediate-Blue Overlap Region . . . . .	50
2.11	<b>Left:</b> The $1\sigma$ scatter from individual measurements of the wavelength and flux of a particular line used to calculate that line’s wavelength and flux, for all lines as a function of S/N. <b>Right:</b> The same information plotted against wavelength ( $\lambda$ ) for all lines $S/N \geq 20$ . . . . .	52
2.12	<b>Top:</b> laboratory minus observed wavelength ( $\Delta\lambda$ ) for lines from Table 2.7 as a function of observed wavelength. <b>Bottom:</b> same versus ionization potential ( $\chi$ ) of parent ion. An obvious trend towards smaller wavelength difference between observed wavelength and laboratory wavelength with increasing ionization potential is evidenced. . . . .	55

2.13	The percentage flux error ( $1\sigma$ measurement scatter) as a function of $-\log(I(\lambda)/I(H\beta))$ . . . . .	59
3.1	A segment of the <i>Matched Line List</i> for the IC 418 data. Listed in columns from left to right are: <b>A.</b> observed wavelength ( $\text{\AA}$ ) <b>B.</b> laboratory wavelength of transition ( $\text{\AA}$ ), <b>C.</b> spectroscopic notation for the transition's source ion <b>D.</b> flux with respect to $H\beta$ . . . . .	67
3.2	A subset of the <i>Input Line List</i> for the IC 418 dataset. Listed in columns from left to right are: <b>A.</b> observed wavelength ( $\text{\AA}$ ) <b>B.,C.</b> errors in measurement ( $\text{\AA}$ ), <b>D.</b> flux with respect to $H\beta$ <b>E.</b> FWHM (km/sec) <b>F.</b> signal to noise. . . . .	68
3.3	The velocity correction, $v_{cor}$ , in $\text{km s}^{-1}$ for all bins "A"-"E", calculated from the <i>Matched Line List</i> from the EMILI run on the present IC 418 dataset. . . . .	72
3.4	A typical multiplet of Fe II showing all allowed transitions under LS coupling. The position of the energy levels is not to any scale. Fraction beside of the levels are the $j$ total angular momentum values of the each of the upper and lower levels. The numbers indicate the transitions and their laboratory wavelengths. . . . .	84
3.5	The header for the EMILI output file generated by its run on IC 418 databaset. The header includes information regarding the input/output files, specified temperature, density, instrumental resolution, and the calculated ICF (labeled here as " <i>ix 1</i> " - " <i>ix 5</i> ") and $v_{cor}$ (labeled here as " <i>irvcor 1</i> " - " <i>irvcor 5</i> ") values for the five ionization energy bins. . . . .	90
3.6	The EMILI output for a line observed at $5179.52\text{\AA}$ in our IC 418 spectrum. Column legend is provided in the text. . . . .	91
3.7	The distribution of flux: $-\log(I(\lambda)/I(H\beta))$ versus S/N for remaining unidentified lines. Small triangles at S/N=150 indicate unidentified lines with indeterminate S/N. . . . .	99
4.1	Diagnostic diagram for IC 418. In the diagram "D" adjacent to the ion denotes a density diagnostic for that ion, while "T" denotes a temperature diagnostic. . . . .	107
4.2	The blue spectrum in the vicinity of the Balmer series limit, including all regions that were fit to establish the continuum levels. The jump is at $3648\text{\AA}$ , indicated by the vertical line. We used two fits to the continuum redward of the jump. The solid horizontal line indicates a fit over the large region of the continuum away from the jump and yields a temp of 5300 K . The dashed line is a fit in immediate vicinity of the jump, and yields a temp of 6600 K . The same fit blueward of the jump, indicated by another horizontal solid line, was used in both temperature determinations. . . . .	112

4.3	Representative line profiles for ions of differing ionization potential with a comparative sample of the instrumental resolution element. The “INS” profile, of the night sky emission line [O I] $\lambda 5577$ , demonstrates the limits of our instrumental resolution. The level of ionization increases clockwise from the instrumental profile. . . . .	164
4.4	Line profiles from C II lines. . . . .	166
4.5	FWHM versus ionization potential $\chi$ for non-blended lines from various ions. Small circles are recombination lines; stars are collisionally excited lines for the same ion. The dashed line is the instrumental resolution limit. . . . .	167
4.6	Line profiles from N I, [N I], and [N II] lines. . . . .	169
4.7	Line profiles from [N II] and N II lines. . . . .	172
4.8	Line profiles from [O I], [O II], and O I lines. . . . .	174
4.9	Line profiles from [O II], [O III], and O II lines. . . . .	176
4.10	Lines profiles from [Ne III] and Ne II lines. . . . .	178
C.1	A sample line detection input file “1zblue418x.6”, with columns entries explained in the text. . . . .	233
C.2	A segment from the output file “res” to the profile fitter. A legend for the various columns is given in the text. The entry for the line fitted in Figure C.3 is listed at the bottom. . . . .	237
C.3	The fitted profile of a line from the full slit, long exposure, blue spectrum. The actual data are the dotted line, superimposed upon the solid line which is the fit. . . . .	238
D.1	A subset of the <i>Input Line List</i> from <b>ic418.in</b> . Listed in columns from left to right are: <b>A.</b> observed wavelength ( $\text{\AA}$ ) <b>B.,C.</b> errors in measurement ( $\text{\AA}$ ), <b>D.</b> flux with respect to $H\beta$ <b>E.</b> FWHM (km/sec) <b>F.</b> signal to noise. . . . .	245
D.2	A <i>Matched Line List</i> ( <b>ic418.match</b> ). Listed in columns from left to right are: <b>A.</b> observed wavelength ( $\text{\AA}$ ) <b>B.</b> laboratory wavelength of transition ( $\text{\AA}$ ), <b>C.</b> spectroscopic notation for the transition’s source ion <b>D.</b> flux with respect to $H\beta$ . . . . .	250
D.3	A <i>Command/Parameter List</i> ( <b>ic418.cmd</b> ). . . . .	253
D.4	The header for the EMILI output file generated by its run on the included data. Information regarding the input/output files, specified temperature, density, and instrumental resolution, is contained here, as are the values for the ICFs (labeled here as “ <i>ix</i> 1” – “ <i>ix</i> 5”) and the velocity corrections (labeled here as “ <i>irvcor</i> 1” – “ <i>irvcor</i> 5”) for the five ionization energy bins. No elements were depleted in this run. . . . .	263

- D.5 An example of EMILI output from the *Full Output List* (**ic418.out**). This is an identification of a line observed at 6347.19Å (after correction to the nebular rest frame as established by the Balmer and Paschen series of H $\beta$ . EMILI suggests that Si II  $\lambda$ 6347.100Å is the most likely ID. This ID has a small residual wavelength difference (indicated by small value in km/sec in column **G**). It also has a *Template Flux* (column **F**) nearly the same value as what was observed (top line, second numeric value). An additional multiplet line, Si II 6371.370Å (column **J**), was found to correspond with another line in the *Input Line List* and indeed the code found the only other multiplet line it expected to find (column **H**). Thus, this putative ID did well (column **I**) with a low score and a primary (“A”) ranking. . . . . 265
- D.6 A segment from a *Summary List* (**ic418.dat**). From left to right the columns are: **A.** a unidentified line’s observed wavelength **B.** that line’s measured flux with respect to H $\beta$  **C.** the EMILI primary IDs (labeled “A” in the *Full Output List*) associated with the line. . . . . 269

# Chapter 1

## Introduction

Planetary Nebulae (hereafter PNe, singular PN) are the remains of stars which began their existence with anywhere from a tenth to ten times the present mass of our sun. Near the end of their lives, such stars bloat, becoming large giant and supergiant stars, the result of rapid burning of nuclear fuel in shells around an inert electron- degenerate core. The burning is erratic, and in concert with the star's outer distended layer's low surface gravity and strong radiation pressure, pulsational instability begins to set in and eventually strip the star of its outer skin. The core is exposed and becomes the "central star" of the PN, whereas the giant star's former outer layers continue to expand to sizes of a light year or more, becoming the shell or ring commonly seen in PNe. While nuclear fusion in the system has ceased with the departure of the outer layers, the still white-hot core is capable of ionizing and exciting the former stellar envelope with its copious UV photons, leading to the emission spectra observed for PNe. Our own sun is predicted to be destined for just such a fate in approximately 4.5-5.0 billion years.

PNe provide a set of universally “old” (at least several billion years, approaching the characteristic age of our galaxy) objects, from whose spectra elemental abundances can be determined. It is thought that the precursors of PNe, asymptotic red giant branch stars, can produce iron-peak and trans-iron elements in the s-process in their distended envelopes, and there is some evidence that elements normally associated with the r-process can also be synthesized there as well (Balteau et al. 1995). However, PNe precursors do not generally process any elements both lighter than iron and heavier than oxygen in their interiors, and their outer shells preserve a record of the level of enrichment of the gas in those elements at the time and place they formed. The spatial and kinematic distribution of PNe, along with the abundances determined from their spectra, provide a means to gauge the chemical composition of the gas throughout our galaxy at a much earlier epoch. Such information provides an important constraint on the chemical enrichment models and mechanisms proposed for galaxies. Thus PNe are important on two levels, as a test of both stellar and galactic evolution.

Emission lines are the chief means of determining the physical attributes of PNe and H II regions such as the Orion Nebula. Indeed almost everything known about PNe properties, including temperature, density, and composition, is derived from understanding and interpreting the strengths and ratios of the strengths of the various emission lines which dominate their spectra. As such, it is important to understand the mechanisms that give rise to individual lines. A significant effort has been invested over the years to do precisely that, and methods of interpreting the strengths of such lines based upon our understanding of their formation mechanisms have been



developed (Osterbrock 1989). These methods have been considered among the most reliable in all of astronomy.

However, the advent of significant improvements in the calculation of important components of line strength equations, the opening of the UV frontier via space-borne instruments, and improving observational techniques, have brought to light a significant aberration in the results obtained with these methods. This casts into doubt the level of our understanding of emission line formation mechanisms which underpin this work.

We begin with a discussion of the components of emission line spectra and the mechanisms which dominate the creation of lines in these spectra. This is followed by a discussion of how abundances and other physical attributes of emission-line regions are determined from the strengths of these lines. The history of the abundance determination problem and the merits of proposed solutions conclude this chapter.

## 1.1 The Emission Line Spectra of PNe

PNe and H II regions have spectra dominated by two types of emission lines which overlie a weaker continuum. The two types of emission lines are *recombination lines* (RL) and *collisionally-excited* (CL) so-called “forbidden” lines. Each has a different formation mechanism.

Recombination lines (RL) are as advertised: lines created from the cascade of an electron recaptured to an excited level en-route to the ground state of an ion. The strongest examples of such lines in the visible part of the spectrum are the Balmer

series of neutral hydrogen. Line strengths for RL are directly proportional to the number density of the source ion. Their value is two-fold.

First, because the lines form during cascades, their strengths depend mainly upon the transition probabilities (i.e. Einstein coefficients) between the initial and final levels along the cascade path, which do not depend on temperature. The strength also depends upon the recombination cross section of the ion, and therefore the thermal properties (temperature) of the free electrons, but the overall temperature dependence is generally very weak. For example for  $H\beta$  the temperature dependence takes the form  $\approx T^{-0.8}$  (Osterbrock 1989). Thus RL are mostly free of the effects of any temperature fluctuations along the observational line of sight. Nebular temperatures can be determined by comparing the strength of strong recombination lines with the continuum difference around the Balmer jump. However, until recently using this method has been difficult due to the confusion of the continuum level in the vicinity of the jump caused by line crowding at the limit, as well as other effects.

Secondly, RL are mostly free of optical depth effects (with the only exception being recaptures into the ground state) and intensities are thought to suffer only minimally from resonance absorption or scattering along the line of sight. This is due primarily to the extremely short ( $\approx 10^{-8}$  s) lifetimes of excited levels relative to the lifetime of ions against ionization. This may not hold, however, for ions with meta-stable excited states (such as the  $2s\ ^3S$  term in neutral helium for example), for which absorption of line photons or the continuum from the central star can be a factor.

Thus RL are ideally suited for abundance determinations of PNe. However only very abundant species, such as hydrogen and helium, have RL that are *strong* enough

to be easily separable from the continuum.

Collisionally excited lines (CL) arise from collisions between free electrons, stripped from abundant elements by the central star's photoionizing radiation, and plentiful ions. The Boltzman factor at typical nebular temperatures limits the excitations from the ground state to only low-lying energy levels. However, in the case of multi-electron ions with energy levels within only a few eV of the ground state, such as exists for  $O^{+2}$ , collisional excitation is the chief populator of such levels, with recombination and cascade to the excited levels providing only a minimal contribution at typical nebular temperatures. Transitions between these levels, so called *forbidden* transitions, are normally prohibited by electric dipole selection rules and *cannot* be excited directly by line photons or by those in the continuum provided by the diffuse gas or the central star. Such transitions can only occur in a diffuse environment where the time scale of collisional *de-excitation* of such levels becomes as long as the lifetime of the collisionally excited level against spontaneous decay and release of a photon. In the diffuse gas of a PN, where the electron density  $N_e \approx 10^3/\text{cm}^3$ , electron collisions are most certainly rare, but collisional de-excitation is even rarer. The emission of a line photon during decay is more likely to occur before collisional de-excitation. Indeed CL are often the strongest and in many cases the *only* lines observed in the visible region of the spectrum for many ions of less abundant heavy elements. The [O III] lines at  $\lambda\lambda 4959, 5007$  are often the strongest emission lines observed in PNe and H II regions.

CL are used to gauge electron properties of PNe, since they arise from electron collisions, and because of their easy observability. The electron temperature is most

often measured by comparing the sum of intensities of [O III]  $\lambda 4959 + \lambda 5007$  which originate from the same level, with the intensity [O III]  $\lambda 4363$ , which terminates at the same level the others begin at. Although these [O III] lines are the most commonly employed, similar temperature measures can be made with other ions with strong CL, such as those of  $N^+$ . Since this ion is of lower ionization energy, and because nebulae have ionization stratification, such diagnostics measure the temperature from different parts of an emission line region. Electron densities can also be measured by comparing the ratios of CL of the same ion, the ratios of [O II]  $\lambda 3729/\lambda 3726$  and [S II]  $\lambda 6716/\lambda 6731$  being the most commonly used.

However, the Maxwell-Boltzman equilibrium distribution established by the rapidly colliding electrons introduces an exponential temperature dependence as well as a  $T^{-1/2}$  factor in the collisional rates. Thus, CL intensities are susceptible to *temperature fluctuations* within the region where they form. Because of this strong dependence on temperature in general, CL are *not* ideally suited for abundance determinations.

Together RL and CL form the emission line spectrum. The underlying continuum radiatively derives from several sources. These include recombination to various abundant ions, such as  $H^+$ ,  $He^+$  (first ionized hydrogen and helium), and  $He^{+2}$ , Bremsstrahlung between free electron states through interactions of free electrons with these ions, the continuum from the central star, and the continuum formed by the two-photon process which dominates the transition from the 2s level of neutral hydrogen to the 1s level of the ground state, a transition ruled out by electric dipole selection rules for single photon emission.

## 1.2 Abundance Determinations

The intensity of a line, regardless of the mechanism which led to the excitation of its source level, is directly proportional to the population of the level within the ion from which it arises,  $n_i$ , the rate at which the transition occurs  $A_{ij}$ , and the photon energy,  $h\nu_{ij}$ :

$$I \propto \int n_i A_{ij} h\nu_{ij} , \quad (1.1)$$

For recombination lines, among levels with energy high energy that collisional excitation from the ground state plays no significant role, the processes which populate and de-populate a particular level must be in equilibrium, since the line strengths are not time varying. In the absence of photoionization from an excited level (a good assumption given the short lifetimes of the excited levels versus the ionization rate under nebular conditions) the population of a level depends upon direct recombination to that level and cascades to and from that level. The population of a level  $i$  may be determined from:

$$NN_e\alpha_i(T_e) + \sum_{k>i}^{\infty} n_k A_{ki} = n_i \sum_{k<i}^{i-1} A_{ik} , \quad (1.2)$$

where  $N$  is the overall ionic abundance,  $N_e$  is the electron density,  $A_{ik}$  and  $A_{ki}$  are the spontaneous transition coefficients (Einstein coefficients), and  $\alpha_i$  the rate of recombination directly to a level  $i$ .

However each level  $n_k$  is in turn itself populated by direct recombination and cascades from above, and de-populated by cascades to lower energy states, and so forth for next higher level, and the next, until  $n = \infty$  at which point only recombinations to that level can populate a level. In essence one can specify a recombination coeffi-

cient which tells the rate of the recombinations to all levels that ultimately lead to a population in the  $i$  state via cascades:

$$NN_e \sum_{k=i}^{\infty} \alpha_k(T) C_{ki} = n_i \sum_{k<i}^{i-1} A_{ik}, \quad (1.3)$$

where  $C_{ki}$  is a probability matrix, made up of combinations and ratios of transition probabilities, and defined as the probability that a recombination to the  $k$  level ultimately follows a cascade path that leads to a population in the  $i$  state, among all such cascade paths available from that level. Selecting a particular downward transition  $i \rightarrow j$ , the intensity of a particular line can then be expressed:

$$I = NN_e \alpha_{ij}^{eff}(T_e) h\nu_{ij}, \quad (1.4)$$

where

$$\alpha_{ij}^{eff}(T_e) = \frac{\sum_{k=i}^{\infty} \alpha_k(T_e) C_{ki}}{\sum_{k<i}^{i-1} A_{ik}} A_{ij}. \quad (1.5)$$

The parameter  $\alpha_{ij}^{eff}$  is called the *effective recombination coefficient* of that particular transition. This coefficient is dependent primarily on atomic parameters, such as the coupling scheme employed to establish the source and destination level, and the associated branching ratios governing the probability of departure from a particular level to other levels (involving ratios and combination of spontaneous transition coefficients). Therefore  $\alpha_{ij}^{eff}$  is only weakly dependent on temperature, often varying with  $T_e^{-(0.8-1.3)}$ . This parameter is therefore insensitive to temperature fluctuations along the line of sight through the nebula, and ideal for abundance determination, provided optical depth effects (such as self-absorption from meta-stable low levels, or H-Lyman series photons) do not complicate the contributions from pure cascades.

With an observed intensity for a particular line, rough knowledge of the nebular temperature and density, and an effective recombination coefficient for that emission line under those temperature and density conditions, one may solve for  $N$  to get the ionic abundance of the line's parent ion. The  $\alpha_{ij}^{eff}$  are generally expressed as tables of values at particular temperatures and densities, and fitted with interpolation functions of temperature, often a power law, at specific densities (Storey 1994, Kisielius & Storey 2002). However, calculations of  $\alpha_{ij}^{eff}$ , are complicated by unknown Einstein coefficients for many transitions, and departures from LS coupling among higher angular momentum  $l$  levels, which can lead to larger numbers of escape routes from a particular excited level. Thus, at present, effective recombination coefficients for individual lines, or for the multiplets to which they belong, exist for only a few ions.

Collisionally excited lines generally originate only from energy levels within a few eV of the ground state. The time scale of collisional excitation exceeds the recombination rate, so collisional excitation dominates the populations of these levels, hence the relative weakness of recombination lines as compared to forbidden lines of many ionic species. The formalism for obtaining abundance is the same as with recombination lines, in that the population of the level responsible for a particular line must be determined by employing equations of statistical equilibrium for every involved level:

$$\sum_{j \neq i} n_j N_e q_{ji} + \sum_{j > i} n_j A_{ji} = \sum_{j \neq i} n_i N_e q_{ij} + \sum_{j < i} n_i A_{ij}. \quad (1.6)$$

Here  $n_i$  and  $n_j$  are the fractions in levels  $i$  and  $j$  respectively for that ion, and  $q_{ij}$  and  $q_{ji}$  are the collisional excitation and de-excitation rates to and from a particular

level. The collisional excitation rate is defined as:

$$q_{ij} \equiv \frac{8.629 \times 10^{-6} \Omega_i}{T_e^{1/2} w_i}, \quad (1.7)$$

where  $w_i$  is the statistical weight of the beginning level of the transition, and  $\Omega_i$  is the collision strength of the transition, a parameter arising from quantum calculations involving the wave functions of the final and initial states. The collisional de-excitation rate is related to the excitation rate for the same pair of levels by:

$$q_{ji} = \frac{w_i}{w_j} q_{ij} \exp(-\chi/kT_e) \quad (1.8)$$

where  $\chi$  is the energy difference between levels  $i$  and  $j$ .

The resulting system of equations for a particular ion can then be solved for either the temperature and density of the region from which the line originates, if only the line intensities are provided; or the abundance of the particular ion, if the temperature and density are specified in addition to the observed line strengths.

For the ions with the strongest optical forbidden lines, generally only five levels are involved: the  $^3P_{2,1,0}$ ,  $^1D_2$ , and  $^1S_0$  levels (for ions with ground state valance electron configuration of  $p^2$  or  $p^4$ ), and the  $^4S_{3/2}$ ,  $^2D_{5/2,3/2}$ , and  $^2P_{3/2,1/2}$  levels of the  $p^3$  configuration. Notable exceptions include iron and nickel which have many low lying energy levels which may be collisionally excited.



## 1.3 Nature and History of Abundance Discrepancies

The advent of precise calculations of the recombination coefficients has made meaningful theoretical calculations of the intensities of RL possible, while the opening of the UV via space-borne observatories has made observable CL (for ions with few other strong RL or CL in the visible). Improved spectral resolution, allows weak RL to be both resolved and detected amid the noise of the continuum. Thus, abundance determinations can now be made and compared via the measured strengths of both RL and CL produced by the same ion. Two major problem areas have emerged:

1. The observed strengths of RL and CL show both a large scatter, and disagree with model calculated values. Esteban et al. (1998) showed that ratios for [Fe II] CL disagreed by up to a factor of 13. Peimbert et al. (1993) found that the observed  $O^{+2}/H^{+}$  RL ratio exceeds the calculated ratio by a factor of 2 in the Orion Nebula (an H II region), while more recently Esteban et al. (1998) found that the discrepancy is closer to 1.5.
2. Ionic abundances from RL intensity measurements do not agree with abundances determined from CL for the same source ion. While some PNe show no discrepancy, for others it differs by more than an order of magnitude. Barker (1991) noticed in NGC 2392 that the UV collisionally excited inter-combination line C III]  $\lambda 1909$  yields an abundance of  $C^{+2}$  that is an order of magnitude lower than that found from the C III  $\lambda 4367$  recombination line, but found no such

discrepancy for ions of either O or N. However Liu et al. (1995a) found that total C, N, and O abundances derived from averages of their constituent ions' RL, differ by a remarkably constant factor of five from the abundances for the same ions same derived from CL in the PN NGC 7009. Liu et al. (2000) surveyed NGC 6153, and found the abundance discrepancies to be nearly tenfold. Dinerstein et al. (1998) surveyed fourteen PNe and found that the discrepancy for  $O^{+2}$  varied from nebula to nebula, from no difference to well over an order of magnitude of difference.

Where the discrepancies occur, the recombination-line derived abundances always exceed those from collisionally-excited lines from the same parent ion.

## 1.4 Proposed Solutions

Many explanations have been advanced to explain these problems, all with attractive features, as well as distinct drawbacks:

### **Temperature Fluctuations:**

The most commonly invoked explanation is temperature fluctuations within the PN, confusing the temperature derivations and driving down the abundance derived from the highly temperature sensitive optical CL. Early on Peimbert (1967) characterized these fluctuations with the factor  $t^2$ , representing the rms fluctuation of temperature in the region producing the line. Rubin (1969) used the  $t^2$  formalism to characterize their effect on the determination of abundances. Another perceived manifestation, is the usually lower Balmer jump temperature, with respect to optical

CL-determined temps (Peimbert 1971).

In some cases the measured  $t^2$  is sufficient to explain the abundance discrepancy (Peimbert et al. 1993), but not in all cases (Liu et al. 1995a, 2000, Garnett & Dinerstein 2001a). It has also proven difficult to construct a physically meaningful photo-ionization model of smooth un-clumped gas incorporating  $t^2$  values large enough to bring abundances into alignment (Viegas & Clegg 1994, Kingdon & Ferland 1995b). The agreements in abundances between those calculated from relatively temperature insensitive fine structure lines (collisionally excited transitions between the individual total angular momentum  $j$  states within the terms of the ground state configurations of many ions) and from their more temperature sensitive optical counterparts, also argues for a minimal effect of temperature fluctuations (Liu et al. 2000).

### **Density Perturbations:**

Numerous PNe have obvious, visually discernible structure: dark knots, filaments, and “comet trails” as seen in HST images of PNe. The Helix Nebula is a prime example. In such structures both the electron and ionic densities might be fluctuating and locally concentrated. It stands to reason that many of these condensations may be small enough to remain unresolved (Viegas & Clegg 1994 and see below). Condensations with large electron densities in addition to ionic concentrations could be sufficiently dense to make collisional de-excitation of the nebular CL significant enough to affect temperature determinations from their intensity ratios, influence density determinations, and consequently affect abundances determined using other RL and CL which utilize those temperatures and densities. Furthermore, density condensations would provide a safe harbor for lower ionization species in the higher

ionization environment closer to the central star, as the cores would be sufficiently shielded from the ionizing flux (Grandi 1975b) to allow low ionization ions to exist and accumulate. Emission in RL arising from condensations, could add to the emission from lower temperature regions where the RL parent species dominates. If one's line of sight intersected both regions, the result would be large differences in determined abundances from place to place in the PN. Viegas & Clegg (1994) made use of an  $\eta^2$  parameter characterizing the filling factor (the amount of volume of a PN taken up by high  $n_e$  condensations). This successfully accounted for the abundance discrepancy exhibited in the CL and RL  $O^{+2}/H^+$  ratios in NGC 6572. Liu et al. (2000) invoked a model cooler metal rich (hydrogen deficient) condensations begetting stronger RL than in the surrounding "normal" abundance gas from which the CL arise.

Nevertheless even the proponents of this explanation acknowledge its weaknesses. Viegas & Clegg (1994) noted that the chief constraint on their scenario is the necessity of these clumps to have  $O^{+2}$ , the origin species of the [O III] CL, as a major component. This limits the placement of such condensations to a narrow region of most PNe, unless the central star happens to be unusually hot ( $T > 10^5 K$ ) or the nebula small (thereby expanding the fractional volume over which  $O^{+2}$  could exist). It would also not affect temperature determinations made from CL of other lower ionization ions located in other parts of the emission-line object. Liu et al. (2000) found that while the abundances of elements as derived from their CL were almost a factor of ten smaller than those derived from their RL, the ratios of CL abundances of one ion to another are *nearly equal* to ratios of RL abundances of the same two ions, a finding that they cannot reconcile with their own two component models of RL

and CL sources. Garnett & Dinerstein (2001b) question both the origin of metal-rich condensations, as proposed by Liu et al. (2001), and why they should appear only in the most evolved PNe, which they claim show the biggest abundance discrepancy in  $O^{+2}$ . Finally such condensations might be too small to directly observe. Viegas & Clegg (1994) predict that the condensations would be of 0.1 " in angular extent, barely resolvable by the HST.

### **Shock Waves:**

It has also been proposed that an additional energy source within a nebula, such as shock waves, may act to contribute additional excitation of both forbidden lines ([S II]  $\lambda 4069, 4076$  Esteban et al. 1998) and recombination lines (e.g. Multiplet 15 lines in  $O^{+2}$ ). Garnett & Dinerstein (2001b) suggest that dielectronic recombination, enhanced by such additional energy input, may totally explain the abundance discrepancy seen in this particular ion. Evidence for shocks in nebulae is not direct, but their existence is widely suspected and indirectly inferred (see Liu et al. 1995a, Esteban et al. 1999 and references therein). These shocks may arise as a consequence of interactions between stellar winds arising in different phases of the PNe evolution and the progenitor's outer envelope gas, or in the case of H II regions, from winds flowing off the ionizing star or stars. The difference seen in the magnitude of the abundance discrepancy from PN to PN would then arise from the propagation time of the shock through the nebular gas. Garnett & Dinerstein (2001a) saw an anti-correlation between surface brightness, a proxy for nebular age, and the level of  $O^{+2}$  abundance discrepancy. They interpreted this as the shock not having propagated as far in the younger PNe.

However as pointed out by Liu et al. (1995a) such processes can only selectively excite *certain lines in certain elements*. It's difficult to see how processes affecting only certain lines can influence abundance determinations enough to obtain the abundance discrepancies seen in *overall* elemental abundances from multiple species, as they are observed in NGC 7009. Liu et al. (2000) saw no correlation between ionic abundance discrepancy and ionization potential in NGC 6153, suggesting that the discrepancy may have nothing to do with the temperature structure or local temperature-driven phenomenon such as di-electronic recombination induced by shocks. The constancy of ratio of collisionally-excited species seen by Liu et al. (2000) also argues for some sort of global problem.

#### **Continuum Fluorescence:**

Excitation from the ground state via the continuum radiation from the central star of a PN or the exciting star of a H II region may play a large role in the excitation of certain levels. Even for forbidden lines, an increased population of their source levels (induced by cascades following excitations to higher permitted levels) may be significant, at low nebular temperatures.

Grandi (1975a) showed that the intensity of the O I permitted line  $\lambda 8446$ , observed in the Orion Nebula, could not be produced entirely by either pure recombination or any other standard mechanism. His calculations failed to reproduce the observed intensity ratio with respect to  $H\alpha$  by any single or combination of methods by over two orders of magnitude, although calculations utilizing continuum fluorescence could explain its strength. Evidence for a strong continuum fluorescence influence on certain lines of N I was advanced in Grandi (1975b), and Grandi (1976) speculated on the

large role it may have in the excitation of numerous other lines in PNe.

More recently, Esteban et al. (1999) saw excessive line strengths for [Fe II] lines of multiplet 7F, as compared to other [Fe II] lines from other multiplets, that may indicate the presence of a large continuum fluorescence contribution. Lucy (1995) invoked starlight continuum fluorescence to explain the apparent super-solar Ni/Fe ratio observed in the Orion Nebula. Both Liu et al. (1995b) and Bautista (1999) saw the potential for continuum fluorescence contributions to the intensity of neutral species forbidden lines. Ferland (1992) suggested that his models (incorporating an attenuated continuum flux) can explain the anomalous difference in intensities seen between two strong lines of  $N^{+2}$  which cannot be explained by the action of the Bowen<sup>1</sup> mechanism alone. Peimbert et al. (1993) confirmed that the starlight continuum may account for the unusual strength of the  $N^{+2}$  permitted line  $\lambda 4641$  in M17, which is one of the products of the above Bowen mechanism. Finally Esteban et al. (1998) identified a variety of permitted lines potentially significantly driven by continuum fluorescence in the Orion Nebula.

As with the other mechanisms, this one too has problems. Often only levels with energy below 1 Ryd can be excited in nebular environments, due to large optical depths for  $\lambda \leq 912\text{\AA}$ , the result of absorption by abundant hydrogen. Stellar continuum radiation also diminishes severally with distance away from the central star. As with di-electronic recombination and Bowen fluorescence, it is a *selective* exciter.

In summary, several different mechanisms and conditions have been advanced to

---

<sup>1</sup>The Bowen Mechanism is the excitation of a specific transition by line photons emitted at a nearly identical wavelength in a strong resonance line of an abundant ion (Bowen 1924).

explain the unusual abundance discrepancy, each showing problems as well as promise. The effects of each mechanism on RL and CL needs to be better understood, so our understanding of line formation mechanisms as a whole may be improved, and our interpretations made more physically meaningful.

## 1.5 IC 418

We choose for observation the bright southern PN IC 418 (PN G# 215.2-24.2) located at RA 5:27:28.3 and Dec -12:41:48.22 (J2000). This PN has attributes which makes it a good target for high resolution spectroscopy, and subsequent abundance analysis.

1. Simple Geometry. Visual inspection of images of IC 418 in wide band filters indicate that the nebula appears visually uncomplicated, consisting of co-centric spherical shells, uncomplicated by large-scale turbulent velocity flows. This view is consistent with early models of IC 418 by Flower (1969) and Reay & Worswick (1979). Thus, line profiles will be dominated by the local thermal properties and the expansion velocity distribution of the nebular gas, making them easier to fit with confidence (in many cases by a simple Gaussian functions). Narrow band, emission line images of IC 418, also suggest a simple ionization stratification. Lines from ions with low ionization potentials are further away from the center, and lines from ions with higher ionization potentials further in. Given the expansion velocity gradient present in the nebula, in which the outer portions of the nebula expand faster than the inner portions, lines from the same ion or from ions with nearly the same ionization potential should show the same



profiles if they are produced *by the same excitation mechanism*, or differing profiles if they are not.

2. Extremely Bright Nebulosity and Central Star IC 418 has the largest surface brightness (measured in terms of the flux of radiation in the  $H\beta$  line per unit area:  $2.33 \times 10^{-12}$  erg sec $^{-1}$  cm $^{-2}$  arcsec $^{-2}$ ) of any PNe available at the time and location of our observations. Thus a small slit area, necessary for high dispersion echelle spectroscopy, can capture a significant amount of flux from the nebula. The bright central star of this nebula, with a  $V$  band magnitude of 10.17, makes it easier to detect resonance absorption lines (Williams et al. 2003).
3. Large Proper/LSR velocity The helio-centric velocity of IC418 is quite large, moving night sky emission lines away from their nebular counterparts. More importantly, the velocity of IC 418 with respect to the local standard or rest (LSR) is also quite large (61 km/s). Since the interstellar medium (ISM) is the primary source of absorption lines, any nebular gas absorption is separated and distinct from the ISM produced absorption components, simplifying their use in abundance analysis.

The only drawback to the choice of IC 418 is its low ionization, meaning lines from ions with high ionization potentials will not be readily observable. However, low ionization generally indicates a young PN. Thus, we should be able to test the theories of Garnett & Dinerstein (2001a,b) that younger PNe should not show a large discrepancy in  $O^{+2}$  abundance due to the absence of shock-enhanced di-electronic

recombination, since our spectra span the richest area of  $O^{+2}$  optical RL.

Finally, IC 418 has seldom been subjected previously to high resolution spectroscopy, Hyung, Aller, & Feibelman (1994) (hereafter HAF) are one of only a handful of known examples, and never to an extensive abundance analysis with as many lines as are expected to be revealed by the depth of the spectroscopy employed here. HAF used a combination of echelle spectroscopy and IUE observations to compare the intensities of the C III]  $\lambda\lambda 1907, 1909$  collisionally excited intercombination lines with the strong C II  $\lambda 4267$  recombination line. They found that the recombination derived abundance exceeded the collisionally excited value by a factor of three. However, they computed abundances for other ions only from collisionally excited lines, deeming the recombinations present in the spectra too weak to make meaningful abundance determinations. Henry, Kwitter, & Bates (2000) (hereafter HKB) also used IUE observations in the UV and optical spectroscopy to make abundance determinations in IC 418. However the spectra sampled different regions in the nebula, the spectroscopy was of much lower resolution than that employed here, and again only collisionally excited lines were used to measure abundances.

Preliminary comparisons between these data and an archival HST STIS absorption spectrum we have obtained of the IC 418 central star, show a disagreement between the ratio of abundances of  $Fe^{+}$  to  $Ni^{+}$  derived from absorption line analysis as compared to the same ratio derived from collisionally excited lines (Williams et al. 2003). This despite the similarities in low level ionization potentials, recombination coefficients, and condensation temperatures. Also, the STIS spectrum shows a distinct  $C^{+4}$  absorption feature, whereas the strongest predicted  $C^{+3}$  recombination

emission lines, which share the same ionic parentage as the absorption feature, are barely visible in our emission spectrum.

So while previous studies have suggested that the abundance problem exists in this object, the full extent of the abundance discrepancy problem if any, has not been determined, and warrants further study.

## 1.6 Goals

The goal of these observations are to gauge the abundance discrepancy problem in IC 418, and to carry out simple tests that can help us to understand the potential origins of the problem, by making use of the advantages of deep (long exposure time), high resolution echelle spectroscopy, which provides here well defined line profiles, minimization of line blending, and continuous coverage over a large bandpass spanning 3500Å to 9850Å. The high resolution will allow us to examine recombination line profiles for consistency within and between multiplets of the same ion, and to compare them with profiles of collisionally excited forbidden lines arising from the same ion. Differences in profiles may indicate differing excitation ionic parentage, and invalidate comparisons in abundance made between such lines. The large bandpass and depth of the observations will allow the simultaneous calculation of abundances from many different ionic species and elements, at the same place within the nebula, including calculations from the strengths of weak recombination lines only revealed in spectra of this depth and quality.

We will also take this opportunity to develop tools to help automate and improve

the processes of line detection, measurement, and identification. The wealth of information provided by spectra of a quality similar to our own, which are now readily available from today's generation of instruments, demands software tools to improve the accuracy and efficiency of the data reduction and analysis.

# Chapter 2

## Observations and Reductions

Here I summarize the equipment used and steps employed to obtain and reduce the observed spectra and to obtain a list of flux-calibrated emission lines for analysis. The accuracy of line measurements post-reduction is provided, and the process utilized to identify the lines concludes this section. Supplemental material may be found in Appendix A, B, and C.

### 2.1 Observations

Spectra were obtained with the echelle spectrograph on the Cassegrain focus of the Blanco 4 m telescope at Cerro-Tololo Inter-American Observatory during the course of five consecutive photometric nights, UT 26-31 December 2001. The spectra were imaged on a SITe 2048×2048 CCD, set to a gain of 1.1 e<sup>-</sup>/ADU and with a read noise of 3 e<sup>-</sup> per pixel. To improve the signal to noise, CCD pixels in the direction of the slit were binned by a factor of two.

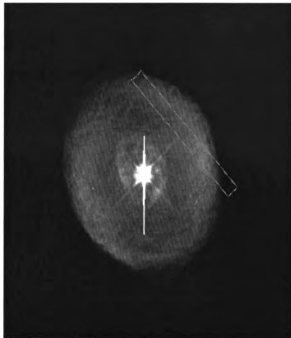


Figure 2.1 Approximate slit position with respect to an HST image of IC 418 (Ciardullo et al. 1999). The width of the slit is  $1''$  and the length shown here corresponds to the  $11.9''$  long decker employed in the blue and intermediate set-ups.

The slit was first centered on the IC 418 at  $\alpha_{2000} = 5^h 27^m 28.3^s$ ,  $\delta_{2000} = -12^\circ 41' 48''$ , rotated to a position angle of 180 degrees, then offset  $\approx 4''$  west, to a final position with respect to the nebula as depicted in Fig. 2.1. The slit was nominally aligned with the same portion of the nebula throughout an observing night. As a consequence there was some spatial smearing at blue wavelengths due to the changing direction of the atmospheric dispersion as the night progressed. The position of the slit avoided the central star, and intersects bright regions of the nebula as seen in emission line HST WFPC2 images (Ciardullo et al. 1999). To reach the desired resolution of 9 km/sec ( $\approx 0.2\text{\AA}$  at  $6500\text{\AA}$ ), a  $1''$  width slit was used. To cover as wide a wavelength range as possible at this resolution, three instrumental set-ups were utilized, designated here

as *blue*, *intermediate*, and *red*. Two observing nights were dedicated to both the *blue* and *red* set-ups, with the final night assigned to the *intermediate* set-up.

The *blue* spectra were taken using a  $79.1 \text{ grooves mm}^{-1}$  echelle grating and a  $316 \text{ grooves mm}^{-1}$  cross disperser (grating KPGL2), with no order separator filter. This set-up utilized the long blue camera and blue collimator, to yield a plate scale of  $0.27''$  per pixel at the CCD ( $0.56''$  per binned pixel). The grating tilt was set to allow full coverage of the wavelength range  $3500\text{--}5950\text{\AA}$ . A  $11.9''$  slit length (decker length) was used, the longest length possible under this set-up to avoid order overlap in the 2-D images. The nebula filled nearly the entire slit (as seen in Figure 2.1). The total area imaged by the slit from the nebula was  $1'' \times 11.9''$ .

The *intermediate red* spectra were taken using a  $31.6 \text{ grooves mm}^{-1}$  echelle grating, a different  $316 \text{ grooves mm}^{-1}$  cross disperser (grating G181), and an order separator filter (GC495). This set-up utilized the long red camera and red collimator, with focal ratios identical to their blue counterparts, yielding the same plate scale at the CCD. The grating tilt ( $1207^\circ$ ) was set to allow continuous wavelength coverage  $5090\text{--}7425\text{\AA}$  which overlaps some of the regions covered by the other two set-ups. The  $11.9''$  decker length was again utilized, with the slit imaging the same  $1'' \times 11.9''$  area of the nebula as was imaged under the blue set-up.

The *red* spectra were taken with the same optical set-up as the intermediate red spectra, but with a different order separator filter (RG610), and with a different grating tilt ( $560^\circ$ ), to allow continuous coverage of the wavelength region  $7350\text{--}9865\text{\AA}$ . Spectral orders under this set-up were spaced further apart on the CCD, allowing the use of a slightly larger decker length, which we employed to maximize the observed

Table 2.1 Observing journal for IC 418 observations.

Date (UT)	Setup	Exposures (number $\times$ sec)
27/12/01	blue	6 $\times$ 1800 2 $\times$ 120
28/12/01	blue	6 $\times$ 1800 2 $\times$ 1000 6 $\times$ 120
29/12/01	red	8 $\times$ 1800 3 $\times$ 300
30/12/01	red	9 $\times$ 1800 3 $\times$ 300
31/12/01	intemediate	10 $\times$ 1800 3 $\times$ 120 3 $\times$ 30

flux from the nebula. An area of  $1'' \times 19.6''$  centered at the same position as the other set-ups, was imaged under this set-up. The nebula filled roughly two-thirds of the length of the slit at this decker size.

A series of short (30-300 sec) and longer (1000-1800 sec) duration exposures were taken throughout each of the observing nights, yielding 2-D spectra, an example of which is shown in Figure 2.2. Table 2.1 lists the numbers and duration of exposures for each observing night, as well as associated instrumental set-ups. The short exposures were used to accurately measure the fluxes of strong emission lines which quickly saturated the CCD. Repeated longer exposures were taken for eventual co-addition to improve signal-to-noise and enhance the detection of weak lines against the continuum. Spectra of flux standard stars and calibration frames were also taken each night.



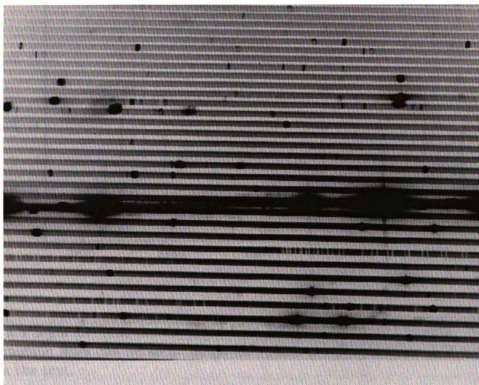


Figure 2.2 An excerpt from a typical 2-D *intermediate* spectrum. Each roughly horizontal dark strip is an echelle order, with wavelength increasing from left to right within an order, and from top to bottom across adjacent orders. Nebular and night sky emission lines, represented as “blobs” and more narrow strips respectively, can be seen superimposed within the orders. Atmospheric absorption bands appear as “bright” bands within an order (see 7 orders from the bottom). Scattered light objects and ghosts (objects between and intruding into orders) can also be seen. Flares emanated from the bright saturated lines of  $H\alpha$  and the flanking  $[N\ II]$  doublet  $\lambda\lambda 6538, 6584\text{\AA}$  at the rough center right of the image. Cosmic rays appear as small pin prick strikes across the entire spectrum.

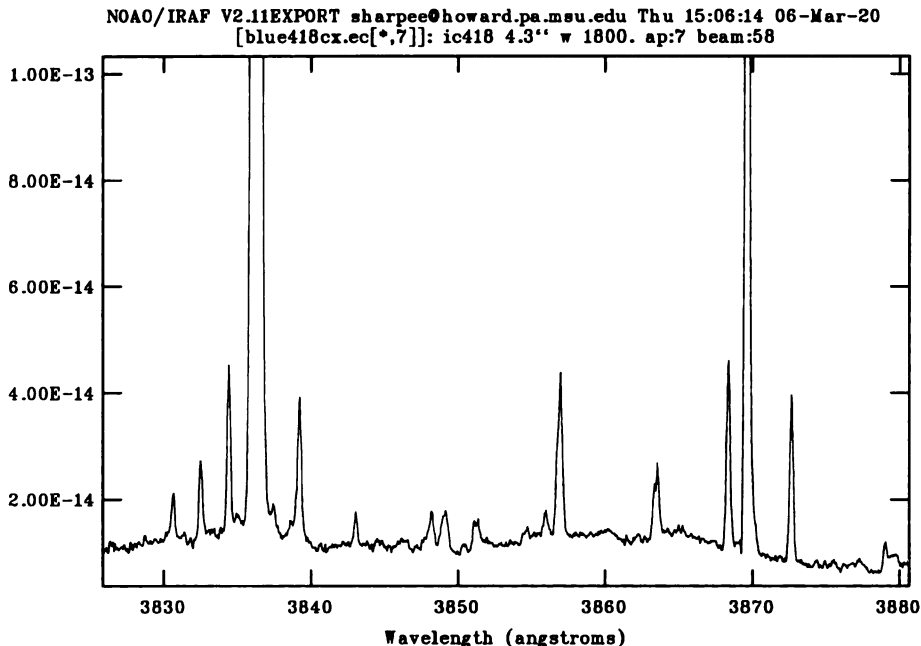


Figure 2.3 Segment from the co-added blue 1-D flux calibrated spectra. Numerous weak emission lines can be seen. Steps for reducing 2-D spectra to 1-D spectra are given in the text.

## 2.2 Reductions

Individual nights were reduced separately to flux calibrated 1-D spectra (see Figure 2.3). Initial processing of the raw 2-D spectra, namely image trimming, bias correction, flat fielding, and scattered light correction were carried out using standard techniques (see Appendix A) as implemented in IRAF<sup>1</sup> tasks. Dark current appeared negligible in our exposures and no attempt was made to correct for it.

<sup>1</sup>IRAF is distributed by National Optical Astronomical Observatories, which is operated by Association of Universities for Research in Astronomy, Inc., under cooperative agreement with National Science Foundation.

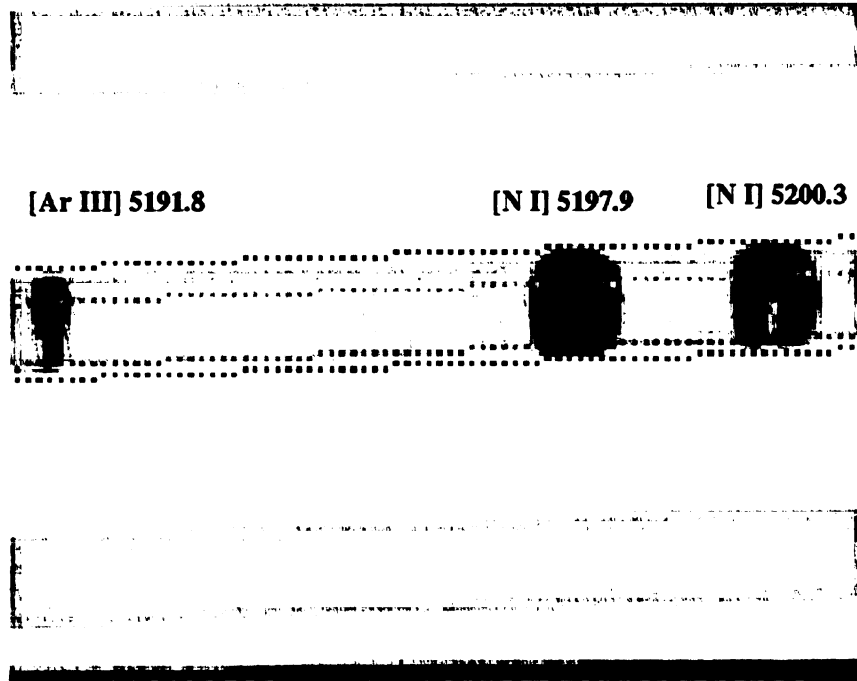


Figure 2.4 A blown-up portion of the 2-D blue spectrum, showing emission lines of differing profile morphology depending upon the ionization energy of the line's parentage. The "central cavity" in the [N I] lines is created by the differential expansion of the nebula, its ionization stratification, and the effect of looking through the nebula to intercept the same spherically expanding shell. At the center of the slit, most of the expansion velocity is in the direction of the observer, leading to a larger Doppler shift in the line profile, whereas at the edges, the expansion velocity is more perpendicular to the line of sight, hence the "donut" shape of the lines on the 2-D spectrum. The dashed lines show the extraction windows over which the order was summed at each column in the CCD.

1-D spectra were extracted from processed images (the 2-D spectra), using a combination of the standard IRAF *echelle* package task *apall* for all flux standard star and calibration spectra, and a modified version of the spectral extraction program employed by Rauch et al. (1990) for all nebular spectra. Both routines sum the counts along a specified fraction of the slit length at each position along the path of each order. The Rauch et al. routines allowed the simultaneous creation of a companion error array, during the extraction process, for each extracted 1-D spectrum. The

errors ( $1\sigma$  uncertainties) were calculated incorporating both the CCD read noise and photon shot noise added in quadrature along the specified extraction length. Spectra were extracted over both the full slit length (11.9" for the blue and intermediate setup, 19.8" in the red), and over a smaller length of 6.5" corresponding to the limits of the "central cavity region" exhibited by many lines of low ionization species (see Figure 2.4). The modified Rauch et al. extraction routines also flagged individual isolated pixels that exceeded a specified flux threshold as probable cosmic rays, by assigning the total flux extracted along the column containing the pixel with a large variance. During later variance weighted co-addition, the positions in each spectrum where these artifacts occurred were given lower weights in the sum. The full slit length spectra were used to detect extremely weak lines more efficiently, while the smaller slit length spectra were used to provide a uniform set of emission line fluxes sampled from the same area of the nebula under each instrumental set-up. Since the nebula completely filled the slit length in two of the instrumental set-ups, no sky subtraction was done during the nebular extraction. The scattered light subtraction, obtained from fits to the regions of the spectra between the orders, was utilized to establish the zero point of the flux scale.

Wavelength calibration was accomplished through the use of ThAr comparison lamp spectra taken periodically throughout the night, using the IRAF task *ecidentify*. The RMS errors of the final fits to the dispersion solution were generally on the order of 0.5-1.0 km sec<sup>-1</sup> for the blue and intermediate set-ups, and 1.0-1.5 km sec<sup>-1</sup> for the red set-up. The smaller number of non-saturated ThAr reference lines in the red spectra, is primarily responsible for the increased scatter in the red spectra solutions.

However the error is well below the individual pixel size of about  $3 \text{ km sec}^{-1}$  in all spectra. Each extracted 1-D standard star and nebular spectrum was re-binned to a linear wavelength scale from the ThAr comparison 1-D spectra taken nearest in time to that spectrum.

The nebular spectra were flux calibrated by employing spectra of the standard stars  $\xi^2$  Cet, 29-Psc, and  $\theta$  Crt, taken with a  $6.6''$  slit oriented parallel to the parallactic angle, obtained at the beginning and end of each night. The spectra of the flux standard stars were extracted, wavelength calibrated, and compared to tabulated, low resolution flux calibrated spectra of the same star taken at contiguous  $16\text{\AA}$  intervals (Hamuy et al. 1994). A “sensitivity” function that converts total counts within a pixel in the extracted spectra to units of flux was then established by fitting a multiplicative function whose effects bring the two standard star spectra into alignment, using in the IRAF task *sensfunc*.

Prior to wavelength calibration, to improve the quality of the fit, each spectra was divided by a spectrum representing the combined signature of the blaze function and a black body. The continuum was strongly non-linear on the edges of the orders, where the blaze function was at its minimum, and in the vicinity of broad stellar and atmospheric absorption features. This division has the effect of flattening the standard star spectra, making it more tractable to fit the sensitivity function with a lower order function. This was necessary in order to constrain the sensitivity function fits which were based upon only a dozen or so calibration points across each echelle order. A flat field spectrum of a quartz-iodide continuum source, taken through the narrowest possible decker ( $1''$ ), was obtained each night for the purpose of flattening

the spectra. This spectrum was extracted in the same manner as the standard star spectra, and divided into each standard star and object spectrum prior to wavelength calibration. The resultant sensitivity functions were then applied to all other object spectra taken within that night. A comparison between a flux calibrated standard star spectrum employing this sensitivity function and the original low-resolution spectrum is shown in Figure 2.5. The two spectra essentially overlap, with only 1-5% difference between continuum levels except along the extreme edges of orders where the echelle blaze yields a minimum intensity.

Individual flux calibrated object spectra within an instrumental set-up, with similar exposure times and extraction widths, were then co-added. A correction for instrumental flexure affecting wavelength alignment between individual spectra was made beforehand. This was accomplished by choosing a fiducial spectrum within an object group, calculating the average shift in wavelength of a series of strong lines observed in each of the other spectra relative to the fiducial's values, then adding an additional shift equal to the amount necessary to bring the fiducial's measure of a strong night sky line wavelength into alignment with the laboratory value. This put each individual spectrum onto an absolute wavelength scale exhibiting an average scatter of about  $\pm 1 \text{ km sec}^{-1}$  within each group. To account for the possibility of variable cloud obscuration of the object in between individual exposures, or between those taken on differing nights, the individual spectra were scaled in flux to another chosen fiducial exhibiting the strongest average flux value for a series of strong emission lines. This assumes that the brightest spectra was the one least likely to have been obscured by clouds. Spectra were then added together using the average value at

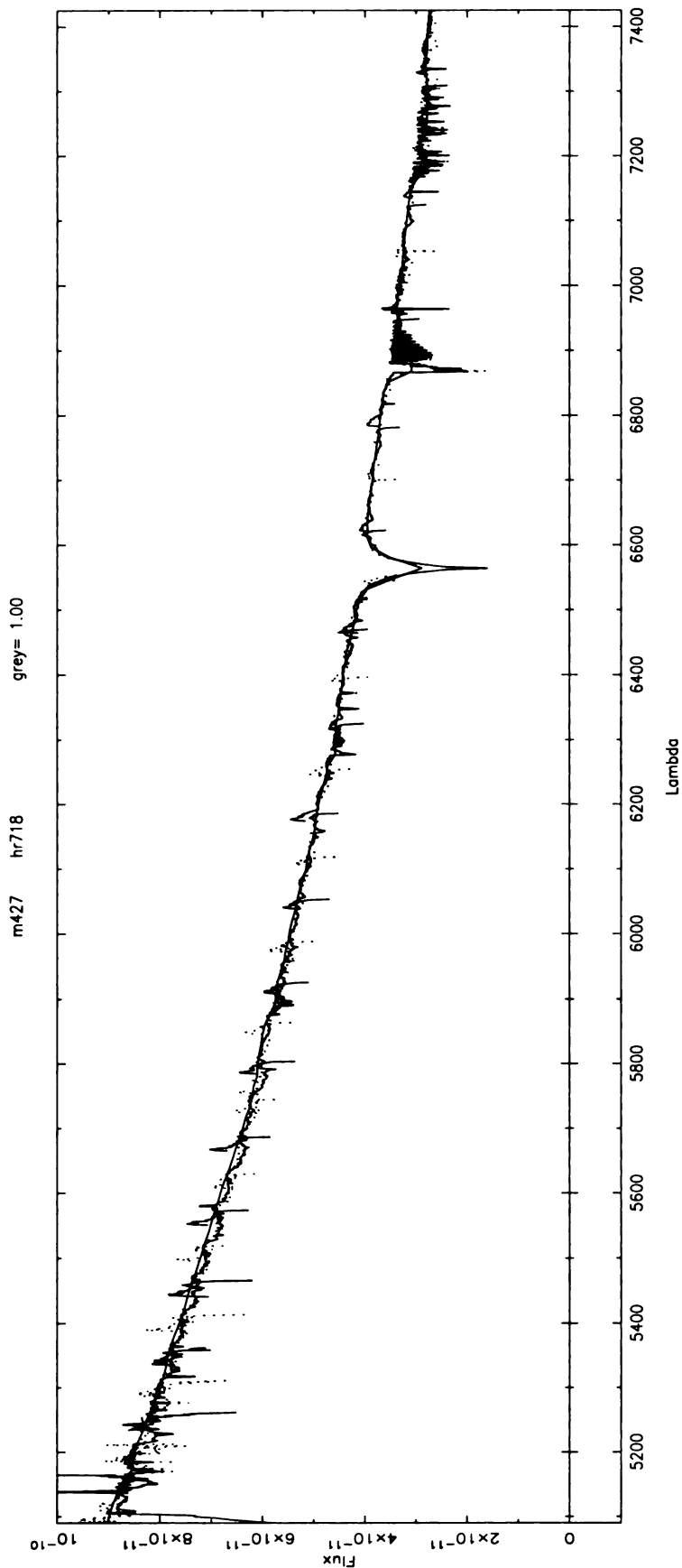


Figure 2.5 A comparison between the extracted spectrum, calibrated with the fit to the sensitivity function used to calibrate the nebular spectra, and a tabulated low resolution spectrum (Humay et al. 1994) for the flux standard star  $\xi^2$  Cet (HR 718). The smooth curve is the tabulated spectrum, whereas the somewhat more broken curve is the flux calibrated spectrum. Over most of the orders the two spectra nearly overlap, typically to better than 5%. There is some deviation on the edges of orders as indicated by the “spikes” sticking out above the smooth curve.

Table 2.2 Effective total integration times of co-added object spectra (in hours).

Set-Up	Exp. Length	Extraction Width: ( <i>full</i> , <i>cavity</i> )	
Blue	<i>short</i>	0.5	0.5
	<i>long</i>	6.6	6.6
Intermediate	<i>short</i>	0.3	0.3
	<i>long</i>	5.0	5.0
Red	<i>short</i>	0.5	0.5
	<i>long</i>	8.5	8.5

each pixel, weighted by the previously mentioned error array, excluding those pixels whose value deviated by more than  $3\sigma$  from the average at that position. Cosmic rays were effectively rejected from the calculated average at each pixel, due to the large sigma assigned to the pixels in which they were located during the extraction process, and the use of sigma clipping. Final spectra derived from individual spectra of both short and long duration and of differing extraction widths along the slit were constructed for all three instrumental set-ups in this manner. Spectra created from individual short duration exposure spectra (30 sec, 120 sec, 300 sec) are denoted *short*, those from long duration exposure (1000 sec, 1800 sec) labeled *long*. Those spectra extracted from the full length of the slit are called *full*, while those from the extracted over the position of the slit corresponding to the central cavity region are called *cavity*. Table 2.2 includes the total effective integration times of each extracted spectra.

The blue spectra exhibited artifacts known as Rowland ghosts, which arise from beat frequencies due to periodic ruling errors from the  $79 \text{ cm}^{-1}$  echelle grating used in the blue set-up, and are a commonly known anomaly of spectra obtained with



this class of grating. These ghosts manifest themselves as two pairs of symmetrically positioned emission lines flanking real, strong emission lines in the extracted spectra. The position and strength of these ghost lines is related to the position and strength of the line they flank. The method of Baldwin et al. (2000) was followed in modeling the ghosts with a kernel, convolving it with the spectra, then subtracting off the convolved spectra from the original spectra. No Rowland ghosts were evident in the intermediate and red set-up spectra, which were taken with a different echelle grating.

Emission line detection was carried out on the long, full object spectra using the program RDGEN (Carswell et al. 2001). This program automatically finds emission lines above a specified threshold related to signal-to-noise (S/N). Details of its operation may be found in Appendix B. RDGEN provided estimates of the center wavelength, full width at half maximum (FWHM), and S/N for each detected line. The original 2-D spectra were then examined to remove spurious line detections caused by residual scattered light artifacts, specifically cross-CCD flares which arise from a combination of the nature of the echelle grating and reflection of strong lines off the optics of the spectrograph. These appeared as roughly horizontal or vertical streaks across the CCD, centered on strong emission lines, and can mimic or blend with real emission lines at the locations of the orders they intersect. Residual cosmic ray strikes were also identified and removed at this stage. Remaining line detections were confirmed by looking for evidence of true nebular origin, i.e. similar line morphology, exclusive filling of the nebular portion of the image slit, and repeated detection within orders with overlapping wavelength coverage. The statistics of the remaining lines detections, as a percentage of those retained versus the total number of lines detected

in particular S/N and FWHM bins suggest that lines with a  $S/N \geq 7$  were at the noise limit, and those above  $S/N = 20$  were clearly detected. Similarly, lines with FWHM in a range bounded by the instrumental resolution at  $\approx 9 \text{ km sec}^{-1}$  and an upper limit of  $50 \text{ km sec}^{-1}$  were considered probable detections when the same statistics were considered. In general only line detections having a  $S/N \geq 7$  and with FWHM in the above range were retained as probable detections of genuine lines. However, exceptions were made for some line detections outside these limits, such as when the lines were clearly evident in the extracted spectra and in the 2-D image, or for line blends detected by the software as a single lines, but having FWHM that exceeded the upper bound.

A portion of the full, long blue spectrum is depicted in Figure 2.6. In general, emission line profiles fell into 3 categories: Gaussian, double peaked, or blends. Any line of sight penetrates through the nebula and intersects both the forward and backward edge of the expanding gas shell, as well any intervening more highly ionized region in between. The double peaks arise from the large change in the radial component of the expansion velocity between the front and back components of the shell (on the order of  $12 \text{ km sec}^{-1}$  for [N II] in IC 418, as determined by Acker et al. (1992), and quoted in Hyung, Aller, & Feibelman (1994) (hereafter HAF)). Thus double peaks generally denote a line originating from the outer, more rapidly expanding portion of the nebula. In contrast, a Gaussian line profile signifies confinement of its parent species to the slower moving inner regions of the nebula, where the differential expansion velocity is either unresolved at our resolution or below the intrinsic profile FWHM of the emitting gas itself (about  $20 \text{ km sec}^{-1}$  for hydrogen). Blended lines

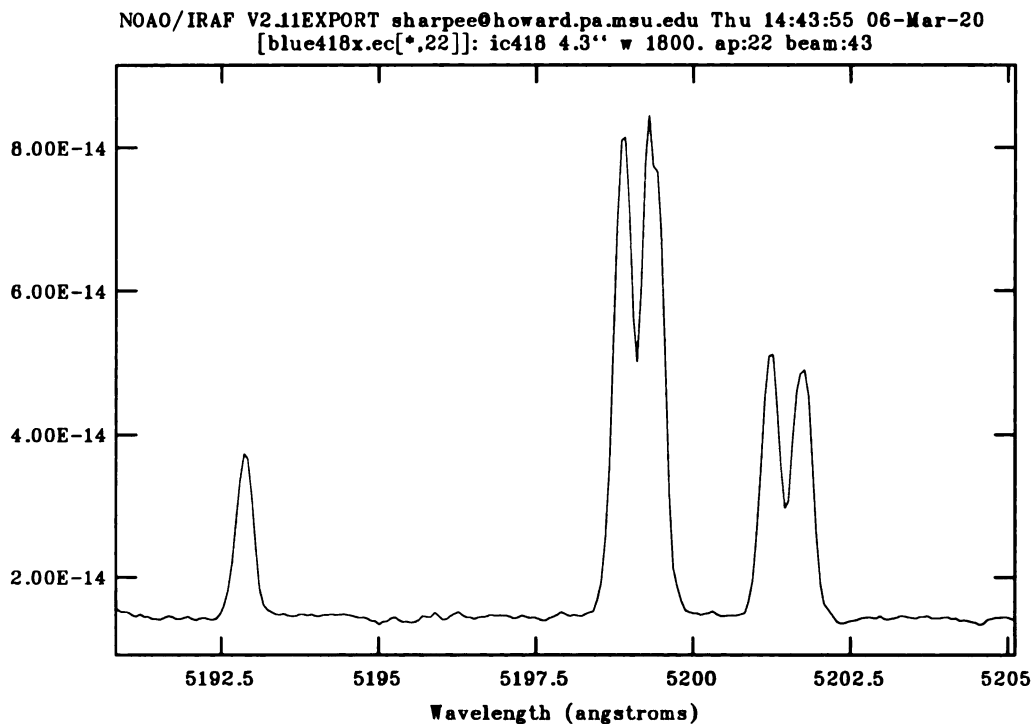


Figure 2.6 A portion of the full slit blue spectrum extracted from the order shown in Figure 2.4. This demonstrates the differing profile morphologies exhibited by lines whose parents ions are of different ionization potentials. Higher ionization lines, such as [Ar III]  $\lambda 5191.8\text{\AA}$  on the left have more Gaussian-like profiles, while low ionization lines, such as the [N I] doublet on the right have double peaked Gaussian-like profiles, as influenced by the differential expansion velocity of the nebula exceeding the thermally generated width of the line.

take on a variety of appearances, depending upon the particular morphology, number, and difference in wavelength of its constituents.

For every line detection made by RDGEN in the full, long spectra, deemed genuine by the above standards, a fit to the local continuum and line profile in the corresponding long, cavity spectrum for the same instrumental set-up was made at the wavelength of the detection. For lines saturated in the long exposures (see Table 2.3), the fit was applied to the short, cavity spectrum. The fitting function was the combi-

Table 2.3 Lines saturated in the *long* spectra.

Set-Up	Lines (Ion/Wavelength (Å))
Blue	H $\beta$ , [O III] 4959,5007 [O II] 3727,3729
Intermediate	H $\alpha$ , [N II] 6548,6583 [O II] 7320,7330 [Ar III] 7137, He I 5876,7067
Red	[S III] 9072,9520

nation of a single Gaussian and linear function representing the line profile shape and the local continuum. Such a function was fit to all lines regardless of a priori knowledge of actual line profile morphology, using a standard  $\chi^2$  minimization software routine, the details of which may be found in Appendix C. The wavelength measure in this case was the center of Gaussian function that best fit the line profile. In cases where the profiles were clearly non-Gaussian, the flux was calculated by fitting the local continuum with a low order polynomial around the line and simply summing the flux contained within the region where the line clearly extends beyond the continuum. The wavelength measure here was the first moment of the line profile, the flux averaged wavelength over the entire line profile. Where line blends were clearly separable by multiple Gaussian, they were fitted using multiple Gaussian functions by the “d-d” (de-blend) option in the IRAF task *splot*. Otherwise the simple sum was retained.

Night sky emission lines from the Earth’s atmosphere also appear in these spectra, particularly in the red spectrum. These lines are narrower than the PN lines in general, and have uniform surface brightness along the slit (see Figure 2.7). With the

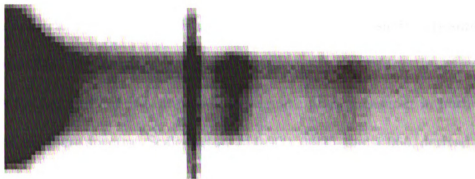


Figure 2.7 A portion of the 2-D red spectrum which depicts an obvious night sky emission line near the center of the image. Note that it fills the entire slit rather than just the portion superimposed on the nebula, as the adjacent nebular line does. Both lines sit on the wing of the broad nebular emission line blend of O I  $\lambda 8446\text{\AA}$  on the left edge of the picture. From Osterbrock et al. (1996) the night sky line is most likely 6-2 P2(3.5)  $\lambda 8452.250\text{\AA}$ , a vibration-rotational transition of the terrestrial OH molecule, and has a FWHM of  $\approx 9 \text{ km s}^{-1}$  which is the instrumental resolution. The adjacent nebular line we believe is He I  $\lambda 8451.158$ .

aid of the Osterbrock (1996,1997) atlases of night sky lines, plus careful examination of the 2D images, it was possible to identify most of these and eliminate them from the line list. However a few such lines in blends may have survived this screening process.

To account for differing photometric conditions on the observing nights, for errors in positioning the slit in exactly the same place between nights, and differences in the wavelength dispersion solutions used in the individual spectra, all line mea-

measurements were normalized to a chosen fiducial, the long intermediate spectra. This was accomplished using the procedure described in Sect 2.3.2, and involved making comparisons between measurements for the same line present in the overlap regions between spectra. Similarly, the line measurements from the short exposure spectra were normalized to their longer exposure counterparts, by taking the average ratio of fluxes for ten well defined intermediate strength lines, measured in both the long and short exposure spectra. Scale factors of 0.900, 0.925, and 1.060, derived from the average ratio of the ten lines, were applied multiplicatively to the line measurements from the short exposures spectra of the blue, intermediate, and red, respectively, in order to align them with the fiducial.

Finally, line measurements were considered arbitrarily to represent the same line if the difference in wavelengths did not exceed  $15 \text{ km sec}^{-1}$ . Only those measurements possessing a S/N within a factor of two of the largest value, among all measurements considered to represent the same line, were included in the final sum. Also rejected were line measurements corresponding to line profiles with obviously poor morphology, such as those on the edges of orders, or in regions where the flux calibration was suspect, such as near strong absorption features in the standard stars. Line measurements meeting the above criteria were averaged together, with the largest S/N among the group of measurements and its FWHM adopted as the S/N and FWHM of the individual line.

The wavelengths for all lines were corrected to the air wavelength in the nebular rest frame by using the median difference between the accepted and observed wavelengths for 47 Balmer and Paschen lines (see Table 2.4). The resultant correction

Table 2.4 Observed versus laboratory wavelengths for Balmer and Paschen lines.

Line	Lab (Å)	Observed (Å)	Vel (km sec <sup>-1</sup> )
Balmer			
H30	3662.256	3663.100	-69.1
H29	3663.404	3664.244	-68.8
H28	3664.676	3665.521	-69.2
H27	3666.095	3666.937	-68.9
H26	3667.681	3668.521	-68.7
H25	3669.464	3670.302	-68.5
H24	3671.475	3672.315	-68.6
H23	3673.758	3674.597	-68.5
H22	3676.362	3677.202	-68.5
H21	3679.352	3680.191	-68.4
H20	3682.808	3683.648	-68.4
H19	3686.830	3687.673	-68.6
H18	3691.554	3692.400	-68.8
H17	3697.152	3698.002	-69.0
H16	3703.852	3704.699	-68.6
H15	3711.971	3712.817	-68.4
H14	3721.938	3722.746	-65.1
H13	3734.368	3735.218	-68.3
H12	3750.151	3751.007	-68.5
H11	3770.630	3771.493	-68.7
H10	3797.898	3798.766	-68.6
H9	3835.384	3836.264	-68.8
H7	3970.072	3970.982	-68.8
H6	4101.734	4102.682	-69.3
H5	4340.464	4341.460	-68.8
H $\beta$	4861.325	4862.439	-68.7
H $\alpha$	6562.800	6564.305	-68.8
Paschen			
P28	8298.834	8300.780	-70.3
P27	8306.112	8307.964	-66.9
P26	8314.260	8316.135	-67.7
P25	8323.424	8325.322	-68.4
P24	8333.783	8335.679	-68.3
P23	8345.552	8347.465	-68.6
P22	8359.003	8360.887	-67.6
P21	8374.475	8376.402	-69.0
P20	8392.396	8394.317	-68.7
P19	8413.317	8415.241	-68.6
P18	8437.955	8439.838	-66.9
P17	8467.253	8469.188	-68.6
P16	8502.483	8504.427	-68.6
P15	8545.382	8547.343	-68.8
P14	8598.392	8600.346	-68.2
P13	8665.018	8667.004	-68.8
P12	8750.473	8752.464	-68.3
P11	8862.783	8864.779	-67.6
P9	9229.014	9231.107	-68.0
P8	9545.972	9548.037	-64.9
Median			-68.6
Standard Dev.			0.9

of  $+68.6 \text{ km sec}^{-1}$  corresponds to a heliocentric velocity of  $+61.3 \text{ km sec}^{-1}$  which agrees well with published values of  $+61.0 \text{ km sec}^{-1}$  (Acker et al. 1992) and  $+62.0 \text{ km sec}^{-1}$  (Wilson 1953).

Intervening nebular and interstellar dust act to preferentially scatter out the blue component of, or “redden”, the inbound flux. To correct for this effect, final line fluxes were de-reddened through the application of the reddening curve of Cardelli, Clayton, & Mathis (1989), with a standard  $R_V$  value of 3.1. The de-reddened intensity of any emission line can be related to the de-reddened intensity of  $H\beta$  through the following relationship:

$$\frac{I_{\lambda o}}{I_{H\beta o}} = \frac{I_{\lambda}}{I_{H\beta}} 10^{c_{H\beta}[f(\lambda)-f(H\beta)]}, \quad (2.1)$$

where  $I_{\lambda}$  is the measured flux of a line,  $I_{\lambda o}$  the measured flux corrected for reddening,  $I_{H\beta}$  and  $I_{H\beta o}$  the same for the  $H\beta$ ,  $c_{H\beta}$  is the log extinction at  $H\beta$ , and the quantities  $f(\lambda)$  and  $f(H\beta)$  are the relative extinction curve values of Cardelli, Clayton, & Mathis normalized to  $H\beta$  at the wavelengths of the lines. The value for  $c_{H\beta}$  was established by comparing the final relative flux values between 20 pairs of Balmer and Paschen lines beginning from the same level. Since these lines arise from the same upper level, their relative intensities should be the simple ratio of the products of their Einstein transition coefficients and photon frequencies. Since the intrinsic intensity ratio is known, the equation:

$$\frac{I_{P11,o}}{I_{H11,o}} = \frac{I_{P11}}{I_{H11}} 10^{c_{H\beta}[f(P11)+f(H11)]}, \quad (2.2)$$

may be solved for  $c_{H\beta}$  for any pair of Paschen (P11) or Balmer (H11) lines.

Carried out for 20 pairs of lines (see Table 2.5), a median value of  $c_{H\beta} = 0.34 \pm 0.5$



Table 2.5 Reddening parameters

Line Ratio	$c_{H\beta}$
P28/H28	0.29
P27/H27	0.40
P26/H26	0.34
P25/H25	0.35
P24/H24	0.34
P23/H23	0.36
P22/H22	0.39
P21/H21	0.30
P20/H20	0.33
P19/H19	0.34
P18/H18	0.32
P17/H17	0.33
P16/H16	0.35
P15/H15	0.33
P14/H14	0.24
P13/H13	0.35
P12/H12	0.37
P11/H11	0.38
P10/H10	0.19
P9/H9	0.32
Median $c_{H\beta}$	0.34
$\Delta c_{H\beta}$ (Stdev)	0.05

was determined where the error refers to the standard deviation about the average. This value exceeds the published values of 0.21 from HAF and 0.14 from HKB, but agrees well with the value of 0.34 determined by the Shaw & Dufour (1995) re-analysis of the HAF data, as well as with the value of 0.29 from Mendez (1989). It is likely that the amount of reddening varies with position in the nebula, so some variance in the coefficient is expected when comparing studies looking at different parts of the nebula. De-reddened using eq. 2.1 above and our determined extinction value at  $H\beta$ , the Balmer to Paschen line intensity ratios show a 6% scatter from the expected

values.

## 2.3 Error Analysis

Here we assess the degree of uncertainty in the wavelength and flux measurements by studying the consistency, within and between each spectrum of repeated measures of the same lines in differing spectral orders and in spectra from different observational set-ups. In addition, we gauge the degree of accuracy of our reduction steps by comparing to theoretical values and previously observed values of the wavelength and flux for a selected group of lines.

### 2.3.1 Internal Agreement

In Figure 2.8, the wavelength difference between the reddest and bluest individual measurements (in the sense of reddest minus bluest) of the same line measured from different orders of the same echelle spectrum, are plotted against the minimal S/N of those measures. Comparison against the minimal S/N, emphasizes the poorest quality measurements, such as those closest to the edges of spectral orders, where the S/N is generally lower, profiles less distinct, and calibration generally the worst. Similarly, we plot the ratio of the fluxes of the reddest and bluest measurements for the same line. The  $1\sigma$  scatter in the wavelength differences (in  $\text{km sec}^{-1}$ ) and flux ratios, and the median values of all such measures in both parameters from different ranges of minimal S/N are compiled in Table 2.6. We include night sky line detections in the wavelength analysis that follows, but not in the flux analysis, since night sky

line intensities vary with time and position in the sky.

The scatter in both wavelength and flux generally falls in all three spectra as one goes beyond the  $S/N=20$  value established for lines “clearly separated” from the continuum. For higher  $S/N$  measurements, the median wavelength difference and the scatter about the average wavelength difference declines down to the level of the individual dispersion solution fits (about  $0.5\text{-}1.0\text{ km sec}^{-1}$  in the blue and intermediate red, and  $1.0\text{-}1.5\text{ km sec}^{-1}$  in the red). Flux agreement also improves across the  $S/N>20$  threshold for all three spectra, again on a par with the 5% uncertainties in the individual sensitivity function fits used to flux calibrate the individual constituent spectra. If the five strongest lines with multiple measurements are chosen from each spectrum, the average velocity difference and ratio of flux between measures is  $0.4\pm0.4\text{ km sec}^{-1}$  and  $0.95\pm0.05$ ,  $0.23\pm0.08\text{ km sec}^{-1}$  and  $1.04\pm0.04$ , and  $1.4\pm1.0\text{ km sec}^{-1}$  and  $1.03\pm0.02$  for the blue, intermediate, and red spectra respectively. The somewhat larger wavelength difference in the red arises directly from the larger residual in the red dispersion solutions. An obvious small shift is seen upon inspection of their respective profiles, but is still well within the uncertainty expected from that source. It is also small compared with the instrumental resolution of  $10\text{ km sec}^{-1}$ . The scatter in wavelength and flux ratio matches the expected uncertainty from calibration for line detections above  $S/N=20$ , suggesting that errors from the calibration steps dominate the total error in the measured parameters for those detections. The increasing amount of scatter below the  $S/N=20$  cutoff, indicates that measurement errors contribute dominate in weaker lines. Since these measurements are made at the edge of each echelle order and thus represent the worst case comparisons, we judged

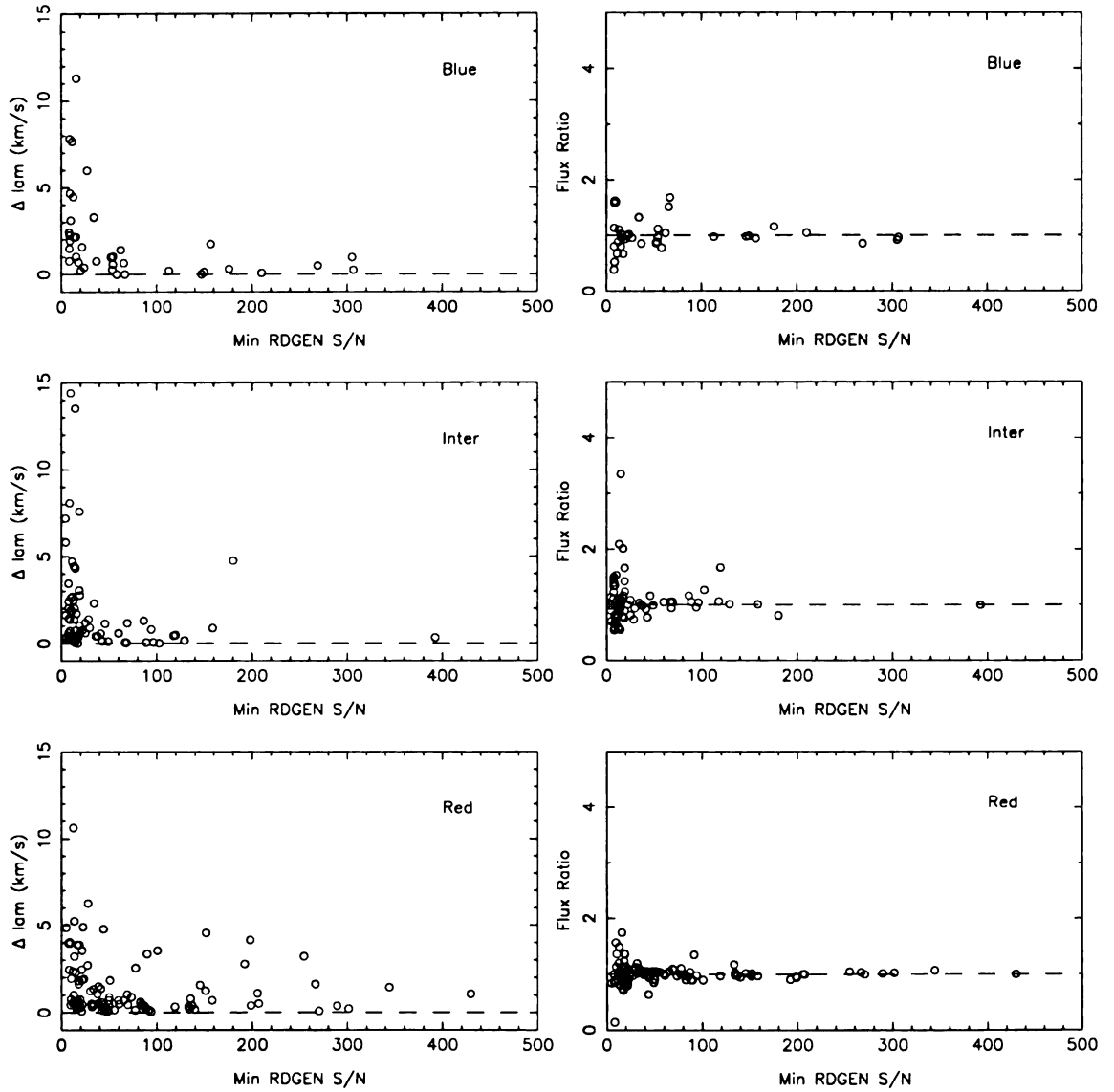


Figure 2.8 The absolute value of the wavelength difference (in  $\text{km sec}^{-1}$ ) between the reddest and bluest measures ( $\Delta \text{lam} \equiv \text{reddest} - \text{bluest}$ ) among those used to compute the final line wavelength values, versus the minimum S/N among all the measures. Similarly, the ratio of the reddest to bluest measurements' fluxes (Flux Ratio  $\equiv \text{reddest}/\text{bluest}$ ).

Table 2.6 Statistics of matched line measurements within blue, intermediate, and red set-ups, and in their overlap regions

Setup/Stat	S/N Range	N	Med <sup>(a)</sup>	$\sigma$
<b>Blue</b>				
Wavelength	> 7	41	0.974	2.457
	> 20	26	0.259	1.260
Flux	> 7	41	0.950	0.284
	> 20	26	0.947	0.199
<b>Intermediate</b>				
Wavelength	> 7	79	0.759	2.641
	> 20	35	0.456	0.750
Flux	> 7	63	1.014	0.405
	> 20	29	1.015	0.089
<b>Red</b>				
Wavelength	> 7	103	0.755	1.768
	> 20	74	0.627	1.480
Flux	> 7	54	1.002	0.151
	> 20	37	1.015	0.089
<b>Intermediate-Blue</b>				
Wavelength <sup>(b)</sup>	> 20	40	1.257	2.290
	*		0.211	3.468
Flux <sup>(c)</sup>	> 20	39	1.138	0.233
	*		0.997	0.205
<b>Intermediate-Red</b>				
Wavelength <sup>(b)</sup>	> 20	4	1.424	1.185
Flux <sup>(c)</sup>	> 20	3	0.972	0.048

<sup>(a)</sup> median and  $\sigma$  for wavelength in  $\text{km s}^{-1}$

<sup>(b)</sup> Intermediate - Other Spectra  $\lambda$

<sup>(c)</sup> Other Spectra Flux / Intermediate Flux

\* after correction for systemic shift (see text Sect 2.3.2)

both the flux and wavelength values to be in tolerable agreement, and the spectra to be self consistent.

In Figure 2.9, the same flux ratios and wavelength differences are plotted as a function of wavelength for all three spectra, including only stronger ( $S/N \geq 20$ ) lines. This is done to look for any gross systemic errors in dispersion solutions or in the sensitivity functions that trend with wavelength (which acts as a proxy for position on the CCD). The general wavelength difference scatter does increase on the edges of all spectra. This is expected from the declining instrumental sensitivity at the edges of spectra, which makes line profiles less distinct, and measures from order to order less certain. Apart from the systemic trend in the red spectrum past 9400Å, due to the previously mentioned deterioration of the dispersion solution fits in this undersampled region, no other apparent trends are evident. No evidence for a wavelength dependent flux ratio is present in any of the three spectra.

### 2.3.2 Systemic Disagreements Between Spectra

Systemic differences between the three different instrumental setups are determined by comparing measurements for lines with at least one measurement in each overlapping spectrum which had sufficient  $S/N$  to be included in the final average values for that line.

In Figure 2.10 the wavelength difference (the average of the intermediate spectrum measurements minus the blue spectrum measurement) and the flux ratio (the blue spectrum measurement divided by the average of the intermediate spectrum mea-

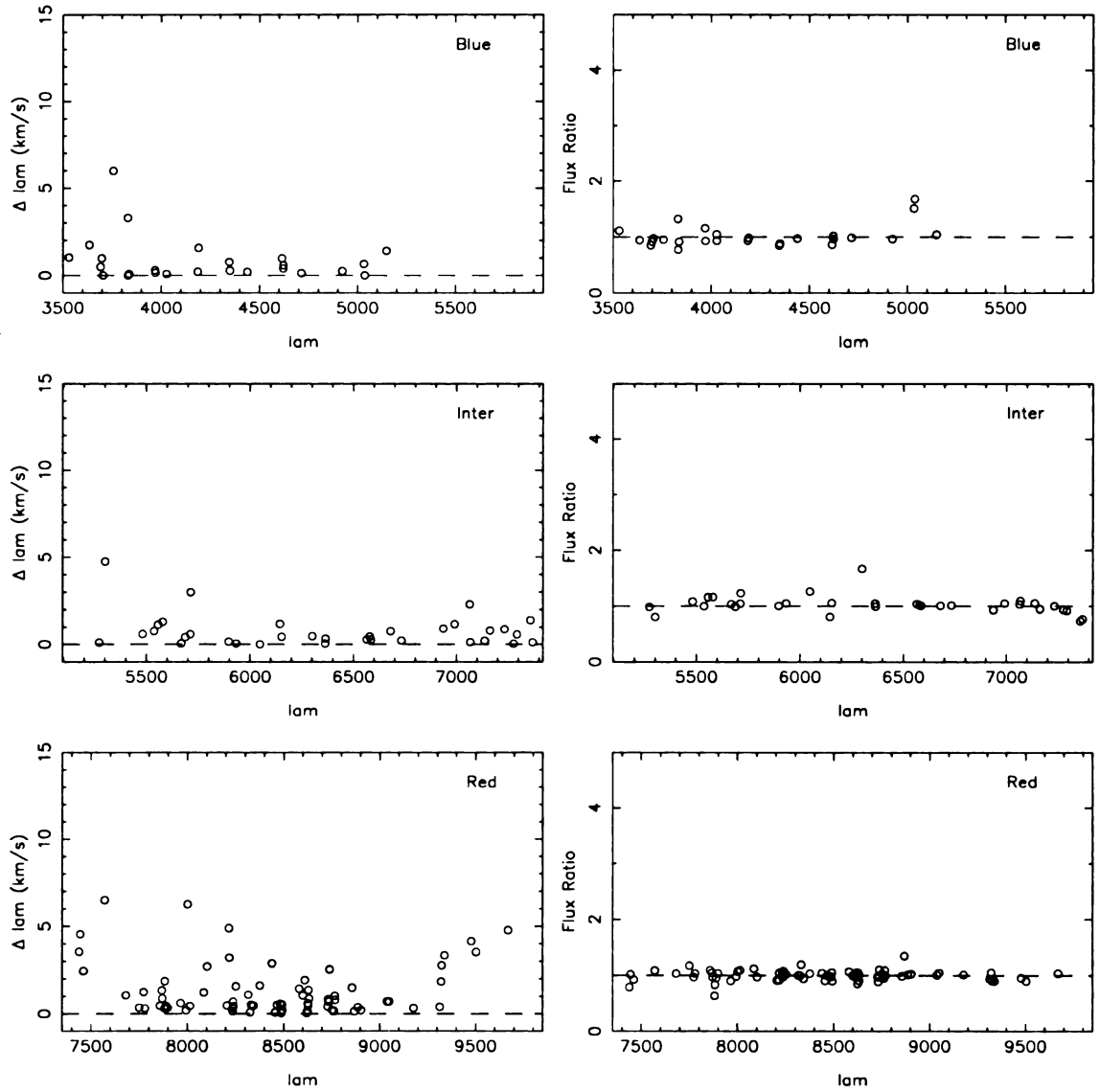


Figure 2.9 Flux and Wavelength Agreement as a Function of Wavelength in Blue, Intermediate, and Red Spectra.

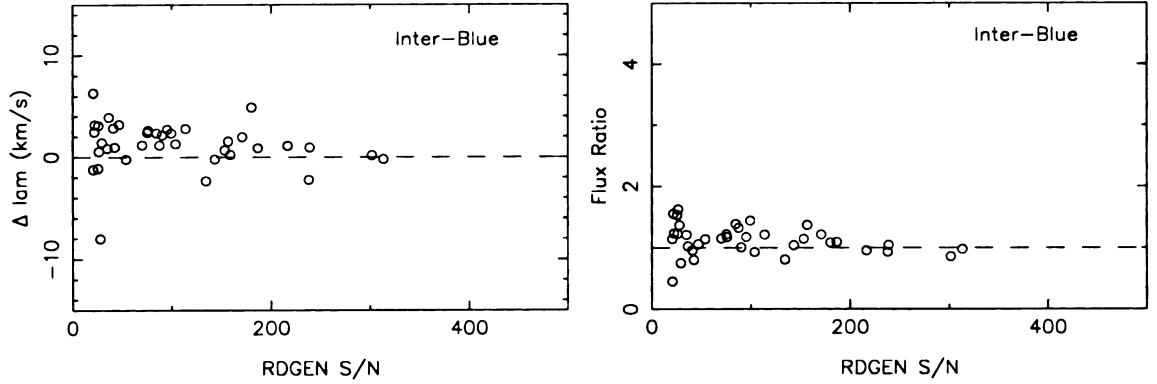


Figure 2.10 Statistics of Multiple Line Measurements in the Intermediate-Blue Overlap Region

surements) are plotted as functions of the final S/N of the line, for all lines with a S/N > 20. The median values of the ratios and differences and the  $1\sigma$  scatter in those values about the mean for all such lines are listed in Table 2.6. The median wavelength difference of approximately  $1.2 \text{ km sec}^{-1}$  was added to the blue measurements to bring the two spectra into alignment. Similarly, a scale factor of 1.138 was divided into every blue measurement to align the two spectra (we arbitrarily chose to use the intermediate spectra as the fiducial for both wavelength and flux). These corrections were applied to the blue measurements prior to collation of the measures to determine the line's wavelength and flux. The asterisked rows in Table 2.6 show the significant improvement in the median value of wavelength difference and flux ratio with blue measurements corrected in this manner. The flux agreement seems tolerable, in light of the expected 5% errors in the flux calibration for each spectrum.

Unfortunately, in the intermediate-red spectra overlap region, similar comparisons are difficult to interpret, because the size of the overlap was small, and due to the lack



of  $S/N \geq 20$  measurements in the portion of the intermediate spectrum corresponding to the overlap with the red. The scatter here is also expected to be somewhat larger given that more individual measurements can contribute to the final line attribute calculations, sometimes as many as four, two from each of the spectra. The results in Table 2.6 suggest that a small offset exists in wavelength between the intermediate and red spectra wavelength measurements. Because the overlap region covers only the extreme end of the intermediate spectrum and the beginning of the red spectrum, covering only about two orders in each setup, it was decided not to adjust all red values based upon results from one or two orders alone. The flux values show the same level of agreement, despite the small number and mostly lower  $S/N$  measurements, as in the blue-intermediate region, again within the expected 5% flux calibrations errors from each spectrum. Increasing our confidence in the match between the red and intermediate measurements, is the agreement between the Balmer (from the blue) and Paschen (from the red) line wavelengths (Table 2.4), and the low scatter in the de-reddened fluxes (Table 2.5). Since the blue and intermediate measures are both fairly close, we infer that the intermediate and red measurements are within 95% or better agreement in flux, and are apart by no more than  $1 \text{ km sec}^{-1}$  in wavelength.

### **2.3.3 Obtaining a Total Error Estimate for Final Line Values**

Consistency has been shown both within and between the spectra, and a reasonable idea of what sources of error dominate particular classes of lines has been determined. Now we attempt to decouple the various sources of error to arrive at a crude estimate

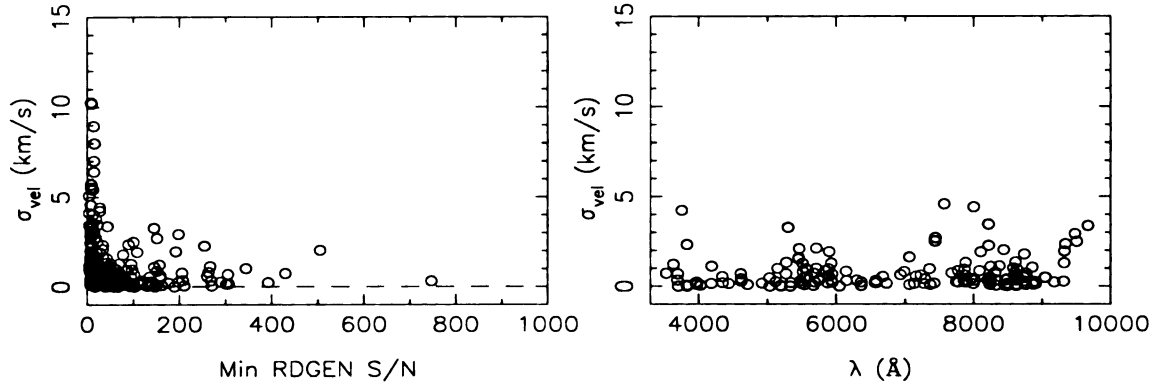


Figure 2.11 **Left:** The  $1\sigma$  scatter from individual measurements of the wavelength and flux of a particular line used to calculate that line's wavelength and flux, for all lines as a function of S/N. **Right:** The same information plotted against wavelength ( $\lambda$ ) for all lines  $S/N \geq 20$ .

of the total error in the final wavelengths and fluxes for the lines.

### Wavelength Uncertainty

One source of wavelength error is poorly defined line profiles, or measurements in the vicinity of scattered light features or flares, problems to which weak lines are more vulnerable. For lines below  $S/N < 20$ , this measurement error dominates. To obtain a value for the likely error due to this effect, we first plot the  $1\sigma$  scatter (in  $\text{km sec}^{-1}$ ) in the individual wavelength measurements for each particular line, for all measurements that went into calculating that line's final wavelength, against the S/N of those lines (left panel Figure 2.11). The average amount of that  $1\sigma$  scatter among those lines above and below the  $S/N=20$  cutoff is then calculated. We make the assumption that these average values of individual measurement's scatter are characteristic of the *measurement* errors for *all* lines within each S/N regime even though, as has been shown, it is more likely the residuals in the wavelength calibration dominate for lines

with  $S/N > 20$ .

To obtain an estimate of the error due to wavelength calibration problems alone, we plot the same  $1\sigma$  scatter in individual measurements as was done before, as a function of wavelength for *only* those lines with a  $S/N > 20$  (right panel Figure 2.11). Then we calculate the average of the  $1\sigma$  scatter within 500 Å bins, and adopt this value as the error arising from the calibration steps for all lines with wavelengths within a specific bin. For the most part these values fall within the expected 0.5 – 1.5 km sec<sup>-1</sup> errors in the dispersion solutions, and including this factor takes into account the deterioration of the dispersion solution in the red spectrum seen in Figure 2.9.

Finally, to look for any absolute systemic bias in the final wavelength values, we determined the difference between the final values of wavelength (corrected to the rest frame of the nebula as established for ionized hydrogen) for several well known un-blended emission lines (Table 2.7) with indisputable identifications, against their accepted wavelengths as drawn from the NIST database <sup>2</sup>. The results are shown in the upper panel of Figure 2.12.

The lower panel of the same figure, shows the wavelength difference plotted as a function of the ionization potential of the lines' parent ions. There is a definite trend towards a higher velocity difference for lower ionization potential ions. This might be reflective of a legitimate differential expansion velocity with ionization potential energy along our line of sight to the nebula, like that predicted by Gesicki, Acker, & Szczerba (1996) for IC 418. It might also simply indicate uncertainties in the accepted wavelengths (indicated by the error bars in the plot) or may be the result

---

<sup>2</sup>[http://physics.nist.gov/cgi-bin/AtData/lines\\_form](http://physics.nist.gov/cgi-bin/AtData/lines_form)

Table 2.7 Wavelengths of strong lines, and ionization potentials of their parent ions.

Line Ion/ $\lambda(\text{\AA})$	Obs $\lambda$ ( $\text{\AA}$ )	Lab $\lambda$ ( $\text{\AA}$ )	$\Delta\lambda$ ( $\text{km sec}^{-1}$ )	I.P. ( $\chi$ ) (eV)
[O II] 3727	3726.035	3726.032	-0.24	35.12
[O II] 3729	3728.785	3728.815	2.41	35.12
[Ne III] 3869	3868.745	3868.75	0.39	63.45
[Ne III] 3968	3967.457	3967.46	0.23	63.45
[S II] 4068	4068.668	4068.6	-5.01	23.34
[S II] 4076	4076.374	4076.35	-1.77	23.34
[O III] 4363	4363.191	4363.209	1.24	54.94
[Ar IV] 4711	4711.352	4711.37	1.15	59.81
[Ar IV] 4740	4740.205	4740.17	-2.22	59.81
[O III] 4959	4958.915	4958.911	-0.24	54.94
[O III] 5007	5006.845	5006.843	-0.12	54.94
[Ar III] 5192	5191.702	5191.816	6.59	40.74
[N I] 5198	5198.012	5197.902	-6.35	14.53
[N I] 5200	5200.329	5200.257	-4.15	14.53
[Cl III] 5517	5517.686	5517.66	-1.41	39.61
[Cl III] 5537	5537.853	5537.7	-8.29	39.61
[O I] 5577	5577.389	5577.339	-2.69	13.62
[N II] 5755	5754.629	5754.59	-2.03	29.60
[O I] 6300	6300.405	6300.304	-4.81	13.62
[S III] 6312	6312.107	6312.06	-2.23	34.79
Si II 6347	6347.193	6347.11	-3.92	33.49
[O I] 6363	6363.886	6363.776	-5.19	13.62
Si II 6371	6371.418	6371.37	-2.26	33.49
[N II] 6548	6548.096	6548.05	-2.11	29.60
[N II] 6583	6583.467	6583.45	-0.77	29.60
[S II] 6717	6716.523	6716.44	-3.71	23.34
[S II] 6730	6730.893	6730.816	-3.43	23.34
[Ar III] 7135	7135.744	7135.79	1.93	40.74
[O II] 7320	7320.135	7319.99	-5.94	35.12
[O II] 7330	7329.679	7329.67	-0.37	35.12
[Ar III] 7751	7751.074	7751.11	1.39	40.74
[Cl II] 8579	8578.795	8578.7	-3.32	23.81
[S III] 9068	9068.905	9068.6	-10.09	34.79
[Cl II] 9123	9123.737	9123.6	-4.50	23.81
[S III] 9531	9530.929	9531.1	5.38	34.79
Mean			-1.90	

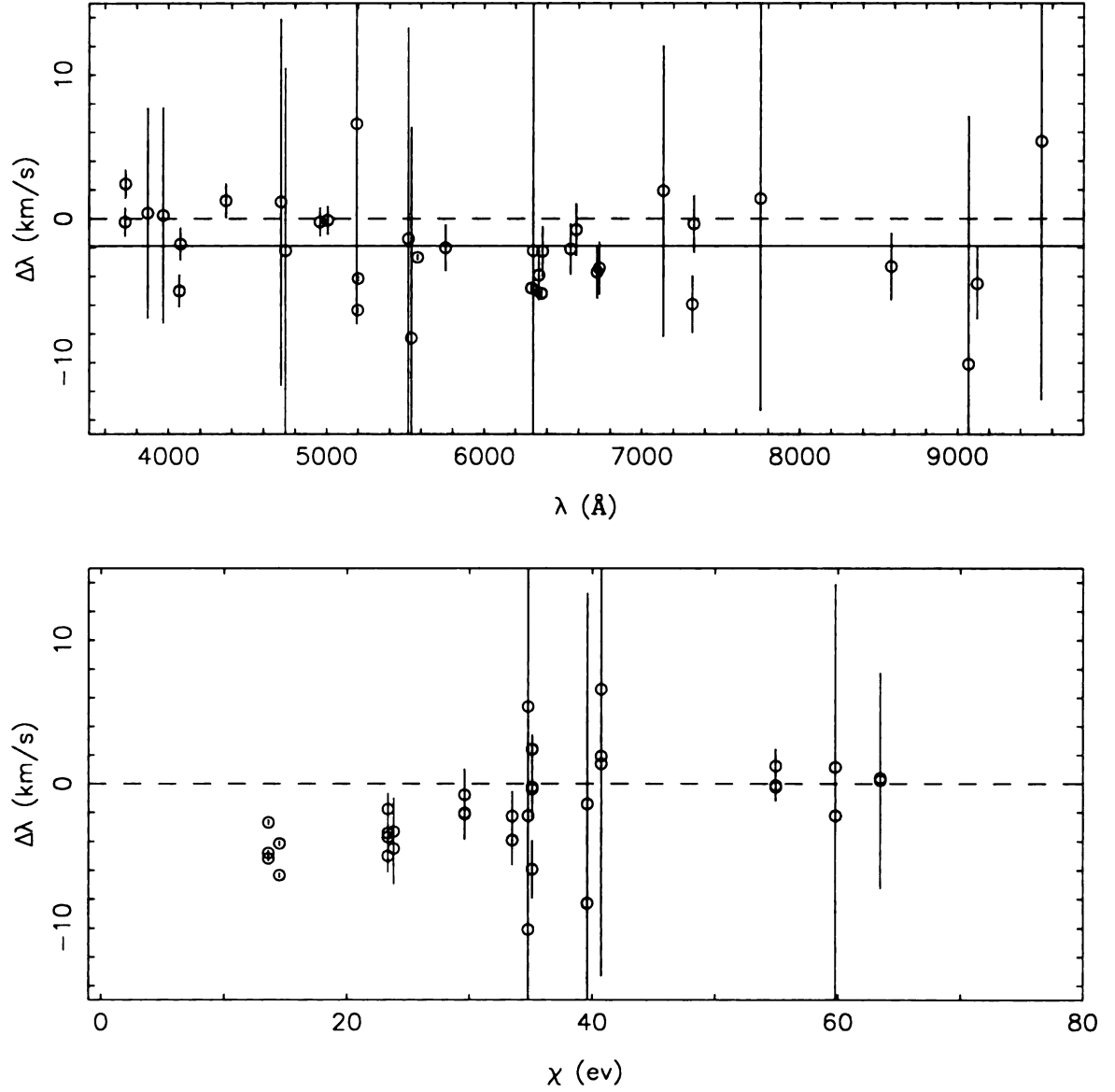


Figure 2.12 **Top:** laboratory minus observed wavelength ( $\Delta\lambda$ ) for lines from Table 2.7 as a function of observed wavelength. **Bottom:** same versus ionization potential ( $\chi$ ) of parent ion. An obvious trend towards smaller wavelength difference between observed wavelength and laboratory wavelength with increasing ionization potential is evidenced.

of the use of the first moment of the line profile in the wavelength measurements of non-symmetric profile emission lines. As no particular source can be ruled out, we assume the worst, that the difference is purely due to the wavelength measurement technique, and adopt a value of  $1.9 \text{ km sec}^{-1}$  (indicated as a straight line in the upper panel of Figure 2.12), as a systemic wavelength uncertainty for all lines. An additional  $\pm 0.9 \text{ km sec}^{-1}$  uncertainty can be added directly to this to represent an additional systemic error arising from the radial velocity correction (see Table 2.4) for a total of  $2.8 \text{ km sec}^{-1}$  for all lines regardless of S/N.

The measurement and calibration errors could conceivably cancel out each other, but the  $2.8 \text{ km sec}^{-1}$  total potential systemic error cannot be added in quadrature with the other errors. We express the total approximated uncertainty in line wavelengths as:

$$\sigma_{tot} = \sqrt{\sigma_M^2 + \sigma_C^2} + \sigma_S, \quad (2.3)$$

where  $\sigma_M$  is the error due to measurement problems,  $\sigma_C$  is the error to wavelength calibration problems, and  $\sigma_S$  is the  $2.8 \text{ km sec}^{-1}$  total systemic error described above. A summary of the components of the estimated total wavelength uncertainty is shown in Table 2.8.

We compared this error,  $\sigma_{tot}$ , calculated for each line, against the original  $1\sigma$  scatter shown among those individual measurement used to calculate that line's wavelength, and adopted the *greater* of the two for the total wavelength uncertainty for that line. The error calculated in eq. 2.3 was adopted for all lines with single contributing measurements. We believe this gives a reasonable upper limit to wavelength

Table 2.8 Estimated wavelength uncertainty budget for each line, depending upon it's S/N and final wavelength. The numbers  $N$  indicate the numbers of lines which were used to calculate the error within the particular S/N or wavelength bin.

	N	(km sec <sup>-1</sup> )
Measurement Error ( $\sigma_M$ )		
S/N < 20	104	2.016
S/N $\geq$ 20	160	0.749
Calibration Error ( $\sigma_C$ )		
$\lambda\lambda$ ( $\text{\AA}$ )		
3500-4000	11	0.901
4000-4500	7	0.321
4500-5000	5	0.328
5000-5500	16	0.807
5500-6000	23	0.735
6500-6500	6	0.290
6500-7000	7	0.410
7000-7500	12	0.837
7500-8000	14	0.802
8000-8500	24	0.911
8500-9000	23	0.523
9000-9500	10	1.592
Systemic Error ( $\sigma_S$ )		
(a)	35	1.899
(b)	–	0.900
(a) For Wavelength: Lab-Obs $\lambda$ , see Figure 2.11		
For Flux: Lab vs. Obs Ratios, see text Sect. 2.3.3		
(b) For Wavelength: Radial Velocity Corr. See Table 2.5		

uncertainty for each line.

### **Flux Uncertainty**

Contributing to the uncertainty in flux measurements, are errors in the flux calibration, systemic errors arising from the peculiarities of observing equipment and variability in observing conditions, and measurement errors due to poorly defined profiles of weak lines. The distinct contributions from these sources are difficult to de-correlate from one another.

Comparisons between previously obtained flux standard star spectra, and spectra of those same stars calibrated in the same way as our object spectra, in all observing set-ups, show that over the majority of most orders, the flux calibration is better than 95% accurate (see for example Figure 2.5). However, on the edges of orders where the echelle blaze function rapidly falls off, the accuracy of the calibration declines. The accuracy also falls in the vicinity of places with problematic calibrations. Specific problems exist at wavelengths near the broad hydrogen absorption features in the standard stars. Nevertheless, since these locations also correspond to places where the S/N is relatively smaller, and the locations in the nebular spectra corresponding to strong absorption lines in the standard stars were carefully screened, the influence of individual measurements from these locations is somewhat mitigated by our measurement selection criteria. Therefore, we simply adopt a value of 5% as the likely error due to errors in flux calibration.

We tested for any bulk systemic errors by comparing observed, reddening corrected, line flux ratios with their theoretically calculated values for several un-blended, un-ambiguous, close pairs of lines, such as those used to calculate electron density.



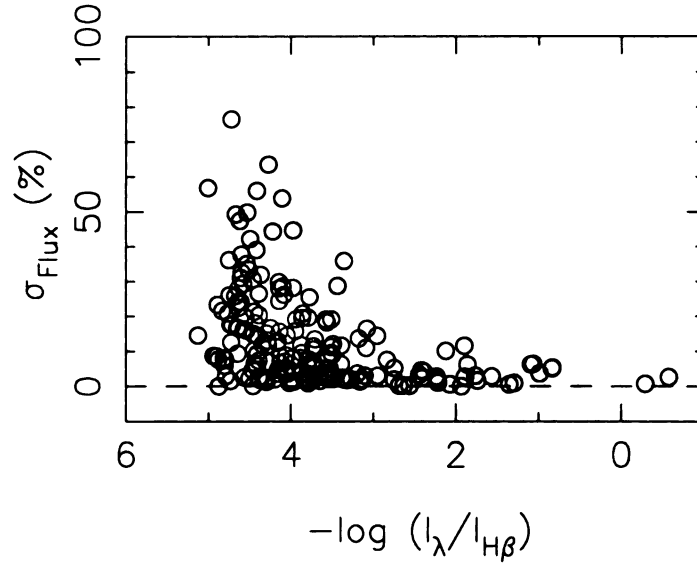


Figure 2.13 The percentage flux error ( $1\sigma$  measurement scatter) as a function of  $-\log(I(\lambda)/I(H\beta))$ .

These pairs were chosen because of their large flux, the fact that their intrinsic flux ratios depend only upon atomic parameters (i.e. spontaneous transition coefficient and wavelengths), and their relative closeness in wavelength which minimize reddening correction problems. For the following pairs of lines: [Ne III]  $\lambda\lambda 3869/3968\text{\AA}$ , [O III]  $\lambda\lambda 5007/4959\text{\AA}$ , [N II]  $\lambda\lambda 6548/6583\text{\AA}$ , and [O II]  $\lambda\lambda 6300/6363\text{\AA}$ , the theoretical ratios exceed the observed ratios by 1.4%. Such a small departure was judged not to be statistically significant.

It is traditional in nebular astrophysics to estimate the errors attributable to measurement problems by determining the scatter in individual flux measurements for those lines having multiple individual contributing measurements, as a function of the fluxes of those lines. In Figure 2.13 we plot the measurement scatter ( $1\sigma$ ) as a percentage of individual flux, against the log of the line fluxes normalized to

the de-reddened flux of  $H\beta$ . We then calculated the average scatter within decadal bins. We find that the average scatter plus systemic error for lines of flux  $I(\lambda)$  to be:  $I(\lambda)/I(H\beta) < 10^{-4} = 20\%$ ,  $10^{-4} < I(\lambda)/I(H\beta) < 10^{-3} = 10\%$ , and for all higher bins  $I(\lambda)/I(H\beta) > 10^{-3} = 5\%$ , the level of the expected uncertainty in the flux calibration alone. While some individual lines exhibit a larger amount of scatter, the general level of uncertainty for the strongest lines compares quite favorably with those levels given by HAF, HKB, Baldwin et al. (2000), and Esteban et al. (1998), to which this work is compared.

To obtain an estimate of the intrinsic uncertainty of the line flux measurements, we adopted the values determined for the measurement uncertainty above, and added in quadrature a potential 5% error due to flux calibration. This yields for lines of differing flux a  $\Delta I$  of:  $I(\lambda)/I(H\beta) < 10^{-4} = 21\%$ ,  $10^{-4} < I(\lambda)/I(H\beta) < 10^{-3} = 11\%$ , and for all higher bins  $I(\lambda)/I(H\beta) > 10^{-3} = 7\%$ . In those cases where lines had higher flux measurement scatter than the value appropriate for its flux under this criteria, the actual measurement scatter was adopted as the flux uncertainty for that line.

Lines fluxes may also be susceptible to uncertainty in the reddening correction. The flux of any reddening corrected line may be represented by the following equation:

$$I_o = I e^{c_{H\beta} D(\lambda)}, \quad (2.4)$$

where  $I_o$  is the reddening-corrected flux,  $I$  the observed flux,  $c_{H\beta}$  the log extinction of  $H\beta$ , and  $D(\lambda) = f(\lambda)/\ln 10$  the rescaled extinction function curve at wavelength  $\lambda$ . Assuming that the reddening error is a systemic error, the flux of a reddening

corrected line and its error may be represented:

$$\begin{aligned}
I_o &= I e^{c_{H\beta} D(\lambda)}, \\
\Delta I_o &= \left( \frac{\partial I_o}{\partial I} \right) \Delta I + \left( \frac{\partial I_o}{\partial c_{H\beta}} \Delta c_{H\beta} \right), \\
&= I_o \left[ \frac{\Delta I}{I} + D(\lambda) \Delta c_{H\beta} \right],
\end{aligned} \tag{2.5}$$

where the  $\Delta c_{H\beta}$  is the uncertainty in the log extinction at  $H\beta$ ,  $c_{H\beta}$  listed in Table 2.5.

## 2.4 Comparisons With Other Spectra

HAF and HKB have previously observed emission lines in IC 418. General comparisons of our final flux values may be made to both studies in order to look for gross problems with the flux calibrations, even though their slits were positioned at different locations within the nebula. In Table 2.9, comparisons between fluxes are made between a wide variety of strong lines with un-ambiguous identifications from the three studies, where the columns (2),(3),(4) are the reddened line strengths, normalized to  $H\beta$ , for the lines listed in column (1). The ratio of each studies' line strengths relative to each other follow in columns (5),(6), and (7). The spectra of HKB was of insufficient resolution to resolve many close line pairs (e.g. [O II]  $\lambda\lambda 3737, 3729\text{\AA}$ ) and thus comparison are made between the sum of the flux in the pair, which is indicated by a dashed line in the row of the line with the redmost wavelength in the pair. The average of the ratios of intensities between each pair of studies is relatively constant around unity, even if the scatter about that average is fairly large. Some individual lines approach a factor of two difference in flux between studies (see for example the

Table 2.9 Comparisons lines ( $I_{H\beta} = 100$ ).

Line (Ion/ $\lambda$ (Å))	Obs	HAF	HKB	HKB/HAF	HAF/Obs	HKB/Obs
[O II] 3727	96.183	79.62	105	0.93	0.83	0.77
[O II] 3729	40.687	33.19	--	—	0.82	—
[Ne III] 3869	2.461	1.84	2	1.09	0.73	0.80
[Ne III] 3968	0.791	0.58			0.72	
[S II] 4068	1.482	2.24	3	0.98	1.48	1.39
[S II] 4076	0.636	0.81	--	--	1.25	--
H $\gamma$	39.638	44.16	40	0.91	0.98	0.89
[O III] 4363	0.832	0.49	0	1.02	0.64	0.66
He I 4471	4.105	3.43	3	0.87	0.82	0.72
H $\beta$	100.000	100.00	100	1.00	1.00	1.00
[O III] 4959	74.199	29.85	37	1.24	0.40	0.50
[O III] 5007	221.374	87.30	125	1.43	0.40	0.57
[Ar III] 5192	0.041	0.03			0.77	
[N I] 5198	0.215	0.44	0.5	0.74	2.37	1.66
[N I] 5200	0.125	0.24	—	—	2.09	—
[Cl III] 5517	0.204	0.20	0.2	1.00	1.11	1.11
[Cl III] 5537	0.400	0.41			1.17	
[O I] 5577	0.030	0.05			1.85	
[N II] 5755	3.191	4.29	4	0.93	1.55	1.45
He I 5876	16.031	12.05	11	0.91	0.79	0.72
[O I] 6300	2.672	4.45	4	0.90	1.86	1.67
[S III] 6312	1.053	1.08	1	0.93	1.14	1.06
Si II 6347	0.063	0.17			2.98	
[O I] 6363	0.939	1.57	1	0.64	1.86	1.19
Si II 6371	0.054	0.06			1.25	
[N II] 6548	67.557	83.18	66	0.79	1.27	1.01
H $\alpha$	393.893	409.26	321	0.78	1.07	0.84
[N II] 6584	206.107	242.10	197	0.81	1.21	0.99
He I 6678	4.947	3.01	3	1.00	0.68	0.68
[S II] 6717	2.672	4.24	3	0.71	1.77	1.25
[S II] 6731	5.679	8.02	6	0.75	1.57	1.18
He I 7065	9.389	6.47	8	1.24	0.72	0.88
[Ar III] 7135	11.069	7.46	9	1.21	0.69	0.84
[O II] 7320 <sup>(a)</sup>	18.779	19.11	42	1.19	1.05	1.25
[O II] 7330 <sup>(a)</sup>	15.725	16.32	--	—	1.07	—
[Ar III] 7751	3.137	0.97	2	2.06	0.34	0.71
He I 8361	0.185	0.07			0.42	
O I 8446	1.741	1.92			1.23	
[Cl II] 8579	0.438	0.35			0.89	
[S III] 9068	28.321	19.50	34	1.74	0.81	1.42
H I P8 9228	4.512	3.36	6	1.79	0.83	1.48
[S III] 9532	68.931	51.40	102	1.98	0.88	1.75
Mean				1.09	1.05	0.98
Standard Dev.				0.38	0.49	0.29

<sup>(a)</sup> Sum of doublet

ratio “HAF/Obs” for [O III]  $\lambda\lambda 4959, 5007\text{\AA}$  which may have some significance). Nevertheless, if there were any large overall systemic problem with the flux calibration, it might be expected that the average of the ratios would be further skewed in a particular direction from unity. We concluded that the present survey’s flux calibration is at least as accurate as the previous surveys it is being compared against here.

Comparisons can also be made to the between observed and theoretical ratio of lines whose relative fluxes depend either only on atomic parameters, as in the case of forbidden lines arising from the same upper level; or only weakly upon nebular physical conditions, such as recombination lines from the same ion. Theoretical ratios were calculated for the list from Table 2.7 and several other line pairs. The inputs included spontaneous transition coefficients and wavelengths drawn from the NIST database, line emissivity ratios for H I recombination lines (Balmer and Paschen series) from Storey & Hummer (1995), typical IC 418 electron temperature (10000 K ) and density of  $10000\text{ cm}^{-3}$  (HAF and here see Section 4.1.1), and the emissivity ratios of Brocklehurst (1972) for He I recombination lines. These flux ratios are compared to observed values from our data, HAF, and HKB in Table 2.10, where column (1) lists the line pair, (2) the theoretical ratio of the line strengths, and (3),(4),and (5) the observed flux ratios of these lines from this study, HAF, and HKB.

As can be seen, good agreement between the theoretical and observed flux ratio values in this study and the close agreement with the observed ratios in the other studies suggest that the present survey’s flux calibration is at least as accurate as previous studies. HKB suggest that their strongest lines are in the neighborhood of 10% flux accuracy. Given the better agreement between our ratios and theory with

Table 2.10 Relative flux in line ratios

Line Pair Ion ( $\lambda$ (Å))	Flux Ratios			
	Theory	Obs	HAF	HKB
[Ne III] 3869/3968	3.27	3.17	3.20	<sup>(a)</sup>
He I 5876/4471	2.76	3.04	3.02	3.33
[O III] 5007/4959	2.90	2.96	2.91	3.42
[N II] 6583/6548	2.96	3.04	2.90	2.97
He I 6678/4922	2.89	3.18	2.77	3.00
[Ar III] 7135/7751	4.14	3.76	7.92	4.00
P8/H $\beta$	0.04	0.04	0.03	0.05
[O II] 6300/6363	3.09	2.86	2.85	4.
[S III] 9532/9069	2.58	2.37	2.62	3.00
(a) [Ne III] 3968Å blended with H $\epsilon$				

respect to HKB, we would estimate the true accuracy of the strongest lines within the present survey to be closer to the 5% accuracy estimated for the strongest lines, as calculated previously.

In summary, we have attempted to calculate and quantify the legitimate sources of error that could contribute to the final wavelength and flux values of each emission line. Our data set has been shown to be both internally consistent and comparable to previous data, with a reasonable degree of confidence. Adjustments have been made to remove systemic sources of error, whenever such adjustments did not introduce additional spurious noise. The remaining errors are most likely a product of the limitations of the instrumentation and reduction techniques, although we believe that their magnitude, approximately equivalent to other nebular abundance studies, should be sufficient for obtaining decent information regarding the physical attributes of IC 418.

## Chapter 3

# A Semi-Automated Emission Line Identifier - EMILI

### 3.1 Introduction

Deep, high-resolution emission spectra of planetary nebulae (PNe) and H II regions obtained with modern instrumentation (Esteban et al. 1999, Baldwin et al. 2000, and this study) reveal hundreds of emission lines, including numerous weak recombination and collisionally excited lines, which have not been routinely identified. The traditional approach for identifying such lines is a manual one. For each observed line, an atlas of known lines is consulted, and candidate lines at about the observed wavelengths are then ruled either in or out on the basis of being from ions in plausible ionization states with plausibly high chemical abundances, on the presence or absence of other member of the same multiplet, and so forth. This procedure is extremely time consuming, demanding, and subject to observer bias.

EMILI, for Emission Line Identifier, is code designed to automate these steps, making use of a portion (3000-11000Å) of a large atomic transition database (Atomic Line List v2.04, van Hoof 1999), which includes  $\approx 200,000$  transitions from all elements  $Z \leq 30$ , from which more possible IDs than could reasonably be considered manually can be tested for suitability. To assist in the identification process, the code models nebular ionic abundances, adjusts for any ionization energy dependent wavelength shifts among the observed lines (nebular velocity structure), and makes order of magnitude estimates of each transition’s possible flux under assumed nebular physical conditions. The latter overcomes a limitation of spectral modeling in which exact atomic parameters, i.e. effective recombination coefficients and collisional cross sections and strengths, need to be known, but are often in short supply. Likely identifications are ranked, with the results presented in a straightforward manner to the end-user.

We present here the basic framework by which EMILI makes its identifications, and provide comparisons between manually and EMILI- derived identifications for high resolution nebular spectra as a gauge of its accuracy. For the actual operation and utilization of the code, the reader is referred to Appendix D, the “EMILI User’s Manual”.

## 3.2 Overview

The steps EMILI utilizes in determining possible IDs for each line can be summarized as:



5006.845	5006.843	[O III]	2.15e+00
6583.467	6583.450	[N II]	1.63e+00
3726.035	3726.032	[O II]	1.24e+00
4958.915	4958.911	[O III]	7.27e-01
6548.088	6548.050	[N II]	5.36e-01
3728.785	3728.815	[O II]	5.23e-01
9530.929	9530.600	[S III]	4.23e-01
9068.905	9068.600	[S III]	1.78e-01
7319.087	7318.920	[O II]	3.69e-02
7320.135	7319.990	[O II]	1.01e-01
7329.679	7329.66	[O II]	5.86e-02
7330.754	7330.73	[O II]	5.63e-02
5875.650	5875.640	He I	1.37e-01
7135.744	7135.773	[Ar III]	8.26e-02
4471.499	4471.486	He I	4.49e-02
6730.893	6730.816	[S II]	4.42e-02
6678.153	6678.152	He I	3.87e-02
3868.745	3868.750	[Ne III]	3.09e-02

**A                      B                      C                      D**

Figure 3.1 A segment of the *Matched Line List* for the IC 418 data. Listed in columns from left to right are: **A.** observed wavelength (Å) **B.** laboratory wavelength of transition (Å), **C.** spectroscopic notation for the transition's source ion **D.** flux with respect to H $\beta$

1. Model the observed object's velocity structure and determine ionic abundances from information supplied in a *Matched Line List* (Figure 3.1), a list of observed and pre-identified lines supplied by the user from the same spectrum in which the user wishes to identify other lines.
2. For each observed line the user wishes to identify in the spectra, contained in an *Input Line List* (Figure 3.2), draw from the transition database all transitions within a set number of measurement uncertainty sigma of the observed

6363.89	-0.08	0.08	7.58e-03	56.70	485.20
6371.42	-0.08	0.08	4.33e-04	31.00	198.30
6379.65	-0.11	0.11	8.62e-06	25.50	10.70
6382.99	-0.11	0.11	1.95e-05	44.10	16.10
6392.50	-0.11	0.11	9.28e-06	17.60	6.20
6402.27	-0.08	0.08	1.07e-04	21.90	75.50
6454.39	-0.11	0.11	1.01e-05	22.40	5.40
6456.00	-0.11	0.11	1.25e-05	19.30	8.70
6461.85	-0.08	0.08	5.83e-04	18.60	93.50
6527.26	-0.08	0.08	2.84e-04	29.30	70.60
6548.10	-0.08	0.08	5.35e-01	39.80	10430.00
6562.80	-0.08	0.08	3.12e+00	31.30	14100.00
6578.05	-0.08	0.08	5.37e-03	18.30	870.50
6583.47	-0.08	0.08	1.63e+00	40.20	11370.00
6610.65	-0.11	0.11	2.79e-05	25.00	11.70
<b>A</b>	<b>B</b>	<b>C</b>	<b>D</b>	<b>E</b>	<b>F</b>

Figure 3.2 A subset of the *Input Line List* for the IC 418 dataset. Listed in columns from left to right are: **A.** observed wavelength (Å) **B.,C.** errors in measurement (Å), **D.** flux with respect to H $\beta$  **E.** FWHM (km/sec) **F.** signal to noise.

wavelength for that line. Correct the observed wavelength with the value appropriate from the velocity structure model for each transition's parent ion's ionization potential.

3. Calculate a *template flux*, the predicted intensity of a line corresponding to a specific transition, for all transitions selected in the previous step. Retain the transitions with the strongest predicted lines.
4. For each surviving transition, look for the presence of additional lines in the *Input Line List* which could correspond to transitions from the same multiplet,

Table 3.1 The ionization potential energy bins and signature lines used to calculate the ICF values

Bin	Energy Range (eV)	Signature Lines
A	0-13.6	Mg I] $\lambda$ 4571, Na I $\lambda$ 5890, 5896, [S I] $\lambda$ 7775, [C I] $\lambda$ 8727 Ca II (H&K) $\lambda$ 3934, 3968
B	13.6-24.7	H $\beta$
C	24.7-54.5	He I $\lambda$ 5876, 4471
D	54.5-100.0	He II $\lambda$ 4686
E	> 100	[Fe X] $\lambda$ 6375, [Ne V] $\lambda$ 3426, [Fe VII] $\lambda$ 6087, [Ar X] $\lambda$ 5533

by meeting certain relative wavelength agreement and flux criteria.

5. Rate each transition's likelihood of being the possible ID for a line, based upon the agreement between laboratory and observed wavelengths, the predicted strength of transition relative to all other possible IDs for that line, and results of the multiplet check, to arrive at a rank-ordered set of possible IDs for presentation to the user.

### 3.3 Modeling the Nebula

EMILI models the observed object as consisting of five distinct zones or bins, each representative of a different range of ionization potential energy. The bounds of each bin are listed in Table 3.1. EMILI utilizes the information provided in the *Matched Line List* to determine the properties of all transitions whose parent ions reside in one of those bins. Specifically, EMILI calculates a correction to the observed wavelength of each unidentified emission line, depending upon the parent ion for the transition

being tested as its possible ID, appropriate to that's ion's residence within one of the energy bins. EMILI also determines the parent ion's abundance, based upon which bin it resides in.

### 3.3.1 Velocity Structure Modeling

Baldwin et al. (2000) showed in their spectrum of the Orion Nebula that among their observed emission lines, the magnitude of the residual wavelength difference between the observed and laboratory values (after correction to the rest frame of the nebula) correlated with the ionization potential of the lines' source ions. They attributed this to a foreground matter flow having a component parallel to the line of sight, with a differential flow velocity. PNe have been shown to have a radially differential expansion velocity (see for example Gesicki, Acker, & Szczerba (1996) for IC 418), with increasing velocity correlated with increasing distance away from the central star. As ionization stratification means higher ionization potential ions concentrated towards the central star, the result is to anti-correlate ionization potential with velocity. This effect, coupled with hypothetical flows and geometric effects, can produce a pattern of velocity residuals similar to that seen among the Orion emission lines.

EMILI calculates a correction to be applied to the observed wavelength of any unidentified line, based upon the ionization potential of a possible ID transition's parent ion. For each line listed in the *Matched Line List*, the bin to which its parent ion belongs is determined, and the velocity difference between the laboratory and

observed wavelength ( $\lambda_{lab}$  and  $\lambda_{obs}$  respectively) is calculated according to the formula:

$$v_{cor} = c \frac{\lambda_{obs} - \lambda_{lab}}{\lambda_{lab}}, \quad (3.1)$$

where  $v_{cor}$  is the velocity difference in  $\text{km sec}^{-1}$  for that transition and  $c$  the speed of light. For each bin the average  $v_{cor}$  is determined from all lines in the *Matched Line List* belonging to that bin, to arrive at a correction for all potential ID transitions whose parent ion falls within it. When a particular transition is being tested as a possible ID, the observed wavelength of the unidentified line is corrected to the “rest” wavelength of that transition ( $\lambda_{cor}$ , according to the formula:

$$\lambda_{cor} = \lambda_{obs} \left( 1 + \frac{v_{cor}}{c} \right), \quad (3.2)$$

where here  $v_{cor}$  is the average wavelength correction (in  $\text{km sec}^{-1}$ ) for ions belonging to the bin in which the parent ion of the transition resides.

The number and extent of these bins were established to match the ionization potentials of the ions producing the most well-observed nebular emission lines, in order to maximize the chance that each bin would be equally and adequately represented in constructing the velocity model. *Matched Line List* has no entry for a bin, the bin adopts the correction value of the nearest bin with a non-zero  $v_{cor}$ .

In Figure 3.3, the correction value,  $v_{cor}$  for each bin for the present IC 418 dataset, as calculated by EMILI, is plotted, indicating that a real ionization energy dependent velocity field attributable to some source is evidenced in the line wavelengths.

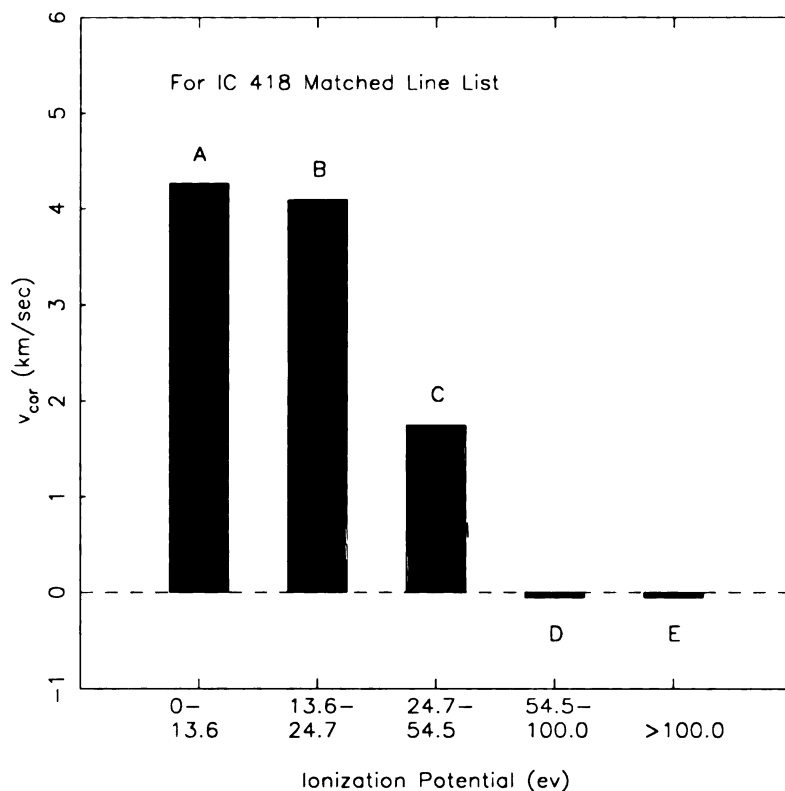


Figure 3.3 The velocity correction,  $v_{cor}$ , in  $\text{km s}^{-1}$  for all bins “A”-“E”, calculated from the *Matched Line List* from the EMILI run on the present IC 418 dataset.

### 3.3.2 Abundances

The second use of the *Matched Line List* is to establish rough estimates of the expected ionic abundances for all ions  $Z \leq 30$ . The overall elemental abundances with respect to hydrogen are read in from the default solar (or user-supplied) abundance table, and are modified by ionization correction factors (ICFs). ICFs are calculated using the strengths of certain “signature” lines (again see Table 3.1) listed by the user in the *Matched Line List*. Each ICF value acts as the fraction of the total elemental abundance present in ions in each of the ionization energy bins. Multiplying the elemental abundance by a combination of these ICF values, as described below, yields

ionic abundances for all ions of that element present in the nebula.

For the first ionization energy bin “A”, the code looks for strong, collisionally excited, forbidden transitions for neutral ions such as [C I]  $\lambda 8727\text{\AA}$ ; or for strong, collisionally excited permitted resonance lines like the Na I  $\lambda\lambda 5890, 5896\text{\AA}$  and the Ca II H&K  $\lambda\lambda 3934, 3968\text{\AA}$  doublets. EMILI arbitrarily assigns a value for  $x_A$ , the ICF for bin “A”, based on the flux,  $I_\lambda/I_{H\beta}$ , of the strongest observed signature line listed in the *Matched Line List* for the bin. If the strongest line has a flux  $I_\lambda/I_{H\beta} < 10^{-4}$  then  $x_A = 0.001$ ; if  $10^{-4} \leq I_\lambda/I_{H\beta} < 10^{-2}$  then  $x_A = 0.01$ , and if  $10^{-2} \leq I_\lambda/I_{H\beta}$  then  $x_A = 0.1$ . A minimum value  $x_A = 0.001$  is assigned if no lines are observed or included from bin “A” in the *Matched Line List*.

In a similar manner, the code looks for lines belonging to ions with large ( $>100$  eV) ionization potentials (the population of bin “E”). Depending upon the strength of the strongest signature line that is found for bin “E” in the *Matched Line List*, EMILI will assign a value:

$$x_E = 10^{-3} + I_\lambda/I_{H\beta}, \quad (3.3)$$

where  $I_\lambda/I_{H\beta}$  is the flux of that indicator line with respect to  $H\beta$ , up to a maximum  $x_E = 0.5$ . Again, a minimum value of  $x_E = 0.001$  is assumed if no lines are present from this bin in the *Matched Line List*.

The ratio of ICFs for the “B” and “C” ionization bins is determined by the code by comparing the ratio of the observed fluxes with the theoretical value. The calculation uses a pair of particularly strong lines:  $H\beta$  from bin “B”, and He I  $\lambda 5876\text{\AA}$  and  $\lambda 4471\text{\AA}$  from bin “C”. The theoretical ratio is related to the observed ratio of the

lines,  $I_{He^+}/I_{H\beta}$ , by:

$$\frac{I_{He^+}}{I_{H\beta}} = \frac{N_{He^+} N_e \alpha_{He^+}^{eff} \lambda_{H\beta}}{N_p N_e \alpha_{H\beta}^{eff} \lambda_{He^+}}, \quad (3.4)$$

where  $N_{He^+}$ ,  $N_p$ , and  $N_e$  are the densities of ionized helium, ionized hydrogen, and electrons respectively. The  $\alpha^{eff}$  factors refer to the effective recombination coefficients for the transitions ( $\alpha_{He^+}^{eff}$  for He I  $\lambda 5876$  or  $\lambda 4471$  etc...), and the  $\lambda$  values are the wavelengths. Some fraction,  $x_C$ , of the helium atoms along the line of sight are singly ionized, and similarly, a fraction,  $x_B$ , of hydrogen atoms are also ionized. These are equivalent to the ICF values  $x_B$  and  $x_C$ . Calling  $y$  the elemental abundance ratio between hydrogen and helium, and assuming completely ionized hydrogen in the ground state at the location of  $He^{++}$  production, the ratio of the fraction  $x_C$  to  $x_B$  may be expressed as:

$$\frac{x_C}{x_B} = \frac{1}{y} \frac{I_{He^+}}{I_{H\beta}} \frac{\alpha_{H\beta}^{eff} \lambda_{He^+}}{\lambda_{H\beta} \alpha_{He^+}^{eff}}. \quad (3.5)$$

We assume (Osterbrock 1989) an intrinsic intensity ratio of  $I_{\lambda 5876}/I_{\lambda 4471} = 2.76$ , and standard values for the effective recombination coefficients for  $H\beta$ ,  $\alpha_{H\beta}^{eff}$ , and for He I  $\lambda 4471$ ,  $\alpha_{\lambda 4471}^{eff}$ , of  $3.03 \times 10^{-14}$  and  $1.37 \times 10^{-14} \text{ cm}^3 \text{ sec}^{-1}$  respectively at an electron temperature of 10000 K and density of  $10000 \text{ cm}^{-3}$  (Osterbrock 1989). These values of the effective recombination coefficients vary less than an order of magnitude over all typical nebular temperatures and densities.

The value of  $x_C/x_B$  is calculated from the intensity, with respect to  $H\beta$ , of either He I line. For He I  $\lambda 5876$ :

$$\frac{x_C}{x_B} = 0.74 \frac{1}{y} \frac{I_{\lambda 5876}}{I_{H\beta}}, \quad (3.6)$$



and for He I  $\lambda 4471$ :

$$\frac{x_C}{x_B} = 2.03 \frac{1}{y} \frac{I_{\lambda 4471}}{I_{H\beta}}. \quad (3.7)$$

The average of the two  $x_C/x_B$  ratios is used if both lines are observed and present in the *Matched Line List*.

The ratio of the ICFs  $x_D$  to  $x_C$  is computed using the observed fluxes of the same two He I lines, and the observed flux of He II  $\lambda 4686\text{\AA}$ :

$$\frac{x_D}{x_C} = \frac{\lambda_{He^+}}{\alpha_{He^+}^{eff}} \frac{\alpha_{\lambda 4686}^{eff}}{\lambda(4686)} \frac{I_{\lambda 4686}}{I_{He^+}}, \quad (3.8)$$

where the  $He^+$  subscript refers to the use of one or the other of the He I lines. Using  $\alpha_{\lambda 4686}^{eff} = 1.37 \times 10^{-13} \text{ cm}^3 \text{ sec}^{-1}$  for the effective recombination coefficient of He II  $\lambda 4686\text{\AA}$ , and the same assumptions used in calculating  $x_C/x_B$ , the ratio of  $x_D$  to  $x_C$  can be expressed in terms of the intensity ratios:

$$\frac{x_D}{x_C} = 0.11 \frac{I_{\lambda 4686}}{I_{\lambda 5876}}, \quad (3.9)$$

or:

$$\frac{x_D}{x_C} = 0.04 \frac{I_{\lambda 4686}}{I_{\lambda 4471}}. \quad (3.10)$$

The average  $x_C/x_D$  is used if both He I lines are observed and listed in the *Matched Line List*.

The values for  $x_A$  and  $x_E$  are then used with the ratios from eqs. 3.6-3.7 and eqs. 3.9-3.10, and all the ICF values normalized to sum to unity, providing a system of equations from which EMILI solves for  $x_B$ ,  $x_C$ , and  $x_D$ .

Where signature lines are not present in any bin “B”-”D”, EMILI assumes the following in its calculations for the remaining ICFs:

- If no signature lines are present in either bins “C” or “D”, the object is assumed to be of extremely low ionization, in which case most of the ions reside in bins “A” or “B”:  $x_C$  and  $x_D$  are assigned values of 0.001 and  $x_B$  assumes the remainder of unity after subtraction of all other ICFs. Alternatively, the object may instead be of extremely high ionization, with most of the ions in bin “E”, indicated by  $x_E$  assigned its maximum value. In this case  $x_B$  through  $x_D$  receive minimum values of 0.001.
- If no signature lines are present in bin “D”, but bin “C” is populated, it is assumed that the object is in fairly low ionization. In this case  $x_D$  takes a minimum value of 0.001, and  $x_B$  and  $x_C$  share the remaining portion of unity according to the value of  $x_C/x_B$ .
- If signature lines are present from all bins “B”-“D”, then the ionization is assumed to be moderate, and the values of  $x_B$ ,  $x_C$ , and  $x_D$  split the remaining portion of unity (after subtraction of  $x_A$  and  $x_E$ ), with  $x_B$  and  $x_C$  getting the majority, and all factors proportioned according to the ratios of  $x_C/x_B$  and  $x_D/x_C$ :

$$\begin{aligned}
x_B &= (1 - x_A - x_E) / (1 + \frac{x_C}{x_B} + \frac{x_C}{x_B} \frac{x_D}{x_C}), \\
x_C &= x_B \frac{x_C}{x_B}, \\
x_D &= x_C \frac{x_D}{x_C}.
\end{aligned}$$

- Finally, if signature lines are absent from bin “B” but present in bins “C” and “D”, the object is considered to be highly ionized. Then  $x_B$  assumes a minimum

value of 0.001, and  $x_C$  and  $x_D$  share the remainder according to  $x_D/x_C$ .

It is important to note that while the ICFs *act* as percentages of a particular element present as a specific ion in the nebula, the sum of the products of the ICFs multiplied by the overall elemental abundance for each of its ions need *not* sum to the elemental abundance. This is the case where elements may have multiple ions within a particular ionization bin. The goal of these calculations are rough estimates of the ionic abundances only.

To smooth out the abundance model, for ions with ionization potentials near the edges of the bins, and a next lower stage of ionization in a different bin, the *average* of the ICF values for those bins is multiplicatively applied to the overall elemental abundance. For example,  $O^{++}$  has an ionization potential of 54.94 eV, while  $O^+$  has an ionization potential of 35.12 eV. Since these energies lie within different bins the abundance of  $O^{+2}$  is calculated as:

$$O^{+2} = \frac{x_B + x_C}{2}(O), \quad (3.11)$$

since the ionization potential of singly and doubly ionized oxygen reside in bins “B” and “C” respectively; “O” is the elemental abundance with respect to hydrogen.

If the ionization potentials for an ion and its predecessor are both in the same bin however, then just the ICF value for that bin is used. For example, the ionization energy of  $N^{+2}$  is 47.45 eV, and for  $N^+$  is 29.60 eV, both in bin “C”. Therefore, the abundance of  $N^{+2}$  is calculated by EMILI, from the elemental abundance of nitrogen, as:

$$N^{+2} = x_C(N), \quad (3.12)$$

For neutral ions, the “next lower” ionization bin is the lowest energy bin. Special cases are established for completely ionized hydrogen and helium:  $\text{H}^+ = x_B$  and  $\text{He}^{+2} = x_D$ . In this manner ionic abundances are calculated for all ions for which line information is stored in the line database.

### 3.4 Template Flux

EMILI draws, from its transition database, dozens of transitions within a few measurement uncertainty sigma of each unidentified line in the *Input Line List*. For each of these possible IDs, EMILI calculates an expected strength, or *template flux* of the emission line produced by such a transition, under the user-specified nebular temperature and density conditions. Only the transitions producing the strongest predicted lines (those within 1/1000 of the strongest predicted transition among all possible IDs for that line) are retained for further analysis, on the assumption that these are the most likely to be observable.

The template flux calculation is meant to be only an order of magnitude estimate of the relative flux (with respect to  $\text{H}\beta$ ) that could be observed in such a line. It is not a calculation of absolute flux, something better accomplished by emission-line region spectral modeling codes such as CLOUDY (Ferland et al. 1998). In any event, an exact calculation of the absolute flux for every transition in the Atomic Line List v2.04 would fail due to lack of atomic parameters for all but a few ions. What the code does attempt, however, is to compare transitions by their relative strengths, calculated and normalized uniformly, so that we may judge those most likely to be the

correct identification because they are the strongest, relative to all other transitions in the unidentified line's immediate vicinity.

When calculating the template flux for a transition, EMILI assumes that a line arising from it may have contributions from *both* standard recombination and collisional excitation. Only  $H\beta$ , the line to which all template fluxes are normalized, is assumed to be entirely created by recombination-cascade. The template flux equation, then, has two distinct components: collisional excitation and recombination excitation. The specified nebular temperature and density, the ionic abundances, and the attributes of the transition, determine their relative contributions.

The template flux equation is based upon a few simplifying assumptions:

1. The nebula has a single electron temperature and density. This is appropriate, given the approximations made for atomic parameters, and the fact that such parameters are unlikely to vary by an order of magnitude except in the most extreme conditions.
2. In the collisional contribution, each ion is modeled as a two level atom, of multiplicity unity on both levels. The upper level may be collisionally excited/de-excited.
3. Only direct recombination and cascade is assumed in the recombination contribution. No allowance is made for possible dielectronic recombination.
4. The vast majority of the parent ion of the transition is assumed to be in the ground state. No levels are considered to be meta-stable, to have sufficiently

small spontaneous emission coefficients to allow self-absorption, or resonance scattering.

The collisional portion of the template flux equation is derived from the equation of statistical equilibrium for the collisionally-excitable upper level of an ion of interest with net nuclear charge  $Z$ . The intensity of a line arising from this level,  $I_\lambda$ , divided by an estimate of the intensity of  $H\beta$ ,  $I_{H\beta}$ , can be shown to be equivalent to (Osterbrock 1989):

$$\frac{I_\lambda}{I_{H\beta}} \approx 1.0 \times 10^{14} N_Z \frac{q_{12}}{1 + N_e q_{21}/A_{21}}. \quad (3.13)$$

An approximate value of  $\alpha_{H\beta}^{eff} \approx 1.0 \times 10^{-14} \text{ cm}^3 \text{ sec}^{-1}$ , the nearly constant effective recombination coefficient for  $H\beta$ , has been used.  $N_Z$  is the overall ionic abundance with respect to hydrogen;  $q_{12}$  and  $q_{21}$  are the rates of collisional excitation and de-excitation of the ground and excited states respectively, and  $A_{21}$  is the spontaneous emission coefficient of the transition.

The rate of collisional de-excitation has the functional form:

$$q_{21} \approx \frac{1.0 \times 10^{-5} \Omega_{12}}{T^{1/2}} \text{ cm}^3 \text{ s}^{-1}, \quad (3.14)$$

where  $\Omega_{12}$  a dimensionless collision strength for the transition, a factor arising from quantum mechanics that is defined as the overlap between the initial and final wave-functions of the excited electron. The collision strength generally has a value between 0.1 and 10 for a wide range of collisionally excited lines. Assuming a typical value of 1, and an average nebular temperature of 10000 K,  $q_{21}$  can be expressed as a simple constant equal to  $10^{-7} \text{ cm}^3 \text{ sec}^{-1}$ .

The collisional excitation rate is related to the de-excitation rate by the Boltzmann factor:

$$q_{12} \approx Z q_{21} \exp\left(\frac{-\chi}{kT}\right) \text{ cm}^3 \text{ s}^{-1}. \quad (3.15)$$

$Z$ , the net nuclear charge, is included here to scale the collisional cross-section which enters into the derivation of the collisional excitation rate for non-hydrogenic ions.  $\chi$  is the energy difference between the ground and excited levels. Assuming that the main temperature dependence is in the exponential factor, and scaling the temperature to units of  $10^4$  K,  $T_4 \equiv T/10^4$ ,  $q_{12}$  can be expressed simply as

$$q_{12} \approx 1.0 \times 10^{-7} Z \exp(-0.8\chi/T_4) \text{ cm}^3 \text{ s}^{-1}. \quad (3.16)$$

Making these substitutions, the collisional portion of template flux equation yields:

$$\frac{I_\lambda}{I_{H\beta}} = 1 \times 10^7 N_Z Z \frac{\exp(-0.8\chi/T_4)}{1 + 1.0 \times 10^{-7} N_e/A_{21}}. \quad (3.17)$$

For a typical allowed, electric dipole, recombination line,  $A_{21} \approx 1.0 \times 10^7 \text{ sec}^{-1}$ , while  $A_{21} \approx 100 \text{ sec}^{-1}$  for intercombination lines, and  $A_{21} \approx 1.0 \times 10^{-1} \text{ sec}^{-1}$  for magnetic dipole and electric quadrupole forbidden lines. These values for  $A_{21}$  are substituted into the final form of the template flux collisional excitation contribution:

$$\frac{I_\lambda}{I_{H\beta}} = 1.0 \times 10^5 N_Z Z \frac{\exp(-0.8\chi/T_4)}{1 + 1.0 \times 10^{-7} N_e/A_{21}}. \quad (3.18)$$

The constant pre-factor is scaled down to yield better agreement with the observed strengths of actual well-known nebular lines. The pre-factor is further diluted by a factor of 10 for transitions arising from neutral ions to account for the greater difficulty in collisionally exciting such ions (in the absence of the Coulomb focusing effect induced by the net nuclear charge of a non-neutral ion).

For the recombination portion of the template flux we start with a generalized version of the effective recombination coefficient interpolation formula of Pequignot et al. (1991), who fitted effective recombination coefficients to numerous C,N,O ions' levels. We divide this by the same approximate value of the effective recombination coefficient of H $\beta$  ( $\alpha_{\text{H}\beta}^{\text{eff}} \approx 1.0 \times 10^{-14}$ ) to yield:

$$\frac{\alpha^{\text{eff}}}{\alpha_{\text{H}\beta}^{\text{eff}}} \approx 10(Z+1) \left( \frac{T_4}{(Z+1)} \right)^{-0.7}, \quad (3.19)$$

where  $Z$  is the net nuclear charge, equal to the ionic charge used in Pequignot et al. (1991) minus one. To convert to an intensity ratio we must multiply through by a branching ratio and by the numeric ionic abundance with respect to hydrogen for the ion  $N_{Z+1}$ , where this ion is in the next *higher* stage than the one used in the collisional portion. Assuming recombination to a non-metastable level, the branching ratios take the form of  $A_{21}/(1.0 \times 10^7 \text{ sec}^{-1})$  where the denominator is an order of magnitude estimate of the typical sum of spontaneous emission coefficients for all permitted transitions off the level, which will dominate the de-population of such a level.  $A_{21}$  is the order of magnitude estimate of the spontaneous emission coefficient for the various types of transitions defined earlier. After simplification we are left with:

$$\frac{I_\lambda}{I_{\text{H}\beta}} = N_{Z+1} \frac{A_{21}}{1.0 \times 10^6} \frac{(Z+1)^{1.7}}{T_4^{0.7}}. \quad (3.20)$$

We dilute the above equation by a factor of ten for electric dipole permitted transitions to again attempt to get better agreement with actually observed line strengths.

For each transition being tested as a possible ID for a particular line in the *Input Line List*, a value for the template flux of that transition is calculated according to



the sum of eqs. 3.18 and 3.20. The template flux is then normalized by the calculated template flux for  $H\beta$ .

### 3.5 Multiplet Check

An important component of EMILI is the automatic checking for additional lines belonging to the same multiplet as a predicted strong transition being tested as a potential ID for an unidentified observed line. Multiplet transitions are those that are between different pairs of  $j$  states in the same upper and lower levels. A typical multiplet, and all of its associated permitted transitions, is depicted in Figure 3.4. The validity of a particular transition as a potential ID is enhanced by evidence of other observed lines which could sensibly correspond to transitions from the same multiplet.

Lines from the same multiplet of the same transition type (electric or magnetic dipole or quadrupole) should exhibit similar wavelength agreement between their matches in the *Input Line List* and the transition’s tabulated “laboratory” wavelengths, since the parent ion is the same, and any errors in the laboratory wavelengths should presumably be of the same magnitude and direction given a common source of measurements.

These lines should also have fluxes within an order of magnitude of each other: they should differ only by the product of the relative occupation of the relevant levels (roughly proportional to their statistical weights), and their Einstein spontaneous emission coefficients (generally also within an order of magnitude of each other). The

### Fe II e4D - u4Fo Multiplet Transitions

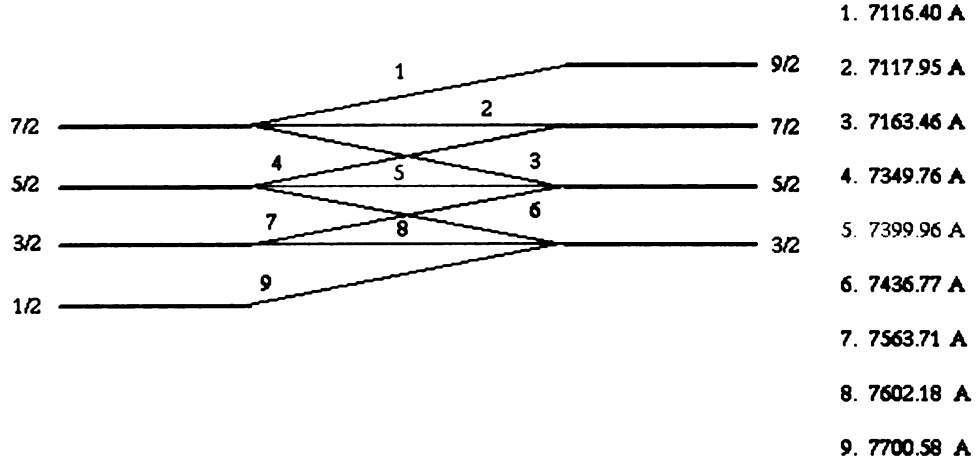


Figure 3.4 A typical multiplet of Fe II showing all allowed transitions under LS coupling. The position of the energy levels is not to any scale. Fraction beside of the levels are the  $j$  total angular momentum values of the each of the upper and lower levels. The numbers indicate the transitions and their laboratory wavelengths.

ratio of strengths of two typical recombination lines from the same multiplet can then be expressed approximately as:

$$\frac{I_1}{I_2} \approx \frac{(2j_1 + 1)A_1}{(2j_2 + 1)A_2}, \quad (3.21)$$

where  $(2j_1 + 1)$  and  $(2j_2 + 1)$  are the statistical weights of the  $j$  states of the upper level of the multiplet from which the lines originate, and  $A_1$  and  $A_2$  are the spontaneous emission coefficients of the two transitions.

For each surviving ID transition, EMILI searches for all multiplet transitions within the wavelength bounds of the *Input Line List* with upper and lower  $j$  values,  $j_{lower}$  and  $j_{upper}$  respectively, which meet the criteria of  $j_{lower} > j'_{lower} - 1$  and  $j_{upper} > j'_{upper} - 1$ , where  $j'_{upper}$  and  $j'_{lower}$  are the values of the upper and lower states

of the transition being tested as an ID. As an example, in Figure 3.4, if the Fe II  $\lambda 7399.96\text{\AA}$  line was being tested as a possible ID, all those other transitions in the multiplet other than line “9”,  $\lambda 7700.58$ , would be searched for. This is done to avoid biasing the total detection statistics, by looking for lines that might be weaker than the transition being tested and potentially undetectable in the spectra because of their smaller statistical weights. Lines from a level with large  $j$  are usually strong given the large statistical weight, while transitions between low  $j$  states are generally weak (Williams, private communication). For the same reason, EMILI will draw only those lines of the same or stronger transition type, electric dipole, magnetic dipole, or electric quadrupole in order of decreasing strength, as the transition being tested. If testing a particular collisionally excited, magnetic dipole, transition, such as the nebular [O III]  $\lambda 4959\text{\AA}$  line, EMILI would not look for the  $\lambda 4923$ , electric quadrupole  $\Delta j = 2$  line arising in the same multiplet, because the quadrupole transition is expected to be generally weaker. However if the  $\lambda 4923$  line were being tested, the code would look for the  $\lambda 4959$  line.

In the list below  $I_1$  and  $\lambda_1$  correspond to the observed intensity and wavelength of the candidate line EMILI is presently attempting to identify.  $A_1$  and  $j_1$  are the spontaneous emission coefficient and  $j$  value of the upper level of the transition EMILI is testing as a possible ID to that un-identified line.  $I_2$  and  $\lambda_2$  are the observed intensity and wavelength for another un-identified line from the *Input Line List* to which a transition of the same multiplet is thought to correspond.  $A_2$  and  $j_2$  are this transition’s spontaneous emission coefficient and upper level  $j$  value. In this example the  $j$  values of the upper and lower levels of the “2” line satisfy the EMILI criteria

for potential detection in the nebula (i.e.  $j_2 \geq j_1 - 1$  for both the upper and lower levels). To be accepted as a detected multiplet line, the following criteria must be satisfied:

1. *Flux Criteria:* If both transitions have  $A$  values in the transition database, then following eq. 3.21,

$$0.333 < \frac{A_1(2j_1 + 1)}{A_2(2j_2 + 1)} / \frac{I_1}{I_2} < 3, \quad (3.22)$$

must be true. If either or both  $A$  values are not known, then a somewhat looser tolerance is allowed:

$$0.1 < \frac{I_1}{I_2} < 10, \quad (3.23)$$

If the transition being tested is of lower expected strength than the other multiplet member, (because of weaker transition type), the upper bound is expanded and the lower bound is dropped when the  $A$  values don't exist.

$$\frac{I_1}{I_2} < 10^4, \quad (3.24)$$

or eq. 3.22 applies if the  $A$  values are known. This reduces the possibility of the code mistaking a much stronger line, relative to the line being ID'd, as a multiplet member. The generous limits are used to accommodate the possibility of errors in the flux measurements of either lines.

2. *Wavelength Criteria:* Since both lines belong to the same ion and multiplet, they each should arise from exactly the same region of the nebula. Thus, the differences between the observed wavelengths, after correction for the multiplet's ionic parentage, and the corresponding laboratory wavelengths of the

transitions, should be nearly the same, assuming that lines of similar strength have similar uncertainties in their wavelength measurements and laboratory-determined values. Velocity differences,  $v_{1,2}$ , are calculated from:

$$v_1 = c \frac{\lambda_1 - \lambda_{lab,1}}{\lambda_{lab,1}}; v_2 = c \frac{\lambda_2 - \lambda_{lab,2}}{\lambda_{lab,2}}, \quad (3.25)$$

where  $\lambda_{lab,1}$  and  $\lambda_{lab,2}$  are the laboratory wavelengths of the multiplet transitions.

In order for EMILI to accept the line “2” as a detected multiplet member the relative difference in velocities should satisfy:

$$|v_1 - v_2| \leq \sigma_2, \quad (3.26)$$

where  $\sigma_2$  is the uncertainty in measured velocity of line “2” in units of km sec<sup>-1</sup>.

If all the lines from a multiplet fall within the larger of the user-specified instrumental resolution or natural line width, it is assumed that the lines are blended. A statistical weight-weighted average wavelength replaces the transition’s laboratory wavelength, all the multiplet lines are considered to form a single line at that wavelength, and the multiplet check is not carried out.

Currently, EMILI carries out the multiplet check for only pure LS-coupled transitions. Future incarnations of the code will include the check for transitions from the three other coupling schemes employed in constructing the current and other transition database.

## 3.6 Ranking the Transitions

EMILI calculates an “Identification Index” or IDI value for each transition considered as an ID for an observed line, assigning an integer value based upon a three part scheme outlined in Table 3.2. The scheme gives equal weight to the relative template fluxes for all possible IDs for a line, the degree of wavelength agreement, and the multiplet check results, to calculate a numeric “score” for each competing ID transition. The relative IDI values within a particular line can be used to judge the most likely ID, while the absolute values may be used to judge the quality of a particular ID. A *lower* value of IDI indicates a *better* identification.

As an aid in visual inspection of the output, in addition to the numeric IDI value, EMILI assigns a alphabetic “rank”: “A”, “B”, “C”, or “D” based upon the relative IDI values for all potential ID transitions within a particular line, with rank “A” being the “best” ID for that line, “B” the second best and so on, with ties in IDI value receiving equal ranks.

## 3.7 Output

EMILI’s output consists of a large ASCII file (referred to as the *Full Output List*). The list begins with a header contains information about the run’s parameters, names of input and output files, the user-specified temperature, density and instrumental resolution, and the calculated velocity corrections,  $v_{cor}$  and ICF values ( $x_A - x_E$ ). The header from the output for the EMILI run on the present IC 418 dataset is shown in Figure 3.5.

Table 3.2 The IDI assignment breakdown for a putative IDs for a given unidentified line. A lower IDI value means a better ID in general.

1. Flux Basis ( $F$ )

A putative ID template flux among all other putative IDs for the same line satisfies the following condition:

$F$	Condition
0	Exceeds computed fluxes of all other putative IDs by factor $\geq 10$ .
1	Within a factor of 10 of the largest putative ID template flux.
2	Within a factor of 100 of the largest putative ID template flux.
3	Within a factor of 1000 of the largest putative ID template flux.

2. Wavelength Basis ( $W$ )

The residual wavelength difference (in km/s) between the observed line's corrected wavelength and that for the putative ID is within a number of measurement sigmas ( $\sigma$ ) of the observed line's corrected value:

$W$	Conditions
0	$\leq 0.5\sigma$
1	$\leq 1.0\sigma$
2	$\leq 1.5\sigma$
3	$\leq 2.0\sigma$

3. Multiplet Basis ( $M$ )

For a putative ID, the number of detected multiplet members,  $D$ , out of  $P$  possibly observable members satisfy:

$M$	Conditions
0	$P/D = 1/1, D > 2$
1	$P/D = 0/0, 2/1$
2	$P/D = 1/0, (> 2/1)$
3	$P/D = (> 1)/0$

$$\text{IDI value} = F + W + M$$

```

EMILI Output File
-----
Input Line List: ic418.in
Input Matched List: ic418.match
Results List: ic418.out
Short Results List: ic418.dat
Abundance Table: abund.dat
Electron Temp: 10000.
Electron Density: 10000.
Inst. Resolution: 10.

ICF Values: Bin/%
ix 1: 0.00999999978
ix 2: 0.498415828
ix 3: 0.489584208
ix 4: 0.00100000005
ix 5: 0.00100000005

Velocity Structure: Bin/Vel (km/s)
irvcor 1: 4.26208973
irvcor 2: 4.08970976
irvcor 3: 1.74469769
irvcor 4: -0.0550202653
irvcor 5: -0.0550202653

```

Figure 3.5 The header for the EMILI output file generated by its run on IC 418 dataset. The header includes information regarding the input/output files, specified temperature, density, instrumental resolution, and the calculated ICF (labeled here as "ix 1" – "ix 5") and  $v_{cor}$  (labeled here as "irvcor 1" – "irvcor 5") values for the five ionization energy bins.

The header is followed by an entry for every unidentified line, similar to that seen in Figure 3.6, containing information regarding possible IDs for that line. In each entry, the top row indicates the observed wavelength of the particular line, its flux, (normalized to the observed  $H\beta$  line strength), and the S/N and FWHM of the line. Each succeeding row is a potential ID for the line, listed in order of increasing velocity difference between laboratory and observed, corrected wavelength. The columns indicate: (1) The observed wavelength of the line, corrected by the  $v_{cor}$  appropriate for the transition. (2) The laboratory wavelength of the transition. (3)



Observed Line: 5179.52 3.3E-05 S/N: 18.40 FWHM: 18.6									
5179.45	5179.000*	S I	1073985643	4	8.3E-06	26.0	0/0	8	
5179.52	5179.178	Fe III	1747436964	263	1.1E-04	19.9	* / 0	9	
5179.49	5179.172\$	Fe II	1746398483	7	1.7E-04	18.4	0/0	60	
5179.49	5179.256	Fe II	1746167982	8	4.7E-04	13.5	7/0	8	
5179.49	5179.262	Ar II	1209154620	265	1.1E-05	13.2	6/0	9	
5179.49	5179.344	N II	471096463	263	3.5E-04	8.4	2/0	7	
+ 5179.49	5179.420	N I	469938193	262	1.1E-04	4.0	7/0	5C	
+ 5179.49	5179.432\$	Ar II	1209296995	9	1.1E-05	3.3	0/0	4B	
+ 5179.49	5179.520	N II	471088267	263	3.5E-04	-1.8	2/1	2A	5175.889 -3.4
5179.52	5179.738\$	Ne II	672424011	7	1.9E-04	-12.6	0/0	60	
5179.49	5179.831	N I	469933071	264	1.2E-04	-19.8	7/0	8	
5179.52	5179.900	C III	404892760	5	1.1E-03	-22.0	0/0	60	
5179.52	5179.900	C III	404893785	5	1.1E-03	-22.0	0/0	60	
5179.49	> 5180.310	[Fe III]	1746959383	54	4.7E-02	-47.5	2/0	0<	
(1)	(2)	(3)	(4)	(5)	(6)	(7)	(8)	(9)	(10)

Figure 3.6 The EMILI output for a line observed at 5179.52Å in our IC 418 spectrum. Column legend is provided in the text.

The parent ion of the transition. (4) and (5) are internal reference numbers for the transition, employed in the transition database. (6) The template flux. (7) The velocity difference between the observed line, post-correction, and the transition's laboratory wavelength. (8) The multiplet statistics with format "X/Y", where out of "X" other multiplet lines expected to be observed, "Y" were actually detected. (9) The IDI value and rank. (10) If additional multiplet lines are found by the code, they are listed along the same row in decreasing observed flux order. The velocity difference between the multiplet transition's laboratory wavelength and the corrected, observed wavelength from its corresponding line are listed for each multiplet line found. Up to

three such lines at maximum are displayed.

Additional marks in the individual line identification entries include a “+” before column (1) which indicates that the laboratory wavelength is within  $1.5\sigma$  of the observed, corrected wavelength, where  $\sigma$  is the observed wavelength’s measurement uncertainty. An “\*” after column (3) indicates that all the lines from the multiplet were within the instrumental resolution or natural line width, and the listed wavelength is a statistical weight-weighted blend wavelength. A “\$” in transition was not a pure LS coupling. The multiplet check is not currently carried out for such transitions, indicated by a “0/0” entry in column (8). Finally the last row in each identification, with a “>” preceding column (3) and a “<” in column (9), indicates the strongest predicted transition in the velocity region between the initial search radius from the transition database, and twice that radius. This allows strong lines with poor theoretically calculated or laboratory observed wavelengths to be considered as possible ID. The multiplet check is carried out for these lines, but the transition is not ranked and no IDI value is calculated.

EMILI suggests that for the weak line ( $3.3 \times 10^{-5}$  times the flux of  $H\beta$ ) whose EMILI output is depicted in Figure 3.6, N II  $\lambda 5179.52\text{\AA}$  is the most likely ID. This is based upon its relatively strong template flux, actually within an order of magnitude of the observed value, close wavelength agreement, post-velocity model correction, and the detection of a second line, out of a possible two, from the same multiplet. It is significant that this line, N II  $\lambda 5179\text{\AA}$  3p  $^5P^o$  - 3d  $^5F$ , must arise from dielectronic recombination, as it belongs to a multiplet with spin multiplicity of 5, a level incapable of being excited by standard one-body recombination between  $N^{++}$

and a free electron. Such a line, unusual among nebular lines, may not have even been considered as a possible ID using “conventional” manual identification procedures, nor have been included in a model spectrum.

A second output file, called the *Summary List*, simply states the observed wavelength and all “A” rank EMILI identification for all unidentified lines. An example, generated by a run on the IC 418 dataset, may be seen in the EMILI User’s Manual (Appendix D)

### 3.8 Application to Other Spectra

EMILI has been applied to several nebular spectra, including the Orion Nebula (Baldwin et al. 2000) and NGC 7027 (Walsh et al. 2001), in addition to the present dataset on IC 418. Manual IDs were available for the Orion and NGC 7027 datasets, which allowed a comparison with the IDs suggested by EMILI. Comparing EMILI primary rank “A” IDs against manual IDs in the two datasets (Tables 3.3 and 3.4) shows that at least 75% of the time, the EMILI primary ID corresponds to the manual ID. Including cases where EMILI secondary and tertiary IDs correspond to the manual IDs are included, the matching statistics improve to about 90% or better in both objects. In these examples where individual lines were listed with multiple IDs, the matches include only the highest ranked EMILI ID among those manual IDs.

Running the present incarnation of EMILI with the IC 418 data of Hyung, Aller, & Fiebelman (1994) (HAF) (at a  $T_e = 10000$  and  $N_e = 11500$ ), yields the results in Table 3.5, where EMILI IDs are compared to manual ones for lines in which HAF

Table 3.3 Manual IDs versus EMILI IDs for emission lines in the Orion Nebula as observed by Baldwin et al. (2000). The second column lists the number of times within each EMILI rank, that a particular manual line identifications matched the EMILI identification of that rank for that line. The bottom row without a rank entry indicates the number of lines for which the manual ID was not ranked by EMILI, or for which the transition was not present in the EMILI transition database. The third column shows the percentage of all 388 lines that fall in each category.

Rank	N	%
A	329	85%
B	34	9%
C	12	3%
D	5	1%
	8	2%
TOTAL	388	

Table 3.4 The same as Table 3.3 for the spectrum of the PN NGC 7009 by Walsh et al. (2001).

Rank	N	%
A	258	73%
B	31	9%
C	23	7%
D	7	2%
	33	10%
TOTAL	352	

Table 3.5 The same as Table 3.3 for the spectrum of IC 418 as observed by HAF. These statistics include only lines assigned single distinct IDs by HAF.

Rank	N	%
A	178	88%
B	4	2%
C	5	2%
D	0	0%
	16	8%
TOTAL	203	

had a distinct single transition as an ID. Good agreement, on a par with the earlier works, is shown between the manual and EMILI-derived IDs. In addition, EMILI provides possible IDs for lines left unidentified in this work. For twenty or so lines, the transitions corresponding to the manual IDs could not be found in the EMILI transition database. In some of these cases HAF did not provide a corresponding multiplet member from which to confirm the wavelengths and transition types, nor did the listed wavelength match any nearby transition for the same ion and transition type in the database. If these lines are thrown out, the EMILI matching statistics improve to nearly 95% for primary rank “A” IDs against manual IDs.

It should be noted that the manual IDs are unlikely always to be correct, so that some EMILI primary IDs may be better than their manual counterparts.

### 3.9 Application to Current Dataset

A list of 805 probable nebular lines were submitted to EMILI for identification. For each line, the observed wavelength was assigned a measurement uncertainty based upon a statistical analysis of agreement between multiple measurements of the same line in differing orders and spectra, and agreement between the observed and laboratory wavelengths of several well know emission lines (see Sect 2.3.3). A subset of this list, including 40 emission lines with unambiguous identification and no obvious blending, were used by the code to establish the velocity model and ionic abundances in the manners described previously. The distribution of velocity corrections and ICF factors for each ionization energy bin are listed in the EMILI output header shown

in Figure 3.5. EMILI was run with  $T_e=10000$  and  $n_e=10000$ , composite values established from various forbidden line diagnostics (see Sect 4.1.1). The instrumental resolution was set to  $10 \text{ km sec}^{-1}$ .

For each unidentified line, the code searched the transition database for all transitions within  $5\sigma$ , where  $\sigma$  is the assigned wavelength measurement uncertainty, then computed template fluxes for emission lines corresponding to them. The multiplet check was carried out for the transitions with the strongest template fluxes in this region, and for the transition with the strongest template flux in the  $5\text{-}10\sigma$  halo region. The boundary condition on the left hand side of eq. 3.22 was removed in an effort to improve multiplet member detection chances, but there appeared to be no significant difference in this regard in comparison with a previous run using both boundary conditions.

Based upon the wavelength agreement between observed, corrected line wavelengths and the laboratory wavelengths of potential ID transitions, the relative strength of their template fluxes, and the results of the multiplet check, an IDI value was calculated and a rank awarded to each possible ID for a particular observed line. A sample of the EMILI output for an individual line in this dataset may be found in Figure 3.6.

The EMILI output was compared to the line identifications from high resolution PN and H II region spectra, including HAF (IC 418), Liu et al. (2000) (PN NGC 6153), Baldwin et al. (2000) (Orion Nebula), and Esteban et al. (1999) (H II region M8). The strongest recombination lines expected from a variety of ions were determined by referencing Williams (1995, and private communication), Liu et al. (2000), Moore

Table 3.6 Numbers and percentage of EMILI IDs chosen as final IDs for each EMILI IDI rank, out of the total number of IDs used from EMILI. The average, minimum, and maximum IDI values among IDs chosen within each rank are also listed. These numbers includes all transitions from lines thought to be blends, or which otherwise had multiple EMILI selected for them. “Total” equals the total number of EMILI IDs selected, not the number of individual emission lines.

Rank	N	%	Avg IDI	Min IDI	Max IDI
A	543	67.5	2.7	0	7
B	91	11.3	5.1	2	9
C	56	7.0	6.3	2	>9
D	38	4.7	6.8	4	9
None	77	9.6	7.8	5	>9
TOTAL	805				

(1945), and Osterbrock, Tran, & Veilleux (1992). These were used to establish likely upper flux limits for lines ID’d as belonging to those ions, and to judge the credibility of identifications made by EMILI of transition arising from ions of comparable and higher ionization potentials. Choices for individual line identifications were then made based upon the EMILI output, and the above information, and incorporated into the final line list (Appendix E).

Table 3.6 lists the numbers of different EMILI ranked IDs which were chosen manually from the output as actual line IDs. Some lines had multiple IDs selected, where it was suspected that the line might be a blend of two or more individual transitions of similar strength, or where two or more IDs were thought to be equally likely. Table 3.6 includes every individually selected ID transition from these lines. On a whole, it appears that EMILI provided reliable IDs (confirmed primarily by previous literature or via the multiplet check) for about 69% (555 lines) of the total number of individual lines originally submitted for identification (805 lines). When

including cases where it was thought that EMILI provided at least a possible ID (624 lines) the estimated success rate rises to 78%.

EMILI was unable to provide any convincing IDs for the remaining unidentified lines. However, a significant number of these lines,  $\approx 50$  or so, were found in the region  $\approx 6700\text{--}8800\text{\AA}$ . Some of these lines are fairly strong ( $> 10^{-4} H\beta$ ) and inspection of the original 2-D images established that many are real, but obvious transitions responsible for them were apparently not included in the EMILI transition database. An inspection of Osterbrock, Tran, & Veilleux (1992) and the Kurucz atomic transition database (Kurucz & Bell 1995) suggested that most of these lines correspond remarkably well to higher ( $n > 15$ ) transitions from He I singlet and triplet states whose upper levels were not included in calculating the transitions in the Atomic Line List v2.04. Several Balmer and Paschen lines for transitions originating above  $n = 40$ , as well as for a handful of iron forbidden lines observed in the spectra, were also not present in the EMILI database. These identifications were made manually using information from the Kurucz database for the hydrogen lines; and Moore (1945) and the NIST database for the iron forbidden lines. These lists also provided quality identifications for a handful of additional lines in this region, with only a possible EMILI-provided ID.

The remaining 120 unidentified lines had no EMILI IDs that were in any way distinguishable from each other in the EMILI output, or had IDs for ions thought not to be abundant enough to be able to produce lines of any observable strength. Many of them are on the extreme edges of the original 2-D spectra, where the signal-to-noise was not as good due to the declining illumination of the spectra at these locations. In



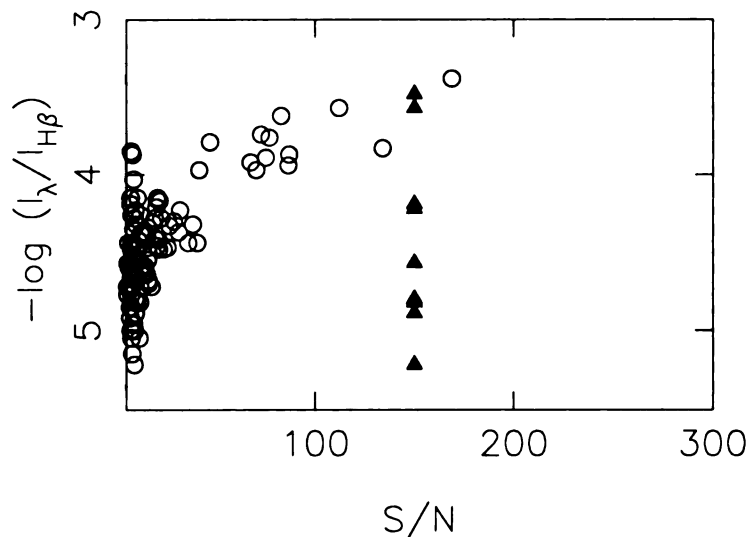


Figure 3.7 The distribution of flux:  $-\log(I(\lambda)/I(H\beta))$  versus  $S/N$  for remaining unidentified lines. Small triangles at  $S/N=150$  indicate unidentified lines with indeterminate  $S/N$ .

addition, most of these lines were not observed in any of the comparison spectra we used to confirm our IDs. However, the distribution of the  $S/N$  and observed fluxes of these lines, as seen in Figure 3.7, shows that some relatively strong lines remain un-identified. Many of these are probably real lines, although some of them may be scattered light artifacts, ghosts, cosmic rays, or night-sky lines that survived the various screening processes.

### 3.10 Future Directions of the Code

The greatest limitation of the present code is the fact that there is no cross correlation between individual line identifications, beyond the multiplet check. For instance, there is no check to see if lines ID'd from a particular ion all exhibit the same wavelength agreement between observed and laboratory values, or all have the

same FWHM. Such a check could further enhance the believability of whole sets of identifications, and might reveal the existence of unresolved blends.

Another limitation of the code is the confinement of the multiplet check to pure LS-coupled level transitions. The current incarnation of the code works extremely well isolating those lines that have pure LS coupling, but is incapable of defining what a multiplet is in the intermediate coupling schemes which apply to many nebular lines (especially to lines from levels with excited electrons of higher angular momentum quantum number  $\ell$  such as the strong 3d-4f lines of the abundant species O II and N II). It would be advantageous to include additional code making the multiplet check available for these important nebular lines.

It is desirable that the template flux values more accurately reflect true observed line fluxes. The template flux equation makes no allowance for dielectronic recombination, Bowen-like fluorescence, charge transfer, or continuum fluorescence by starlight from the central star. In addition, no provision is made for the difference in observed flux between lines in the same multiplet, but of different transition type. For instance, the [O III]  $^3P_0 - ^1D_2$   $\lambda 4923$  transition (an electric quadrupole transition) has the same template flux as the [O III]  $^3P_1 - ^1D_2$   $\lambda 4959$  magnetic dipole transition, but is observed to be nearly four orders of magnitude stronger in our IC 418 spectrum. This occurs because the branching ratios and spontaneous emission coefficients of individual transitions are not incorporated into the collisional part of the template flux equation.

Finally, the results obtained from using EMILI with PN spectra have shown that the code is somewhat too reliant on good wavelength agreement between the observed

and laboratory wavelengths of an observed line and that of its potential ID. This allows transitions of iron, nickel, and less abundant species to often times be ranked higher than other more obvious IDs, because of a coincidence of one of their innumerable transitions with an observed wavelength. Furthermore, laboratory transitions, although called “laboratory”, are more often calculated from theoretical levels, rather than actually observed in an arc or in some other fashion, and their wavelengths are sometimes not as accurately determined as the actual observed wavelengths of nebular emission lines. A poignant example of this from the Atomic Line List v2.04 is the strong [Ne III] doublet  $\lambda\lambda 3869, 3968$ , with both lines’ laboratory wavelengths differing from their observed wavelengths by  $> 20 \text{ km sec}^{-1}$  more than twice the instrumental resolution.

In future releases we will address these problems, by adding additional logic to further cross-correlate line identifications, to carry out the multiplet check for all transitions regardless of coupling scheme, and to improve the accuracy of the template flux equations with respect to actually observed relative line strengths. Furthermore, our wish is to eventually make the code iterative. For example, a user would interpret the output from an initial run and make decisions as to possible identifications for each of the lines. The user could then adjust nebular physical parameters or initial elemental abundances and re-run the code, using the chosen IDs from the previous run to re-calculate the velocity model and ionic abundances, and refine the quality of the line identifications.

The detection of He I lines in our spectra which were not present in the transition database, as well as Balmer and Paschen lines above  $n = 40$ , demonstrates the need

to link, broader transition databases to the program. Presently, the Atomic Line List v2.04 is virtually meshed into the code, making updating to a more expansive database difficult. However, plans are in the works to incorporate its successor, the Atomic Line List v2.05, into EMILI. This line list expands the available ion list to  $Z \leq 36$ , and includes He I out to  $n = 50$ . Because of the similarity to the presently utilized transition database, its incorporation into EMILI should not require extraordinary effort.

A longer-range goal is the establishment of an EMILI “standard” to which any transition database can be converted and utilized, and to allow multiple databases to be accessed simultaneously. Not only would this allow rapid upgradability, it would also allow EMILI to utilize transition lists more appropriate to specific classes of emission-line objects such as PN, quasars, or novae, or to incorporate molecular lines, or even to make EMILI applicable to stellar absorption spectra.

### 3.11 Conclusions

We have presented a software package called EMILI, which is specifically designed to take advantage of the vast amount of information available in modern atomic transition databases, to aid in the identification of atomic emission lines in PN, H II regions, and other emission-line region objects. EMILI overcomes some limitations present in model spectra by using generic values of scarce atomic parameters. EMILI is a tool specifically tailored to PN and H II region emission line identification, by employing techniques to model the expansion velocity distribution along the line

of sight to a such an object, and to calculate rough ionic abundances. The code minimizes the observer bias that could go into the line identification by providing a uniform set of criteria by which individual potential identifications can be judged. The code automates a time consuming and tedious process. Finally EMILI provides good agreement between manual and code-derived IDs. We believe that EMILI is an invaluable tool for those studying emission line regions and their spectra, which should only improve with further work.

The code is publically available at:

[www.pa.msu.edu/people/sharpee/emili.html](http://www.pa.msu.edu/people/sharpee/emili.html)

# Chapter 4

## Results

### 4.1 Plasma Diagnostics

#### 4.1.1 Temperature and Density Diagnostics

Electron temperature and density estimates were established from the relative strengths of various collisionally excited lines in particular combinations (diagnostic line ratios). Tasks from the IRAF *nebular* package (Shaw & Dufour 1995), which solve the statistical equilibrium equations for the collisionally-excitable levels of the involved ions, using a five or greater level ion, were used along with the observed values of the diagnostic ratios to make the density and temperature determinations.

We used the most recent version (2.0) of *nebular*. However, it was found that the default transition probabilities and collision strengths that came with the package produced unlikely results. The densities and temperatures that were found using different ions did not agree well with each other, and when we ran the test cases

Table 4.1 References for Atomic Data for Collisionally Excited Lines.

Ion	Transition Probabilities	Collision Strengths
C I	Froese-Fischer & Saha (1985)	Johnson, Burke, & Kingston (1987) ( $\Omega_{21}, \Omega_{31}, \Omega_{32}$ )
		Pequignot & Aldrovandi (1976) (remaining)
N I	Mendoza (1983)	Mendoza (1983)
N II	Mendoza (1983) (1-5) <sup>(a)</sup>	Mendoza (1983) (1-5)
	Weise, Fuhr, & Deters (1995) (6)	Dopita, Mason, & Robb (1976) (6)
O I	Mendoza (1983)	Mendoza (1983)
O II	Mendoza (1983) (1-5)	Mendoza (1983) (1-5)
	Weise, Fuhr, & Deters (1995) (6)	Dopita, Mason, & Robb (1976) (6)
Ne III	Butler & Mendoza (1984)	Butler & Mendoza (1984)
S II	Cai & Pradhan (1993) (1-5)	Cai & Pradhan (1993) (1-5)
	Verner, Verner, & Ferland (1996) ( $A_{61}, A_{71}, A_{81}$ )	Ramsbottom, Bell, & Stafford (1996)
	Keenan, Hibbert Ojha, & Caylon (1994) (remaining for 6)	
S III	Mendoza (1983) (1-5)	Mendoza (1983) (1-5)
	Heise, Smith, & Calamai (1995) ( $A_{62}, A_{63}$ )	Galavis, Mendoza, & Zeippen (1995) (6)
	LaJohn & Luke (1993) ( $A_{64}$ )	
	Kaufman & Sugar (1986) ( $A_{65}$ )	
Cl II	Wilson & Bell (2002)	Wilson & Bell (2002)
Cl III	Butler & Zeippen (1987)	Butler & Zeippen (1987)
Ar III	Mendoza (1983)	Mendoza (1983)
Ar IV	Butler, Zeippen, & Le Bourlot (1987) (1-5)	Butler, Zeippen, & Le Bourlot (1987)
	Kaufman & Sugar (1986) (6-8)	

<sup>(a)</sup> Indicates levels/parameters used from reference.

Note: References not listed in bibliography are referenced in the *nebular* package help file: *at\_data.hlp* distributed with the package.

given with the package task *temden*, substantially different results were obtained. Further investigation showed that the atomic parameters had been updated since the original thorough testing that led up to the release of the package. After considerable investigation, it was decided to go back to the original atomic parameters for most ions, which came from the sources that still are the most widely used. Table 4.1 lists the references for the atomic data that were eventually adopted.

Calculated temperatures and densities can be found in Table 4.2. To solve for the electron temperature and density, a density and temperature diagnostic from the same ion, or from ions with similar ionization potential energies of the previous

Table 4.2 Plasma Diagnostics and Their Uncertainties for IC 418.

Ref	Diagnostic	Energy <sup>(a)</sup>			X-Ref	
Density		$n_e(\text{cm}^{-3})$				
(1)	[N I] $\lambda 5200/\lambda 5198$	0.0	9000	...	-6000 (1)	
(2)	[S II] $\lambda 6716/\lambda 6730$	10.4	17000	...	-9000 (2)	
			18000	...	-10000 (3)	
			10000	+20000	-5000 (3)	
(3)	[O II] $\lambda 3726/\lambda 3729$	13.6	10000	+17000	-4000 (4)	
			10000	+20000	-5000 (5)	
			11000	+3000	-2000 (6)	
(4)	[Cl III] $\lambda 5517/\lambda 5537$	23.8	10000	+3000	-2000 (7)	
			6000	+10000	-4000 (8)	
(5)	[Ar IV] $\lambda 4711/\lambda 4740$	40.9				
Temperature		$T_e(K)$				
(1)	[O I] $(\lambda 6300 + \lambda 6363)/\lambda 5577$	0.0	9400	+600	...	(1)
(2)	[S II] $(\lambda 6716 + \lambda 6731)/(\lambda 4068 + \lambda 4076)$	10.4	7000	+5000	...	(2)
(3)	[Cl II] $(\lambda 8579 + \lambda 9124)/\lambda 6162$	13.0	10100	+700	-500	(2)
			10200	+700	-500	(3)
(4)	[O II] $(\lambda 3726 + \lambda 3729)/(\lambda 7320 + \lambda 7330)$	13.6	10000	+4000	-3000	(3)
(5)	[N II] $(\lambda 6548 + \lambda 6583)/\lambda 5755$	14.5	9400	+500	-1100	(3)
(6)	[S III] $(\lambda 9069 + \lambda 9532)/\lambda 6312$	23.4	9500	+600	-500	(4)
(7)	[Ar III] $(\lambda 7136 + \lambda 7751)/\lambda 5192$	27.6	9000	+500	-400	(4)
(8)	[O III] $(\lambda 4959 + \lambda 5007)/\lambda 4363$	35.1	8900	+300	-300	(5)
Balmer Jump		5300	6600	$\pm 500$		
<sup>(a)</sup>	Ionization potential of previous stage of ionization for ion					
<sup>(b)</sup>	Upper density uncertainty/lower temp uncertainly unavailable for combinations with [N I] and [S II] density diagnostics, see not in text					

stage of ionization, were paired off (see “X-Ref” numbers in the Table). The *nebular* task *temden* was used iteratively between the two diagnostics, taking the output from the density diagnostic as the assumed density for the temperature diagnostic, and vice-versa, until both diagnostics returned the same temperature and density. These intersection points between diagnostics may also be directly inferred from the diagnostic diagram shown in Figure 4.1.

Errors for each diagnostic line intensity and the reddening uncertainties, were propagated through the ratio calculation to yield the errors in the listed temperatures



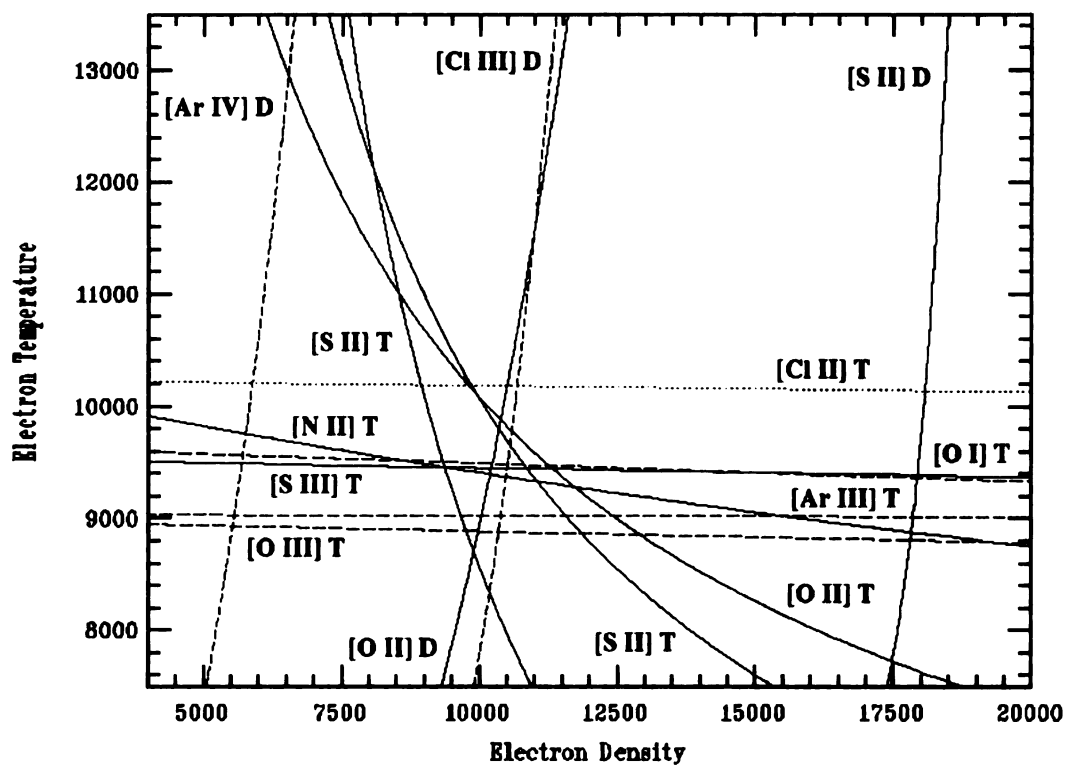


Figure 4.1 Diagnostic diagram for IC 418. In the diagram “D” adjacent to the ion denotes a density diagnostic for that ion, while “T” denotes a temperature diagnostic.

and densities. These errors may be overestimates, as the measurement scatter for all the diagnostic lines with repeated measurements was smaller than the tabulated error value. Since diagnostic ratios match lines of neighboring wavelength, the effects of flux calibration and reddening errors are minimized when their strengths are compared in ratio.

As seen in the figure, nearly all the diagnostics seem to converge in the vicinity of  $10000 \text{ cm}^{-3}$  and  $9600 \text{ K}$  (the average values excluding the [S II] temperature, and [S II] and [Ar IV] densities). There is a general trend in increasing temperature with decreasing energy of ionization. This is in line with the notion of the general

hardening of the central star radiation with increasing distance from the central star, assuming that decreasing ionization potential energy also correlates with increasing distance from the star. The lower [O III] (source ion  $O^{+2}$ ) temperature with respect to [O II] value is also in line with the probable effects of efficient cooling by strong  $O^{+2}$  IR fine structure lines, to which  $O^{+}$  has no analog (Garnett 1992). The lower [S II] temp is a direct consequence of its pairing with the (probably saturated) [S II] density diagnostic, and its curve does pass through the region where many of the other diagnostics intersect. The composite temperature from the diagnostics is about 1000 K less than that observed in Hyung, Aller, & Feibelman (1994) (HAF), but our data show greater internal consistency than the various temperature diagnostics calculated by HAF and Henry, Kwitter, & Bates (2000) (HKB) for IC 418.

The [N I] and [S II] diagnostic ratios are most likely saturated: observed values place them at the high density limit of their theoretical intensity ratio versus density curves (Stanghellini & Kaler 1989). In the high density limit the theoretical ratios become essentially constant with respect to density. Small observational errors in the observed ratio can lead to large uncertainties in the calculated densities. This is reflected in the tabulated null uncertainties recorded for the upper [N I] and [S II] uncertainties and their matched temperature diagnostic lower bound uncertainties. Interestingly, both HAF and HKB determined [S II] densities,  $5600 \text{ cm}^{-3}$  and  $3300 \text{ cm}^{-3}$  respectively, that were much *lower* than the value determined here, and in the case of HAF, lower than those from any of their other observed density diagnostics. However, a compilation of previous IC 418 [S II] density determinations made by Stanghellini & Kaler show a wide range of observed values,  $4300\text{-}25000 \text{ cm}^{-3}$ .

Furthermore, Copetti & Writzl (2002) have shown that [S II] densities are statistically higher than [O II] densities for the densest nebulae from a compendium of PN observations.

The [Ar IV] density diagnostic, observed in IC418 for the first time here and the highest ionization diagnostic we observed, yields the lowest density value. This lends credence to the notion that these lines arise from the central cavity observed often in other PNe (Stanghellini & Kaler 1989). For IC 418, such a cavity has been previously conjectured to be of lower density than the surrounding nebular shell in order to explain the deficit of  $H\alpha$  emission observed spectra-photometrically in the central region of the nebula (Reay & Worswick 1979). However, the location of the slit (see Figure 2.1) doesn't appear to correspond to the obvious visual location of the central cavity. The atomic data may also be incorrect for this ion; the use of the  $Ar^{+3}$  atomic parameters used presently in *nebular* (Kaufman & Sugar 1986) at the [O III] temp of 8900 K, returns a somewhat higher value of  $7800\text{ cm}^{-3}$ , even though other diagnostic show tighter agreement when the previous atomic data is used. Alternatively, these lines are also the weakest of our observed diagnostic lines with uncertainties which would bring it into alignment with the other diagnostics. However, since both diagnostic lines are distinct in profile and free of blending in our spectra, we assume that lower density is not an observational artifact.

We conclude that the agreement among the diagnostics is very good. The disagreements are attributable to expected observational errors in the line intensities, real effects such as diagnostic line ratio saturation, or inaccuracies in atomic parameters, and a (probably) non-homogeneous, stratified ionization structure, even though

IC 418 appears to be a uncomplicated system.

### 4.1.2 Balmer Jump Temperature

The difference in the continuum levels across the Balmer jump (at 3646.97Å), compared to the strength of a Balmer line, may also be used to measure the nebular temperature. From the Milne relation, the emission coefficient of the continuum due to recombinations to the first excited state alone,  $j_2$ , can be written as (Kwok 2000):

$$j_2 = \frac{2.16 \times 10^{-38} N_p N_e}{4\pi} \frac{0.8761}{T_4^{3/2} 8}, \quad (4.1)$$

where all other symbols are defined as before. Dividing by the emission coefficient for H $\beta$ , incorporating the weakly temperature dependent formula for  $\alpha_{H\beta}^{eff}(T_4)$  from Pequignot et al. (1991) leaves

$$\frac{j_2}{j_{H\beta}} = \frac{\mathcal{C}}{\alpha_{H\beta}^{eff}(T_4) T_4^{3/2}}, \quad (4.2)$$

where  $\mathcal{C}$  is a constant. Since the intensity of a line is directly proportional to the integral of the emission coefficient along the line of sight, the observed intensity difference in the continuum across the jump divided by the observed H $\beta$  intensity can be equated to eq. 4.2, and the equation solved for temperature.

To obtain the value of the jump, a linear least squares fit to the continuum excluding obvious emission lines and scattered light features, was made blueward (3500-3645Å) and redward (3775-4065Å) of the discontinuity. The jump values was then determined by extrapolating the fits on both ends to the Balmer series-limit wavelength (3646.97Å). These fits sampled wavelengths in overlapping orders twice. The

continuum values were weighted by the associated spectrum error array, and subjected to three cycles of sigma clipping to reduce the effects of remaining weak lines and artifacts within the fitted regions. The resulting fits are displayed in Figure 4.2. The He I recombination discontinuity at  $3680\text{\AA}$  wasn't accounted for as it wasn't clearly evident in the spectrum. The redward fit value was then subtracted from the blueward fit value to yield a jump intensity.

The jump intensity was then corrected for reddening, and divided by the dereddened intensity of  $H\beta$ . The observed ratio was equated to eq. 4.2, and the relation solved for temperature. A temperature of  $5300\text{ K} \pm 500\text{ K}$  was determined, where the error is derived from the formal errors in the fit coefficients and reddening correction, propagated through the temperature calculation. The region immediate redward of the jump was not originally included in the fit due to the confusion of the continuum level by crowded lines at the series limit, and an overlaying contribution to the continuum by a broad flare from the  $[\text{O II}] \lambda\lambda 3727, 3729$  doublet in an adjacent order. Carefully selecting only a narrow region of relatively flat continuum nearer to the jump than the previous fit ( $3673\text{-}3686\text{\AA}$ ) yields a somewhat higher value of  $6600\text{ K} \pm 600\text{ K}$ .

The resultant temperatures agree with the standard observation of lower Balmer jump temperatures with respect to the forbidden line measures. This is attributed to recombination-derived temperatures giving a large weight to cooler regions where recombination is the most efficient, while collisionally excited line-derived temperatures tend to weight more strongly the warmer regions where collisional excitation is most efficient (Liu & Danziger 1993). However, as seen in Figure 4.2, scattered light

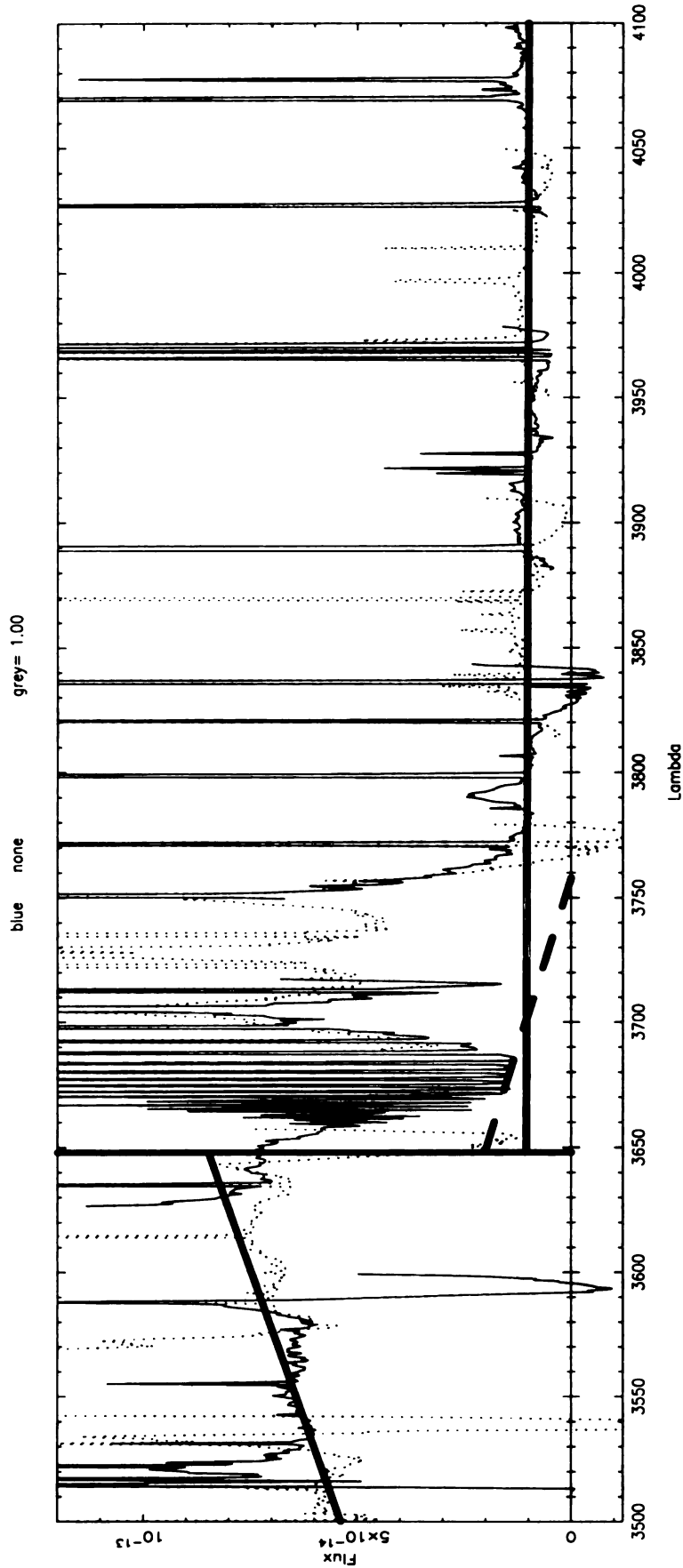


Figure 4.2 The blue spectrum in the vicinity of the Balmer series limit, including all regions that were fit to establish the continuum levels. The jump is at  $3648\text{\AA}$ , indicated by the vertical line. We used two fits to the continuum redward of the jump. The solid horizontal line indicates a fit over the large region of the continuum away from the jump and yields a temp of  $5300\text{ K}$ . The dashed line is a fit in immediate vicinity of the jump, and yields a temp of  $6600\text{ K}$ . The same fit blueward of the jump, indicated by another horizontal solid line, was used in both temperature determinations.

artifacts, the inaccuracy of the scattered light correction, lingering intensity profiles inherited from the echelle blaze even after correction by quartz lamp division, and the weakness of the continuum level itself, all contribute to making this determination somewhat dubious. Finally, the choice of where to fit the continuum redward of the jump also plays a significant role in the determined temperature.

A similar temperature calculation in the Paschen continuum is complicated by the presence of numerous broad and deep atmospheric absorption bands, which contrive, along with the problems described above, to confuse the true continuum level. Therefore, this calculation was not carried out.

## 4.2 Abundances

### 4.2.1 Ionic Abundances from Collisionally Excited Lines

We calculated abundances for C,N,O,Ne,S,Ar,and Cl ions, with respect to ionized hydrogen ( $N^{+i}/H^+$ ), where  $i$  is the ionization state of the particular ion, from the intensities of their collisionally excited lines, using the *abundance* and *ionic* tasks from the IRAF *nebular* package (Shaw & Dufour 1995). This task solves for the populations of the affected levels of these ion and returns an abundance, given the intensity or intensities of observed lines corresponding to transitions between these levels, and a temperature and density value. In the case where multiple lines from the same ion are observed, the task returns an abundance value that is average of the abundances determined from each transition, weighted by their relative intrinsic

strengths. The atomic information used in these tasks is derived from the references in Table 4.1.

For each ion’s abundance calculation we used the temperature and density determined from its forbidden line diagnostics (an “ion-specific” temperature and density), or those from the ion with the closest previous stage ionization potential. This approach, in the absence of an explicit ionization model, is superior to using a single temperature and density: the different ionization zones in the gas are expected to have different temperatures due to differing cooling mechanisms (Garnett 1992) and characteristics of the local radiation field (Osterbrock 1989). Our observations suggest a real scatter in the nebular diagnostics that goes beyond observational errors, where the application of a single set of parameters could be un-physical. However, we also repeated our calculations using a single set of temperature and density values: 9600 K and  $10000 \text{ cm}^{-3}$  which represent an average of our diagnostics except those from the [S II] and [Ar IV] lines. This allows a direct comparison with the results of Liu et al. (2000) in NGC 6153, who employed a single set of temperature and density values for most of their own abundance calculations.

Calculations were carried out for individual lines in *ionic* and for line groups and ionic averages in *abundance*. The matrix of results from various combinations of lines within each ion is listed in Table 4.3. The entry for each ion in this table concludes with the weighted average of the abundances from multiple collisional lines, calculated at the ion specific parameters, as determined by *abundance*.

In general, the abundances of individual lines within an ion show as good or better internal agreement when calculated at the ion specific parameters, than they do when



the average temperature and density are used. This is not surprising since the same lines were employed to calculate the density and abundance in the first place. However for three ions,  $N^+$ ,  $O^{+2}$ , and  $S^{+2}$  an additional non-diagnostic collisional line yields an abundance that closely matches those calculated from the diagnostic lines. The large scatter in the  $C^o/H^+$  ratio is the result of the  $\lambda 9824$  line being on the extreme edge of the final order of the red spectrum, where the flux calibration is dubious. The calculated  $S^+$  abundances are probably overestimates, given the artificially low ion diagnostic temperature employed. The slightly better internal abundance agreement for this ion using the average as opposed to ion specific parameters, suggests that the  $S^+$  temperature is probably closer to those values determined from the other diagnostics coming from ions with similar ionization potential.

We note that the auroral line  $[N\ II]\ \lambda 5755$ , and the trans-auroral lines  $[O\ II]\ \lambda\lambda 7320, 7330$  do not exhibit a noticeable departure in abundance from the other lines from the same ion. It has been conjectured that these lines could have significant contributions to their strengths from recombination cascade, roughly proportional to the ionic abundances of their parent ions (Liu et al. 2000). Because these lines give similar abundances, and because the ionic abundances determined from the recombination lines of their parent ions are at least two orders of magnitude below their measured intensities, we don't believe recombination plays a significant role in their excitation.

We adopted for all ions the abundance determined from the weighted average of the ion's diagnostic lines calculated at ion specific diagnostic parameters, except for  $C^o$  and  $S^+$ , where we used the  $[C\ I]\ \lambda 8728$  abundance and the weighted value

at the average nebular diagnostic parameters, respectively. Temperature uncertainty dominates collisional abundances determinations, incorporating the uncertainties in the intensities of the individual diagnostic lines. We determined the uncertainties in collisional abundances by taking the extreme temperature and densities values, determining the abundances again, then using the extremes in the abundances as the uncertainty limits of the abundance. For ions of particular interest (those with directly comparable recombination lines) the final abundances and their uncertainties are:

$$\begin{aligned}
\text{N}^+/\text{H}^+ &= 4.124(+3.204, -0.556) \times 10^{-5}, \\
\text{O}^+/\text{H}^+ &= 1.663(+19.687, -1.308) \times 10^{-4}, \\
\text{O}^{+2}/\text{H}^+ &= 1.201(+0.188, -0.142) \times 10^{-4}, \\
\text{Ne}^{+2}/\text{H}^+ &= 4.344(+0.761, -0.616) \times 10^{-6}.
\end{aligned}$$

The larger relative uncertainty in the  $\text{O}^+/\text{H}^+$  value is due to the large temperature errors from the  $[\text{O II}]$  temperature diagnostic ratio. These propagate into large errors in abundance when those errors are calculated using the method described above. However, given the relative agreement of the  $[\text{O II}]$  diagnostic temperature with other temperature diagnostics of similar ionization potential, and the realistic trend in temperature with ionization potential among the diagnostics (see Figure 4.1), the actual uncertainty in the  $[\text{O II}]$  temperature is probably smaller than our best determination of the formal error from line intensities and the reddening correction. Thus, while we quote here and will continue to quote the formal error in the  $\text{O}^+$  abundance as a manner of form, we believe it to be too large.

Table 4.3: Ionic abundances from collisionally excited lines

$N^{+i}/H^+$	Line(s) - $\lambda(\text{\AA})$	$T_e(\text{K})$	$N_e(\text{cm}^{-3})$	Value ( $N^{+i}/H^+$ ) <sup>(a,b)</sup>
				(1) (2)
$C^o/H^+$	[C I]	9400([O I])	9000([N I])	1.647 (-7) 1.480 (-7)
	$\lambda 8727$			
$N^o/H^+$		9400([O I])	9000 ([N I])	8.170 (-8) 8.069 (-8)
	$\lambda 9824$			
	$\lambda 5198$			8.612 (-7) 8.619 (-7)
	$\lambda 5200$			8.560 (-7) 8.646 (-7)
$N^+/H^+$	$\lambda\lambda 5198, 5200$	9400([N II])	10000([O II])	8.593 (-7) 8.629 (-7)
	$\lambda 5755$			4.133 (-5) 3.697 (-5)
	$\lambda 6529$			4.029 (-5) 3.800 (-5)
	$\lambda 6548$			4.027 (-5) 3.798 (-5)
	$\lambda 6583$			4.157 (-5) 3.921 (-5)
	$\lambda\lambda 6548, 6583$			4.124 (-5) 3.890 (-5)
	$\lambda 6548, \lambda 6583, \lambda 5755$			4.124 (-5) 3.885 (-5)
	$\lambda 5577$			5.911 (-6) 5.147 (-6)
$O^o/H^+$	[O I]	9400([O I])	9000([N I])	5.730 (-6) 5.295 (-6)
	$\lambda 6300$			
	$\lambda 6363$			6.072 (-6) 5.611 (-6)
	$\lambda\lambda 6300, 6363$			5.816 (-6) 5.374 (-6)
$O^+/H^+$	[O II]	10000([O II])	10000([O II])	1.657 (-4) 1.992 (-4)
	$\lambda 3726$			
	$\lambda 3729$			1.670 (-4) 2.013 (-4)
	$\lambda 7320$			1.650 (-4) 2.121 (-4)
	$\lambda 7330$			1.718 (-4) 2.208 (-4)
	$\lambda\lambda 3726, 3729$			1.661 (-4) 1.998 (-4)
	$\lambda\lambda 7320, 7330$			1.681 (-4) 2.159 (-4)
$O^{+2}/H^+$	$\lambda 3726, \lambda 3729, \lambda 7320, \lambda 7330$	8900([O III])	6000 ([Ar IV])	1.663 (-4) 2.013 (-4)
	$\lambda 4363$			1.213 (-4) 6.926 (-5)
	$\lambda 4931$			1.165 (-4) 8.878 (-5)
	$\lambda 4959$			1.178 (-4) 8.978 (-5)
	$\lambda 5007$			1.208 (-4) 9.213 (-5)
	$\lambda\lambda 4959, 5007$			1.201 (-4) 9.154 (-5)
	$\lambda 4959, \lambda 5007, \lambda 4363$			1.201 (-4) 9.100 (-5)

Table 4.3 (continued) - Ionic abundances from collisionally excited lines

$N^{+i}/H^+$	Line(s) - $\lambda(\text{\AA})$	$T_e(\text{K})$	$N_e(\text{cm}^{-3})$	Value ( $N^{+i}/H^+$ ) <sup>(a,b)</sup>	
				(1)	(2)
$\text{Ne}^{+2}/\text{H}^+$	[Ne III]	$\lambda 3869$	8900([O III])	6000([Ar IV])	4.278 (-6) 3.060 (-6)
		$\lambda 3969$			4.366 (-6) 3.123 (-6)
$\text{S}^+/\text{H}^+$	[S II]	$\lambda\lambda 3869, 3969$			4.344 (-6) 3.107 (-6)
		$\lambda 4068$	7000([S II])	17000([S II])	1.559 (-6) 4.338 (-7)
		$\lambda 4076$			2.046 (-6) 5.726 (-7)
		$\lambda 6716$			1.655 (-6) 4.266 (-7)
		$\lambda 6731$			1.653 (-6) 4.521 (-7)
		$\lambda\lambda 4068, 4076$			2.226 (-6) 6.195 (-7)
$\text{S}^{+2}/\text{H}^+$	[S III]	$\lambda\lambda 6716, 6731$			1.653 (-6) 4.436 (-7)
		$\lambda 4068, \lambda 4076, \lambda 6716, \lambda 6731$			1.768 (-6) 4.788 (-7)
		$\lambda 6312$	9500([S III])	11000([Cl III])	2.343 (-6) 2.245 (-6)
		$\lambda 8829$			2.427 (-6) 2.376 (-6)
		$\lambda 9069$			2.433 (-6) 2.382 (-6)
		$\lambda 9532$			2.330 (-6) 2.281 (-6)
$\text{Cl}^+/\text{H}^+$	[Cl II]	$\lambda\lambda 9069, 9532$			2.356 (-6) 2.307 (-6)
		$\lambda\lambda 6312, 9069, 9532$			2.356 (-6) 2.305 (-6)
		$\lambda 6162$	10100([Cl III])	17000([S II])	1.304 (-8) 1.641 (-8)
			10200([Cl III])	10000([O II])	1.256 (-8)
		$\lambda 8579$	10100([Cl III])	17000([S II])	1.238 (-8) 1.369 (-8)
			10200([Cl III])	10000([O II])	1.209 (-8)
$\text{Cl}^{+2}/\text{H}^+$	[Cl III]	$\lambda 9124$	10100([Cl III])	17000([S II])	1.540 (-8) 1.704 (-8)
			10200([Cl III])	10000([O II])	1.505 (-8)
		$\lambda 5517$	9500([S III])	11000([Cl III])	5.147 (-8) 4.758 (-8)
			9000([Ar III])	10000([Cl III])	5.901 (-8)
		$\lambda 5537$	9500([S III])	11000([Cl III])	5.036 (-8) 4.862 (-8)
			9000([Ar III])	10000([Cl III])	5.988 (-8)
$\text{Ar}^{+2}/\text{H}^+$	[Ar III]	$\lambda\lambda 5517, 5537$	9500([S III])	11000([Cl III])	5.073 (-8) 4.826 (-8)
		$\lambda 5192$	9000([Ar III])	10000([Cl III])	5.958 (-8) 7.250 (-7)

Table 4.3 (continued) - Ionic abundances from collisionally excited lines

$N^{+i}/H^+$	Line(s) - $\lambda(\text{\AA})$	$T_e(\text{K})$	$N_e(\text{cm}^{-3})$	Value ( $N^{+i}/H^+$ ) <sup>(a,b)</sup>	
				(1)	(2)
	$\lambda 7136$			1.010	(-6) 8.568 (-7)
	$\lambda 7751$			1.101	(-6) 9.340 (-7)
	$\lambda \lambda 7136, 7751$			1.010	(-6) 8.568 (-7)
	$\lambda 5192, \lambda 7135, \lambda 7751$			1.012	(-6) 8.448 (-7)
$\text{Ar}^{+3}/H^+$	$\lambda 4711$	8900([O III])	6000([Ar IV])	9.205	(-10) 8.405 (-10)
	$\lambda 4740$			8.848	(-10) 6.528 (-10)
	$\lambda \lambda 4711, 4740$			9.02	(-10) 7.46 (-10)

<sup>(a)</sup> Column (1) is abundance with powers of ten in parentheses for ion specific temperature/density

<sup>(b)</sup> Column (2) is abundance at  $T_e=9600$  K and  $N_e=10000 \text{ cm}^{-3}$ .

## 4.2.2 Ionic Abundances from Recombination Lines

We calculated the ionic abundances from the relative strengths of the numerous recombination lines of the following ions:  $C^+$ ,  $C^{+2}$ ,  $N^+$ ,  $N^{+2}$ ,  $O^+$ ,  $O^{+2}$ , and  $Ne^{+2}$ . The abundance of a particular ionic species of ionization state  $i$  with respect to ionized hydrogen ( $N^{+i}/H^+$ ), as determined from a specific recombination line of that ion, can be expressed as:

$$\frac{N^{+i}}{H^+} = \frac{\lambda_{H\beta}}{\lambda(\text{\AA})} \frac{\alpha^{eff}(\lambda, T_e)}{\alpha_{H\beta}^{eff}(T_e)} \frac{I_\lambda}{I_{H\beta}}, \quad (4.3)$$

where  $\lambda$  is the air wavelength of the recombination line,  $\lambda_{H\beta}$  is the air wavelength of the  $H\beta$  line (4861.325Å),  $\alpha^{eff}(\lambda, T_e)$  and  $\alpha_{H\beta}^{eff}$  are the weakly temperature dependent effective recombination coefficients of the ionic transition corresponding to the line and  $H\beta$  respectively, and  $I_\lambda/I_{H\beta}$  is the de-reddened intensity of the line with respect to  $H\beta$ .

We used the emissivity interpolation formula of Aller (1984) to calculate  $\alpha_{eff}^{H\beta}$ , as this was the formula employed by the IRAF tasks *nebular* and *ionic* which were used to calculate the ionic abundances from collisionally excited lines.

Table 4.4 lists the references for the atomic data we used in our recombination line abundance calculations. Most of the references do not list values for effective recombination coefficients for individual transitions, only for the entire multiplet to which a transition belongs. The multiplet values must be multiplied by a branching ratio to get an individual transition's effective recombination coefficient. This ratio accounts for the likely population among the multiplet's fine-structure states and the relative contribution of each multiplet transition to the multiplet's total intrinsic

intensity.

To obtain unknown branching ratios, we adopted a technique described in the NIST database <sup>1</sup>. The branching ratio,  $B$ , for a particular transition is derived from the ratio of its atomic parameters to those from all transitions in the multiplet:

$$B = \frac{2(j+1)A\lambda}{\sum_i 2(j_i+1)A_i\lambda_i}, \quad (4.4)$$

where  $A$  is the spontaneous emission coefficient for the transition of interest,  $2(j+1)$  is the statistical weight of the level from which the transition originates within the multiplet, and  $\lambda$  is the air wavelength of the transition. The denominator is the same for all  $i$  permitted transitions of the multiplet.

The above scheme assumes that all levels in the multiplet are populated according to their relative statistical weights, a common assumption for all but metastable levels. Eq. 4.4 assumes that all transitions follow LS coupling selection rules, which falls short for transitions from levels generated by a valence orbital of angular momentum quantum number  $\ell > 2$  (i.e. 3d-4f transitions in  $N^{+2}$ ,  $O^{+2}$ , and  $Ne^{+2}$ ).

Calculations were carried out for the following opacity cases for which atomic data was available. Specifically...

- Case A: All transitions are optically thin.
- Case B: All transitions which terminate on the term of the ground electron configuration with the lowest energy are considered optically thick. As an example, for O II recombination lines, this would mean that all transitions ending on the

---

<sup>1</sup>Equation 23, <http://physics.nist.gov/Pubs/AtSpec/node17.html#node175>.

Table 4.4 References for atomic data for recombination excited lines.

Ion	Source	Transitions/Case <sup>(a)</sup>
Effective recombination coefficients/emmissivities		
H I	Aller (1984)	
He I	Smits (1996)	
C I	Victor & Escalante (1990)	
	Pequignot et al. (1991)	
C II	Davey et al. (1999)	
N I	Pequignot et al. (1991)	
N II	Victor & Escalante (1990)	
	Kisieliuss & Storey (2002)	(3-3)
O I	Pequignot et al. (1991)	
O II	Storey (1994)	(3s-3p)
	Liu et al. (1995)	(3p-3d,3d-4f)
Ne II	Kisieliuss et al. (1998)	(3-3)
	Liu et al. (2000) <sup>(b)</sup>	(3d-4f)
Spontaneous emission coefficients		
Atomic Line List v2.04 (van Hoof 2001)		
(a)	No entry indicates same source for all transitions.	
(b)	From unpublished calculations by Storey.	

$2s^2 2p^3 \ ^4S^o$  term of  $O^+$  would be considered optically thick, and no radiative decays would be allowed to this term.

- Case C: (O II recombination lines only) All transitions which terminate on the  $O^+ \ 2s^2 2p^3 \ ^4S^o$  and  $^2D^o$  (the term with the next highest energy) terms, are considered optically thick and no radiative decays to these terms are allowed.

For each ionic abundance calculation, the ion specific temperature or that from a ion with a similar ionization potential, as determined from the diagnostic line ratios, was utilized. Table 4.5 lists the temperatures used for each ion. The same temper-



Table 4.5 Temperatures used for recombination line abundance calculations.

Ion	$T_e(K)/\text{Source}$
He I	9600
C I	10100([Cl II])
C II	9500([S III])
N I	9400([N II])
N II	9000([Ar III])
O I	10000([O II])
O II	8900([O III])
Ne II	8900([O III])

atures were used in the emissivity formula for  $H\beta$ . Recombination line abundances are mostly insensitive to density and all calculations were carried out using the mean density of  $10000 \text{ cm}^{-3}$ .

Within each multiplet of an ion, abundances from individual lines, as well as a complete “summed” multiplet abundance, were calculated. In the summed multiplet abundance, the numerator of eq. 4.4 is replaced with the sum of the atomic parameters for all lines observed from the same multiplet, and the intensity used in eq. 4.3 is the sum of their observed intensities. This approach is superior to averaging individual line abundances, because large deviations arising from poorly observed individual lines are smoothed out. In the following abundance tables, summed multiplet abundances are referred to as “Sum”, while a colon after the intensities of lines indicate that the line intensity is suspect, due to poor measurement, uncertain identification, or suspected blending. Multiplets with at least two lines observed and included, will have a summed abundance, set off by bold typeface.

Finally, for recombination lines the main source of error is the uncertainty in the intensity measurement. Abundance is linearly proportion to intensity, as seen in

eq. 4.3, so the errors in abundance may be determined directly from the intensity errors for individual lines. Calculating a summed multiplet abundance reduces the influence of intensity uncertainties.

### **He<sup>+</sup>/H<sup>+</sup> and He<sup>+2</sup>/H<sup>+</sup>**

We follow Liu et al. (2000) in obtaining the He<sup>+</sup> abundance from the arithmetic average of the He<sup>+</sup>/H<sup>+</sup> values determined from He I  $\lambda\lambda 4471, \lambda 5876$ , and  $\lambda 6678$ , weighting by their rough intrinsic uncertainty ratio, 1:3:1, respectively. Prior to the abundance calculations, the line intensities were corrected for electron collisional excitations from the He<sup>o</sup> 2s <sup>3</sup>S metastable level. These excitations alter the populations of the lines' origin levels, according to the formalism of Kingdon & Ferland (1995b) at the mean temperature and density (9600 K and 10000 cm<sup>-3</sup>). The emissivities<sup>2</sup> and intrinsic intensity ratios of Smits (1996) tabulated at 10000 K and 10000 cm<sup>-3</sup>, the closest to our mean diagnostic temperature and density, were used to make the abundance calculations for the individual lines. Emissivities were only available for hydrogen case A for the He I triplet lines  $\lambda\lambda 4471, 5876$ , while both case A and B were used for  $\lambda 6678$ . The resultant abundances are listed in Table 4.6.

The line abundances show a systematic increase with wavelength which could be indicative of an error in the reddening correction, or an effect of the flux calibration disagreement between the blue ( $\lambda 4471$ ) and intermediate spectra ( $\lambda 5876, 6678$ ). Corrections for the collisional excitation from the 2s <sup>3</sup>S level are sizable: 5% for  $\lambda\lambda 4471, 6678$  and 11% for  $\lambda 5876$ . However, the disagreement only gets worse if these

---

<sup>2</sup>Emissivity  $\equiv hc/\lambda \times \alpha^{eff}(\lambda, T_e)$

Table 4.6 Recombination line  $\text{He}^+/\text{H}^+$  abundances.

Line $\text{\AA}$ ( $\text{\AA}$ )	$\lambda_o$ ( $\text{\AA}$ )	S/N	FWHM (km/s)	$I(\lambda)/I(\text{H}\beta)$ $I(\text{H}\beta=100)$	Value ( $\text{He}^+/\text{H}^+$ ) ( $\times 10^2$ )		Notes
					Case A	Case B	
Singlet							
4471.474	4471.499	1935.0	23.7	4.4921	9.027	...	...
5875.615	5875.650	5395.0	25.9	13.6746	9.452	...	...
Triplet							
6678.152	6678.153	2346.0	21.6	3.8721	10.300	10.073	...
Average					<b>9.537</b>	<b>9.491</b>	(1)
(1)	Case B average includes case A $\lambda\lambda 4471, 5876$ .						

corrections are ignored. Examining Smits (1996) Table 4 shows that for two surveyed PN, the ratio of observed to theoretically calculated flux of  $\lambda 6678$  is consistently less than 1.0, while the same ratio for  $\lambda 4471$  was unity. Decreasing the emissivity of  $\lambda 6678$  with respect to  $\lambda 4471$  would bring the  $\lambda 6678$  abundance in closer agreement with the  $\lambda 4471$  value. However,  $\lambda 5876$  shows a neutral or opposite trend in those same PNe, and Liu et al. (2000) found the opposite trend from ours in their  $\lambda 6678$  abundance.

Alternatively, since the emissivity ratios of  $\lambda\lambda 5876, 6678$  to  $\lambda 4471$  decrease with temperature, a lower temperature could also bring their abundances into alignment. Using Smits (1996) at 5000 K and  $10000 \text{ cm}^{-3}$  reduces the scatter in the line abundances from 12% to about 3%, and simultaneously removes the wavelength trend. The line abundances also decline 5, 6, and 13%, for  $\lambda 4471$ ,  $\lambda 5876$ , and  $\lambda 6678$  respectively, from their higher temperature values. This suggests that the  $\text{He}^+$  ion is more accurately described by a temperature characterizing a larger portion of the nebula, such as the Balmer jump temperature, than by temperatures determined from relatively

smaller zones.

For the final  $\text{He}^+$  abundance, we adopted the 9600 K case B average, which uses the case A  $\lambda\lambda 4471, 5876$  and case B  $\lambda 6678$  abundances. We caution, however, that the actual abundance may likely be somewhat smaller, for the reason described above. Errors in reddening, the collisional excitation correction, and the flux calibration, may also play a role.

Our deep spectra exhibit a rich He I recombination spectrum, with some triplet sequences observable out to principal quantum number  $n = 27$ . However, no observable He II lines, even the intrinsically strongest  $\lambda 4686$  line, were observed by us or by Hyung, Aller, & Feibelman (1994) (HAF). Interestingly, three of the remaining unidentified lines in our IC 418 line list correspond in wavelength to He II recombination lines identified in NGC 6153 by Liu et al. (2000). However the lack of an observable  $\lambda 4686$  line suggest that these are probably just a coincidence. We conclude that the value of  $\text{He}^{+2}/\text{H}^+$  is probably negligible.

## $\text{C}^+/\text{H}^+$

No C I recombination lines were observed in IC 418 by HAF. This is probably because the expected strongest C I multiplets are either located in the near-IR (multiplet 1 at  $\approx 10695\text{\AA}$ ) and beyond their wavelength coverage, or correspond to possibly optically thick resonance lines in the UV (Pequignot et al. 1991).

We observe only one C I line with a credible ID,  $\lambda 9094.830$  ( $\text{S/N} = 127.4$ ,  $\text{FWHM} = 80.8 \text{ km sec}^{-1}$ ,  $\text{flux} = 0.0103$ ) from multiplet 3. According to eq. 4.4, this transition has the highest branching ratio among all transitions of the multiplet, so

its appearance, coupled with the reasonably large multiplet effective recombination coefficient, appears genuine. Other transitions of this multiplet have branching ratios a factor of four lower, so their absence among our detected lines is not necessarily significant.

Using the effective recombination coefficient for the multiplet from Pequignot et al. (1991), the ionic abundances are  $C^+/H^+ = 2.274 \times 10^{-4}$  and  $C^+/H^+ = 0.673 \times 10^{-4}$  for cases A and B respectively. Given that the resonance C I recombination lines<sup>3</sup> in the UV were not detected by HAF or Henry, Kwitter, & Bates (2000) (HKB) in their UV surveys of IC 418, we assume that case B prevails for this ion and adopt the  $\lambda 9094.830$  abundance for this case as the ionic abundance.

Additional C I recombination lines were identified in the vicinity of 6000-6020 Å. Examination of the spectrum show that most are probably real lines. Effective recombination coefficients for their multiplets are available only for case B in Escalante & Victor (1990). Abundances calculations from un-blended lines are two orders of magnitude greater than for the  $\lambda 9094.380$  line. The lines seem inordinately strong if they are true C I recombination lines. The line ID'd as C I  $\lambda 5990.980$   $3p \ ^3D - 5d \ ^3D^\circ$  could conceivably be pumped from the ground state by starlight fluorescence or a unknown Bowen-like mechanism. However, the line ID'd as C I  $\lambda 6019.890$   $^3D - 5d \ ^3F^\circ$  is unlikely to be pumped, given its large angular momentum difference with the ground  $2s^2 2p^2 \ ^3P$ . The more likely explanation is that these lines are mis-identified, and we do not use them to calculate abundances.

---

<sup>3</sup>Resonance lines are transitions from the ground state directly to an excited level. Most often the lines leading to levels from which permitted transitions can occur are in the UV.

## $C^{+2}/H^{+}$

Many strong C II recombination line multiplets are observed in our spectra. However, effective recombination coefficients are available only for doublets. Calculated individual line and summed multiplet abundance values for our observed doublets are listed in Table 4.7.

Multiplets 3 and 6 are in excellent agreement. The latter includes the  $\lambda 4267$  lines often used to determine ionic abundance due to their strength and lack of contributions from continuum fluorescence and dielectronic recombination. Since it is also case-insensitive, a comparison with the extremely case-sensitive multiplet 3 lines argues that case B prevails for the ion.

The overabundance in multiplets 2, 4, and 5, with respect to  $\lambda 4267$  is probably not due to incorrect atomic parameters, since the same reference was used by Liu et al. (2000) and their results show much better agreement than that seen here. Enhanced dielectronic recombination is also probably not to blame, as effective recombination coefficients (Davey et al. 2000) exceed by at least two orders of magnitude coefficients measuring dielectronic recombination alone (Nussbaumer & Storey 1984) for all the upper levels of the multiplets considered here.

Grandi (1976) has shown that continuum fluorescence by starlight in the Orion Nebula is extremely important in feeding the levels from which many of the lines observed here. Continuum fluorescence from the the  $2p\ ^2P^o$  ground state of  $C^{+}$  by central star radiation can populate higher  $^2S$  and  $^2P$  terms directly (e.g. the upper levels of multiplets 3 and 4), or indirectly following cascades from those levels (mul-

triplets 2 and 5). The sense of the abundance enhancements observed here suggest a similar mechanism here: lines from levels that could be directly populated by this mechanism show strongly enhanced intensities, whereas lines from levels one step down the cascade chain show lesser degrees of enhancement. Angular momentum states further removed from the ground state (the upper level of multiplet 6) are affected much less, as enhanced populations are diluted by longer cascade changes distributing the excess. The close agreement between multiplets 3 and 6 suggest that the population of the upper level of multiplet 3 is dominated by contributions following strong  $\lambda 4267$ , fluorescence-immune emission, despite the fact that the upper level of multiplet 3 can also be directly populated by continuum fluorescence.

There are flaws to the above argument. Recombination occurs at the boundary between the  $C^+$  and  $C^{+2}$  zones in the nebula, whereas continuum emission should take place only where  $C^+$  is most abundant. These locations should have different physical conditions, temperatures and expansion velocities, which should affect the line profiles and their FWHM. However we note no difference in FWHM between lines enhanced by or immune to this mechanism. We will examine the actual line profiles in § 4.3.1. Also, a large population of  $C^+$  is not suggested by the strength or number of observed C I recombination lines, although the strongest C I multiplets are outside our observing bandwidth. Finally resonance transitions for these levels are all blueward of the Lyman limit. If fluorescence fuels these lines, significant  $C^+$  should exist *behind* the ionization front, where such lines are not optically thick due to ionizing hydrogen.

Nevertheless, we follow Liu et al. (2000) in simply using the case B  $\lambda 4267$  abun-

dance as the final  $C^{+2}/H^{+}$  value. Our deep spectra allow the observation of high excitation C II recombination lines, whose intensities can be predicted using this abundance and recombination theory. The resulting calculated intensities (Table 4.8) show excellent agreement.

A number of quintet multiplets and  $C^{+} 2s2p (^3P^o) n\ell$  series lines are present in our spectrum (see § reddielec). The former are most likely created by dielectronic recombination, since the alternative: recombination directly onto the  $C^{+2} 2s2p (^3P^o)$  state, is unlikely given significant populations of this level are not expected at nebular temperatures (Davey et al. 2000). The quartet lines are generally less intense, by an order of magnitude or more, than their singly excited doublet counterparts. Since, they are weak, and because interactions with doublets may only proceed via intercombination lines which are not seen in our spectra, we don't believe they contribute significantly to level populations in the doublet states. The good agreement between predicted and observed intensities of several higher excitation lines, suggests that we are safe using the  $\lambda 4267$  abundance as the final value for this ion.



Table 4.7: Recombination line  $C^{+2}/H^+$  abundances.

Line(s) $\lambda$ (Å)	$\lambda_o$ (Å)	S/N	FWHM (km/s)	$I(\lambda)/I(H\beta)$ $I(H\beta)=100$	Value ( $C^{+2}/H^+$ ) ( $\times 10^3$ )	Notes
Multiplet 2 (3s $^2S$ - 3p $^2P^o$ )						
6578.05	6578.050	870.5	18.3	0.5374	5.645	1.033
Multiplet 3 (3p $^2P^o$ - 3d $^2D$ )						
7231.340	7231.329	255.3	23.6	0.1692	29.413	0.417 (1)
7236.420	7236.414	...	21.1	0.4673	45.172	0.640 ...
7237.170	7237.145	15.4	16.6	0.0489	42.563	0.603 ...
Sum:				<b>0.6854</b>	<b>39.743</b>	<b>0.563</b>
Multiplet 4 (3p $^2P^o$ - 4s $^2S$ )						
3918.967	3918.930	226.4	18.7	0.1068	18.244	5.938 ...
3920.682	3920.640	372.8	18.3	0.2052	17.535	5.713 ...
Sum:				<b>0.3100</b>	<b>17.764</b>	<b>5.788</b>
Multiplet 5 (3d $^2D$ - 4p $^2P^o$ )						
5889.780	5889.960	301.5	44.8	0.0793	8.027	3.420 (2)
5891.600	5891.565	99.2	18.6	0.0181	3.299	1.406 ...
Sum:				<b>0.0974</b>	<b>5.916</b>	<b>2.521</b>
Multiplet 6 (3d $^2D$ - 4f $^2F^o$ )						
4267.001, 183, 261	4267.161	536.0	38.7	<b>0.5712</b>	<b>0.561</b>	<b>0.555</b>
(1)	Has an unusual profile.					
(2)	Contaminated by nebular Na I $\lambda 5889.951$ emission, indicative if its relatively large FWHM.					

Table 4.8 High excitation C II recombination lines.

	Line(s) $\lambda$ (Å)	$\lambda_o$ (Å)	S/N	FWHM (km/s)	Observed $I(\lambda)/I(H\beta)$ $I(H\beta)=100$	Predicted $I(\lambda)/I(H\beta)$ $I(H\beta)=100$
4d-6f	6151.270,540	6151.336	127.3	26.7	0.0306	0.0242
4d-8f	4620.185	4620.348	41.7	18.0	0.0107	0.0103
4d-9f	4329.675	4329.876	20.7	21.4	0.0070	0.0074
4f-6g	6461.950	6461.848	93.5	18.6	0.0584	0.0587
4f-7g	5342.370	5342.392	153.2	18.4	0.0277	0.0303
4f-8g	4802.740	4802.454	72.8	19.5	0.0183	0.0179
4f-10g	4292.250	4292.406	35.2	21.2	0.0089	0.0080

### $N^+/H^+$

We observed four multiplets for which effective recombination coefficients are available in Pequignot et al. (1991). The calculated abundances, listed in Table 4.9, scatter considerably both among the multiplets, and within the individual lines comprising the multiplets. Multiplet 1 is case-insensitive, but the derived abundances from other multiplets do not show better agreement under either case.

Grandi (1975a) predicted that the 3d  $^4P$  and 4s  $^4P$  levels are strongly enhanced by continuum fluorescence from the ground  $2p^3\ ^4S^o$  ground state through particularly strong resonance transitions in the UV near or redward of the Lyman limit. Subsequent cascades in the IR from these terms can then feed the upper levels of multiplets 1, 2, and 3, leading to an enhancement of their line strengths. Our observed intensities concur with this scenario. The upper level of multiplet 19, 3d  $^4D$ , is also connected to the ground state, albeit by a multiplet of strictly LS-forbidden UV transition around  $\lambda 953\text{\AA}$ , and is also possibly excited by continuum fluorescence since its energy is close to the 3d  $^4P$  term. The lower transition probability (a.k.a.

lower stimulated absorption coefficient) in the  $3d\ ^4D$  resonance lines, about a factor of ten less than the resonance lines feeding the  $3d\ ^4P$  and  $4s\ ^4P$  levels, is probably compensated for in the multiplet 19 line strengths, because those lines arise directly from the excited level, as opposed to falling through a cascade chain to the origin levels of multiplets 1, 2, and 3.

It is obvious that the individual lines within the multiplets are not populated according to LS coupling, given their large scatter; Esteban et al. (1999) reached a similar conclusion for the N I lines of the Orion Nebula. The lack of an exact estimate of the continuum fluorescence contribution to the line strengths (for which an explicit radiation model of the nebula is necessary), suggests that abundances determined from this ion are not reliable. We assume that the lowest summed multiplet abundance is most likely the closest to the actual abundance due to recombination alone, and take it as an “upper” limit for comparison purposes with the collisionally excited lines. The profiles of these lines should provide an important test of where the lines arise within the nebula. If continuum fluorescence dominates these lines, they should have identical profiles and FWHM to collisionally excited [N II]  $\lambda\lambda 6548, 6583$ . We will examine this in § 4.3.1.

Table 4.9: Recombination line  $N^+/H^+$  abundances.

Line(s) $\lambda$ (Å)	$\lambda_o$ (Å)	S/N	FWHM (km/s)	I( $\lambda$ )/I(H $\beta$ ) I(H $\beta$ )=100	Value (N <sup>+</sup> /H <sup>+</sup> ) ( $\times 10^4$ )		Notes
					Case A	Case B	
Multiplet 1 (3s <sup>4</sup> P - 3p <sup>4</sup> D <sup>o</sup> )							
8680.282	8680.370	396.1	56.8	0.0385	11.741	11.389	...
8683.403	8683.525	382.0	57.6	0.0417	24.373	23.644	...
8686.149	8686.267	...	52.3	0.0220	32.358	31.389	...
8703.247	8703.334	254.2	54.0	0.0268	39.573	38.389	...
8711.703	8711.778	234.7	52.8	0.0273	31.617	30.671	...
8718.837	8718.959	143.9	53.4	0.0135	18.566	18.011	...
Sum:				<b>0.1698</b>	<b>21.395</b>	<b>20.755</b>	
Multiplet 2 (3s <sup>4</sup> P - 3p <sup>4</sup> P <sup>o</sup> )							
8184.862	8185.270	168.0	20.8	0.0152	29.273	24.898	(1)
8188.012	8188.451	152.9	51.1	0.0381	79.391	67.527	(2)
8200.357	8200.503	138.6	51.5	0.0131	137.038	116.559	...
8210.715	8210.965	92.0	45.4	0.0198	130.193	110.737	...
8216.336	8216.298	304.1	62.2	0.0598	50.045	42.566	(3)
8223.128	8223.205	347.8	50.4	0.0623	131.673	111.996	...
8242.389	8242.508	...	53.9	0.0551	108.692	92.449	...
Sum:				<b>0.2634</b>	<b>76.979</b>	<b>65.475</b>	
Multiplet 3 (3s <sup>4</sup> P - 3p <sup>4</sup> S <sup>o</sup> )							
7423.641	7423.733	119.4	58.3	0.0156	157.648	52.104	...
7442.298	7442.351	219.9	57.7	0.0363	185.041	61.157	...
7468.312	7468.457	...	59.2	0.0583	200.919	66.405	...
Sum:				<b>0.1102</b>	<b>188.280</b>	<b>62.228</b>	
Multiplet 19 (3p <sup>4</sup> D <sup>o</sup> - 3d <sup>4</sup> D)							
9810.010	9809.767	40.5	57.5	0.0082	247.988	...	...
9822.750	9822.279	...	40.6	0.0076	66.698	...	...
9834.610	9834.627	14.7	51.5	0.0082	178.536	...	...
Sum:				<b>0.0240</b>	<b>124.461</b>	...	
(1)	Irregular profile complicated by adjacent absorption feature.						
(2)	Blend with O II $\lambda$ 8188.520?						
(3)	High FWHM, Blend?						

## $\text{N}^{+2}/\text{H}^{+}$

We observed numerous N II recombination lines, including lines from ten triplets, a singlet line, and numerous 3d-4f transition lines. For the singlet and triplets' lines, effective recombination coefficients were available from both Escalante & Victor (1990) (EV) and more recently from Kisielius & Storey (2002) (KS). However, effective recombination coefficients for the 3d-4f transition were not published by KS due to departures from LS coupling. Instead we worked backwards from the results of Liu et al. (2000) to obtain coefficients for individual lines, for a temperature of 9100 K. Using these coefficients at our assigned  $\text{N}^{+2}$  temperature of 9000 K increases the abundance artificially by 1-2%. A density of  $10000 \text{ cm}^{-3}$  was used with the KS fitting function for the coefficients. Abundances were calculated under both opacity cases, where the relevant atomic data was available. The results are listed in Table 4.10.

For nearly all the triplets, the KS values, resulted in lower abundances, than those calculated using EV values. The general scatter does not favor either opacity case A or B, though the case B values yield more realistic abundances. Comparing summed multiplet abundances for triplets, our abundances show a larger scatter ( $\sigma = 38\%$ ) than the Liu et al. (2000) abundances ( $\sigma = 29\%$ ) for multiplets observed in common (3, 5, 20, 28), calculated using EV case B coefficients. Our abundances calculated using KS case B coefficients have less scatter ( $\sigma = 25\%$ ). We therefore adopt for all triplets the KS derived case B abundances, acknowledging that not all multiplets may adhere to it strictly. For the lone singlet line observed,  $\lambda 4437.030 \text{ } 3p \text{ } ^1\text{P} - 3d \text{ } ^1\text{D}^\circ$ , the EV coefficient greatly exceeded the KS value, resulting in a higher abundance.

We arbitrarily chose to use the case A EV values, as was done for singlets in Liu et al. (2000). A second ID'd N II singlet line,  $\lambda 6610.560$  ( $3p\ ^1D - 3d\ ^1F^\circ$ ), yields an abundance 5 times higher than for  $\lambda 4447.030$  under case A EV, and is likely a mis-identification.

The overabundance exhibited by multiplet 30 could be explained by a highly efficient Bowen-like fluorescence arising from the near coincidence between the He I  $1s^2\ ^1S - 1s8p\ ^1P^\circ$   $\lambda 505.68\text{\AA}$  line and the resonance transition N II  $2p\ ^3P - 4s\ ^3P^\circ$   $\lambda 508.608\text{\AA}$  from the ground state (Grandi 1976). Given the  $3\text{\AA}$  wavelength difference, however, it seems unlikely that this mechanism will work here, and it is more likely that the level is pumped via continuum fluorescence. Liu et al. (2002) reached the same conclusion based on the greater relative strength of the  $3s-3p$  and  $3p-3d$  lines compared to the  $3p-4s$  lines of this multiplet in several of their PNe spectra. However, our observations show that the lines are of nearly comparable strength. We conclude only that some sort of ground state fluorescence is exciting this level, whether Bowen, continuum, or a combination of the two.

Transitions in the cascade path are similarly enhanced (multiplets 3 and 5). Grandi (1976) also suggests that the intensity of multiplet 20 can be explained by a combination of continuum fluorescence through the resonance transition to the  $3d\ ^3D^\circ$  level, and standard recombination-cascade from levels above. Since multiplet 28 shares the same upper level, presumably it too can be enhanced. Resonance transitions also connect the ground state with the  $3d\ ^3P^\circ$  state, which in turn can enhance the strengths of multiplets 21, 24, and 29. Only multiplet 36 is probably not enhanced, since no resonance transition exists to its upper  $4p\ ^3D$  level, and because it

is far removed any of the previously described cascade paths. It is not surprising that this multiplet, apart from the 3d-4f states, yields the smallest abundance.

For the 3d-4f transitions, the abundances were smaller still. This isn't necessarily due to measurement error from the weakness of the 3d-4f lines, since the abundance from the 3d-4f  $\lambda 4447.030$  line, which has a strength comparable to some of the 3-3 transition lines, exhibits yields a small abundance. The general decrease in abundance with increasing level energy or multiplet number might naively suggest the importance of the continuum fluorescence in the exciting the lower levels of the ion. However, the true explanation is unclear. The effective recombination coefficients may also be in error, being inferred from other data rather than drawn from a tabulated source. For these reasons we did not include these transitions in the final ionic abundance.

We confirm the observations of Esteban et al. (1999) in the Orion Nebula: multiplets 3 and 5 abundances agree well, “middle” multiplets 20, 24, and 28 less well, but multiplets 30 and 36 again agree well. It is unclear why the middle four 3d multiplets, show such large scatter, and why the agreement gets better again for levels of still higher energy. The 3d multiplets' fine-structure states are apparently not populated according to relative statistical weights. If the problem were due to continuum or Bowen-like fluorescence, it seems odd that multiplet 30, the upper level of which can be excited by either process, shows relatively good agreement. LS coupling may fail for the 3d multiplets, or the scatter among the lines of the 3d multiplets might be due in part to their lower S/N, while multiplet 30 lines are generally stronger.

In addition to the N II singlet and triplet lines, members of at least two quintet multiplets are present in our spectra. These lines appear genuine: most ID'd by

EMILI as primary “A” IDs. Some of these lines have been tentatively observed in the Orion Nebula (Baldwin et al. 2000). They all have an intensity of approximately  $0.60 - 5.0 \times 10^{-5} H\beta$ , which is an order of magnitude less than the average value from the standard N II recombination lines. These lines must be created by a mechanism that preserves total angular momentum. While Grandi (1976) suggests that dielectronic recombination is unlikely to populate the levels from which these lines arise, it remains a possible excitation mechanism for them. As with the  $C^+$  quartet lines, their strengths, and the lack of distinct inter-combination (spin changing) transitions observed in our spectrum, suggest that if dielectronic recombination or some other process is responsible for their existence, they contribute little to the populations of the levels from which one-body recombination lines arise. We will list all of these lines in § 4.3.2.

A few other, mostly weak, N II recombination lines were observed in our spectrum, but generally only single members of a multiplet; some with no effective recombination coefficients. We chose not to calculate abundances from these lines.

With the great uncertainty in the excitation source for the lower term multiplets, we will adopt the summed multiplet 36 abundance for  $N^{+2}$  based this multiplet’s apparent independence from opacity case and immunity from continuum fluorescence. Abundances from the 3d-4f lines, however, suggest that this estimate may still be a factor of two too high.



Table 4.10: Recombination line  $N^{+2}/H^{+}$  abundances.

Line(s) $\lambda$ ( $\text{\AA}$ )	$\lambda_o$ ( $\text{\AA}$ )	S/N	FWHM (km/s)	$I(\lambda)/I(H\beta)$ $I(H\beta)=100$	Value ( $N^{+2}/H^{+}$ ) ( $\times 10^4$ )				Notes
					EV		KS		
					Case A	Case B	Case A	Case B	
<b>Multiplet 3 (<math>3s\ 3P^o - 3p\ 3D</math>)</b>									
5666.629	5666.630	176.9	17.9	0.0414	3.834	3.233	1.938	2.361	...
5676.017	5676.023	123.4	17.6	0.0197	4.122	3.476	2.084	2.538	...
5679.558	5679.552	170.8	20.7	0.0674	3.366	2.838	1.702	2.073	...
5686.212	5686.199	70.1	18.5	0.0127	3.560	3.002	1.800	2.192	...
5710.766	5710.763	75.9	18.7	0.0136	3.880	3.271	1.961	2.389	...
5730.656	5730.637	8.9	17.5	0.0013	5.599	4.720	2.830	3.447	...
Sum:					<b>3.639</b>	<b>3.068</b>	<b>1.839</b>	<b>2.241</b>	
<b>Multiplet 4 (<math>3s\ 3P^o - 3p\ 3S</math>)</b>									
5045.099	5045.092	112.9	18.1	0.0289	68.481	11.066	33.850	4.816	(1)
<b>Multiplet 5 (<math>3s\ 3P^o - 3p\ 3P</math>)</b>									
4601.478	4601.471	104.0	17.3	0.0263	35.779	6.626	21.042	3.651	...
4607.153	4607.140	96.0	17.5	0.0257	43.871	8.125	25.801	4.477	(2)
4613.868	4613.858	59.1	19.6	0.0182	41.583	7.702	24.455	4.244	(3)
4621.393	4621.384	103.9	18.0	0.0264	45.678	8.460	26.864	4.662	(4)
4630.539	4630.531	217.7	16.8	0.0805	37.215	6.892	21.886	3.798	...
4643.086	4643.078	140.5	17.0	0.0344	48.083	8.905	28.278	4.907	...
Sum:					<b>40.554</b>	<b>7.511</b>	<b>23.850</b>	<b>4.139</b>	
<b>Multiplet 15 (<math>3p\ 1P^o - 3d\ 1D^o</math>)</b>									
EV $\equiv$ Escalante & Victor (1990)					KS $\equiv$ Kisielius & Storey (2002)				

Table 4.10 (continued) - Recombination line  $N^{+2}/H^{+}$  abundances.

Line(s) $\lambda$ (Å)	$\lambda_o$ (Å)	S/N	FWHM (km/s)	$I(\lambda)/I(H\beta)$ $I(H\beta)=100$	Value ( $N^{+2}/H^{+}$ ) ( $\times 10^4$ )				Notes
					EV		KS		
					Case A	Case B	Case A	Case B	
4447.030	4447.060	19.7	16.5	<b>0.0039</b>	<b>2.691</b>	<b>2.717</b>	<b>6.183</b>	...	
Multiplet 20 (3p $^3D$ - 3d $^3D^o$ )									
4774.244	4774.263	15.0	13.5	0.0022	97.071	2.753	116.684	2.266	...
4779.723	4779.715	88.9	17.8	0.0179	264.287	7.496	317.687	6.169	...
4781.190	4781.311	7.9	28.8	0.0013	55.558	1.576	66.784	1.297	...
4788.137	4788.127	101.9	15.6	0.0195	187.263	5.311	225.100	4.371	...
4803.286	4803.276	76.5	16.9	0.0261	141.560	4.015	170.162	3.304	...
4810.299	4810.209	12.9	49.2	0.0040	174.139	4.939	209.324	4.065	(5)
Sum:				<b>0.0710</b>	<b>166.973</b>	<b>4.736</b>	<b>200.710</b>	<b>3.897</b>	
Multiplet 21 (3p $^3D$ - 3d $^3P^o$ )									
4459.937	4459.898	14.3	17.2	0.0025	...	20.385	215.851	8.623	...
4465.529	4465.404	32.4	14.8	0.0059	:	64.377	681.689	27.233	(6)
4477.682	4477.745	29.9	25.1	0.0061	...	22.405	237.241	9.478	...
4488.095	4488.194	9.7	18.9	0.0024	:	26.575	281.405	11.242	(7)
4507.560	4507.554	25.8	13.1	0.0051	...	10.233	108.360	4.329	...
Sum:				<b>0.0220</b>	...	<b>20.468</b>	<b>216.736</b>	<b>8.658</b>	
Multiplet 24 (3p $^3S$ - 3d $^3P^o$ )									
4987.377	4987.360	71.1	19.4	0.0165	:	203.988	196.713	7.918	(8)
4994.371	4994.374	146.2	18.6	0.0423	:	174.977	168.737	6.792	(9)
Sum:				<b>0.0588</b>	<b>182.556</b>	<b>9.404</b>	<b>176.046</b>	<b>7.086</b>	
EV $\equiv$ Escalante & Victor (1990)					KS $\equiv$ Kisielius & Storey (2002)				

Table 4.10 (continued) - Recombination line  $N^{+2}/H^{+}$  abundances.

Line(s) $\lambda$ (Å)	$\lambda_o$ (Å)	S/N	FWHM (km/s)	$I(\lambda)/I(H\beta)$ $I(H\beta)=100$	Value ( $N^{+2}/H^{+}$ ) ( $\times 10^4$ )				Notes
					EV		KS		
					Case A	Case B	Case A	Case B	
Multiplet 28 (3p $^3P$ - 3d $^3D^o$ )									
5927.820	5927.802	113.8	17.4	0.0191	277.392	7.866	343.718	6.679	...
5931.790	5931.773	156.7	16.7	0.0273	176.571	5.007	218.791	4.251	...
5940.240	5940.264	63.0	18.2	0.0139	270.612	7.674	335.317	6.515	...
5941.650	5941.663	137.3	16.0	0.0315	109.668	3.110	135.890	2.640	...
5952.390	5952.385	33.7	13.8	0.0052	102.117	2.896	126.533	2.459	...
Sum:				<b>0.0970</b>	<b>158.285</b>	<b>4.488</b>	<b>196.132</b>	<b>3.811</b>	
Multiplet 29 (3p $^3P$ - 3d $^3P^o$ )									
5452.071	5452.063	25.9	20.2	0.0042	90.202	4.662	134.097	5.374	...
5454.215	5454.035	46.8	43.2	0.0083	:	178.846	265.878	10.656	(10)
5462.581	5452.568	36.4	26.2	0.0045	129.975	6.717	193.225	7.744	...
5478.086	5478.087	19.6	16.6	0.0030	52.409	2.708	77.912	3.123	...
5480.050	5480.050	34.9	17.0	0.0056	97.961	5.063	145.632	5.837	...
5495.655	5495.655	87.5	19.1	0.0148	87.158	4.504	129.572	5.193	(11)
Sum:				<b>0.0404</b>	<b>98.128</b>	<b>5.071</b>	<b>145.880</b>	<b>5.847</b>	
Multiplet 30 (3d $^3P$ - 4s $^3P^o$ )									
3829.795	3829.745	34.2	21.3	0.0232	290.276	94.401	174.998	59.259	...
3838.374	3838.349	98.5	25.5	0.0734	308.730	100.403	186.123	63.026	(12)
3842.187	3842.183	33.6	19.1	0.0126	199.589	64.909	120.326	40.746	...
3855.096	3855.089	29.9	29.6	0.0098	:	156.574	94.393	31.964	...
3856.063	3856.054	188.1	45.6	0.0240	307.287	99.934	185.253	62.732	(13)
Sum:				<b>0.1190</b>	<b>268.614</b>	<b>87.357</b>	<b>161.938</b>	<b>54.837</b>	
EV $\equiv$ Escalante & Victor (1990)					KS $\equiv$ Kisielius & Storey (2002)				

Table 4.10 (continued) - Recombination line  $N^{+2}/H^{+}$  abundances.

Line(s) $\lambda$ (Å)	$\lambda_o$ (Å)	S/N	FWHM (km/s)	$I(\lambda)/I(H\beta)$ $I(H\beta)=100$	Value ( $N^{+2}/H^{+}$ ) ( $\times 10^4$ )				Notes
					EV		KS		
					Case A	Case B	Case A	Case B	
Multiplet 36 (3d $^3F^o$ - 4p $^3D$ )									
6167.750	6167.678	15.0	36.4	0.0025	1.968	1.733	1.180	1.013	...
6170.160	6170.170	8.7	15.5	0.0009	1.522	1.340	0.912	0.783	...
6173.310	6173.331	20.1	13.6	0.0023	2.626	2.312	1.574	1.351	...
Sum:				<b>0.0057</b>	<b>2.082</b>	<b>1.833</b>	<b>1.248</b>	<b>1.071</b>	
3d- 4f Transitions									
4035.081	4035.165	16.6	37.9	0.0071	0.798	...	...	...	(14)
4043.532	4043.460	8.7	24.3	0.0041	0.351	...	...	...	...
4041.310	4041.303	30.2	24.9	0.0121	0.793	...	...	...	(15)
4176.159	4176.145	13.0	27.3	0.0064	0.898	...	...	...	...
4236.927	4236.926	18.0	14.3	0.0030	0.281	...	...	...	...
4433.475	4433.769	11.9	23.6	0.0028	2.503	...	...	...	(16)
4552.522	4552.505	34.1	43.9	0.0026	1.030	...	...	...	...
4530.410	4530.404	21.6	16.7	0.0042	0.400	...	...	...	(17)
4678.153	4678.137	5.8	24.3	0.0014	0.219	...	...	...	...
Sum:					<b>0.441</b>	...	...	...	

EV  $\equiv$  Escalante & Victor (1990)

KS  $\equiv$  Kisielius & Storey (2002)

(1) Other members lost in glare from  $H\beta$ , [O III]  $\lambda 5007$ , or underneath ghosts.

(2) May have contribution from [Fe III]  $\lambda 4607.030$ .

(3) Uncorrected for 2% contribution from O II 3d  $^2D-2[3]^o$  4f.F  $\lambda 4613.681$  line.

(4) May have contributions from Si II  $\lambda 4621.419$  and [C I]  $\lambda 4621.570$ .

(5) May have a small contribution Ne II  $\lambda 4810.214$

- (6) Blended with O II 3s  $^6S^\circ$  - 3p  $^6P$   $\lambda$ 4465.408 sextet line, whose contribution is not directly estimatable.
- (7) May have contributions from O II 3d  $^2P$  - 2[2] $^\circ$  4f.D  $\lambda$ 4488.184, O II 3d  $^2P$  - 2[2] $^\circ$  4f.D  $\lambda$ 4488.18, and S II  $\lambda$ 4488.188.
- (8) May have contributions from C II  $\lambda$ 4987.300 and [Fe III]  $\lambda$ 4987.200
- (9) Blended with a cross-CCD flare.
- (10) May have a contribution from S II  $\lambda$ 5453.855.
- (11) May have a contribution from [Fe II]  $\lambda$ 5495.824.
- (12) May have a contribution from S III  $\lambda$ 3838.268.
- (13) Has a contribution from O II 3p  $^4D^\circ$  - 3d  $^4D$   $\lambda$ 3856.134, and an unknown contribution from Si II  $\lambda$ 3856.018. Predicted intensity for N II  $\lambda$ 3856.063 is  $I_{\lambda 3856.063} = 0.0240$  based upon  $I_{\lambda 3856.063}/I_{\lambda 3838.374} = 0.327$
- (14) Not corrected for small contribution from O II 3d  $^4F$  - 2[3] $^\circ$  4f.F  $\lambda$ 4035.0731.
- (15) Not corrected for small contribution from O II 3d  $^4F$  - 2[2] $^\circ$  4f.F  $\lambda$ 4041.278.
- (16) Dubious identification.
- (17) Not corrected for nearby N III  $\lambda$ 4530.86 on the basis of assumed negligible strength of any N III lines.

## O<sup>+</sup>/H<sup>+</sup>

We observed numerous O I recombination lines, including all of the triplet series of transitions  $3p\ ^3P - ns\ ^3S^\circ$  and  $3p\ ^3P - nd\ ^3D^\circ$ , up to order  $n=8$  and  $n=9$  respectively, and nearly all of the quintet series  $3p\ ^5P - ns\ ^5D^\circ$  transitions out to order  $n=8$ .

The O I line  $\lambda 8446$  line is predominantly excited by continuum fluorescence from starlight, in which resonance transitions excite upper  $^3S^\circ$  and  $^3D^\circ$  terms, which are then followed by cascades to the  $\lambda 8446$  origin level (Grandi 1975a). Grandi (1975a) has shown that continuum fluorescence by starlight is 9 times more effective than fluorescence via  $L\beta$  photons directly through the resonance transition at  $\lambda 1012\text{\AA}$  for the  $3d\ ^3D^\circ$  level followed by cascade to the  $3p\ ^3P\ \lambda 8446$  origin level.

All of the levels of the  $ns\ ^3S^\circ$  and  $nd\ ^3D^\circ$  sequences have resonance transitions to the ground state, but only some have coincidences with a specific Lyman series photon energy. Though the  $3p\ ^3P - 7s\ ^3S^\circ\ \lambda 5555$  transitions lacks this coincidence, its observed intensity fits well with the rest of the sequence. These sequences were still readily detectable at the highest excitation upper levels observed in our spectrum, yet both abruptly terminated when their upper levels exceeded exactly 13.40 eV. If these lines are continuum fluorescence lines, the source ion, neutral oxygen, would reside outside the ionization front beyond which the continuum radiation is truncated blueward of the Lyman limit. The Lyman limit corresponds roughly to that 13.40 eV “cut-off” energy. Thus, it is likely the same process excites all of the excited levels which feed the  $\lambda 8446$  line.

Recombination is also ruled out in dominating the excitation of the triplet lines

we observed based upon the comparative intensities of the  $\lambda 8446$  line (multiplet 4) to its quintet counterpart,  $3s\ ^5S^\circ - 3p\ ^5P$ , at  $\lambda 7773$  (multiplet 1). If recombination dominated both spin multiplicity groups, then the relative strengths of comparative lines, such as  $\lambda 8446$  and  $\lambda 7773$  should be roughly proportional to their statistical weights. However,  $\lambda 8446$  is observed to be stronger than  $\lambda 7773$  by roughly 20 times, exceeding the ratio of statistical weights which is unity. Fluorescence process from the ground state can't strengthen quintet lines, but it can strengthen triplet lines.

Our abundances are listed in Table 4.12. The excellent abundances agreement of the quintet multiplets indicates strict LS coupling with little additional excitation mechanism contribution beyond recombination. The much larger calculated abundance of  $\lambda 8446$  attests to the efficiency of continuum fluorescence in its excitation as compared to recombination. For the quintets, effective recombination coefficients were available only for case A. Therefore we adopt the average of the case A abundances from the quintet multiplets as our final value.

Table 4.12: Recombination line  $O^+/H^+$  abundances.

Line(s) $\lambda$ (Å)	$\lambda_o$ (Å)	S/N	FWHM (km/s)	$I(\lambda)/I(H\beta)$ $I(H\beta)=100$	Value ( $O^+/H^+$ ) ( $\times 10^4$ )		Notes
					Case A	Case B	
Multiplet 1 ( $3s\ ^5S^o - 3p\ ^5P$ )							
7771.944	7771.921	157.4	38.4	0.0352	3.694	...	...
7774.166	7774.170	148.9	27.1	0.0215	3.160	...	...
7775.387	7775.372	148.9	28.6	0.0130	3.193	...	...
Sum:				<b>0.0697</b>	<b>3.416</b>	...	
Multiplet 4 ( $3s\ ^3S^o - 3p\ ^2P$ )							
8446.247,.359,.758	8446.549	...	68.1	<b>1.1419</b>	<b>439.635</b>	<b>101.334</b>	
Multiplet 8 ( $3p\ ^5P - 3d\ ^5D^o$ )							
9260.806,.848,.937	9260.917	...	43.8	0.0047	3.107	...	...
9262.582,.670,.776	9262.702	...	43.7	0.0097	3.850	...	...
9265.826,.932,66.005	9265.934	99.0	27.8	0.0125	3.549	...	...
Sum:				<b>0.0269</b>	<b>3.561</b>	...	



## $\text{O}^{+2}/\text{H}^{+}$

Our IC 418 spectra reveals a rich O II recombination line spectrum. We followed Liu et al. (2000) in using for the 3s-3p transitions the LS-coupling based effective recombination coefficients from Storey (1994). For 3p-3d and 3d-4f transitions we used Liu et al. (1995a) who calculated effective recombination coefficients based on an intermediate coupling scheme. Abundances calculated from both individual lines, and from the sum of those lines observed within each multiplet are listed in Table 4.13. Calculations were carried out under all opacity case for which atomic data existed (no case C calculations were available for the 3p-3s transitions from Storey (1994)). Blank entries under each case in the table indicate missing coefficients. Comments regarding individual lines and multiplets can be found immediately following the table.

The most striking thing is the excellent agreement shown between summed abundances from nearly all multiplets, under the opacity case C. The large population of the  $2p^4\ ^2D^o$  that this would entail would require electron densities in the vicinity of the  $\text{O}^{+}$  to be near that level's critical density, so that a more Boltzmann-like population distribution is set up between the collisionally-excitable levels. Our electron density, determined directly from  $\text{O}^{+}$  forbidden lines, is  $10000\text{ cm}^{-3}$ , which exceeds the critical density of  $\approx 4000\text{ cm}^{-3}$  at the assigned ionic temperature of 8900 K. Thus it is conceivable that a significant population could be present in the  $2p^4\ ^2D^o$  state, to allow transitions terminating at the state to become optically thick, establishing case C conditions. This argues against the choice of case A for doublets, as was done by Liu et al. (2000) in their study of NGC 6153. But their density was only 3500

$\text{cm}^{-3}$  so our choice for case C is more valid in IC 418 than it would be in NGC 6153. The idea that IC 418 might be in case C has been previously proposed by Harrington et al. (1980). We adopted case C for all doublets, where atomic information for this case was available.

For the quartets, Liu et al. (2000) chose case B, which gave better agreement between case-sensitive and case-insensitive multiplet abundances. Our data also suggests that either case B or C prevails for quartets. Abundances for case insensitive multiplets, such as from multiplets 1 and 2, agree much better with case B and C abundance from case-sensitive multiplets 19, 20, and 28. Case C does yields more consistent results between the doublet and quartet multiplets, for those multiplets with atomic data available to allow a calculation of case C conditions. Though case C would seem only to affect doublets, non LS-coupling schemes relax selection rules, allowing interplay between doublet and quartet states that is not allowed in strict-LS coupling. Because the 3p state was calculated here in LS coupling, adopting case C will not have a significant effect upon its level populations. So, case C values for multiplets 1 and 2 should be fairly close to case B values.

The origin of the large abundance for multiplet 11 is not clear. This was not seen by Liu et al. (2000) for this multiplet. Hyung, Aller, & Feibelman (1994) speculate that several O II recombination lines in IC 418 could be strengthened by continuum fluorescence by starlight. The upper level of multiplet 11,  $3d\ ^4F$ , is connected to the ground state by a resonance transition at  $\lambda 430\text{\AA}$ . However, Grandi (1976) has calculated that continuum fluorescence can at most make a 20% contribution to the lines of multiplet 2, and much less to other quartet multiplets, under the physical

conditions prevailing in the Orion Nebula, or IC 418. Multiplet 2 does not exhibit a distinct overabundance in our data.  $O^+$  lies near the interface region where hydrogen is changing from ionized to neutral, so the optical depth of radiation capable of exciting its resonance transitions is extremely large. We note that Storey (1984) predicts zero intensity in this multiplet under case A conditions, and the effective recombination coefficient for the multiplet for case B is eight times smaller than that determined by Liu et al. (1995a), so we might conclude that in this particular case the atomic data might truly be uncertain.

Within the multiplets, individual line abundances seem to show good agreement. Much of the scatter here can be attributed to individual measurement uncertainties and blends with other lines. However, in multiplet 12 several additional lines should have been detected ( $\lambda\lambda 3847.893, 3864.667$ ) according to the relative branching ratios provided by Liu et al. (2000). For multiplet 20, the LS-coupled values for abundances, using Storey (1994) effective recombination coefficients and branching ratios defined as in eq. 4.4, seem to show less scatter than the abundances calculated using Liu et al. values.

The 3d-4f transitions show excellent agreement among themselves, and with abundances determined from other multiplets under case B or C conditions. These transitions are immune to fluorescence excitation and are case insensitive. Although weak, they seem to serve as excellent abundance indicators. Because of the greater consistency of case C abundances across all types of multiplets, we will use the average of the summed abundances from each multiplet (except multiplet 11) using the highest opacity case available (using case C when available, else case B). Included in this

average is the sum of the 3d-4f values.

We observed enhanced abundances from multiplets 15, 16, and 36, all of which have large low-temperature dielectronic recombination coefficients (Nussbaumer & Storey 1984). This agrees with the trend seen by Garnett & Dinerstein (2001a) in other PNe. However the abundances of these lines cannot be reconciled with other O II recombination line abundances, within the temperature range for which the Nussbaumer & Storey formalism is valid (to 60000 K ). This may indicate that high-temperature, “enhanced” dielectronic recombination is occurring as is argued by Garnett & Dinerstein (2001a). We also observe several O II sextet lines, which must be formed exclusively by dielectronic recombination. The lines appear to be genuine detections according to EMILI. Their strengths are generally an order of magnitude less than recombination lines. As with the N II quintets, dielectronic effective recombination coefficients are not available. Since sextet line can not directly interact with levels from which standard recombination lines occur, and because they are extremely weak, we assume they do not affect the abundances determined from the conventional recombination lines. All of these multiplets are discussed further in § 4.3.2.

Table 4.13: Recombination line  $O^{+2}/H^{+}$  abundances.

Line(s) $\lambda$ ( $\text{\AA}$ )	$\lambda_o$ ( $\text{\AA}$ )	S/N	FWHM (km/s)	$I(\lambda)/I(H\beta)$ $I(H\beta)=100$	Value ( $O^{+2}/H^{+}$ ) ( $\times 10^4$ )			Notes
					Case A	Case B	Case C	
Multiplet 1 ( $3s\ ^4P - 3p\ ^4D^o$ )								
4638.856	4638.816	125.4	18.4	0.0297	3.026	2.919	...	...
4641.810	4641.802	156.1	15.1	0.0428	1.731	1.670	...	(1)
4649.135	4649.128	210.8	15.6	0.0670	1.430	1.379	...	...
4650.838	4650.826	99.3	15.5	0.0217	2.227	2.148	...	...
4661.633	4661.625	115.0	15.6	0.0231	1.867	1.801	...	...
4673.733	4673.725	22.8	16.4	0.0041	2.128	2.053	...	...
4676.235	4676.225	77.3	16.2	0.0158	1.529	1.474	...	...
4696.353	4696.335	14.4	14.7	0.0027	2.377	2.292	...	(2)
Sum:				<b>0.2069</b>	<b>1.770</b>	<b>1.707</b>	...	
Multiplet 2 ( $3s\ ^4P - 3p\ ^4P^o$ )								
4317.139	4317.119	57.8	16.4	0.0159	3.010	2.140	...	(3)
4319.630	4319.618	38.4	13.8	0.0083	1.458	1.036	...	(4)
4325.761	4325.866	49.4	45.0	0.0171	16.265	11.562	...	(5)
4336.859	4336.830	12.2	11.5	0.0037	2.220	1.578	...	...
4345.560	4345.546	39.6	15.8	0.0192	3.707	2.635	...	...
4349.426	4349.409	77.3	18.6	0.0330	2.535	1.802	...	...
4366.895	4366.875	53.0	13.4	0.0136	2.467	1.754	...	...
Sum:				<b>0.0937</b>	<b>2.577</b>	<b>1.832</b>	...	

Table 4.13 (continued) - Recombination line  $O^{+2}/H^{+}$  abundances.

Line(S) $\lambda$ (Å)	$\lambda_o$ (Å)	S/N	FWHM (km/s)	$I(\lambda)/I(H\beta)$ $I(H\beta)=100$	Value ( $O^{+2}/H^{+}$ ) ( $\times 10^4$ )			Notes
					Case A	Case B	Case C	
Multiplet 5 ( $3s^2P - 3p^2D^o$ )								
4414.899	4414.888	113.7	15.0	0.0303	6.136	...	0.976	...
4416.975	4416.969	92.2	15.5	0.0197	7.193	...	1.144	...
4452.378	4452.262	34.1	43.9	0.0088	16.418	...	2.610	(6)
Sum:				<b>0.0500</b>	<b>6.517</b>	...	<b>1.036</b>	
Multiplet 10 ( $3p^4D^o - 3d^4F$ )								
4069.623	4069.626	25.0	18.9	0.0204	2.104	...	...	(7)
4069.882	4069.888	25.0	13.0	0.0199	1.288	...	...	(7)
4072.153	4072.149	100.3	15.2	0.0327	1.395	...	...	...
4075.862	4075.889	25.0	17.0	0.0442	1.306	...	...	(8)
4078.842	4078.808	23.0	16.3	0.0056	1.574	...	...	...
4085.112	4085.101	22.5	16.7	0.0076	1.737	...	...	...
4092.929	4092.920	37.9	10.8	0.0032	1.006	...	...	...
4094.140	4093.921	11.0	39.5	0.0049	22.725	...	...	(9)
Sum:				<b>0.1336</b>	<b>1.428</b>	...	...	
Multiplet 11 ( $3p^4D^o - 3d^4P$ )								
3882.446	3882.178	27.4	13.7	0.0063	177.655	9.799	9.172	(10)
3896.303	3896.201	13.7	27.7	0.0055	466.947	45.504	44.199	(11)
3907.455	3907.470	13.5	21.9	0.0035	99.333	3.585	3.358	...
Sum:				<b>0.0153</b>	<b>185.5093</b>	<b>8.254</b>		

Table 4.13 (continued) - Recombination line  $O^{+2}/H^{+}$  abundances.

Line(S) $\lambda$ ( $\text{\AA}$ )	$\lambda_o$ ( $\text{\AA}$ )	S/N	FWHM (km/s)	$I(\lambda)/I(H\beta)$ $I(H\beta)=100$	Value ( $O^{+2}/H^{+}$ ) ( $\times 10^4$ )			Notes
					Case A	Case B	Case C	
Multiplet 12 ( $3p\ ^4D^o - 3d\ ^4D$ )								
3856.134	3856.054	188.1	45.6	0.1013	1215.951	159.511	150.592	(12)
3882.194	3882.178	27.4	13.7	0.0063	0.867	1.206	0.647	(13)
3883.137	3883.110	10.3	23.7	0.0027	30.461	24.736	3.353	(14)
Sum:				<b>0.0090</b>	<b>1.653</b>	<b>1.962</b>	<b>0.976</b>	
Multiplet 19 ( $3p\ ^4P^o - 3d\ ^4P$ )								
4121.463	4121.434	...	17.5	0.0166	106.484	6.066	5.667	(15)
4132.800	4132.789	34.8	11.5	0.0083	29.898	1.553	1.456	...
4153.298	4153.287	75.7	15.1	0.0184	55.506	2.409	2.260	...
4156.530	4156.328	48.5	30.3	0.0159	240.010	13.115	12.280	(16)
4169.224	4168.955	140.0	24.3	0.0051	44.125	1.967	1.839	(17)
Sum:				<b>0.0484</b>	<b>39.465</b>	<b>1.836</b>	<b>1.721</b>	(18)
Multiplet 20 ( $3p\ ^4P^o - 3d\ ^4D$ )								
4097.225	4097.265	42.8	14.9	0.0045	36.523	5.757	5.511	(19)
4104.723	4104.747	18.1	55.1	0.0160	53.002	38.738	5.407	(20)
4104.990	4104.996	10.4	14.2	0.0046	5.414	0.891	0.848	(20)
4110.786	4110.766	19.2	15.0	0.0075	23.993	3.193	3.007	...
4119.217	4119.214	61.2	17.3	0.0219	2.600	2.534	1.356	...
4120.278,.547	4120.312	...	17.4	0.0068	7.827	2.581	0.911	...
Sum:				<b>0.0613</b>	<b>5.635</b>	<b>3.068</b>	<b>1.737</b>	(21)

Table 4.13 (continued) - Recombination line  $O^{+2}/H^{+}$  abundances.

Line(S) $\lambda$ (Å)	$\lambda_o$ (Å)	S/N	FWHM (km/s)	$I(\lambda)/I(H\beta)$ $I(H\beta)=100$	Value ( $O^{+2}/H^{+}$ ) ( $\times 10^4$ )			Notes
					Case A	Case B	Case C	
Multiplet 25 ( $3p^2D^o - 3d^2F$ )								
4699.219	4699.129	42.0	38.9	0.0107	16.600	14.526	1.500	(22)
4705.346	4705.344	61.4	14.6	0.0183	17.057	16.600	0.969	...
Sum:				<b>0.0290</b>	<b>16.886</b>	<b>15.782</b>	<b>1.115</b>	
Multiplet 28 ( $3p^4S^o - 3d^4P$ )								
4890.856	4890.905	50.5	33.5	0.0137	208.574	12.057	11.236	(23)
4906.830	4906.809	22.5	13.1	0.0042	34.543	1.723	1.610	...
4924.529	4924.524	25.1	16.4	0.0089	48.975	2.147	2.009	(24)
Sum:				<b>0.0131</b>	<b>43.190</b>	<b>1.990</b>	<b>1.861</b>	
3d - 4f Transitions								
4083.899	4083.874	17.9	14.3	0.0049	1.563	...	...	(25)
4087.153	4087.146	24.5	14.5	0.0045	1.513	...	...	...
4089.288	4089.290	37.9	13.3	0.0114	1.039	...	...	...
4095.644	4095.648	10.5	19.4	0.0042	1.943	...	...	(26)
4275.551	4275.535	33.4	13.5	0.0065	1.091	...	...	(27)
4277.427	4277.481	10.7	24.6	0.0033	2.252	...	...	(28)
4282.961	4282.957	13.4	16.1	0.0026	2.305	...	...	...
4285.684	4285.699	16.5	13.2	0.0031	1.490	...	...	(29)
4294.782,.919	4294.717	21.1	27.8	0.0059	1.877	...	...	...
4303.823	4303.819	34.1	14.6	0.0066	1.942	...	...	...
4466.435,.583	4466.390	9.9	25.1	0.0029	2.597	...	...	...
4602.129	4602.121	12.5	12.6	0.0022	1.172	...	...	...
4609.436	4609.436	23.7	15.3	0.0060	1.275	...	...	...



Table 4.13 (continued) - Recombination line  $O^{+2}/H^{+}$  abundances.

Line(S) $\lambda$ (Å)	$\lambda_o$ (Å)	S/N	FWHM (km/s)	$I(\lambda)/I(H\beta)$ $I(H\beta)=100$	Value ( $O^{+2}/H^{+}$ ) ( $\times 10^4$ )	Notes
					Case A	Case B
					Case C	
Sum:	<b>1.453</b>					
(1)	May have a contribution from N III $\lambda 4641.850$ . Based on strength of other N III lines, the contribution is probably less than 10%.					
(2)	Potential small contribution from O II 3d $^2D - 4f.F$ 2[3] <sup>o</sup> $\lambda 4393.357$ , amounting to 8% based from $I_{\lambda 4696.357}/I_{\lambda 4089.288} = 0.018$ is ignored. Adjusted abundance would be $O^{+2}/H^{+}=2.175$ (case A) or 2.097 (case B).					
(3)	May have a contribution from C II $\lambda 4317.265$ from the same multiplet as those blendin with the $\lambda 4325.761$ line. The abundance determined for this though seems in line with other lines considered not to be blends.					
(4)	May be blended with [Fe II] $\lambda 4319.620$ and Fe I $\lambda 4319.680$ .					
(5)	May be blended with C II $\lambda 4325.833$ and C II $\lambda 4326.164$ . If C II $\lambda 4318.606$ , same multiplet (3p $^4P - 4s$ $^4P^o$ ), is a correct ID for another line than it is predicted that $I_{\lambda 4325.833}/I_{\lambda 4318.606} = 1.072$ and $I_{\lambda 4326.164}/I_{\lambda 4318.606} = 0.993$ which would mean that $I_{\lambda 4325.833}=0.0092$ and $I_{\lambda 4326.164}=0.0085$ together would account for the observed strength of the line IDd as O II $\lambda 4325.761$ . All lines from that multiplet would be present except for C II $\lambda 4313.106$ which is near a flare. Could also be blended with Fe I $\lambda 4325.762$ . Not included in summed multiplet abundance.					
(6)	Blended with [Fe II] $\lambda 4452.098$ .					
(7)	Ignores a possible small contribution from C II 3d-4f $\lambda 4075.940$ line.					

- (8) Lines O II  $\lambda\lambda 4069.623, 4069.882$  were blended together, and split manually. If both fluxes are considered together the abundance becomes  $O^{+2}/H^{+}=1.602$  (case A), which is more in line with the other multiplet members.
- (9) Is possibly blended with Fe III  $\lambda 4093.645$  and possibly N III  $\lambda 4093.680$ . or another unknown blend. Not used in the summed multiplet value.
- (10) Abundances here corrected for contribution from blend with O II  $3p\ ^4D^{\circ} - 3d\ ^4D\ \lambda 3882.194$  (multiplet 12). From estimates with the line strength of O II  $\lambda 3907.46$ , we predict that the intensity of this line due to this O II  $\lambda 3882.446$  alone is  $I_{\lambda 3882.446} = 0.0035$  (case A),  $I_{\lambda 3882.446} = 0.0023$  (case B and C).
- (11) Line appears much too strong. Might be a blend with Fe I  $\lambda 3896.349$ ?
- (12) Line O II  $\lambda 3856.134$  is blended with N II  $3p\ ^3P - 4s\ ^3P^{\circ}\ \lambda 3856.063$  and Si II  $\lambda 3856.015$ . Not included in summed multiplet abundance.
- (13) Blended with O II  $3p\ ^4D^{\circ} - 3d\ ^4P$  (multiplet 11).  $I_{\lambda 3882.194} = 0.0028$  (case A) and  $I_{\lambda 3882.194} = 0.0040$  (case B and C). This would return corrected abundances of 0.867 (case A), 1.206 (case B), 0.647 (case C). Should be strongest line in multiplet based upon its branching ratio values and large statistical weight.
- (14) Line O II  $\lambda 3883.137$  seems unusually strong. Unknown blend?
- (15) May be poorly manually de-blended from neighboring He I  $\lambda 4120.811$ .
- (16) May be blended with N II  $3d\ ^3D^{\circ} - 4f.D\ 2[3/2]\ \lambda 4156.358$  or other unknown line. Not included in the summed multiplet abundance.
- (17) Blended with He I  $\lambda 4168.972$ . Intensity here is corrected for its contribution assuming  $I_{\lambda 4168.972}/I_{\lambda 4437.552} = 0.52$  (Brocklehurst 1972)
- (18) O II  $\lambda 4129.320$  might be present in the spectra, but sits upon a cross-CCD flare, and was not included in the original line list.
- (19) Blended with O II  $\lambda\ 3d\ ^4F - 4f.G\ 2[4]^{\circ}\ \lambda 4097.257$ . Intensity here is corrected by an amount established from  $I_{\lambda 4097.257}/I_{\lambda 4089.288} = 0.61$  which leads to a 61% correction to the measured intensity of the line.

- (20) O II  $\lambda\lambda 4104.723, 4104.990$  were observed as a single blended lines and were manually split. There may be a contribution from a Rowland Ghost from nearby H6 line. The combined average of their individual abundances is  $2.458 \times 10^{-4}$ .
- (21) From this multiplet  $\lambda 4102.999$  is on the wing of H6, but isn't measured.
- (22) May have an unknown contribution from the di-electronic line  $\lambda 4699.011$ . (multiplet 40).
- (23) Unusually strong and bright. The only other likely ID is O III  $\lambda 4890.858$ , but no other lines from this multiplet are seen elsewhere, nor is it expected to be a strong line. Not included in summed multiplet abundance.
- (24) O II May have a contribution from [Fe III]  $\lambda 4924.500$ .
- (25) Not corrected for blending with [Fe II]  $\lambda 4083.781$ .
- (26) May be blended with N III  $\lambda 4095.340$ .
- (27) Blended with Fe II]  $\lambda 4275.492$ .
- (28) Ignoring a small contribution (4%) from O II 3d  $^4D - 4f.F$  2[3] $^{\circ}$   $\lambda 4277.427$
- (29) Possibly blended with Fe II  $\lambda 4285.716$ .

### 4.2.3 $\text{Ne}^{+2}/\text{H}^{+}$

Only a handful of Ne II lines were definitively detected in our spectra. Our calculated abundances from them are listed in Table 4.15. We again deduced the unpublished intermediate coupling-calculated effective recombination coefficients for individual lines that were used by Liu et al. (2000) for their 3d-4f transition abundance calculations, which we determined by working backwards from their tabulated intensities and abundances. We assumed that the calculations were carried out in case A, as was used for their 3-3 transition quartets, but it is not explicitly stated there. However, it is likely that they are case insensitive anyway.

Unfortunately, the positions of many of the strongest predicted lines coincide with a region of the relevant spectrum which is particularly noisy due to nearby saturated lines and crowding at the Balmer limit confusing the continuum level. The Ne II lines aren't strong enough to be clearly separable from the continuum in the short duration spectrum either. Many other lines observed by Liu et al. (2000) are outside our bandpass. The sole detected 3s-3p line, Ne II  $\lambda 3777.134$ , was marginal ID'd, due to its amorphous line profile and its small theoretical strength with respect to the other lines of the same multiplet which were not clearly visible. Some of the strongest 3d-4f transitions observed by Liu et al. (2000), such as Ne II 3d  $^4\text{F} - 4\text{f } 2[5]^{\circ}$   $\lambda 4409.298$  and a complex of lines featuring Ne II  $\lambda 4428.634$  3d  $^2\text{D} - 4\text{f } 2[3]^{\circ}$  are clearly not present in our spectrum. None of the strongest optical recombination lines of Ne II were seen by HAF, so it may simply be that IC 418 is neon poor.

Table 4.15: Recombination line  $\text{Ne}^{+2}/\text{H}^{+}$  abundances.

Line(s) $\lambda$ (Å)	$\lambda_o$ (Å)	S/N	FWHM (km/s)	$I(\lambda)/I(\text{H}\beta)$ $I(\text{H}\beta)=100$	Value ( $\text{Ne}^+/\text{H}^+$ ) ( $\times 10^5$ )		Notes
					Case A	Case B	
Multiplet 1 ( $3s\ ^4\text{P} - 3p\ ^4\text{P}^o$ )							
3777.134	3777.164	9.4	41.5	0.0050	4.143	4.114	...
3d - 4f Transitions							
4219.745	4219.753	8.0	19.9	0.0015	2.796	...	...
4391.991	4391.963	7.4	15.8	0.0022	2.276	...	...
4457.050	4457.091	59.4	26.0	0.0134	140.834	...	...
Average:				...	<b>2.536</b>	...	(1)
(1)	Does not include $\lambda 4457.050$ .						

The data of Liu et al. (2000) and Luo, Liu, & Barlow (2001) showed that abundances from 3d-4f transitions are consistently a factor of two larger than from 3-3 transitions. Our data actually show the opposite trend. This casts further doubt on our  $\lambda 3777.134$  ID. However, the effective recombination coefficients for the 3d-4f may themselves be in error by a factor of 2 (Liu et al. 2001). The higher abundance from Ne II  $\lambda 4457.050$  does not arise from this effect, but probably from the existence of an unknown blend. However an obvious alternate candidate does not exist in our the EMILI output. The 3d-4f transitions.

Despite the uncertainty of the effective recombination coefficients of the two probable 3d-4f transitions IDs, their IDs were simply deemed more trustworthy than the  $\lambda 3777.134$  line. The final adopted ionic abundance was the average of their abundances.

#### 4.2.4 Other Ions

Besides the ions listed here, effective recombination coefficients exist for only a handful of additional ions.

We observed numerous S II lines whose excitation is most likely recombination. While effective recombination coefficients exist for the *upper levels* of the transitions (Nahar 1995), specific branching ratios for multiplets don't as yet exist. We welcome future calculations of S II effective recombination coefficients, as their recombination lines in conjunction with the strong [S III]  $\lambda\lambda 9072, 9530$  collisionally-excited lines, can provide another excellent test of relative abundances.

We also observed numerous Si, Fe, and Ni permitted and forbidden lines. As our analysis concentrates upon the C,N,O,Ne ions which have previously shown a history of the forbidden line/recombination line abundances discrepancy problem, we chose not to calculate abundances from these lines.

Finally, the strongest transitions of C III, N III, and O III, as determined from Williams (1995) are simply not present in our spectra. Many lines of these ions are excited either by continuum fluorescence, or a resonance fluorescence with a He II line photon (Grandi 1976). Given the lack of He II photons for excitation to allow weaker transitions to manifest themselves, and the low level of ionization in IC 418, we chose not to calculate abundances for these ions from the small number of measured lines.

### 4.2.5 Comparative Ionic Abundances

Listed in Table 4.16 are the final ionic abundances determined in this study, and in other recent studies of IC 418. Bold items in this table indicate ionic abundances for the same ion derived from both recombination and collisionally excited lines observed in the present study.

Table 4.16 Comparative ionic abundances for IC 418 from collisional/recombination lines, in units such that  $\log (H^+)=12.0$ , for present and other surveys.

Ion	Line Type	Present	HAF	HKB	Notes
He <sup>+</sup>	Recombination	10.973	10.844	10.839	(1)
C <sup>o</sup>	Collision	5.217	...	...	...
C <sup>+</sup>	Recombination	7.828	...	...	...
	Collision	...	8.230	...	(2)
C <sup>+2</sup>	Recombination	8.744	...	...	...
	Collision	...	7.968	8.446	...
N <sup>o</sup>	Collision	5.934	6.484	...	...
N <sup>+</sup>	Recombination	< <b>9.317</b>	...	...	...
	Collision	<b>7.615</b>	7.713	7.567	...
N <sup>+2</sup>	Recombination	≤8.030	7.491	...	(3)
	Collision	...	...	...	...
O <sup>o</sup>	Collision	6.765	6.954	...	(4)
O <sup>+</sup>	Recombination	<b>8.543</b>	...	...	...
	Collision	<b>8.221</b>	8.246	7.792	...
O <sup>+2</sup>	Recombination	<b>8.172</b>	...	...	...
	Collision	<b>8.080</b>	7.540	7.886	...
Ne <sup>+2</sup>	Recombination	<b>7.404</b>	...	...	...
	Collision	<b>6.637</b>	6.281	6.623	...
S <sup>+</sup>	Collision	6.247	5.903	...	(5)
S <sup>+2</sup>	Collision	6.372	6.276	...	...
Cl <sup>+</sup>	Collision	4.128	4.439	...	...
Cl <sup>+2</sup>	Collision	4.742	4.696	...	...
Ar <sup>+2</sup>	Collision	6.005	5.703	...	...
Ar <sup>+3</sup>	Collision	2.955	...	...	...
HAF = Hyung, Aller, & Feibelman (1994) HKB = Henry, Kwitter, & Bates (2000)					

- (1) In HAF, average of tabulated He I  $\lambda\lambda 4471, 5876$  values.
- (2) In HAF, tabulated value at  $N_e=11500 \text{ cm}^{-3}$ . Decreases to 8.133 at  $N_e=5600 \text{ cm}^{-3}$ .
- (3) In HAF, calculated from an unknown recombination line, using coefficients of Pequignot et al. (1991)
- (4) In HAF, tabulated value at  $N_e=11500 \text{ cm}^{-3}$ . Decreases to 6.687 at  $N_e=5600 \text{ cm}^{-3}$ .
- (5) In HAF, average of tabulated S II  $\lambda\lambda 4068, 4076$  and  $\lambda\lambda 6716, 6713$  values calculated at  $N_e=5600 \text{ cm}^{-3}$ .



## 4.3 Sources of Abundance Discrepancy

### 4.3.1 Continuum Fluorescence

Continuum fluorescence from the ground state, due to radiation from the central star exciting levels through resonance transitions, has been suggested to explain the excess emission from several multiplets belonging to  $C^+$ ,  $N^+$ ,  $N^{+2}$ , and  $O^+$ .

We will seek confirmation of this process, as well as other additional information, through an examination of the detailed line profiles from this study's high level of resolution ( $10 \text{ km sec}^{-1}$ ). Line profiles, in velocity space, are the product of the emissivity of the source ion and the thermal width of the line, as functions of radial velocity (i.e. position in the nebula), and the radial velocity distribution, convolved with the instrumental profile. We will make use of a fundamental property of line profiles: lines belonging to the same parent ion should have nearly *identical* profiles. Specifically, we will compare recombination line profiles with collisionally excited lines from the same source ion, or from an ion in the *next lower ionization stage*. Profile agreement with the same source ion favors recombination as the dominant excitation process, while profile agreement with the differing ions favors continuum fluorescence as a large contributor to a line's strength.

As seen in Figure 4.3, lines belonging to ions of increasing ionization potential, have generally narrower profiles (clockwise around the figure starting with "INS"). At low ionization, the ion is distributed further away from the central star, where the expansion velocity is the largest. Our line of sight intercepts both the front and back edges of expanding, roughly spherical shells. At our instrumental resolution

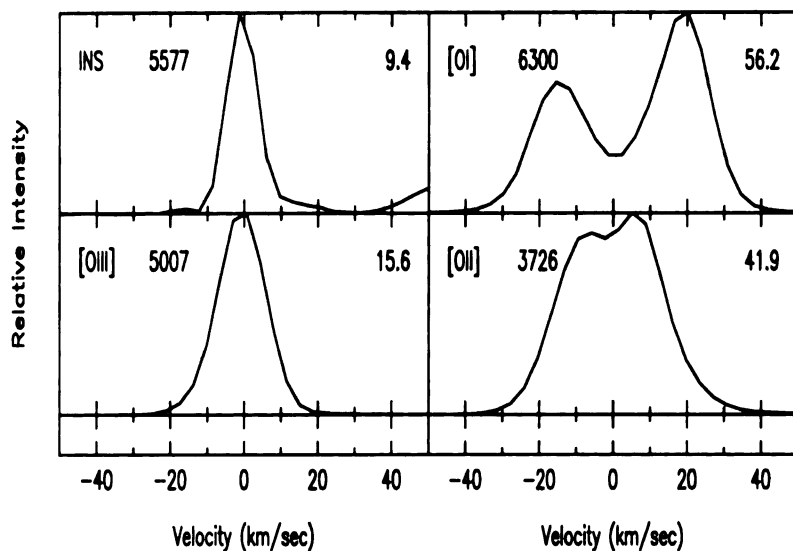


Figure 4.3 Representative line profiles for ions of differing ionization potential with a comparative sample of the instrumental resolution element. The “INS” profile, of the night sky emission line [O I]  $\lambda 5577$ , demonstrates the limits of our instrumental resolution. The level of ionization increases clockwise from the instrumental profile.

the individual components of emission from both edges are separated in the profile, as in [O I]  $\lambda 6300$  above in Figure 4.3. At higher ionization potentials, the ions are concentrated nearer the central star where the expansion velocities are less, and it become increasingly more difficult to separate “forward” and “rearward” nebular emission components (see [O II]  $\lambda 3726$ , Figure 4.3). Eventually the intrinsic full width half maximum of the nebular lines due to thermal motions (about  $20 \text{ km sec}^{-1}$ ) prohibits separation at our resolution as the components merge together ([O III]  $\lambda 5007$ , Figure 4.3). This clear sequence of profile width with ionization energy is a consequence of the comparatively simple expansion geometry of IC 418, and is a primary reason why this PN was chosen for observation.

In the following plots we show, the profiles of representative lines from each multiplet from which abundances were determined, choosing the strongest line most likely

not to be part of a blend. The abscissa of each plot is line intensity normalized to the largest intensity within the line, while the ordinate is the wavelength spread of the profile in velocity space, centered on the line ID's tabulated wavelength. In each profile box are listed the ID (upper left hand corner, with wavelength rounded to nearest Å), the FWHM (in  $\text{km sec}^{-1}$ , upper right corner), and if applicable, the multiplet to which the line belongs (below the FWHM).

## C II

In addition to the strongest lines, the profiles of the high-excitation lines from Table 4.8 are also included for comparison purposes. The C II  $\lambda 4267$  line includes all of multiplet 6. This line is a blend, as are the high-excitation lines. Line profiles are shown in Figure 4.4.

As mentioned earlier, the pattern of abundance enhancement shown by the other C II lines with respect to  $\lambda 4267$  is in general agreement with potential continuum fluorescence excitation of some of the upper levels of the observed multiplets (multiplets 3 and 4) followed by cascade through additional observed multiplets (2 and 5), as proposed by Grandi (1976). Multiplet 6,  $\lambda 4267$ , being of higher orbital angular momentum, is removed from both direct excitation of its upper level, as well as cascade from higher energy levels which could be so excited.

Unfortunately, no collisionally excited lines of either  $\text{C}^+$  or  $\text{C}^{+2}$  are present in our observed bandpass, nor is the FWHM listed in HAF or HKB for UV lines of those ions. However, C II, N II, and O II “recombination” lines have similar FWHM (see Figure 4.5). The C II lines here are narrow, and show negligible evidence of the type

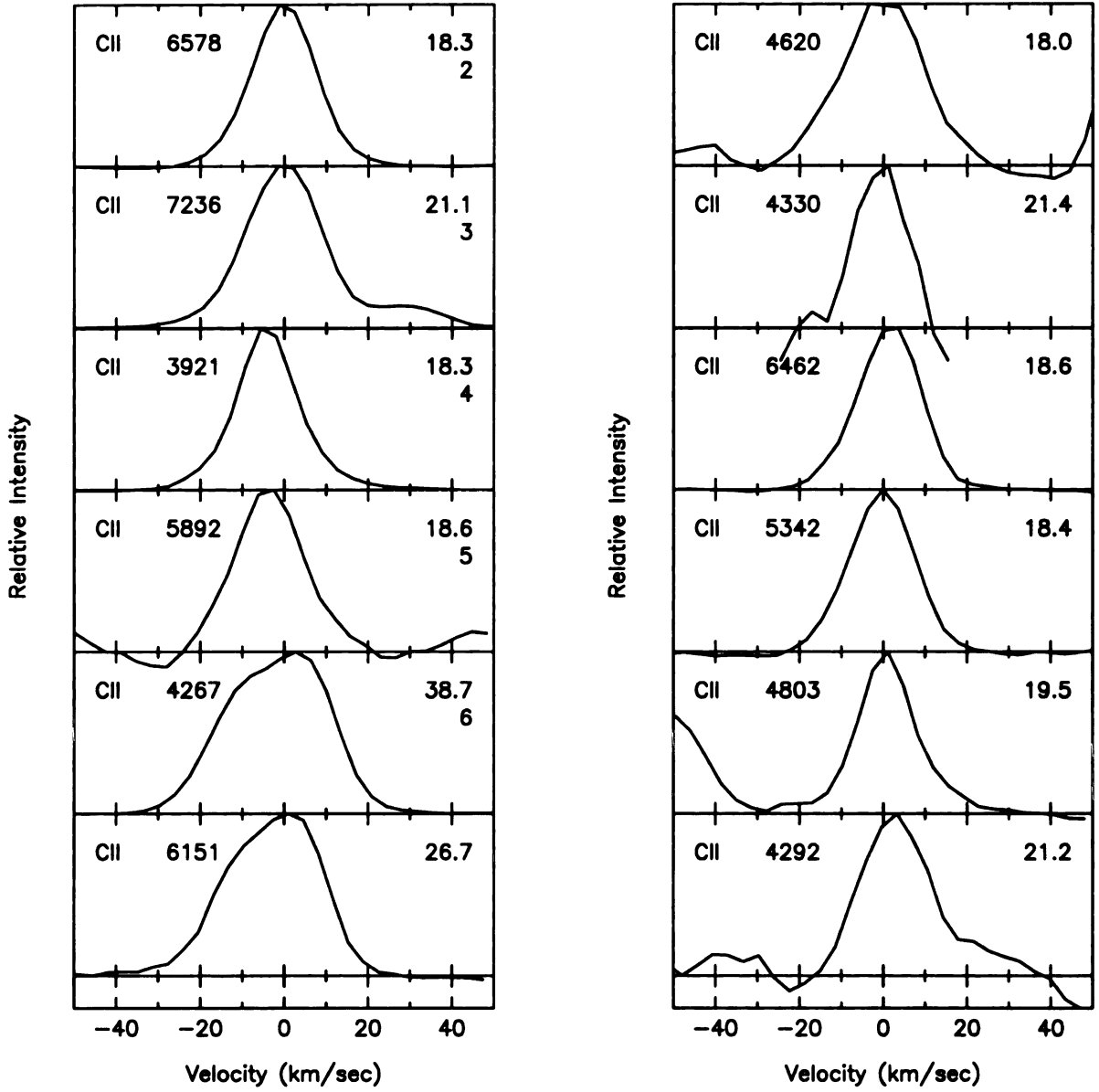


Figure 4.4 Line profiles from C II lines.

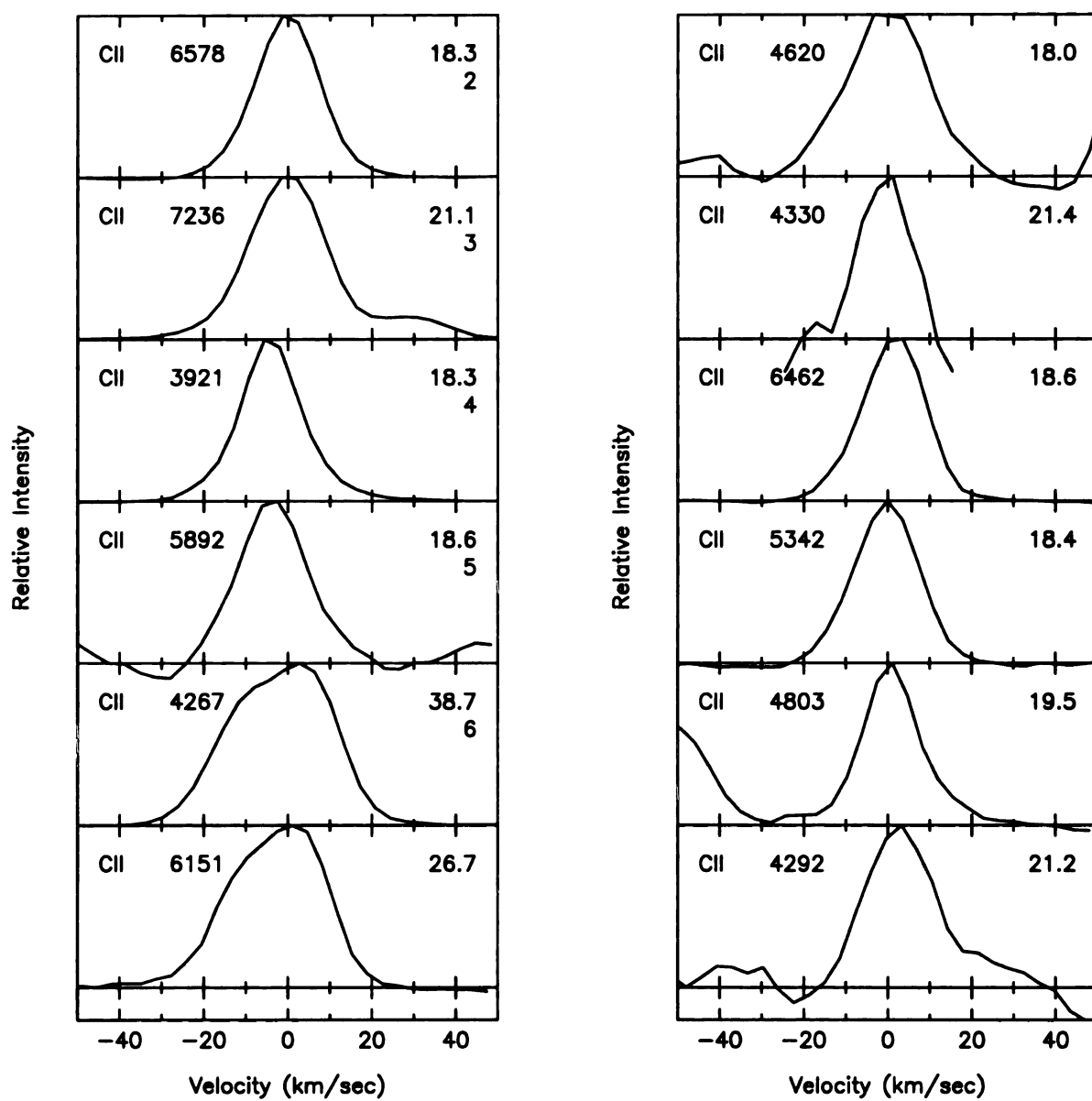


Figure 4.4 Line profiles from C II lines.

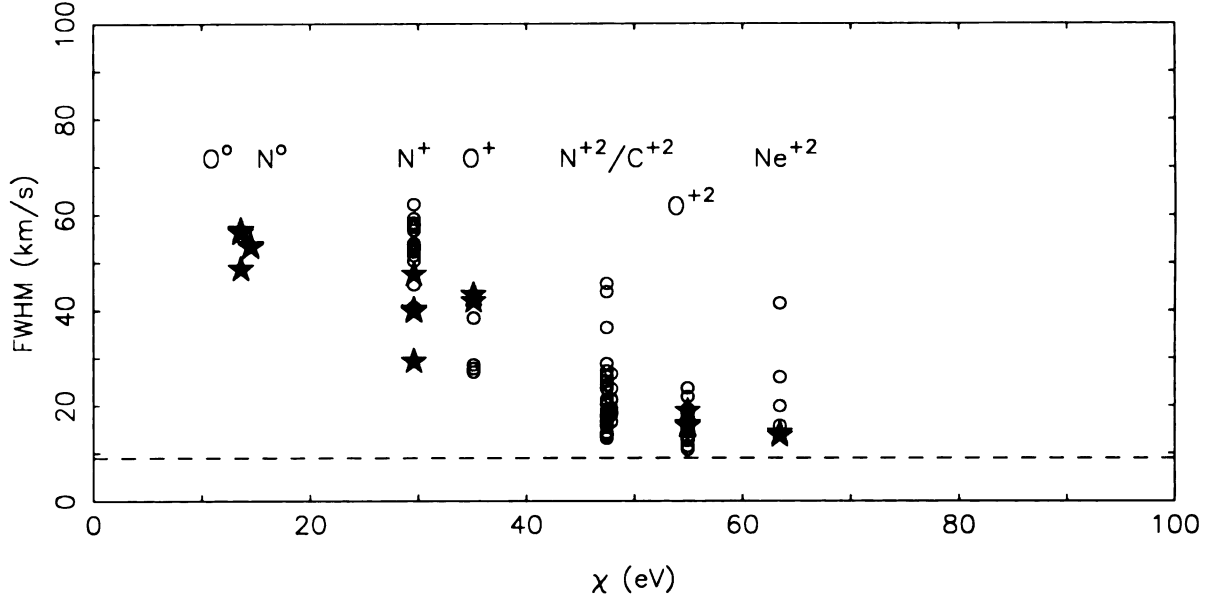


Figure 4.5 FWHM versus ionization potential  $\chi$  for non-blended lines from various ions. Small circles are recombination lines; stars are collisionally excited lines for the same ion. The dashed line is the instrumental resolution limit.

of double lobe profile indicative of lines of lower ionization.

The proposal of continuum fluorescence of multiplets 4 is challenged by the similarity of their line profiles with the high-excitation C II lines, which would not be excited by this mechanism. Nor do multiplets 2 and 5 exhibit larger FWHM than other multiplets' lines as would be expected from cascades following fluorescence. Only the lines of multiplet 3, whose upper level has the possibility of being directly excited by continuum fluorescence, show a slight increase in FWHM. However the agreement between  $\lambda 4267$  and the summed abundance of multiplet 3, would seem to confirm that the population of the upper level of multiplet 3 is dominated by strong recombination and cascade from  $\lambda 4267$ , rather than continuum fluorescence.

Therefore, we conclude that the line profiles do not support a large contribution from continuum fluorescence. These lines appear to be most strongly excited by

recombination. Since the contribution of continuum fluorescence can not be exactly quantified without a model of the central star radiation and radiative transfer through the nebula, it is unknown what ratio of  $C^+$  to  $C^{+2}$  would give a small enhancement to line strengths, but leave the profiles relatively unchanged, from the straight recombination case. The effects of continuum fluorescence over recombination are more clearly demonstrated in the N I profiles.

## N I

Recall from Table 4.9 that each observed multiplet returned a vastly different abundance, when calculated on the basis of pure recombination excitation. The overabundance was attributed to strong continuum fluorescence and subsequent cascade through the upper levels of multiplets 1, 2, 3. As can be seen in Figure 4.6, the profiles of the strongest non-blend member of the each of these multiplets resemble the [N I]  $\lambda\lambda 5198, 5200$  lines more than any of the [N II] lines. These lines FWHM also agree well with those for the [N I] lines. The  $\lambda 9810.010$  line from multiplet 19, was theorized here to be strengthened directly by continuum fluorescence excitation of its  $3d\ ^4D$  upper level. Although the profile is less distinct, and perhaps affected by its location on the extreme edge of the red spectrum, it is again more indicative of [N I] rather than [N II]. We conclude that all of these lines are powered primarily by continuum fluorescence, and that the abundances determined from these lines' strengths under pure recombination are untrustworthy.

Splitting the two lobes of the emission in each profile yields an expansion velocity of the object. All lines (except  $\lambda 9810.010$  of multiplet 19) were split with the “d-

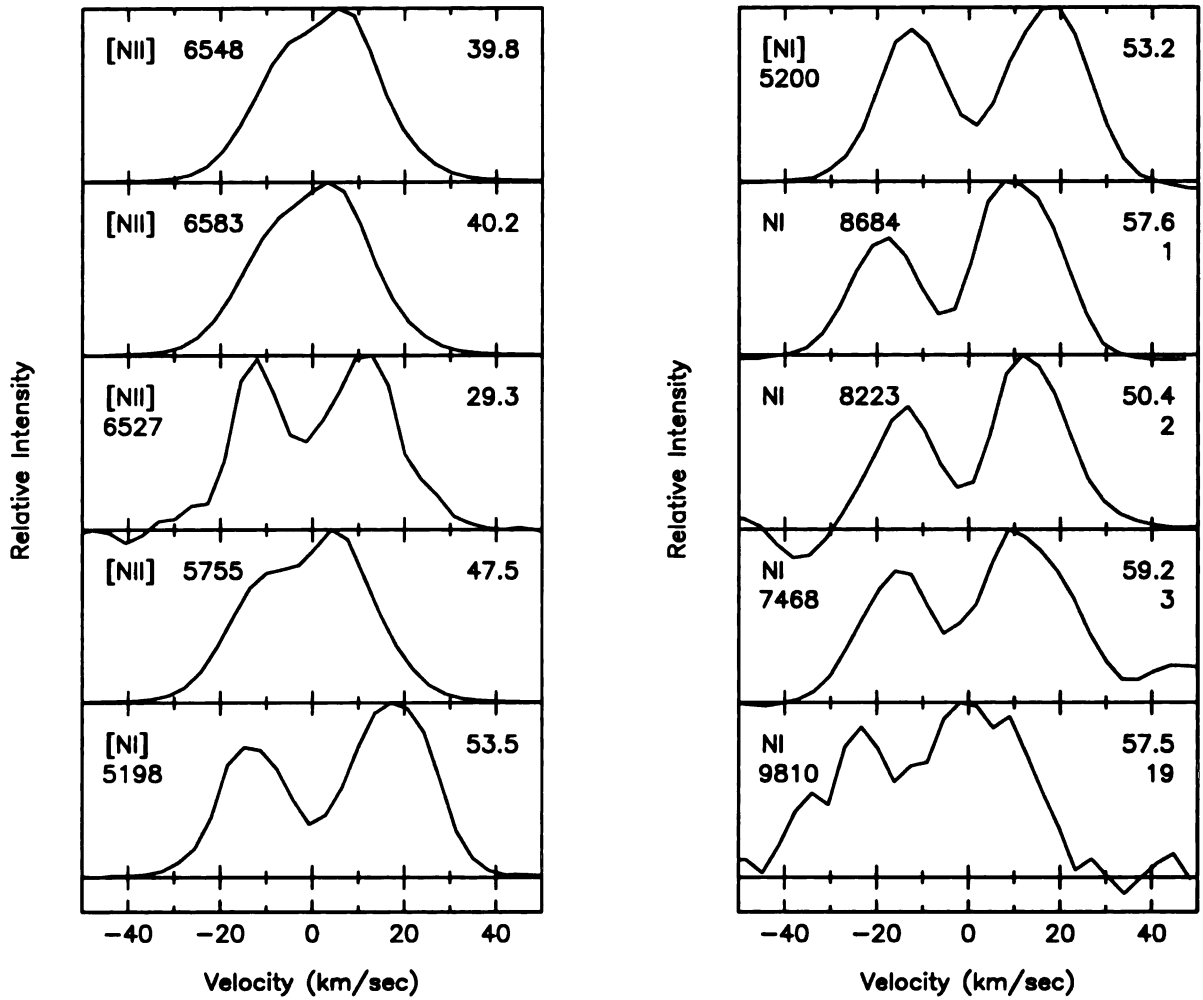


Figure 4.6 Line profiles from N I, [N I], and [N II] lines.

d" function of the IRAF task *splot* which fits multiple Gaussians. The expansion velocities of  $N^0$  and  $N^+$ , as well for as other ions as determined from their profiles, is listed in Table 4.17. The [N II] expansion velocity agrees well with the  $12.0 \text{ km sec}^{-1}$  given in Acker et al. (1992).

We note that each profile exhibits a velocity dependent structure which is not symmetric about the line center, indicating that forward component emission is not as strong as the rearward component. This is a common feature of many PNe lines at



Table 4.17 Measured IC 418 expansion velocity from line profiles.

Ion	Line (Å)	Velocity (km/sec)
N <sup>o</sup>	[N I] λ5198	15.3
	[N I] λ5200	14.9
	N I λ8683.525	14.8
	N I λ8223.128	13.7
	N I λ7468.312	14.5
N <sup>+</sup>	[N II] λ6527	11.7
O <sup>o</sup>	[O I] λ5577	14.5
	[O I] λ6300	16.0
	[O I] λ6363	15.9

high resolution (Osterbrock 1989), and indicates a departure from spherical symmetry for the real object. It may also indicate a slit location off-center from an axis through the central star. However, a comparison of the [N I] λ5198,5200 density diagnostic line profiles shows that the rearward component of [N I] λ5200 exceeds that of [N I] λ5198 even when the relative differences in scaling are taken into account. This would indicate differing densities in the forward and rear components of the shell occupied by N<sup>o</sup>.

For the [N II] lines a similar determination of temperature is complicated by the “filling in” of the line profile centers by emission from the strong [N II] λ5755 and nearly saturated [N II] λλ6548,6583 lines bleeding over to adjacent pixels. The much weaker [N II] λ6527 possesses the two lobe pattern characterizing foreground and background emission from the same expanding shell, but in a symmetric profile. While the difference in FWHM between the λ6527 and other [N I] lines can be explained by broad non-Gaussian wings in their near-saturated profiles, it is not immediately clear why the intensity ratio between [N II] λ6527 and λλ6548,6583 appears to be velocity

dependent. Since all three lines originate from the same upper level, their intrinsic intensity ratios should be equal to a ratio of their spontaneous emission coefficients. However, since the line profiles are drawn from different spectra ( $\lambda\lambda 6548, 6583$  from the short duration intermediate spectrum,  $\lambda 6527$  from the long duration intermediate spectrum) we believe it is likely that the extraction windows used for the two spectra were mis-aligned, giving rise to the different profile for  $\lambda 6527$ .

## N II

In addition to the strongest non-blended lines, we include the strongest of the 3d-4f transitions we observed, as well as the strongest quintet line (multiplet 66  $\lambda 5173.385$ ) in Figure 4.7.

Our earlier conclusion was that there was no consensus on the large scatter in abundance exhibited from the various multiplets. Grandi (1976) specifically names multiplet 30 to be excited by pumping via the He I  $\lambda 505.68$  photons. However, Liu et al. (2002) concluded that it is more likely that this multiplet is excited by continuum fluorescence from the ground state. In either case the possibility exists for enhancement of lines in multiplets down the cascade path. The profile of  $\lambda 3829.795$  (multiplet 30) is somewhat broader than  $\lambda 6167.750$  (multiplet 36), the latter thought here to be less likely affected by any fluorescence process. The profile of  $\lambda 5679.558$  (multiplet 3), on the cascade path, also appears slightly broader than other lines. However,  $\lambda 4601.478$  (multiplet 5), also on the cascade path does not appear noticeably different or broader than other lines. Grandi (1976) also suggests that lines of multiplet 20 may be excited by a mix of continuum fluorescence and standard recombination. The

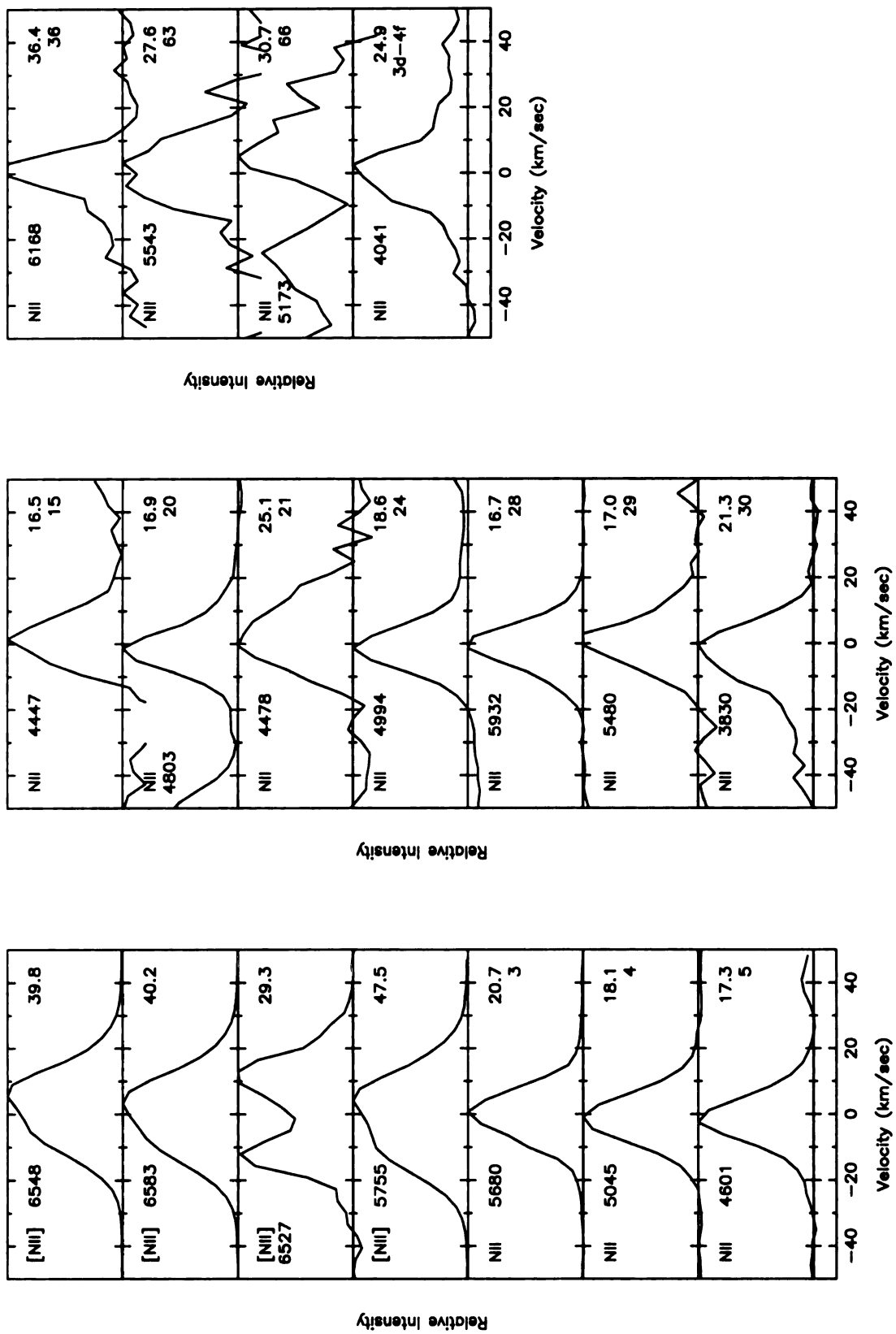


Figure 4.7 Line profiles from [N II] and N II lines.

idea that other lines may also have a similar mix of contributions from both processes is reinforced by the similarity of profile and FWHM of  $\lambda 4803.286$  (multiplet 20) with other lines outside of multiplets 20 and 26. The broad profile of  $\lambda 4478.682$  (multiplet 21) is more likely due to the irregular profile of a comparatively weaker line with respect to the other lines, than to broadening due to significant fluorescence contribution. Unfortunately the  $\lambda 5173.385$  line is weak, from which no real conclusions can be drawn. The strongest 3d-4f transition,  $\lambda 4041.310$ , has a profile that agrees well with other N II lines, despite a slightly higher FWHM.

As with C II, no collisionally excited lines of  $N^{+2}$  were observed in our spectra, nor are statistics for IC 418 available elsewhere for comparison. However, it is clear from a comparison with the  $N^+$  collisionally excited line profiles, that this ion is not the majority parent ion of these lines. This is evident not only in FWHM, but also in the lack of a two-lobe structure characterizing lines of lower ionization potential. The asymmetry in the profiles are also not evident in the N II lines.

We conclude therefore that these lines' strengths are most likely not dominated by fluorescence. Nevertheless, a small contribution from continuum fluorescence cannot be ruled out on the basis of the relative line profiles alone.

## O I

Confirmation of  $\lambda 8446$  (multiplet 4) being strongly fluorescent-enhanced is clear by comparing its line profile, with that of the  $O^o$  collisionally excited lines [O I]  $\lambda 6300$ ,  $\lambda 6363$ , and  $\lambda 5577$ , in Figure 4.8. The two lobe signature of lower ionization is present despite the fact the  $\lambda 8446$  is a blend of several transitions.

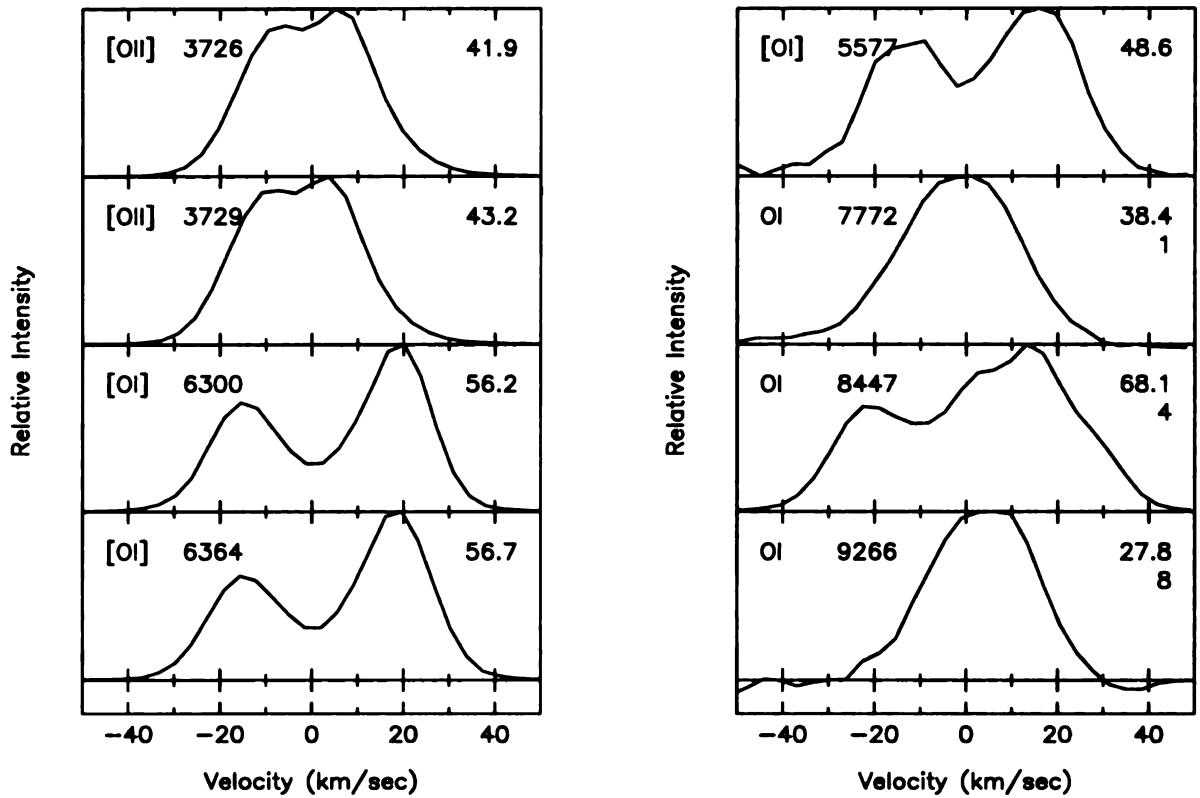


Figure 4.8 Line profiles from [O I], [O II], and O I lines.

The profiles of the line  $\lambda 7771.944$  (multiplet 8) and the blend at  $\lambda 9266$  (multiplet 8), show excellent agreement with one another, and align fairly well with the profiles of  $O^{+2}$  collisionally excited lines [O II]  $\lambda\lambda 3726, 3729$ . However both lines lack the two lobe signature and/or asymmetric profile indicative of lower ionization that [O II]  $\lambda\lambda 3726, 3729$  possess. The difference in profile may be due to a slight difference in the position of the slit from the blue ( $\lambda\lambda 3726, 3729$ ) to the red spectrum ( $\lambda\lambda 7771.944, 9266$ ). The O I lines might also arise from a slightly different portion of the nebula than do the [O II] lines. Recombination lines will tend to form in the portion of a particular zone occupied by an ion where recombination is most effective (cooler temperature), while collisional lines favor regions where collisional excitation

is the highest (warmer temperatures). This is the notion of temperature fluctuations within the region in which  $O^+$  resides. We will test for this in § 4.3.3.

Given the excellent agreement between abundances determined from the  $\lambda 7771.944$  line and the  $\lambda 9266$  blend, based on pure recombination theory alone, reinforced by the obvious disagreement between their profiles and those of [O I] collisionally excited lines, we rule out fluorescence processes as major contributors to the O I line strengths.

## O II

In addition to the strongest lines from those multiplets which were used for abundance determination, we plot the strongest 3d-4f transition at  $\lambda 4089.288$ , and the strongest lines from multiplet 15, 16, and 36 in Figure 4.9. Lines from the latter multiplets are thought to be excited primarily through dielectronic recombination and they yield larger abundances than most of the other O II lines (see § 4.3.2).

The line profiles generally confirm what our abundance measurements told us: all lines strengths appear to be well-described by recombination *alone*. The profiles of the representative lines agree extremely well with those of the  $O^{+2}$  collisionally-excited lines, and do not conform to the  $O^+$  collisionally-excited lines. There is no evidence for the double lobe/asymmetric structure in the O II lines that is evidence in [O II]  $\lambda\lambda 3726, 3729$ . Specifically, we don't see any obvious signature of fluorescence activity in the profiles of the representatives from the “dielectronic” multiplets  $\lambda 4590.974$  (multiplet 15),  $\lambda 4351.260$  (multiplet 16; actually a blend of two transitions), and  $\lambda 4185$  (multiplet 36), which could be acting to enhance their respective

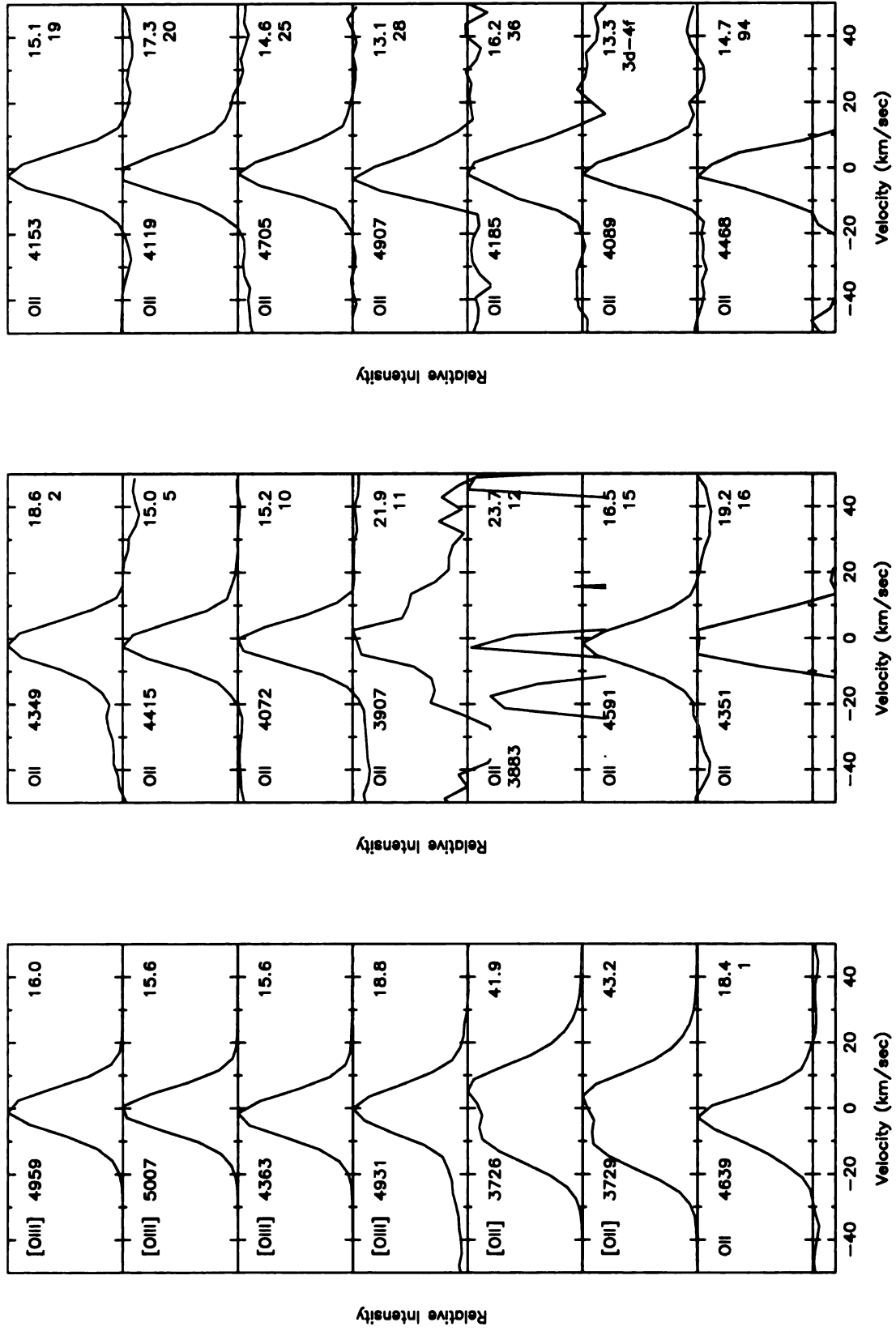


Figure 4.9 Line profiles from [O II], [O III], and O II lines.

lines' strengths. The profile from the representative of the multiplet which yielded the most discrepant abundance ( $\lambda 3907.455$ , multiplet 11) is somewhat broader than the other O II lines. However, this is also among the weakest lines in the group, so its irregularly shaped profile could be a function of marginal detectability. Nor are there even vague traits that could cause us to think it might be similar to the [O II] lines. Finally, the profile of  $\lambda 3883.137$  (multiplet 12) is extremely irregular, since it's the weakest among non 3d-4f O II transitions. It was included here because the other two observed multiplet members are parts of blends.

We conclude that if any continuum fluorescence is acting to strengthen the lines, it is at a level that is even less pronounced than in C II or N II, and certainly not at the level of N I or O I.

## Ne II

We plot in Figure 4.10 the profiles of all the lines we used to determine the  $\text{Ne}^{+2}$  abundance.

All the Ne II lines, except Ne II  $\lambda 4457.050$ , are extremely weak. Unfortunately the profiles are not distinct enough to draw many conclusions. However it does appear that  $\lambda 3777.134$  (multiplet 1), the only non 3d-4f transition of Ne II we observed, appears to have a similar profile, in its primary peak, to those exhibited by the  $\text{Ne}^{+2}$  collisionally excited lines [Ne III]  $\lambda\lambda 3869, 3968$ . The secondary peak may be indicative of a second blended line or a noise spike from the continuum; it is difficult to tell. Even if it was a second line, its inclusion into the summed flux for this line (the reason for the large FWHM was the inclusion of the secondary smaller peak in the



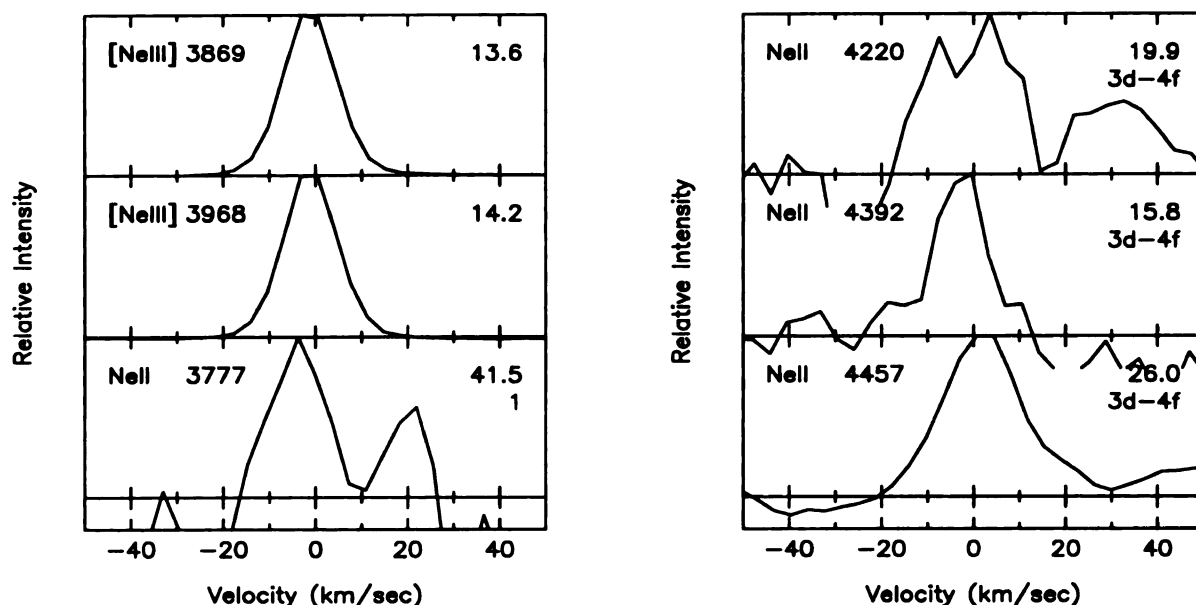


Figure 4.10 Lines profiles from [Ne III] and Ne II lines.

FWHM measurement) would be insufficient to explain the factor of six difference in the abundances derived for recombination versus collisionally excited lines.

For the 3d-4f transitions,  $\lambda 4219.745$  is somewhat broader than the [Ne III] lines, but this could again be contributed to noise. The  $\lambda 4391.991$  line, which is somewhat stronger, shows good agreement with the [Ne III] lines in its profile. For  $\lambda 4457.050$ , we note that the profile is distinctly broader than any of the other Ne II or [Ne III] lines. It is not clear why this 3d-4f transition should be strengthened when others are not. The 3d-4f transitions should be immune to ground state fluorescence processes. This leads us to believe that this is a line from a different ion, with Ne II  $\lambda 4457.050$  at most part of a blend with that line.

## Conclusions

- Where continuum fluorescence is predicted or shown to dominate the contribution to a line strength, such as for the N I lines of the same multiplicity as the ground state, or the O I  $\lambda 8446$  lines, it is readily apparent from the profiles that this is the case. Their profiles clearly resemble those of collisionally excited lines of the same ionization state, as opposed to those of the next higher ionization state.
- Where continuum or Bowen-like fluorescences are thought to contribute a significant amount to a line's strength, there are hints of larger FWHM and broader profiles. However these subtle differences may be masked by irregularly shaped profiles from weaker lines. There is no distinct signature for enhancement on a lower level than that shown for the O I  $\lambda 8446$ . The dependence of a profile's morphology on the degree of continuum fluorescence enhancement is not clearly demonstrated in our dataset.
- The profiles of [N I]  $\lambda\lambda 5198, 5200$  suggest that electron densities may vary between the forward and rearward portions of the shell, evidence not seen in the [O I] temperature diagnostic lines' profiles.
- O I recombination lines lack the asymmetric profile of the [O II] collisionally excited lines. This suggests that these O I recombination lines may be formed interior to [O II] lines, or that temperature fluctuations may be present in the region of the nebula occupied by  $O^+$ . Alternatively, this may also be due to

observational differences between the individual spectra.

### 4.3.2 Enhanced Dielectronic Recombination

Our long duration exposure spectra reveal numerous lines which, according to both LS selection rules and the effective recombination coefficients of Nussbaumer & Storey (1984), are either primarily or solely produced by dielectronic recombination. We list some of the brightest of these lines, and the ones with the most certain IDs, for  $C^{+2}$  in Table 4.18,  $N^{+2}$  in Table 4.19, and  $O^{+2}$  in Table 4.20. This includes numerous doublet  $C^{+2}$  lines, whose presence is not surprising given that dielectronic recombination is dominant recombination mechanism for  $C^{+3}$  (Osterbrock 1989, Kwok 2000). However, several quartet  $C^{+2}$  quartet lines are also observed in our spectra, as are  $N^{+2}$  quintet and  $O^{+2}$  sextet lines, more tentatively ID'd. These lines must be formed by dielectronic recombination, and their presence is a signature of its operation at the location we observed in IC 418. Unfortunately, recombination coefficients for their multiplets are unavailable for direct abundance determination.

It should be noted that the effective recombination coefficients for abundances calculations from the majority of  $C^{+2}$ ,  $N^{+2}$ , and  $O^{+2}$  lines are derived directly from the photoionization cross-sections of the initial states, with special attention paid to the resonances within them that give rise to dielectronic recombination. Separate coefficients gauging the effects of low-temperature dielectronic recombination alone on one-body recombination lines, from Nussbaumer & Storey (1984), have shown that, with the exception of a few cases listed below, dielectronic recombination makes

Table 4.18 C II dielectronic lines.

Line(s) $\lambda$ (Å)	$\lambda_o$ (Å)	S/N	FWHM (km/s)	$I(\lambda)/I(H\beta)$ $I(H\beta)=100$	Notes
Multiplet 12 ( $2s^24p\ ^2P^o - 2s2p(^3P^o)3p\ ^2P$ )					
5121.828	5121.850	103.7	20.8	0.0268	...
5125.208	5125.232	29.6	14.9	0.0058	...
5126.963	5126.960	12.7	16.9	0.0030	...
Multiplet 14 ( $2s2p(^3P^o)3s\ ^4P^o - 2s2p(^3P^o)3p\ ^4D$ )					
6779.940	6779.954	...	17.9	0.0109	...
6780.600	6780.626	...	17.7	0.0055	...
6783.910	6783.937	12.4	19.1	0.0022	...
6787.210	6787.361	45.5	46.1	0.0073	(1)
6791.470	6791.466	51.5	19.2	0.0066	...
6800.680	6800.678	33.1	17.7	0.0050	...
Multiplet 16 ( $2s2p(^3P^o)3s\ ^4P^o - 2s2p(^3P^o)3p\ ^4P$ )					
5132.947,3.282	5133.114	14.9	39.5	0.0044	...
5143.494	5143.424	19.6	51.8	0.0095	(2)
5145.165	5145.165	12.3	14.8	0.0040	...
5151.085	5151.117	16.4	20.5	0.0046	...
Multiplet 17 ( $2p^3\ ^2P^o - 2s2p(^3P^o)3p\ ^2D$ )					
5032.128	5031.963	69.0	19.3	0.0434	...
5035.943	5035.808	75.7	21.7	0.0558	(3)
Multiplet 20 ( $2s2p(^3P^o)3p\ ^4D - 2s2p(^3P^o)3d\ ^4F^o$ )					
7113.040	7112.965	34.6	35.4	0.0052	...
7115.630	7115.642	30.8	21.1	0.0043	...
7119..760,.910	7120.052	41.5	42.1	0.0070	...
Multiplet 30 $2s2p(^3P^o)3d\ ^4F^o - 2s2p(^3P^o)4p\ ^4D$ )					
5259.055	5258.999	7.6	24.3	0.0031	...
5259.664,.758	5259.664	7.2	28.9	0.0032	...
(1)	Large FWHM, could be blend.				
(2)	In blend with [Fe III] $\lambda$ 5143.290?				
(3)	In blend with [Fe II] $\lambda$ 5035.484.				

Table 4.19 N II dielectronic lines.

Line(s) $\lambda$ (Å)	$\lambda_o$ (Å)	S/N	FWHM (km/s)	$I(\lambda)/I(H\beta)$ $I(H\beta)=100$	Notes
Multiplet 63 ( $3s\ ^5P - 3p\ ^5D^o$ )					
5526.234	5526.212	7.1	25.8	0.0015	(1)
5530.242	5530.215	10.8	19.2	0.0021	...
5535.347, 384	5535.359	16.9	26.4	0.0050	(2)
5543.471	5543.517	15.3	27.6	0.0045	...
5551.922	5551.930	7.5	12.0	0.0006	...
Multiplet 66 ( $3p\ ^5D^o - 3d\ ^5F$ )					
5172.973	5172.786	...	56.4	0.0049	(3)
5173.385	5173.564	...	30.7	0.0045	...
5175.889	5175.862	8.1	14.0	0.0018	...
5179.520	5179.521	18.4	18.6	0.0033	...
(1)	Perhaps S II $\lambda 5526.243$ ?				
(2)	Probably dominated by C II $4s\ ^2S - 5p\ ^2P^o$ but could include these two lines.				
(3)	Probably dominated by [Fe III] $\lambda 5172.640$ , may also include a contribution from N II $\lambda 5172.344$ line from the same multiplet, which according to LS coupling, should be as strong as $\lambda 5172.973$ or stronger.				

only a minimal contribution to each line's total recombination coefficient. Given the generally weaker strengths of lines which are powered exclusively by dielectronic recombination ( $C^{+2}$  quartets,  $N^{+2}$  quintets, and  $O^{+2}$  sextets), as compared to the other lines assumed well described by one-body recombination alone, we believe it would take a significant enhancement of dielectronic rates to seriously compromise calculations made upon that assumption.

Garnett & Dinerstein (2001a) have reported an overabundance of  $O^{+2}$  calculated from multiplet 15, with respect to other multiplets, in numerous PNe. This multiplet's upper level is primarily populated by dielectronic recombination, and the overabundance persists even when taking into account the low temperature dielec-

Table 4.20 O II dielectronic lines and abundances.

Line(s) $\lambda$ (Å)	$\lambda_o$ (Å)	S/N	FWHM (km/s)	$I(\lambda)/I(H\beta)$ $I(H\beta)=100$	Value ( $O^{+2}/H^+$ ) $\times 10^4$	Notes
Multiplet 15 ( $3s' \ ^2D - 3p' \ ^2F^o$ )						
4590.974	4590.959	73.2	16.5	0.0143	7.856	...
4595.957,6.176	4596.171	37.8	15.5	0.0095	6.906	...
Multiplet 16 ( $3s' \ ^2D - 3p' \ ^2D^o$ )						
4347.217,413	4347.990	9.3	26.0	0.0052	4.213	(1)
4351.260,457	4351.266	16.5	19.2	0.0080	4.331	...
Multiplet 36 ( $3p' \ ^2F^o - 3d' \ ^2G$ )						
4185.439	4185.433	22.9	16.2	0.0081	3.190	...
4189.581,788	4189.783	34.0	21.2	0.0124	3.664	...
Multiplet 94? ( $3s''' \ ^6S^o - 3p''' \ ^6P$ )						
4465.408	4465.404	32.4	14.8	0.0059	...	(2)
4467.924	4467.919	22.6	14.7	0.0041	...	(3)
4469.378	4469.375	12.1	13.5	0.0022	...	(4)
Multiplet 106? ( $3p''' \ ^6P^o - 3d''' \ ^6D^o$ )						
4143.522,733	4143.758	226.1	23.1	0.3140	...	(5)
4145.906,6.076	4146.047	17.3	19.9	0.0059	...	(6)

- (1) Large wavelength difference between observed and tabulated values but abundance fits well with other member of multiplet.
- (2) Most likely N II  $3p \ ^3D - 3d \ ^3P^o$   $\lambda 4465.529$ .
- (3) Alternate ID is Fe II  $\lambda 4467.931$ .
- (4) More likely O II  $3d \ ^2P - 4f.D \ 2[1]^o$   $\lambda 4469.462$ , but sextet line is positioned well and is at about the right intensity.
- (5) This is He I  $\lambda 4143.759$ , but the sextet line could be blended with it.
- (6) Alternate ID is Ne II  $4s \ ^2P - 5p \ ^2S^o$   $\lambda 4146.064$ . Given the apparent lack of lower order Ne II lines, it seems unlikely that a higher order line is present, so the sextet line could be a good choice.

tronic recombination rates of Nussbaumer & Storey (1984). Dinerstein & Garnett (2001b) proposed “enhanced” dielectronic recombination, perhaps on the interface of a significantly hotter central “bubble” of the nebula and the nebular shell itself, to be potentially responsible. The authors show that a correlation exists between nebular surface brightness (a proxy for age), and the amount of the discrepancy between recombination and collisionally excited line  $O^{+2}$  abundances. Smaller, younger, and higher surface brightness PNe exhibit less of a discrepancy than older, dimmer, and larger PNe. This represents the bubble, expanding with time, carved out the center of the PNe by a strong central star wind.

High temperature dielectronic recombination is an attractive alternative excitation mechanism. At higher temperatures, higher energy autoionizing states are accessible by recombining electrons. These add more contributions to the total recombination rate to a particular ion than are included in the low temperature case. Furthermore, Storey (1981) has shown that these higher energy states are more likely than low lying autoionization state to decay via stabilizing transitions rather than autoionizing. Other ions in the vicinity of the interface could also be affected.  $Ne^{+2}$ , with the highest ionization potential of any recombination line for which abundances were measured, would possibly be the most susceptible to this mechanism. The inclusion of its possible effects would probably reduce its factor of six abundance discrepancy.

IC 418, with an estimated age of perhaps less than a thousand years (Phillips, Riera, & Mampaso 1990), high surface brightness, ( $2.3 \times 10^{-12}$  in units of absolute  $H\beta$  flux per square arcsec as determined by Acker et al. 1992), and low abundance discrepancy in  $O^{+2}$ , would seem to fit this paradigm well (i.e. have a smaller bub-

ble size). Yet, our calculations of  $O^{+2}/H^{+}$  from multiplet 15, using the coefficients of Nussbaumer & Storey (1984) (see Table 4.20), reveals a significant departure from the abundances determined from other multiplets under opacity case C. Our long duration observations revealed two additional multiplets (16 and 36) that are also primarily populated by dielectronic recombination (Nussbaumer & Storey 1984), yielding similar but smaller overabundances. This would seem to conflict with the Garnet & Dinerstein notion of younger PNe not having a significantly large “bubble” for this enhancement to be seen over a large portion of the nebula, or specifically at the large distance from the central star we observed at.

Prior to adjustment to case C, the other  $O^{+2}$  multiplet abundances showed much *greater* scatter and were *higher* overall. We note also that the calculations of Nussbaumer & Storey (1984) assume optically thin conditions for all lines. Could a similar adjustment to case C reconcile the abundances from multiplets 15, 16, and 36? An examination of the Grotrian diagrams of  $O^{+2}$  from Bashkin & Stoner (1976) shows that none of the suspect multiplets originates from a level that has an obvious resonance transition to the doublet sequence’s  $2p^3\ ^2D^o$  “ground state”, although two of the multiplets are one step removed down a cascade path from an upper level that does. However, no members of the multiplet that would connect the  $4d\ ^2F$  level with the upper level of multiplet 15 ( $3p'\ ^2F^o$ ) are visible in our spectra. Unfortunately, for the other multiplets, similar connecting transitions listed in Bashkin & Stoner (1976) are not accessible in our bandpass. Given that multiplets 15 and 36 follow the same cascade path, that the upper level of 36 is inaccessible to the “ground state” either directly or via a direct cascade from another level, and that these levels are of high



orbital angular momentum, it is likely that these multiplets' strengths are immune to changes in opacity case.

For enhanced dielectronic recombination to work, significantly higher temperatures would be needed; on the order of 35,000-65,000 K estimated to reconcile the abundances discrepancy of NGC 6720 (Garnett & Dinerstein 2001b). At such temperatures it might be expected that the thermal widths of lines from these multiplets would be much broader. No distinct evidence of broadening is seen of this in our line profiles, but this is not conclusive. The thermal width of an O II line is only 5 km sec<sup>-1</sup> at 10000 K ; a five fold increase in temperature would only increase this width by a factor of 2.2, just over our instrumental resolution. Furthermore, Dinerstein & Garnett (2001b) are unable to adjust physical parameters to retain other observed properties, such as the strengths of [O III] lines, under these scenarios. Finally, the strengths of the sextet lines, weaker by an order of magnitude than most other O II recombination lines, suggest that dielectronic recombination is probably not going on at enhanced rate, perhaps not enough to explain the over-large strengths of multiplets 15, 16, and 36.

We wonder instead if the dielectronic recombination coefficients for these multiplets are erroneous. Garnett & Dinerstein (2001a) data shows that multiplet 15 yields a consistently higher O II abundance with respect to other O II lines. Multiplet 36, in the same cascade path of multiplet 15, also yields a higher abundance. It would make sense that transitions along this same cascade path could all be miscalculated.

Finally, any enhanced processes should go on in a narrow zone (e.g. the interface region between the bubble and the shell). Since ions are concentrated at different

locations, it seems unlikely that enhanced dielectronic recombination can explain *all* their abundance discrepancies, as well as  $O^{+2}$ .

### 4.3.3 Temperature Fluctuations

Temperatures as determined from collisionally excited lines may be overestimates, because collisional excitation is the strongest at the highest temperature portions the region occupied by a particular ion. Overestimates in temperature lead to underestimates in ionic abundances. Such fluctuations in temperature arise from naturally occurring density variations within those regions, subtly affecting temperature diagnostic line intensities differently (Kingdon & Ferland 1995b).

To gauge the level of deviation in temperature from the diagnostic line derived value in the region occupied by a particular ion, Peimbert (1967) defines a temperature fluctuation parameter,  $t^2$ , the rms scatter about an average or “ion weighted” temperature,  $T_o$ :

$$T_o(X) \equiv \frac{\int T_e N_e N(X) d\Omega d\ell}{\int N_e N(X) d\Omega d\ell}, \quad (4.5)$$

and

$$t^2(X) \equiv \frac{\int [T_e - T_o(X)]^2 N(X) N_e d\Omega d\ell}{T_o^2(X) \int N_e N(X) d\Omega d\ell}, \quad (4.6)$$

where  $\Omega$  is the solid angle observed and the integration is along the line of sight through the nebula, and  $N(X)$  and  $N_e$  are the population of a particular ion “X” in the source level of a particular emission line and the local electron density respectively. Each ion observed will have its own  $t^2(X)$  and  $T_o(X)$  (Kingdon & Ferland 1995b).

In the low density limit, a collisional line’s emissivity can be expressed as a single

collisional term. If the fluctuations are small, the emissivities may be expanded about the ion-weighted temperature  $T_o(X)$ . Two such expansions may be taken in ratio, to yield a relation between the temperature  $T_e(X)$  measured from the diagnostic line ratios,  $T_o(X)$ , and  $t^2(X)$  (Peimbert 1967):

$$T_e(X) \approx T_o(X) \left[ 1 + \left( \frac{\Delta E}{T_o(X)} - 3 \right) \frac{t^2(X)}{2} \right], \quad (4.7)$$

where  $\Delta E$  is the sum of energies of the upper levels from which the two lines arise. This relation may be calculated for any pair of lines of the same ion, provided they don't arise from the same level (i.e. from the same fine structure state in a multiplet) and that satisfy  $\Delta E \ll KT_e$ . Unfortunately, this rules out an analysis of  $\text{Ne}^{+2}$  for which only  $\lambda\lambda 3869, 3969$  (from the same level) are available. We used  $[\text{O II}] \lambda\lambda 7319, 7330$  ( $\Delta E = 116448 \text{ K}^{-1}$ ) from the  $\text{O}^+ 2p^3 \ ^2P^\circ$  level, to remain as close as possible to the low density limit, since ample evidence suggests that the critical density is reached for the lower energy  $\text{O}^+ 2p^3 \ ^2D^\circ$  level. At the critical density, the emissivities for the lines ( $\lambda\lambda 3726, 3729$  for  $\text{O}^+$ ) no longer consist of only a single collisional term; collisional de-excitation must also be taken into account, and the emissivity can no longer be simply expanded. The  $\lambda\lambda 7319, 7330$  lines originate from levels with higher critical densities. Nevertheless, no correction is made for collisional excitation from the  $2p^3 \ ^2D^\circ$  level itself (i.e. the emissivities of the  $\lambda\lambda 7319, 7330$  lines may also not consist of a single collisional term), so the results here must be treated with some caution. A more thorough numerical treatment of this problem (Rubin et al. 2001), would be more appropriate for dealing with  $\text{O}^+$ . For  $\text{O}^{+2}$  we used the  $[\text{O III}] \lambda\lambda 4363, 5007$  lines ( $\Delta E = 91303 \text{ K}^{-1}$ ), which are from levels of higher critical

density than any density calculated from forbidden line diagnostics in this study.

To observationally determine the parameters  $T_o(X)$  and  $t^2(X)$ , a second independent temperature indicator, expandable in terms of its own  $T_o$  and  $t^2$ , must be employed. We used the Balmer jump temperature,  $T_e(H^+)$ , with temperature parameter inter-dependence (Liu et al. 2000):

$$T_e(H^+) = T_o(H^+)[1 - 1.67t^2(H^+)]. \quad (4.8)$$

For IC 418 we assumed that  $T_o(H^+) \approx T_o(X)$  and  $t^2(H^+) \approx t^2(X)$ , which holds fairly well for  $O^{+2}$ , according to the models of Garnett (1992) and Kingdon & Ferland (1995b), at the IC 418 central star temperature,  $\log T_{eff} \approx 4.6$ , and hydrogen column density,  $\log N(H) \approx 4.5$  (HAF). Kingdon & Ferland (1995b) have also shown that the departures of the observationally determined  $t^2$  and the value determined directly from its definition (eq. 4.6) via direct integration of the radiation field of model spectra, should be minimal for the physical conditions exhibited by IC 418. The validity of the above assumptions for the case of  $O^+$  is not discussed in the literature. However, it seems reasonable since these assumptions are often made for  $N^+$ , an ion which should reside in a similar portion of the nebula as  $O^+$  does.

The resulting system of equations (eqs. 4.7 and 4.8) can be solved for  $T_o(X)$  and  $t^2(X)$ , which are in turn used to recalculate  $T_e(X)$  and  $T_e(H^+)$  from Taylor expansions around  $T_o$  of the individual diagnostic line and  $H\beta$  line emissivities. Finally, ionic abundances are recalculated employing the new electron temperatures. The resultant parameters and abundances are listed in Table 4.21, where we have employed both the listed Balmer jump temperatures from Table 4.2 and the higher value

Table 4.21 Temperature fluctuation  $t^2$  and  $T_o$  values and corrected abundances,  $N^{+i}/H^+$ , using different Balmer jump temperatures  $T_e(H^+)$  and Model value of  $t^2 = 0.005$ .

Ion	Lines $\lambda$ (Å)	$T_e(H^+)$ (K)	$T_o$ (K)	$t^2$	Value ( $N^{+i}/H^+$ ) ( $\times 10^{-4}$ )	
					(1)	(2)
$O^+$	[O II] $\lambda\lambda 7319, 7330$	5300	6106	0.079	8.995	
		6600	7294	0.057	4.140	3.491
		Model	9781	0.005	1.770	
$O^{+2}$	[O III] $\lambda\lambda 4363, 5007$	5300	6299	0.095	3.289	
		6600	7188	0.049	2.377	1.486
		Model	8737	0.005	1.288	
(1)	Corrected abundance from collisionally excited lines.					
(2)	Recombination line abundance.					

using a continuum fit more immediately redward of the discontinuity (5300 K and 6600 K respectively).

It is immediately apparent that the level of fluctuations are much too strong for the level of abundance disagreement exhibited by the ions. Observationally determined values of  $t^2$  (from a variety of ions, but usually  $O^{+2}$ ) range from PNe 0.00 to 0.09 (Esteban et al. 1999), with typical value of  $t^2=0.03-0.04$  (Liu & Danziger 1993, Garnett & Dinerstein 2001b). It is difficult to reconcile any of these  $t^2$  values with model predicted  $t^2$  values for the IC 418 physical parameters, such as  $t^2=0.006$  from Garnett (1992) or  $t^2=0.005$  from Kingdon & Ferland (1995b) for  $O^{+2}$ . Model predictions are generally much lower than observed values, due to the real difficulty in inducing large scale fluctuations within the small region in which a particular ion is confined, without invoking an external excitation mechanism, other than natural occurring density variations.

Large values of temperature fluctuations might cause the temperature sensitive auroral line [O III] ( $O^{+2}$ )  $\lambda 4363$  to yield a very different abundance from other individual [O III] lines. Yet, the other [O III] lines don't show extremely different abundance from [O III]  $\lambda 4363$ . did not show an excessive amount of abundance scatter. Marginally tighter abundance agreement is exhibited when  $t^2=0.005$  is adopted for  $O^{+2}$ , but the same is not true for  $O^+$ . The large  $t^2$  for  $O^+$  may be due to ignoring the collisional contribution from the critically dense  $2p^3\ ^2D^\circ$  level.

Since we see better agreement in abundances when using smaller  $t^2$  values than the ones calculated observationally, the uncertainty in our Balmer jump temperature and diagnostic line temperature determinations are the most likely reason for the large  $t^2$  values. Kingdon & Ferland (1995b) provide an order of magnitude estimate of the error in the  $t^2$  value:

$$\sigma(t^2) \approx \frac{1}{2} \frac{\sigma(T_o)}{T_o}. \quad (4.9)$$

In the system of eqs. 4.7 and 4.8, for  $O^+$ , the dominant source of error is the 40% uncertainty in  $T_e(O^+)$  value (see Table 4.2). Using 40% for  $\sigma(T_o)$  and  $T_o(O^{+2})=T_e(O^+)$  results in  $\sigma(t^2)(O^+) \approx 0.20$ . The tabulated error for  $T_e(O^+)$  is most likely overestimated, given the agreement with other temperature diagnostics of similar ionization potential, and external agreement of this temperature with that calculated from the same ion in other studies of IC 418. However, even a more likely figure of 5-10% can still significantly affect the value of  $\sigma(t^2)(O^+)$ . Similarly, for  $O^{+2}$  the largest uncertainty is in the Balmer jump temperature. The difference between the “high” and “low” Balmer jump temperatures yields an error of about 25% and  $\sigma(t^2)(O^{+2}) \approx$

0.125. Even the uncertainties in the fits to the continua (about 600 K ), used in Balmer jump temperature derivations, significantly affect the recalculated temperatures and abundances. Given the extraordinary accuracy needed to pin down  $t^2$ , moderate *real* temperature fluctuations arising from mundane sources, can easily go undetected.

Diagnostic line temperatures of 8600 K for  $O^+$  and 8430 K for  $O^{+2}$  are necessary to bring the collisional abundance into agreement with the recombination values. Using these values as their respective ion's  $T_o$  we obtain  $t^2(O^+)=0.031$  and  $t^2(O^{+2})=0.014$ , which are in line with commonly observed values of  $t^2$  (Liu & Danziger 1993, Garnett & Dinerstein 2001b), and are larger but more comparable to the model values than the values we determine observationally. Liu & Danziger (1993) suggested that all values of  $t^2 \geq 0.04$  require a non-conventional excitation source. One such mechanism is shocks induced by a radiation driven, “fast” wind from the central star, impinging on the slower wind generated during the PN pre-cursor’s asymptotic giant branch phase (Peimbert, Sarmiento, & Fierro 1991). The wind deposits significant kinetic energy into the gas. IC 418 has been shown to have a strong central star wind; a terminal velocity  $940 \text{ km sec}^{-1}$  was determined from P Cygni profiles in central star emission lines (Cerruti-Sola & Perinotto 1989). The calculated amount of power carried by the wind in IC 418 is low among PNe studied by Capriotti (1998), but the fraction of momentum absorbed to the momentum carried by the wind is in the middle of the range. So it is conceivable that shocks could play a role in creating temperature fluctuations.

Signatures of shocks (Frank 1994) include line broadening, or a sharp temperature discontinuity at the boundary between the central hot bubble carved out by the fast

wind, and the dense shell created during the “slower” wind phase. Such signatures are not obvious in our line profiles or temperature diagnostics. Since we obtain more realistic abundances as well as better agreement between collisionally excited line and recombination line abundances when the model  $t^2$  values are adopted, we attribute our larger calculated  $t^2$  values primarily to Balmer jump temperature determination uncertainties, or uncertainties in our diagnostic line temperatures.



# Chapter 5

## Conclusions

We have presented here emission line spectra of the planetary nebula IC 418. The spectra are the richest ever acquired for this PN, and among the most detailed of any PNe spectra. Roughly 600 lines in the spectra with credible identifications are revealed. Emission lines from a wide variety of ions are observed in these spectra, produced through both recombination-cascade and collisional excitation. We have compared the ionic abundances calculated from lines of both production mechanisms, in an effort to better understand the nature of discrepancies seen in such comparisons in other PNe spectra (Liu et al. 1995a,2000). Finally, we tested leading candidate explanations of these discrepancies, taking direct advantage of the assets of our observations: numerous lines and well-defined line profiles.

The steps used in the reduction and analysis of the spectra have been discussed, with particular attention paid to automated processes, which reduce the time investment and provide increased accuracy.

## Abundance Discrepancies

It has been shown repeatedly elsewhere that recombination line derived abundances always exceed those determined from collisionally excited lines of the same ion. Our results allows us to make several comments on this issue:

**1) Our data shows enhanced recombination line abundances, but at a different level and nature than is exhibited in other PNe.**

For  $O^+$ ,  $O^{+2}$ ,  $Ne^{+2}$  we measured collisionally excited and recombination lines. For these ions the recombination line abundance excess depended upon the ion. The magnitude of this discrepancy ranges from a factor 1.2 for  $O^{+2}$ , to 2.1 for  $O^+$ , and 5.8 for  $Ne^{+2}$ . The  $O^+$  excess has seldom been measured. The  $N^+$  recombination lines were too seriously contaminated by continuum fluorescence to use.

Our  $O^{+2}$  and  $Ne^{+2}$  overabundances differ from the trend seen by Liu et al. (1995a) in NGC 7009 and Liu et al. (2000) in NGC 6153, where the recombination line ionic abundances showed remarkably similar enhancements over their collisional counterparts. The NGC 7009 analysis indicates about a factor of five abundance discrepancy for  $C^{+2}$ ,  $N^{+2}$ , and  $O^{+2}$ , while for NGC 6153 including  $Ne^{+2}$  a constant factor of ten enhancement was found. The  $C^{+2}$  collisional abundance from HAF or HKB in IC 418, derived from  $C\ III\ \lambda\lambda 1907, 1909$ , yielded a recombination line overabundance ranging from 2-5. The overabundance factors among all these ions has no distinct trend in ionization potential. This argues for an ion-specific process acting to enhance recombination line strengths, rather than a universal process affecting all the ions similarly argued for Liu et al. (2000). It should be noted that NGC 6153 and

NGC 7009 are higher ionization PNe, so the scatter in overabundance factors might be typical of lower ionization, younger PNe.

## 2) Abundance discrepancies appear to be real.

For  $O^+$  and  $O^{+2}$ , the collisional abundances do overlap the recombination abundances, within their mutual uncertainties:

$$\begin{aligned}\text{Collisional: } O^+/H^+ &= 1.663(+19.687, -1.308) \times 10^{-4}, \\ O^{+2}/H^+ &= 1.201(+0.188, -0.142) \times 10^{-4},\end{aligned}$$

$$\begin{aligned}\text{Recombination: } O^+/H^+ &= 3.489(\pm 0.103) \times 10^{-4}, \\ O^{+2}/H^+ &= 1.487(\pm 0.338) \times 10^{-4}.\end{aligned}$$

The errors in the recombination line abundances reflect  $1\sigma$  errors about the average of the summed multiplets used to calculate the final abundances. The errors in the collisional abundances reflect the line intensity measurement and reddening uncertainties.

However we believe that the collisional abundance uncertainty for  $O^+$  is greatly overestimated, despite our best efforts at providing as realistic an uncertainty estimate as possible (see § 4.2.1). Apart from this we note the collisional abundances from individual  $O^+$  forbidden lines agree better than the formal uncertainty estimate (see Table 4.3). The abundances from individual recombination lines within multiplets also show good agreement.

For  $O^{+2}$ , we note the large scatter in the recombination lines is mainly due to the inclusion of three particular multiplets in the total ionic recombination value. In seven of the ten multiplets included in the recombination average, the summed

abundance exceeds the collisionally excited value. If the contributions to the average are weighted by the total observed multiplet intensity, the resultant abundance is  $O^{+2}/H^{+}=1.574\times 10^{-4}$  which suggests that much of that lower abundances generally come from weaker, less accurately measured lines.

In the case of  $Ne^{+2}$ :

$$\text{Collisional: } Ne^{+2}/H^{+} = 4.344(+0.761, -0.616) \times 10^{-6},$$

$$\text{Recombination: } Ne^{+2}/H^{+} = 2.536(\pm 0.367) \times 10^{-5},$$

the collisional and recombination abundances do not overlap, differing by more than generous uncertainty estimates.

Independent measurements of the collisional line abundances in IC 418 (HAF,HKB) also show smaller ionic abundances for these ions than the recombination values calculated here. Therefore, while the uncertainty estimates we have made would allow the abundances for  $O^{+}$  and  $O^{+2}$  to overlap, we conclude there is ample corroborating evidence for the abundance discrepancies in these ions and  $Ne^{+2}$  to be real.

**3) The choice of coupling scheme and opacity conditions is shown to be important for individual emission line abundances, but its importance in some ions is masked by non-recombination excitation processes.**

Abundances from individual O II recombination lines showed less scatter than their counterparts in C II and N II. This suggests the advantages of non-LS coupling, as we used for O II.

Our evidence suggests that opacity case C (in which transitions terminating on the  $O^+ 2p^3 {}^2D^o$  level are optically thick) best describes IC 418. This choice has a physical basis. Densities from multiple diagnostic ratios indicate that IC 418 has an aggregate density exceeding the critical densities of the  $O^+ 2p^3 {}^2D^o$  fine structure states, leading to significant populations in those states, and consequent strong self-absorption of photons from transitions ending on those states. This is the definition of case C. Finally, the idea that  $O^+$  may be in case C in IC 418 has precedent in Harrington et al. (1980).

The union of intermediate coupling and case C serves to bring  $O^{+2}$  abundances derived from the doublets and quartets into much closer agreement with one another than is achieved under either case A (all lines optically thin) or case B (same as case C except with  $O^+ 2p^3 {}^4S^o$ ). This was especially true for certain doublets.

The pattern of recombination line abundance scatter among the multiplets of  $O^o$ ,  $N^o$ ,  $C^+$ , and  $N^+$  is generally in line with ground state enhancement mechanisms predicted by Grandi (1975a,1976) for those ions, particularly continuum fluorescence. These abundances were calculated employing effective recombination coefficients calculated under pure LS coupling. But the potential advantages of using a better coupling scheme may have been cloaked by the ground state enhancement effects. It is *not clear* what the overall agreement would be in their absence.

### **Sources for Abundance Discrepancies:**

Numerous solutions have been proposed to solve the abundance discrepancy problem.

We have tested some of the most applicable to our data.

**1) Continuum fluorescence from the ground state is evidenced in many ions.**

Grandi (1975a,1976) has demonstrated that several ions are susceptible to excitation via continuum fluorescence from the ground state. Our observations confirm that many of the recombination lines in C II, N I, N II, and O I, predicted to be enhanced by continuum fluorescence, indeed evidence an enhancement. These lines are generally super-luminous as compared to other recombination lines considered “immune” to ground fluorescent contributions, because they arise from multiplets of higher energy and angular momentum more different from the ground state. The pattern of their enhancement also fits a picture of the strongest lines emanating from multiplets fed directly by a resonance transition, with weaker, but still enhanced, strengths for lines within multiplets further down the cascade chain.

Profiles for lines enhanced by continuum fluorescence generally fall into two categories. The first category includes lines in which continuum fluorescence is the dominant excitation mechanism, such as O I  $\lambda 8446$ . This category also includes lines for which the calculated abundances are extremely unrealistic, ten to a hundred times greater than the general  $N^{+i}/H^{+} \approx 10^{-4}$  exhibited by collisionally excited lines or recombination lines from other ions, including many lines of N I. The profiles in this category clearly resemble the profiles of the collisionally excited lines of the *recombined* atom, as opposed to the ion of the next higher stage of ionization.

The second category includes lines which show less enhancement (a factor of 2-10) above the strength of lines from fluorescent “immune” multiplets. This category includes numerous C II and N II recombination lines we observed. Yet, their line

profiles are *indistinguishable* from other recombination lines of the same ion, or from the collisionally excited line of the next higher ionization state, and do not conform to collisionally excited lines of the recombined ion.

It is not intuitively obvious why lines with lower but still substantially enhanced strengths do not more closely resemble the profiles of lines from the recombined atom. This may indicate that for these C II and N II lines, the bulk of the continuum fluorescence comes from gas closer to the region where the recombination is occurring, whereas for lines of lower ionization parentage, the regions of recombination and continuum fluorescence are more separated. There is no obvious progression in profile size or morphology with enhancement, though subtle details might have been missed even at our high resolution.

Another probable manifestation of continuum fluorescence is the probable enhancement of the [N I]  $\lambda\lambda 5198, 5200$  density diagnostic lines. As mentioned in § 4.1.1, the intensity ratio is near the high density limit. Bautista (1999) has shown that continuum fluorescence is capable of pushing their diagnostic intensity ratio beyond the high density limit. Because of the strong enhancement exhibited by N I recombination lines, we believe it likely that the diagnostic ratio is affected. None of the ions showing discrepancies were calculated with this density, although the C<sup>o</sup>, N<sup>o</sup>, and O<sup>o</sup> abundances may have been slightly affected.

**2) Dielectronic recombination is occurring in IC 418. But there is no evidence for “enhanced” dielectronic recombination affecting standard recombination line-derived abundances.**

Garnett & Dinerstein (2001a) have suggested that smaller, younger PNe should

show less of an abundance discrepancy in  $O^{+2}$  than older, larger PNe. They attributed  $O^{+2}$  abundance discrepancies to an enhancement in dielectronic recombination brought on by shocks created at the boundary of a hot bubble and the denser nebular gas shell. For younger PNe, this bubble has not yet had time to propagate very far through the nebula, leading to less enhancement. As evidence of this mechanism, these authors point to enhanced abundances from multiplet 15, which is primarily populated by dielectronic recombination (Nussbaumer & Storey 1984).

IC 418 is a fairly young and small PNe, and does exhibit a low abundance discrepancy in  $O^{+2}$ . However, abundances determined from multiplets 15, 16, and 36, all of which are populated primarily by dielectronic recombination, greatly exceed the average  $O^{+2}$  abundance from the other recombination lines. This is unexpected, since according to the Garnett & Dinerstein (2001a), younger PNe shouldn't show much of an enhancement in dielectronic recombination, because the "bubble" hasn't had sufficient time to propagate through the nebula. It seems unlikely that our observations, at a significant distance away from the central star, would intercept the region of enhancement.

We lack compelling physical evidence for such a process within our data: there is no obvious line broadening or temperature discontinuities among our diagnostics. The observed strengths of lines which must exclusively be created by dielectronic recombination (C II quartets, N II quintet, O II sextets), indicates that dielectronic recombination is probably not going on at a rate which would substantially affect abundances from recombination lines, or explain the over-large strengths of multiplets 15, 16, and 36 of O II. Finally, enhanced dielectronic recombination should



occur in only a small area, so this mechanism cannot be used to explain abundance discrepancies in other ions. A plausible explanation of the abundance discrepancies in multiplets 15, 16, and 36 of O II, is that the published dielectronic recombination coefficients are erroneous.

Without enhanced dielectronic recombination, the generally weak dielectronic recombination rates with respect to one body recombination rates, suggest that dielectronic process are probably not responsible for the levels of discrepancy that do exist in our data.

### **3) Temperature fluctuation determinations are inconclusive.**

We calculated the  $t^2$  parameter of Peimbert (1967) to gauge the effects of temperature fluctuations within the zones of the nebula occupied by  $O^+$  and  $O^{+2}$ . We obtain  $t^2$  which would yield significant overabundances from collisionally excited lines with respect to recombination lines when they are used to recalculate abundances. The  $t^2$  value for  $O^{+2}$  in particular conflicts with the much lower model values of Garnett (1992) and Kingdon & Ferland (1995b) for the IC 418 physical parameters. This low model values reflect the real difficulty in establishing large  $t^2$  over the limited regions in which any particular ion resides in the nebula, assuming that the cause of such fluctuations are restricted to moderate natural variations in density that are present throughout that region. However, the application of the model determined  $t^2$  values is insufficient to reconcile abundances (see Table 4.21).

The calculated  $t^2$  value for  $O^{+2}$  also greatly exceeds the observed average  $O^{+2}$   $t^2$  value of 0.03–0.04 among PNe (Liu & Danziger 1993), and the  $O^+$   $t^2$  value is higher still. To reconcile abundances, values of  $t^2(O^+)$  and  $t^2(O^{+2})$  smaller than

what we observed, larger than the model values, but closer to the composite PNe observed “average”, are needed. However, these values necessitate the existence of external excitation mechanisms (e.g. shocks), not included in models of smooth gas with only small density variations (Kingdon & Ferland 1995b), and for which there is no evidence in our data (line broadening, temperature discontinuities).

We note that the  $t^2$  values for both ions decline significantly when a higher Balmer jump temperature is utilized, but insufficiently to remove the overabundances in  $O^+$  and  $O^{+2}$  (see Table 4.21). We believe that a poorly determined Balmer jump temperature is mostly to blame for the high  $t^2$  value for both ions  $O^+$  and  $O^{+2}$ . As seen in eq. 4.9 a small error in Balmer jump temperature can lead to a large error in  $t^2$ . The jump temperature is used by both ions in their  $t^2$  calculations. The calculation in the jump temperature was complicated by many factors (see § 4.1.2) which lead us to believe it is extremely untrustworthy.

While our observed levels of  $t^2$  are not entirely dismissable (values as large have been observed in other PNe), without a good determination of the jump temperature, we cannot say whether fluctuations at the level we observe, or at level necessary to reconcile recombination and collisional abundances, actually exist in IC 418. We can only say that model  $t^2$  values are insufficient for this purpose.

### **Automated Processes for Spectral Reduction/Line Identification**

We have demonstrated the utility of various automated software packages, designed specifically for the reduction and analysis of emission-line region spectra. Among these, are our new routines for fitting Gaussians to line profiles, and code designed to

aid in the identification of emission lines. Some work remains in perfecting the fitting routine, specifically in the areas of error estimates and multiple Gaussian fitting.

EMILI, the code designed to aid in emission line identifications, was an essential tool for this analysis. Manual identification of 805 lines would have been tortuous and error prone. The use of EMILI allowed non-conventional lines, such as the sextets of O II, to be considered as possible IDs, on an equal footing with other lines. Numerous improvements are envisioned for the code in subsequent versions, based partly on the experience of using it on this data set. However, we believe that even as it stands now, EMILI is a useful tool, and we have decided to make it available in the public domain in its present form.

## **Future Work**

Unanswered questions remain. For example, why does IC 418 have a distinct C IV absorption line (Williams et al. 2003) yet barely detectable C III recombination lines? And, why does the  $\text{Ne}^{+2}$  abundance show the greatest discrepancy among all the ions selected. As always, follow-up work is essential.

Some of the future work would include additional observations in the UV, IR, and optical. Many nebular ions have important transitions in the UV such as collisionally excited lines C III]  $\lambda\lambda 1907, 1909$  and N III]  $\lambda\lambda 1747, 1754$ . The latter has not yet been observed in IC 418 and is an important comparison for the N II recombination lines. In the IR, fine structure lines of [O III] are temperature insensitive, and serve as a check of the effects of temperature and density fluctuations. It does not appear that an IR IC 418 spectrum has been obtained recently. Additional deep observations

in the optical, concentrating on an approximate range of  $\approx 3300\text{-}7500\text{\AA}$ , would add strong Ne II recombination lines as well as covering the rich C II, N II, O II spectra in this bandwidth. A large departure in our  $\text{O}^{+2}$  abundance from HAF can be directly attributed to our far stronger [O III]  $\lambda\lambda 4959, 5007$  lines. We observed  $I_{\lambda 4959} = 72.7233$  and  $I_{\lambda 5007} = 214.9530$ , where  $I(\text{H}\beta=100)$ , and they measured  $I_{\lambda 4959} = 29.52$  and  $I_{\lambda 5007} = 85.87$ . It would be interesting to see if our particular choice of position for this study “hit the jackpot” with [O III] emission. Abundance gradients in IC 418 would be sought through multiple spectra at different locations in all bandwidths. Finally, the construction of a model nebula (determined with the CLOUDY ionization code) could address questions regarding the extent of continuum fluorescence contributions on many ions, and refine our list of trustworthy transitions for abundance determination.

In summary, we have created one of the most extensive lists of emission lines in a PNe ever compiled. Using this information, our observations of IC 418 have shown that an abundance discrepancy exists in this object, as in other PNe, with some differences exist in its nature. The most prominent difference is that no common factor for  $\text{O}^+$ ,  $\text{O}^{+2}$ , and  $\text{Ne}^{+2}$  describes each ion’s recombination line overabundance with respect to collisionally excited line derived value. Recent surveys of NGC 7009 and NGC 6153 (Liu et al. 1995a, 2000), both higher ionization objects, have observed such a factor among the doubly ionized ions. After the examination of various possible mechanisms for explaining the discrepancy, we find that no single mechanism appears satisfactory as a sole explanation, at least within the limits of our data. Finally, we have determined numerous lines which yield untrustworthy abundances, and which should perhaps be avoided in abundance determinations of this and other PNe.

## APPENDICES

# Appendix A

## Mechanics of Data Reduction Steps

The majority of the data reduction steps detailed here utilized various tasks of the data reduction package IRAF.

### A.1 Bias Correction and Image Trimming

The initial step in image processing is the removal of the pedestal voltage or bias that is applied to the CCD before exposure, to guarantee a correct reading by the chip's analog to digital converter. A so-called "overscan" region adjacent to the portion of the CCD used for imaging records this bias level for individual frames. This bias level must be removed to insure a linear ratio between the counts in each pixel and the number of photons recorded in that pixel. The columns in each line of the overscan region are averaged, then the variation from line to line, if any, is fit with a low order polynomial, in the case of these observations the with a constant slope. The need for a non-linear fit would indicate a serious problem with the particular image. This

function is then subtracted column by column from the actual imaging portion of the CCD. The overscan region is then removed or “trimmed” from the image section.

Any residual bias level remaining after subtraction is in turn subtracted out through the use of a bias frame. This bias frame is constructed by taking several 0 second exposures of the CCD which record only the bias level across the chip. Each of these frames is inspected for large scale defects, such as a slope across the chip or a concentration of unusually high pixel values, which greatly exceed the average for the entire image. The frames are then co-added using the median of each pixel value. The combined bias frame is corrected for its own bias level in the same manner as object frames. The overscan region is then trimmed from the image section, and the remaining image subtracted from the object frames.

In the blue set-up, two amplifiers with different gains were used, in order to speed up the read out times. Each amplifier had its own overscan regions, and the regions of the CCD covered by each amplifier were calibrated separately employing tasks customized for IRAF by CTIO staff in the *ared* package.

## A.2 Flat Fielding

The response of individual pixels in a CCD to illumination is non-uniform. In addition, the echelle spectrograph has a response function which varies systematically over the whole CCD (due to vignetting in the optics) and along each echelle order (the echelle blaze function). To account for these factors object frames must be “flat fielded”. Two different methods were used to construct the flat field, depending upon

the instrumental set-up.

Within the blue and intermediate instrumental set-ups, a bright quartz lamp uniformly illuminates the slit, and several brief exposures are taken with the decker completely open. The images, after the bias removal steps, are inspected for defects and co-added, with a common region within each image chosen from which to calculate the relative scaling. We scaled by the mode of the pixel values in the common region for each image, then coadded all the images using the median at each pixel, across the entire image. This takes into account the time intensity variation of the quartz lamp (i.e. the lamp “warms up”). The combined image is then fitted with a high order polynomial in both directions. To prevent functional “ringing” in these fits as the result of bad columns on the CCD, these columns are “patched” with a similarly sized copy of the image from the immediately adjacent region. The order of the fit was adjusted until functional ringing was minimized. The resulting fitted image is then operated on by a wide-windowed boxcar median smoother along each line of the image to provide a smoothed version of the image which records only the overall instrumental intensity signature. The smoothed version is then divided into the fitted version, to create a final flat field, normalized to unity. This flat field records individual pixel to pixel variation of intensity response that can be divided in turn into each object frame after bias correction and trimming.

In the red instrumental set-up, the flat field frames were taken in a similar manner, but with a decker, larger than the that used in obtaining the object spectra, but not large enough to cause overlapping of the orders in the bluest portion of the spectra. This resulted in an object-like 2-D spectrum of the bright quartz lamp used



to illuminate the slit. The flat field images were then co-added with median filtering, employing the mode from a section of one of the central orders for scaling. The portions of the CCD containing the individual orders were isolated from the inter-order region. The total intensity was summed along the total length of the slit at each column along the path or “trace” followed by the order across the CCD, to yield a 1-D spectrum of the flat field. Data within the order at a particular column on the 2-D spectrum were divided by the value of the 1-D spectrum at that same column in order to normalize them. Then a series of low order polynomial fits was made to smooth the data in swaths parallel to the center of the trace across the length of the slit. Thus both the intensity profile within the slit and the individual pixel variations can be accounted for, and the smoothed flat field could be divided into all other spectra.

The departure in the flat field creation method from the method followed for the blue and intermediate set-ups is required by the presence of fringing. Fringing results from internal reflections and consequent interference of light bouncing off the interfaces of the air-substrate and substrate-silicon layer (CCDs are back illuminated through the substrate). It is further complicated by variations of the thickness of the substrate layer across the entire breadth of the chip on a size scale similar to the wavelength of the light. This appears as narrow waving bands of higher or lower sensitivity in the 2-D flat field spectra, which must be eliminated. The strong wavelength dependence of the fringing necessitated the use of a finite decker to isolate the wavelengths involved for the correction method described above. Fringing was not evident in either the intermediate or blue set-ups.

## A.3 Scattered Light and Sky Background Corrections

For nebular object spectra, the next reduction step involves the removal of scattered light. Scattered light manifests itself in a variety of localized phenomena, including phantom orders between and within spectral orders, and fuzzy ghost images. In addition, there is a general scattered light profile which contributes to the nebular continuum where it falls inside orders. Localized scattered light artifacts must be recognized by eye and excluded on a individually. However, it is possible to globally fit and remove the overall scattered light profile, since this information is recorded in the regions in between spectral orders. We began by isolating the regions in between the orders, then fitting low ordered functions first across the dispersion to the data within these orders. A second fit was made in the dispersion direction to the first fit's values at each point across the dispersion. The resultant scattered light spectrum was then subtracted from the original 2-D object spectrum. Care was taken to exclude from the fits regions of the spectra contaminated by flaring in the vicinity of strongly saturated lines (spill over of saturate pixels into adjacent columns and rows). Afterwards, 1-D cuts were taken across the scattered light subtracted 2-D spectra, to confirm that the inter-order regions were properly normalized to zero by this process. These operations were carried out in the IRAF *echelle* package tasks *apall*, which allows the isolation of the inter-order regions, followed by *apscat*, which performs the fitting and scattered light subtraction.

For the flux standard star spectra and narrow decker quartz spectra used for flux

calibration, sky subtraction, as opposed to scattered light subtraction, establishes the zero point of the flux calibration scale. This process occurs during the extraction of the 1-D spectrum from the 2-D image, rather than beforehand, for the scattered light subtraction. It was possible to use this procedure for these spectra because the standard star and quartz lamp profiles did not fill the entire slit and a region existed between each end of the slit and where the profile tapers off from its center to a constant, which is the ambient background or “sky” illumination level. A linearly fit established in these sky regions interpolates the sky contribution to the standard’s profile. As each pixel was summed over the portion of the slit designated for the standard star, the value of the background at that same pixel from the interpolation function was subtracted.

The 1-D PNe spectra were extracted from the 2D images using the routine *optext* (Rauch et al. 1990), in the mode where no sky subtraction is done, by summing along the slit at each position in a particular order, across the CCD. The 1-D standard star and quartz calibration frames were extracted with the IRAF *echelle* package task *apall*, with sky subtraction carried out as described above.

# Appendix B

## RDGEN

RDGEN is a component of the publically available spectral line detection and measurement software package known as VPFIT, written in FORTRAN by Carswell et al. (2001). RDGEN is specifically tailored to detect and provide rapid measurements of emission and absorption lines in extracted, wavelength calibrated object spectra with non-negligible continua, such as the planetary nebula spectrum examined in this project. Only the emission line detection feature in RDGEN was used in the present study. I was the first MSU user of this program, and this appendix is designed as a “user’s guide” intended for those (e.g. my thesis advisor) who will want to use this program in the future. Further information for this program may be found at:

<http://www.ast.cam.ac.uk/~rfc/rdgen.html>

### B.1 Inputs

RDGEN requires as its inputs an array of flux measurements, wavelength values, the

accumulated error in those fluxes, and estimates of the flux in continuum, at all points in a particular extracted spectra. RDGEN accepts standard IRAF format extracted long slit and echelle spectra, where the information is encoded at each image pixel or “channel” along the spectra or spectral order. Other options allow the use of ASCII tables of these values. The IRAF format is the most convenient if standard IRAF tasks were employed to reduce the object’s spectra. If the spectrum has been wavelength calibrated to a linear scale (relating each channel number to a specific wavelength as was done here), an estimate of the instrumental resolution, in terms of the number of channels spanned, must be provided for each pixel in the spectrum or across each spectral order. The user must also specify the detection limits down to which they wish the code to attempt to locate lines, in terms of the accumulated probability of finding a line at random amid the continuum at the local level of noise. This parameter is referred to in the code as “-log probability of chance occurrence”. The value of this parameter differs from the S/N in a particular line, and setting its value generally will depend upon the characteristics of the spectra and user preference.

## B.2 Method

RDGEN considers a line, a local region of the object spectrum, spanning several channels, in which the flux value in the object spectrum exceeds the value in the continuum. Progressing from lower to higher numbered channels, the code begins a prospective emission line at the first channel in which the flux value exceeds the continuum value, and ends when the flux falls below the continuum value. If the number of pixels

spanned exceeds the instrumental resolution, and exceeds the lower detection limit in terms of likelihood of non-random occurrence, it is considered a “detected emission line”. The search continues until the end of the spectrum or spectral order, or a user-defined wavelength limit.

Over each pixel which the line spans, the code keeps track of several parameters:

- The sums of the signal,  $s_i$  (object spectrum flux value minus the continuum value); continuum,  $c_i$ ; and the ratio of the signal to continuum values,  $s_i/c_i$ , i.e. the equivalent width per unit channel, in each channel  $i$ .
- The sum of the product of the equivalent width per unit channel and the wavelength  $\lambda_i$  at that channel,  $(\lambda_i \times (s_i/c_i))$ .
- The channel number possessing the highest equivalent width per unit channel within the line (the channel  $i$  where  $s_i/c_i$  is the maximum), essentially the “peak” of the line, and the wavelength value at that channel.
- The code also keeps a separate tally over those channels in which the error value  $\sigma_i$  is positive. This includes the sum of the variances  $\sigma_i^2$ , the signal, and the cumulative “-log probability” of the line. The latter measures the probability in each channel of the channel’s signal value appearing completely at random in that channel, given the channel’s error value and Gaussian statistics. This quantity is essentially one minus the area under the normalized Gaussian curve out to the number of  $\sigma$  by which the signal exceeds the error estimate. The

code defines the log probability as:

$$p_i = -\log \left[ \frac{1}{2} \operatorname{erfc} \left( \frac{s_i}{\sqrt{2}c_i} \right) \right], \quad (\text{B.1})$$

where  $\operatorname{erfc}(s_i/\sqrt{2}c_i)$  is a modified version of the complimentary error function.

After summing all quantities over the line, the code checks that the user's inclusion criteria. The number of channels spanned by the line are compared against the instrumental resolution. The line is checked for “real” detection, by comparing the line's overall minus log probability against chance occurrence, defined by:

$$x = \frac{\sum_i s_i}{\sqrt{\sum_i \sigma_i^2}}, \quad (\text{B.2})$$

$$px = -\log \left[ \frac{1}{2} \operatorname{erfc} \left( \frac{x}{\sqrt{2}} \right) \right], \quad (\text{B.3})$$

where  $px$  is the value of minus log probability parameter and all quantities sum over  $n$  channels in the line. The code limits  $px$  to a maximum value of 40 for the strongest line in the spectrum.

The code then also computes the flux, central wavelength, S/N, and equivalent width, employing the following ratios of tabulated sums acquired while scanning the line. The flux,  $F$ , is calculated by averaging:

$$F = \frac{\Delta\lambda}{n} \sum_i s_i, \quad (\text{B.4})$$

wavelength  $\lambda$ :

$$\lambda = \frac{\sum_i \lambda_i \frac{s_i}{c_i}}{\sum_i \frac{s_i}{c_i}}, \quad (\text{B.5})$$

S/N:

$$\text{S/N} = \frac{\sum_i \frac{s_i}{c_i} \sum_i c_i}{n \sqrt{\sum_i \sigma_i^2}}, \quad (\text{B.6})$$

and equivalent width EW:

$$EW = \frac{\Delta\lambda}{n} \sum_i \frac{s_i}{c_i}, \quad (\text{B.7})$$

where  $\Delta\lambda$  is the wavelength difference between the first and final channel over which the line spans. No profile fitting is done to make any of the measurements above.

Finallyn the code calculates various other line attributes, such as FWHM and line skew, linearly interpolating between the channel values for the wavelengths where necessary.

The code may also be utilized to detect absorption lines, as numerous tools exist within RDGEN to break up blended line profiles into components and to carry out other absorption line specific tasks, as described in Carswell et al. (2001). RDGEN cannot be set manually to look only for emission lines, but the absorption line detection process does not interfere with the emission line detection process, and both go on simultaneously. However, program output must be manually filtered to screen out absorption line detections if the code's primary use is emission line detection.

Output is stored by default in a file called "fort.9" in the working directory. Each row in the file contains one detected spectral line and its statistics. Absorption lines may be part of blends or complexes which RDGEN may break up, and thus several subsequent rows may be related to an initial absorption line. A "em" entry in the first column indicates the detection of an emission line, whereas "abs" indicates an absorption line, with subsequent rows, until the next "em" prefaced row, containing related measures for the absorption line complex. Each emission line will have only *one* row.



## B.3 Operation

Here we demonstrate the use of RDGEN to detect emission lines in the full, long spectra “blue418x.ec”. The input files used in this example were all in IRAF echelle format.

For each individual flux calibrated emission spectrum, the extraction process yielded an error array. These error arrays were co-added together at the time their companion object spectra from within the same instrumental set-up were co-added, and the same scaling was applied to both the object spectra and error arrays, during the co-addition, to maintain the same S/N. For the blue, full, long spectra the error array took the form of a standard IRAF image file of exactly the same dimension as its respective object spectrum: “blue418x.sig”. RDGEN automatically accepts an IRAF image sharing the same root as the object spectrum with a “.sig” or “.err” suffix as an array of  $1\sigma$  error values, and will assume an array of  $1\sigma$  variance values when the image has a “.var” suffix. RDGEN will prompt if it finds no error file sharing the same root name as the object spectrum, or doesn’t find an image file with one of three suffixes listed.

RDGEN also requires an array of continuum flux values, or an object spectrum normalized through division by a fit to the continuum. The estimates of the continuum were made by applying a running boxcar median filter of various window sizes (51, 81, and 101 pixels) to the object spectra. This lends itself to a quick and fairly accurate estimate of the continuum level in locations away from strong lines. However, the presence of strong, wide, and closely spaced lines leads to a corresponding “bump” in

the continuum. The extent and magnitude of these bumps increases with decreasing window size, but the ability to correctly follow small scale variations in the continuum improves. For each individual order of the object spectra, a median filter spectrum which best fit the continuum sharpe across the order with a minimum of “bumpiness”, was chosen to represent the continuum for that order. In some cases bumps were manually interpolated under, while in other cases, with a foreknowledge of the program’s mechanism, a bump was retained to force the detection of lines residing on the wings of stronger lines. RDGEN will first look for an image with the same root name as the object spectrum but with a “.cont” suffix. For example, “blue418x.cont” is the final fit to the continuum for the long, blue, spectrum “blue418x.ec”. If no file with this suffix is present, RDGEN will ask manually for the name of the continuum fit file. If none is specified, RDGEN will assume that the spectrum has been *pre-divided* by the continuum (i.e. the continuum level will be assumed to be one everywhere in the spectrum).

The object, error, and continuum spectra were all wavelength calibrated by the same dispersion solution, and shared the same linear wavelength relationship between pixel and wavelength value. The image header for the dispersion solution information contains the wavelength span per channel ratio for every echelle order. This ratio, along with the instrumental resolution (in this example  $10 \text{ km sec}^{-1}$  ), allows the calculation of the instrumental resolution element in pixel space. For all orders, the instrumental resoultion was a uniform 3 pixels/channels.

RDGEN is invoked by executing the **rdgen** command in the directory containing the VPFIT software package. Executing **rdgen** yields:

```

*****
* ALL SIGMAS MULTIPLIED BY    1.00000    *
* SEE VP_SETUP.DAT FILE                      *
*****

0.0500000007< b < 100.
Drop system if b < 0.0500009991 & logN < 14.
or if logN < 8.
or if b > 1001.
Maximum data array length: 125000

Failed to find help file
>>

```

The RDGEN command prompt is >>. As in IRAF, an external batch file is allowed to be used. The mechanism is:

```
>><blue418x.scr
```

where “blue418x.scr” is a batch file made up of many commands to be read in order.

The first command from the batch file is:

```

>>rd
Filename for data?
>

```

where rd requests that RDGEN read in the data from an object spectra or file. In this example the reply is:

```

>>rd
Filename for data?
> blue418x.ec
> Order number? [ 14], max 27
> 6

```

```
> IRAF v2.10 wavelength coefficients
>>
```

RDGEN will recognize an echelle format spectrum with multiple orders from the construction of the image file, and will prompt for an order number. Only one order may be operated on at a time. Upon successfully reading the data and interpreting the wavelength linearization information in the object spectra's header, RDGEN will confirm its success with the "wavelength coefficients line" comment as seen above. RDGEN will also prompt for continuum and error array spectra information if suffix formats are missing.

To get RDGEN to begin line detections, the command "ab" must be issued at the command prompt:

```
>>ab
Restricted output(r), fluxes (f)? [neither]
```

Choosing **r** will print the S/N statistic in the "flux" column, while choosing **f**, will print the flux in the "flux" column. The default (choosing "neither") is to print the flux statistic. Selecting "neither" or any other option returns:

```
Sig. lims.: line, components, cpt peak [5.0,same,as cpts] :
```

This line queries the user to enter what "significance limit" (Sig. lims.) the code should attempt to detect lines down to. This is the "-log probability against chance occurrence" statistic that was mentioned previously. A value must be set that is

high enough to screen out completely spurious detections, yet be low enough to allow extremely weak legitimate lines to be picked up. For emission line detection, only the “line” parameter is relevant, with the other parameters used only for absorption lines, and their default values of 5.0 can be retained. A value of 3-5 seems to work best for “line”, as determined from previous uses of the program with similar spectra. These values yield line detections of a S/N at which the detection is considered “legitimate” from manual inspection of the program’s output.

Next the code inquires about the size of the resolution element in the particular spectrum or spectral order:

**Resolution, min sepn (chan) [3,nres/2+1]**

For each echelle order, it was determined that the default value of 3 was correct for the present spectra. The “min sepn (chan)” statistic is used exclusively for the absorption line detection portion of the code, and thus the default was selected.

Finally the code inquires about the range of wavelengths to search:

**Wavelength range -low, high [ 3814.5, 3909.7]:**

The prompt displays the wavelength limits, as determined from the image header, for the particular order or spectrum under examination. The user may accept the entire order by using a carriage return, or specify the wavelength limits manually. Only one range in wavelength may be specified. To search over multiple ranges in one particular order or spectrum, additional calls to **ab** and **rd** are needed.

After answering the query, RDGEN proceeds to find emission lines within the specified wavelength range, down to the probability parameter and other limits specified by the user. The output is echoed to the screen and to the file “fort.9”. The output consists of a FORTRAN formatted list of lines, each containing information about a particular emission line, or a component of an absorption line. The user is then returned to the standard RDGEN command prompt: >>, where the entire process may be repeated. If a batch file has been used, the next instruction in is then immediately implemented, and successive output is concatenated to the “fort.9” file. For the study here the final output file was interpreted by PERL scripts, to generate input files suitable to various plotting programs, for use in screening spurious detections and establishing S/N limits, and for use by the Gaussian fitting program detailed in Appendix C.

## B.4 Code Benefits and Limitations

RDGEN provides a quick, un-biased, approach to emission line detection, calculating many line attributes that can immediately be used in additional programs. Its information is drawn directly from standard format IRAF images, necessitating little preparatory work. The ability to use simple ASCII format input files means that the program can be easily adapted to handle non-IRAF image formats. In general, the code automates a manually difficult and demanding chore, the detection of emission lines in an even handed and quantified manner, and does so with a minimum of preparatory work to the actual object spectra.

To use the code, however, both an error estimate and continuum fit for the spectrum must be present. Standard IRAF extraction techniques do not necessarily generate either of these companion spectra, although the modified Rauch et al. (1990) routines do generate an error array. Since the line detection scheme employed by the code utilizes the difference between a perceived level of the continuum and the actual signal in the spectrum, in spectra with a noisy continuum where one searches for extremely weak lines, an extremely accurate value of the continuum must be assured to avoid missing legitimate lines or interpreting spurious noise as a line. An incorrectly flat continuum also may undercut strong blended lines and cause the code to interpret close lines (i.e. [O II]  $\lambda\lambda 3727, 3729\text{\AA}$ ) as a single line; or undercut scattered light features, and interpret them as lines as well. Where the continuum fit falls into negative values (on the edges of some orders in the blue and intermediate spectra where the scattered light subtraction over compensated for the actual level), the code will refuse to detect lines. In essence, the line detection is only as good as the continuum fit. Constructing accurate continuum fits and error arrays can be a time consuming process, especially when their creation is not an automatic part of the extraction process, or when it is necessary to tailor them to the various artifacts, line types, and general continuum shapes found within individual spectral orders.

# Appendix C

## Profile Fitter

### C.1 Introduction

It is desirable to systematically and impartially fit Gaussian profiles to more than 1500 lines originally detected by RDGEN and deemed legitimate after manual inspection. Measurements and fitting by hand suffers from a line to line bias in both the extent of the line's profile above the continuum, and the level of the continuum itself. Instead we have coded a program in FORTRAN that attempts to fit single Gaussian profiles at all positions at which legitimate lines were detected in each spectrum's full slit extraction, using the data from their respective central cavity extraction spectra. Either the long or short duration spectra was used, depending upon whether the line was saturated according to Table 2.3. Simultaneously, it fits the local continuum level immediately surrounding the line with a linear function. This removes much of the observer bias regarding the line extent and continuum level, and puts all measurements on a more equal-footing, measured in precisely the same way. This appendix



is intended to both describe the method used and to serve as a user's manual for this code.

## C.2 Method

A typical line profile is spread over a number of individual pixels in an extracted spectrum. The input spectrum contains the amount of flux at each pixel or location (nebular signal plus continuum), and each pixel has a wavelength value assigned to it. The functional form of a Gaussian line profile superimposed on a linear continuum may be represented as:

$$y(x) = A + Bx + C \exp \left[ -\frac{(x - D)^2}{2\sigma^2} \right], \quad (\text{C.1})$$

where  $x$  is the wavelength,  $y(x)$  is the flux at wavelength  $x$ ,  $A$  is the *zero point* of the line describing the local continuum fit, and  $B$  the slope of that fitted line,  $C$  the amplitude of the Gaussian function at its peak,  $D$  the center of the Gaussian line profile, and  $\sigma$  the width of the distribution. The flux in a particular line is the integral of the entire profile over the entire breadth of the line minus the contribution from the continuum:

$$\mathcal{F} = C \int_{-\infty}^{\infty} \exp \left[ -\frac{(x - D)^2}{2\sigma^2} \right] dx. \quad (\text{C.2})$$

where I integrate over a wide pixel window, much larger than the profile, as an approximation, so as to take advantage of the symmetry in the integrand. Recasting  $\sigma$  into  $F$ , the full width at half maximum (FWHM) with the following form:

$$F = 2\sigma\sqrt{2 \ln 2}, \quad (\text{C.3})$$

we arrive at an expression for the flux, after integration, equal to

$$\mathcal{F} = \frac{\sqrt{\pi}FC}{2\sqrt{\ln 2}}, \quad (\text{C.4})$$

and where the original equation eq. C.1 can now be described as...

$$y(x) = A + Bx + \frac{2\sqrt{\ln 2} \mathcal{F}}{\sqrt{\pi} F} \exp \left( - \left[ \frac{2\sqrt{\ln 2}(x - D)}{F} \right]^2 \right), \quad (\text{C.5})$$

where again  $x$  represents the wavelength value minus some starting point, at each pixel in which the line profile resides, and  $y(x)$  is the flux value, signal plus continuum) at that pixel.

The code attempts to fit the best profile by altering the five adjustable parameters:

$A, B, D, \mathcal{F}, F$  and solving for the minimum  $\chi^2$  as defined by

$$\chi^2 = \sum_{i=1}^n \frac{\left( y_i - A - Bx_i - \frac{2\sqrt{\ln 2} \mathcal{F}}{\sqrt{\pi} F} \exp \left[ - \frac{2\sqrt{\ln 2}(x_i - D)}{F} \right]^2 \right)^2}{\sigma_i^2}, \quad (\text{C.6})$$

where  $\sigma_i$  is the error, provided by the complimentary error array to the object spectra, at each pixel  $i$  over which the line spans ( $i = 1..n$ ).

To perform the  $\chi^2$  minimization, the CERN code function minimization subroutines MINUIT were employed. The MINUIT subroutines may be called as external functions to any FORTRAN program, and the function a user wishes to minimize may be constructed as a separate FORTRAN function, whose name can be fed to the specific MINUIT routines of interest. The MINUIT routines used here are *migrad* which does the function minimization, and *minos* which does the error matrix calculation and provides the final errors on the fitted parameters. As mentioned, the adjustable parameters are wavelength, line flux, FWHM, and the slope and zero point of the local continuum.

The *migrad* routine operates, in the case of this profile fitting code, by calculating the function:  $\chi^2$  (eq. C.6) and perturbing repeatedly the adjustable parameters by user-supplied characteristic step sizes, following a path towards the minimization of the function, until such time that the change in the function between the parameters drops below a user-specified tolerance, or a user-supplied number of parameter adjustment iterations has been exhausted. The *minos* routine then follows, attempting to calculate an error matrix at the end of a run, and the specific numeric uncertainties in the fitted parameters. The errors in each parameter may or may not be symmetric about the final value.

As input *migrad* requires an initial estimate of each of the parameters, and an initial step size by which to perturb those parameters when looking for the path towards minimization. In addition *migrad* also requires the name of the external FORTRAN function which holds the function to be minimized, the number of calls to the minimization routine, and the aforementioned tolerance value at which further calls to the minimization routine are curtailed. The user must also include an associated error array, binned to the same wavelength scale as the object spectra under scrutiny, in the format of a IRAF echelle spectra.

Operation of the profile fitter begins with the submission of a group of line detections, one for each order or spectrum, in this case of the present data from the RDGEN line detector program, and the associated parameters for those lines, specifically wavelength and FWHM. Also required is the name of the spectrum in which to make the measurements, the format of which again must be an extracted wavelength calibrated echelle spectrum, in standard IRAF echelle format, with the wavelength

solution for each pixel previously binned to a linear scale. The user then specifies two parameters known as the *window* and *halo*, in units of  $\text{km s}^{-1}$ , to be used with every line in the input list of detections. The window indicates the actual perceived size of the line, *i.e.* the width that is clearly visible above the continuum. The halo should cover a wider range, including a region immediately outside of the window, from which information regarding the local continuum in the vicinity of each line detection is drawn.

Selecting the first line detection from the input list, the code fits eq. C.6 to the set of pixels centered on the nominal wavelength supplied by RDGEN and extending over the halo pixels to either side. The wavelength value at the bluemost pixel within this group is treated as a “reference” wavelength from which all wavelength values are measured at all other pixels within the line’s pixel group. The MINUIT function minimization routine *absolutely* requires that all parameters be nearly the same order of magnitude to avoid precision problems. Since the flux values at each pixel, which are typically  $10^{-14} - 10^{-16} \text{ erg cm}^{-2} \text{ \AA}^{-1} \text{ s}^{-1}$  and the error array the square of that, greatly differ from the wavelength and FWHM (the former in  $\text{\AA}$  from the “reference” pixel and the latter converted to  $\text{\AA}$  in the code) are typically on the order of unity, it was necessary to rescale all the flux and error values at each pixel in the line’s group within the object before submitting the data to the fitting routines. This was accomplished by taking the logarithm of the flux and its error at each pixel within the line, summing these logarithms, obtaining the average, taking the inverse logarithm of that average, then dividing the flux and errors at each pixel by the resultant values. If the flux was negative in a pixel or pixels, the logarithm was taken of the negative

of the flux in that pixel or pixels.

The code proceeds by calculating the initial values of the slope and zero point of the local continuum fit. Only the rescaled flux values for those pixels in the region *between* the halo and window on either side of the line are included. The flux values for the pixels in this region are then fitted with a linear least squares algorithm, weighted by the error amounts at those pixels, to establish a linear fit approximating the continuum in the immediate vicinity of the line. The zero point need not necessarily be the flux value at the “reference” wavelength pixel, although all wavelength values remain measured against it. The step sizes by which to adjust the slope and zero point are taken as three times the uncertainties in the parameters as determined from the fit. Next, the code calculates an initial flux value in the line by employing eq. C.4 and the FWHM included with the line’s input information. The peak flux within the line profile (signal including the continuum contribution) is sought, and the interpolated continuum level from the fit is subtracted to yield the parameter  $C$  in the equation. The initial wavelength and FWHM values are drawn directly from the input list. The step sizes are arbitrarily taken to be 10%, 1%, and 10% of their initial values respectively for the flux, wavelength, and FWHM. These values seem to work best from repeated use of the code, and have been hard-wired into it. Finally, upper and lower bounds to the line flux, FWHM, and wavelength are set, with values equal to those reported in Table C.1. These are used as a sanity check for the output parameters, and to prevent the *migrad* from running away from a physically sensible set of values. The error calculation routine *minos* will fail to calculate an error matrix if any parameter has exceeded this value after the termination of the

*migrad* run. The slope and zero point of the local continuum are unbounded.

The code then commences to send the initial parameters and step sizes, the array of data points (flux versus wavelength at each pixel within the line), and the tolerance and number of desired iterations, to the embedded calls in *migrad*. Repeated use of the code has demonstrated that a value of 0.001 for the tolerance and 5000 for the number of iterations applied by MINUIT seem to work well, although the routines appear to be fairly insensitive to the choice of these parameters. The MINUIT routines attempt to minimize the function of eq. C.6, until either satisfactory results have been reached (tolerance has been achieved between successive iterations) or the number of function iterative calls has been exhausted. From this point the associated MINOS routines attempt to generate an error matrix, from which the uncertainties in the fitted parameters can be drawn. Upon completion, if the MINUIT has failed to converge to a good minimization, or if the resultant output parameters violate the upper or lower bounds set for them, the original estimates are retained.

After completion of minimization, the code returns all parameters to their original scales. It then writes a new IRAF echelle spectrum in which the fitted profile, using the returned parameter values, replaces the original data. This output spectrum can then be plotted on top of the input spectrum as a way of visually assessing the quality of the fit. The values of the parameters are also written to another output file. In the event that *migrad* fails to converge to physically meaningful parameters and *minos* fails to arrive at a good error matrix, the original estimates for the parameters are utilized instead of the originals, and the occurrence is noted in the output file. If the parameters exceed the upper and lower bounds set for them, the occurrence is noted

in the output file, but the parameters are retained for inspection. The code then proceeds to the next line detection.

## C.3 Operation

The code is invoked by writing on the unix command line `gmod`. Optionally a single numeric argument may follow the command, if the user wishes the code to only make measurements in one particular echelle order i.e. `gmod 6` would request that the code only make measurements in order 6 of the spectrum to be specified later.

Upon execution the code will request the following information:

```
> gmod
  Enter the root name of the Line List
1zblue418x
  Enter the root name of the IRAF echelle image
blue418x.ec
  Enter the name of resulting fitted IRAF image
testblue
  Enter the distance bounds from line centroid (km/s)
  to sample continuum from (outer then inner):
75 30
```

The first questions ask for the root name of the input line detection list. The code requests that each echelle order have a list of lines in the format diagramed in Figure C.1, with nomenclature: “root.?”, where the “?” refers to individual aperture (not absolute order number) in the echelle spectrum. A separate list of line detections *must* be included for every order in the spectrum, unless single order mode has been invoked on the command line, in which case only the file for the specified order need be present. In the above example the root specified is “1zblue418x”. A segment of a

8	3756.88	0.008	3756.46	3757.29	0.444	27.13
33	3769.63	0.004	3769.28	3769.88	0.225	38.30
35	3771.49	0.000	3770.94	3772.14	0.393	1284.00
42	3778.01	0.018	3777.67	3778.32	0.166	9.39
45	3780.97	0.017	3780.67	3781.22	0.338	8.60
51	3785.70	0.002	3785.37	3785.97	0.257	71.58
1	3787.39	9.999	3787.16	3787.54	0.228	99990.00
69	3802.28	0.017	3801.93	3802.62	0.410	10.73
71	3803.54	0.016	3803.26	3803.96	0.329	11.87
75	3806.59	0.002	3806.26	3806.91	0.239	99.49
86	3812.69	0.009	3812.49	3812.85	0.144	9.93
91	3814.29	0.016	3814.01	3814.47	0.176	7.58
94	3817.97	0.014	3817.74	3818.16	0.256	7.73
99	3820.49	0.002	3820.00	3821.11	0.295	167.60
102	3822.64	0.009	3822.26	3822.91	0.388	18.33
1	3830.57	9.999	3830.04	3831.06	0.540	99990.00
1	3832.50	9.999	3832.15	3832.92	0.202	99990.00
1	3834.41	9.999	3834.06	3834.76	0.252	99990.00
(1)	(2)	(3)	(4)	(5)	(6)	(7)

Figure C.1 A sample line detection input file “1zblue418x.6”, with columns entries explained in the text.

sample line detection file, “1zblue418x.6”, is detailed in Figure C.1. These files must be ASCII files in free FORTRAN format, where each row includes information about one particular line detection. The use of a “Z” as the first character of any row in such a file causes the code to skip the line in that row. Column (1) is the RDGEN “ID” number for line detection and column (7) is the RDGEN S/N for the detection, which are simply echoed to the output and not used by the code. Columns (3)-(5) are information from RDGEN no longer required in the code in its current incarnation. Numeric place-holders may be used in each of these columns instead, although some value must be present. Column (2) is the wavelength of the line detection, and column (6) is the FWHM, both in Å, which are directly used by the code. The line detections within an order *must* be listed in increasing wavelength order for the code to operate.



The second question requests the root name of the IRAF echelle spectrum from which you wish to measure the profiles. This name need not share the same nomenclature as the line list root, but it must end in a “.ec”, the standard suffix which indicates an echelle spectrum generated by standard IRAF tasks. The code will also look for a companion error spectrum with the same prefix (before the “.ec”) but with a “.sig” suffix. The code will again warn if this file cannot be found. Both the object and error spectrum *must* be wavelength calibrated in exactly the same manner.

The third question requests the name for an output spectrum that will be generated using the fitted values of the parameters. The output will be named precisely what is stated here, without any extensions such as “.ec”. This output spectrum will be the input spectrum, but with the fitted profiles written in place of the original data. Across each order the bluest lines are written in the output spectrum first, so where there are closely spaced lines, the output profile of one line may be overwritten by that of the successive line, if the lines halos overlap. The output spectrum can then be used like any other IRAF format spectrum, and may be operated on by any standard spectral tools included in the relevant IRAF packages.

The last question requests the range of the halo and window for each line respectively in units of  $\text{km s}^{-1}$ . In the example above all pixels within  $70 \text{ km s}^{-1}$  to *either* side of the specified wavelength center, are included in the fit are included for profile fitting purposes, while only those pixels between  $35\text{-}70 \text{ km s}^{-1}$  are included for determining the local continuum values. Only one set of values may be used per application of the program. Thus if the user requires multiple window and halo sizes, the program must be run again. The use of the “Z” comment character in the input

lists may facilitate repeated application using the same input list.

For this data analyzed here, the window size was adjusted so as to encompass the entire line profile including the expansive wings of strong lines and to place the continuum sampling region as far away from the wings as possible. Meanwhile, for weak lines, the window and halo were shortened so as to not include too much continuum in the fit, and to minimize overlapping halos from closely spaced weak lines. A series of three different halo and window sizes were used (in  $\text{km s}^{-1}$ ): (55,35), (90,65), and for the broadest lines (300,250).

Upon answering this question the code will echo the chosen parameters to the screen:

```
Line List Root:
1zblue418x
IRAF Image Root:
blue418x.ec
IRAF sig file:
blue418x.sig
Extent of continuum window from centroid:   75.   30.
Output name:
testblue
```

then wait for a carriage return to commence the process.

A string of information from MINUIT will then flow onto the screen. Currently the code does not echo the information to a separate file, due the vast quantity of information provided, and the fact that where MINUIT fails to converge to a good minimization, or when the parameters it provides violate the set upper or lower bounds, this information is echoed into the profile fitter's own output file. This output file, named "res" is placed in the working directory, and the output spectrum

containing the fitted profiles is also placed in that directory. A segment from a sample output file, created by using a segment of the data analyzed here, using the above response to the queries in this example are shown in Figures C.2-C.3

The output format consists of the following information inscribed in the columns of Figure C.2. The first three rows name the input line detection list root name, the spectra in which the fitting and measurements were accomplished, and the window and halo sizes used for the particular run of the code, respectively. After the “column descriptor” rows, column (1) is the echelle aperture number from which the line was drawn, column (2) is the fitted wavelength (in Å), and columns (3) and (4) are the possibly non-symmetric errors (in Å) arising from the fit. Column (5) lists the change from the RDGEN determined wavelength (in  $\text{km sec}^{-1}$ ): the profile fitted value minus the RDGEN value. Column (6)–(8) yield the fitted FWHM and its associated, possibly non-symmetric errors (all measured in  $\text{km sec}^{-1}$ ), and columns (9)–(11) are the same for the line flux (as measured in  $\text{erg cm}^{-2} \text{ sec}^{-1}$  for the flux, and the percentage of the final line flux divided by a hundred). Column (12) echoes the S/N determined by RDGEN for the line or a numeric place-holder, and columns (13) and (14) state the “ID” assigned by RDGEN (or again a numeric place-holder) and wavelength value (in Å) for the detection respectively. Finally, entries in the final column, column (15), as detailed in Table C.1, indicate lines where the various MINUIT routine returned a value significantly different from the initially determined value, failed to converge to a good fit, or was unable to determine an uncertainty value for a parameter or parameters.

1zblue418x blue418x.ec 75. 30. ord lambda	1am+ A	1am- A	d-rdgen km/s	fw+ km/s	fw- km	flux	f1+ f1-	S/N (rdgen)																
4 3659.462	0.094	-0.096	0.2	17.3	14.4	0.0	1.47E-14	0.009	-0.008	102.10	41	3659.46												
4 3660.246	0.079	-0.078	-0.3	19.3	11.8	0.0	2.00E-14	0.007	-0.006	126.50	43	3660.25												
4 3661.107	0.059	-0.059	-0.3	21.8	9.4	-8.2	2.93E-14	0.005	-0.005	152.80	45	3661.11												
4 3662.056	0.057	-0.054	3.0	23.8	8.9	-7.9	3.66E-14	0.005	-0.005	193.00	47	3662.02												
4 3663.086	0.044	-0.043	0.5	25.9	8.0	-6.8	4.65E-14	0.004	-0.003	266.40	49	3663.08												
4 3664.235	0.044	-0.043	-0.4	28.3	8.3	-7.0	5.83E-14	0.004	-0.003	267.60	51	3664.24												
4 3665.510	0.040	-0.040	-2.5	31.2	8.6	-7.0	7.28E-14	0.003	-0.003	353.90	53	3665.54												
4 3666.926	0.040	-0.040	-0.3	30.8	8.4	-6.8	8.11E-14	0.003	-0.003	364.10	55	3666.93												
4 3668.508	0.031	-0.031	0.7	29.7	6.6	-5.5	8.71E-14	0.002	-0.002	435.30	57	3668.50												
4 3670.289	0.029	-0.029	0.7	30.8	6.0	-5.2	1.02E-13	0.002	-0.002	456.30	59	3670.28												
4 3672.300	0.026	-0.026	0.0	30.6	5.0	-4.5	1.08E-13	0.002	-0.002	557.60	61	3672.30												
4 3674.986	0.025	-0.025	-0.4	31.7	4.8	-4.3	1.22E-13	0.002	-0.002	565.00	63	3674.59												
4 3677.189	0.026	-0.026	-0.1	32.2	4.9	-4.3	1.35E-13	0.002	-0.002	486.90	66	3677.19												
4 3683.635	0.036	-0.035	-0.4	32.6	6.2	-5.1	1.73E-13	0.004	-0.004	256.70	72	3683.64												
4 3705.859	0.057	-0.053	-0.1	21.2	11.1	-8.1	1.08E-13	0.005	-0.005	224.30	101	3705.86												
5 3705.850	0.103	-0.112	0.0	23.5	24.1	-14.4	1.15E-13	0.007	-0.006	146.90	24	3705.85												
5 3735.205	0.019	-0.019	-0.4	30.6	3.6	-3.2	4.84E-13	0.001	-0.001	614.90	56	3735.21												
5 3735.885	0.223	0.000	-34.1	20.0	30.3	0.0	-1.18E-14	0.000	0.000	35.07	57	3736.31												
5 3742.983	0.000	0.000	1.8	28.4	0.0	0.0	3.20E-15	0.084	0.000	22.74	65	3742.96												
5 3744.196	0.000	0.000	0.5	50.9	0.0	0.0	5.67E-15	0.058	0.000	14.85	67	3744.19												
5 3746.354	0.000	0.000	-33.3	60.0	0.0	0.0	4.51E-15	0.079	0.000	8.27	69	3746.77												
15 4438.554	0.054	-0.054	0.3	21.2	10.4	-7.4	1.43E-14	0.005	-0.004	211.50	14	4438.55												
(1)	(3)	(4)	(5)	(6)	(7)	(8)	(9)	(10)	(11)	(12)	(13)	(14)	(15)											

Figure C.2 A segment from the output file “res” to the profile fitter. A legend for the various columns is given in the text. The entry for the line fitted in Figure C.3 is listed at the bottom.

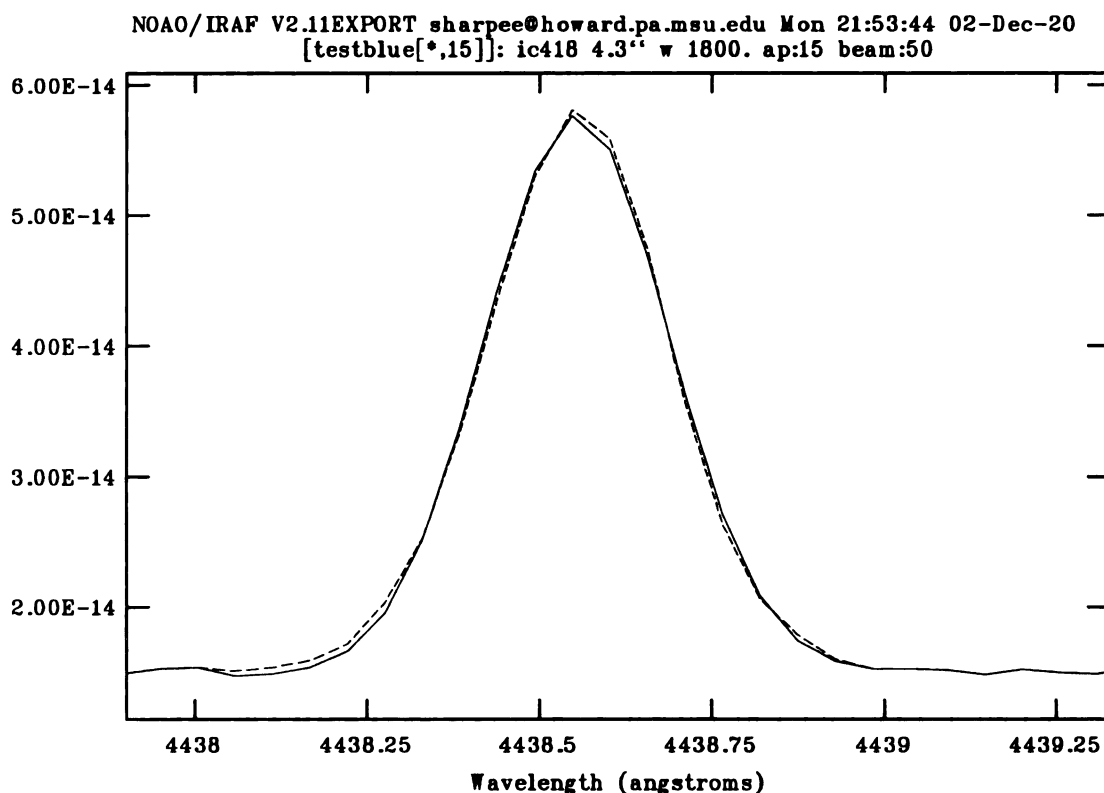


Figure C.3 The fitted profile of a line from the full slit, long exposure, blue spectrum. The actual data are the dotted line, superimposed upon the solid line which is the fit.

## C.4 Benefits and Limitations of the Code

The benefits to utilizing such a code are three fold. First, for the measurement of line wavelengths, FWHM, and fluxes, it is important to measure each line consistently, that is by applying the same methods of determining the continuum level and fitting the profiles. This is a difficult task to perform repeatedly for a large number of lines. Secondly, the code operates directly from IRAF input spectra, with a minimum of preparatory work. Finally, the code automatically calculates the errors in the fitted parameters.

Table C.1 Legend for entries in final column of the profile fitter output.

Entry	Meaning
<b>3</b>	Final line flux is $>3$ or $< \frac{1}{3}$ initial value
<b>4</b>	Final wavelength is outside of specified <i>window</i> bounds
<b>5</b>	FWHM is $<$ instrumental resolution (here $9 \text{ km s}^{-1}$ ) or exceeds twice the <i>window</i> size
<b>M</b>	<i>migrad</i> failed to converge to a set of physically meaningful values within the number of iterations or down to the tolerance
<b>E</b>	<i>minos</i> failed to calculate an error matrix

However, the code currently suffers from a number of limitations in its current incarnation. First, it is limited to single Gaussian fits. Several of the lines in the present study are blended Gaussians that had to be manually de-convolved using the “d-d” operation in the IRAF task *splot*. Secondly, the code has no way of knowing *a priori* of the location of lines it is currently attempting to fit, as it acts sequentially in order of wavelength. Thus, line halos may overlap, and the local continuum estimates may include pixels from the previous or next line to be fitted. This can skew the fit, despite the use of weighted least squares to de-value those pixels in the fit. This necessitated a manual inspection of fitted profiles against their observed counterparts, and in some case manual fitting with the Gaussian profile fitter “s-s” in *splot*.

Finally, an area of continuing work is the inability of the code to generate reliable errors for the fitted parameters in every line detection. This was a main impetus in using the MINUIT code in place of a simplex method such as “amoeba” which does

not have such a mechanism for formal error determination. Currently only about a quarter of line detections return a set of error estimates. The code may fail to return error estimates because *minos* is unable to provide a positive definite error matrix after parameter fitting by *migrad*, or because it is prevented from doing so because during minimization *migrad* has perturbed a parameter or parameters beyond the upper and lower “sanity” bounds. Both the numbers and quality of error values returned, in the sense that they agree with eyeball estimates of the wavelength and flux uncertainties from comparing the fitted profiles with the original spectra, have improved with successive incarnations of the program. However, due to the nature of the function being minimized here, or as yet undetermined error in the correct usage of the MINUIT routines, it cannot be said with certainty that the error estimates are completely accurate. Thus, it was decided to not employ the errors determined by MINUIT for the IC 418 data analysis.

Nevertheless, as evidenced in Figure C.3, the code is highly successful in providing good fits to almost all of the line profiles with single Gaussian morphologies, in a bare fraction of the time that would be required to manually make such measurements. The profiles that we had to measure by hand were either double-peaked, or blended on wings of other lines. While the code is currently keyed to output from the RDGEN line detection routine, the input list flexibility in the free FORTRAN format, and the minimum of information required, makes it highly adaptable to the results of other procedures that provide wavelengths and FWHM initial estimates for lines to be fitted. The use of a separate FORTRAN function for the actual function to be minimized, means that new functions, such as one allowing the simultaneous fitting

of two Gaussian profiles as an example, can be easily swapped in without disturbing the main body of the code. Because the input spectrum is drawn directly from an IRAF format spectrum, a minimum of work was necessary to utilize the code, whereas other automatic fitters might require additional preparatory steps to convert IRAF echelle spectra to some other format.

## C.5 Future Work

It is desired that the code return accurate estimates for all parameters and their errors as often as possible. Therefore additional work will go into investigating procedures that will allow *minos* to calculate accurate error estimates for a majority of line detections, or determining if the nature of the particular function simply prohibits this.

A number of values, such as the parameter adjustment step size for the flux, FWHM, and wavelength, and the number of iterations and fitting tolerance are currently hard wired into the code. Although these parameters work fairly well in the function minimization portion of the code, it might be advantageous to allow users to be able to adjust these on an individual run basis, without recompiling the source code.

Finally, multiple Gaussian fitting would be of great benefit in resolving line blends, which are still numerous even at the spectral resolution used here.



# Appendix D

## EMILI User's Manual

Presented here is the user's manual for the current public release version of EMILI (Version 4.0). It is intended as a stand-alone manual giving the EMILI user explicit instructions as to the structure of input files, the format of the output files, and how to use the program. Greater detail relating to the EMILI logic and process can be found in § 3.

### D.1 Introduction and Purpose

The EMILI code is designed to aid in the identification of weak emission lines, particularly those weak recombination lines seen in high dispersion, signal to noise spectra. The program utilizes a three facet approach to obtain this goal. First, we derive maximum utility from a large atomic transition database: Atomic Line List v2.04 (van Hoof 1999). Even for those transitions which lack values for atomic parameters, we can make rough estimates of line strengths, so that every transition can be con-

sidered as a possible ID for some observed line. Thus, many more transitions can be utilized here than could be considered manually, or that could be included in emission spectra models which rely on precise knowledge of such atomic parameters. Secondly, the code carries out time-consuming checks, which are usually done manually, such as searches for other multiplet lines, in a rapid and automated fashion free from observer bias. Finally, the program provides an easily understood ranking criteria to allow the user to readily chose among potential IDs.

The code is not meant to model the emission spectra of its target objects, but rather to aid in the identification of weak lines by providing many alternative IDs and by informing the user of the results of simple tests that can strengthen or weaken each IDs' case. It is an efficient, automated version of the sort of traditional line identification methods used manually for decades.

The code is written entirely in FORTRAN 77, for ease of interpretation by other users (maybe I speak too soon before you get a chance to actually LOOK at the code!). This distribution (number 4) contains all of the subroutines, default data files, and sample input and output, in a single zipped file. Please see Section D.3 for the installation and operation of the code.

## **D.2 User Inputs**

EMILI recognizes the following user inputs, some required and some optional, depending upon which facilities of the program the user wishes to utilize.

**Required:** *Input Line List*

**Optional:** *Matched Line List,*  
*Abundance Table*

In addition a *Command/Parameter List* is required to set global parameters and the names of input/output files.

### D.2.1 Input Line List

This is a list of unidentified lines that the user wants to identify. These lines must have observed wavelengths between 3000-11000Å, the range of a typical optical echelle spectrum. The user specifies the observed wavelength in Å, the measurement/systemic error on either side of the observed value, also in Å, the flux of the line with respect to H $\beta$ , the FWHM in km/s, and the signal-to-noise of the line. Currently the final two parameters, FWHM and signal to noise, are not employed directly by the EMILI code, and are simply propagated into the output to give the user full knowledge of each line the code identifies. Placeholder numeric values can be employed for these parameters.

Users submit a line list in the form of an ASCII text table, with the information for each unidentified line comprising one line in the table ended with a carriage return. Information is read in FORTRAN free format, with blank space separating each individual element on the line. Each element in the line is a FORTRAN “REAL” variable. The code currently accepts up to 1500 unidentified lines. No blank lines

6363.89	-0.08	0.08	7.58e-03	56.70	485.20
6371.42	-0.08	0.08	4.33e-04	31.00	198.30
6379.65	-0.11	0.11	8.62e-06	25.50	10.70
6382.99	-0.11	0.11	1.95e-05	44.10	16.10
6392.50	-0.11	0.11	9.28e-06	17.60	6.20
6402.27	-0.08	0.08	1.07e-04	21.90	75.50
6454.39	-0.11	0.11	1.01e-05	22.40	5.40
6456.00	-0.11	0.11	1.25e-05	19.30	8.70
6461.85	-0.08	0.08	5.83e-04	18.60	93.50
6527.26	-0.08	0.08	2.84e-04	29.30	70.60
6548.10	-0.08	0.08	5.35e-01	39.80	10430.00
6562.80	-0.08	0.08	3.12e+00	31.30	14100.00
6578.05	-0.08	0.08	5.37e-03	18.30	870.50
6583.47	-0.08	0.08	1.63e+00	40.20	11370.00
6610.65	-0.11	0.11	2.79e-05	25.00	11.70
<b>A</b>	<b>B</b>	<b>C</b>	<b>D</b>	<b>E</b>	<b>F</b>

Figure D.1 A subset of the *Input Line List* from **ic418.in**. Listed in columns from left to right are: **A.** observed wavelength ( $\text{\AA}$ ) **B.,C.** errors in measurement ( $\text{\AA}$ ), **D.** flux with respect to  $H\beta$  **E.** FWHM (km/sec) **F.** signal to noise.

should be left at the end of the table, and no special indicators are needed to signify the end of the file. The *Input Line List* is read in by a statement in the main routine: **em4.f**. An example of a segment of an *Input Line List* is given in Figure D.1 (from the file **ic418.in** included with the distribution).

## D.2.2 Matched Line List

This list includes manual identifications made for some of the unidentified lines in the *Input Line List*, usually for strong lines where the identifications are unambiguous. The user specifies the observed wavelength (in  $\text{\AA}$ ), the laboratory wavelength of the

Table D.1 The ionization energy bins used to determine ICF values and velocity corrections to the observed line as a function of putative ID ion's ionization energy.

Bin	Ionization Energy (ev)
1	0-13.6
2	13.6-24.7
3	24.7-54.5
4	54.5-100.0
5	> 100

Table D.2 The lines specifically used to calculate the ICF values, and their defaults in each bin.

Bin	Energy Range (ev)	Default Value	Signature Lines
1	0-13.6	0.01	Mg I] $\lambda 4571$ , Na I $\lambda\lambda 5890, 5896$ , [S I] $\lambda 7775$ , [C I] $\lambda 8727$ , Ca II (H&K) $\lambda\lambda 3934, 3968$
2	13.6-24.7	0.3	H $\beta$
3	24.7-54.5	0.3	He I $\lambda 5876, 4471$
4	54.5-100.0	0.2	He II $\lambda 4686$
5	> 100	0.1	[Fe X] $\lambda 6375$ , [Ne V] $\lambda 3426$ , [Fe VII] $\lambda 6087$ , [Ar X] $\lambda 5533$

transition he or she believes is responsible for the line (also in Å), the ion responsible for the transition in spectroscopic notation, and the observed flux in the line with respect to H $\beta$ . EMILI can use this information in two ways:

1. *Velocity Structure Correction:* All the ions from elements  $Z \leq 30$ , are grouped together into five “bins” determined by ionization energy. The energy bounds of these bins are described in Table D.1. For each manual identification in the *Matched Line List* the velocity difference between the observed and laboratory transition is credited to the bin in which the source ion belongs. Recombination lines here are assumed to originate from the ion of the next higher ionization

state than that given in the spectroscopic notation, while collisionally excited and a few intercombination lines (those going to near-ground energy levels) are assumed to originate from the ionization state indicated by the notation. The average is then taken for each bin to establish a correction to be applied to the wavelength of each observed line, appropriate for the ion responsible for a transition being tested as a possible match to that line. Thus, the systemic velocity and any ionization energy dependence of the expansion velocity of the object can be accounted for, if not already done beforehand in the data. Alternatively, this feature may be turned off, or manual values for the correction in each bin can be specified in the *Command/Parameter List*. The calculated or submitted values will be listed in the *Full Output List* (see Sect. D.5.1).

2. *Ionic Abundances*: To establish ionic abundances for all ions  $Z \leq 30$  the presence of certain “signature” lines (see Table D.2) is sought in the *Matched Line List*. The relative strengths of these lines with respect to  $H\beta$ , if present in the spectra and recorded in this list, are used to establish ionization correction factor (ICF) values for each energy bin. These are roughly percentages that particular ions of that element take up of the entire abundance for that element. Ionic abundances are calculated from the bin for the ion, and the bin for its next lower stage of ionization. If the ion and the next lower stage ion have ionization potentials which reside in the same bin, the ICF value for that bin is multiplied by the abundance for the overall element listed in the *Abundance Table*. If they reside in different bins, then the average of the ICF values is

utilized to obtain an ionic abundance through multiplication with the overall elemental abundance. Exceptions to these rules include the ionic abundance for ionized hydrogen, which is defined as the second bin ICF value times the hydrogen abundance, and the ionic abundances for first and completely ionized helium, which are defined as the overall helium abundance multiplied by the third and fourth ICF bin values respectively. If some of the signature lines are not present in the spectra or not recorded in the *Matched Line List* because their manual identification is ambiguous, the code will attempt to make reasonable guesses as to the ICF values from those lines that are present. Alternatively, the program can use a default set of reasonable ICF values, or a manually chosen set, as specified in the *Command/Parameter List*. The calculated or default values will be recorded in the *Full Output List*.

While the *Matched Line List* is optional, it must be present to utilize the ICF value and velocity correction calculation routines present in EMILI. If a *Matched Line List* is not used, one must specify the ICF and velocity correction values for each energy bin manually in the *Command/Parameter List*, or indicate in the *Command/Parameter List* the desire to use the default values.

If included, the *Matched Line List* must take the form of an ASCII table, with the information about each specified line comprising one line of the table, and ended by a carriage return. These values must appear in the following order:

- observed wavelength: A FORTRAN “REAL” variable, read in free format.
- laboratory wavelength: Also a FORTRAN “REAL” variable, read in free format.

- the element notation: This is a three place character variable: FORTRAN “CHARACTER\*3”. If the line is a forbidden line, the first character must include the “[“ symbol. Non-forbidden lines or intercombination lines must start with the elemental notation. If the notation doesn’t reach three characters the remaining space should be filled with *blank* spaces.
- a single *blank* space between arguments.
- the ion notation: This is a six character variable: FORTRAN “CHARACTER\*6”. The particular ion must be specified in Roman numeral format, with the standard astronomical convention (i.e. Na I is neutral sodium, Na II is first ionized sodium etc...). If the line is an intercombination or forbidden line, the next character immediately after the end of the Roman numeral specification must be the “]” character. If the entire information comprises less than six characters, *blank* spaces should be used to fill out the remaining places.
- the flux with respect to  $H\beta$ : A FORTRAN “REAL” variable, read in free format.

Users are limited to 50 matched lines in total. A line with a “Z” in its first character will be ignored by the code and does not count in the total number of matched lines that can be specified. No blank lines should exist in the file, and no special end of file indicators are necessary. The *Matched Line List* is read by the subroutine: **matchlist4.f**. An example of a *Matched Line List* is given in Figure D.2 (from the file **ic418.match** included with the distribution).



5006.845	5006.843	[O III]	2.15e+00
6583.467	6583.450	[N II]	1.63e+00
3726.035	3726.032	[O II]	1.24e+00
4958.915	4958.911	[O III]	7.27e-01
6548.088	6548.050	[N II]	5.36e-01
3728.785	3728.815	[O II]	5.23e-01
9530.929	9530.600	[S III]	4.23e-01
9068.905	9068.600	[S III]	1.78e-01
7319.087	7318.920	[O II]	3.69e-02
7320.135	7319.990	[O II]	1.01e-01
7329.679	7329.66	[O II]	5.86e-02
7330.754	7330.73	[O II]	5.63e-02
5875.650	5875.640	He I	1.37e-01
7135.744	7135.773	[Ar III]	8.26e-02
4471.499	4471.486	He I	4.49e-02
6730.893	6730.816	[S II]	4.42e-02
6678.153	6678.152	He I	3.87e-02
3868.745	3868.750	[Ne III]	3.09e-02

**A                      B                      C                      D**

Figure D.2 A *Matched Line List* (`ic418.match`). Listed in columns from left to right are: **A.** observed wavelength (Å) **B.** laboratory wavelength of transition (Å), **C.** spectroscopic notation for the transition's source ion **D.** flux with respect to H $\beta$

### D.2.3 Abundance Table

EMILI comes with a default abundance table: `abun.dat`, which are solar abundance values for each element  $Z \leq 30$ , with respect to hydrogen. One may specify an alternative abundance table in the *Command/Parameter List*. Values need not be with respect to hydrogen in a user supplied table, but in that case the numeric absolute abundance of hydrogen must be specified. This is necessary in order to normalize the other elemental abundances to the values used by the code to calculate the *Template flux* (see Sect. D.4). EMILI will query you if a possible line ID does not have a

matching abundance for its source ion.

If an abundance table is specified, it must be in the format of an ASCII table, where information about individual elements must be placed on an individual line in the that table, one element per line. As usual, blank spaces must separate the information on each line, and each line must be ended by a carriage return. Each line must follow this order: The element, listed in standard notation, is a FORTRAN “CHARACTER\*2” variable, followed by a blank space, followed by the value of the numeric abundance (read in as a free format FORTRAN “REAL” variable). Again, no end of file indicator is necessary, and the file must not include blank lines. The user must use elements which are only  $Z \leq 30$ . The code currently can’t accept additional elements, and the transition database only has information for  $Z \leq 30$  elements.

The abundance table is read into the program from the subroutine: **matchlist4.f**. For an example of a properly formatted *Abundance Table*, see **abun.dat**, included with the distribution.

## D.2.4 Command/Parameter List

Here is where EMILI receives additional information for its calculations. This information comes in two classes: input and output file names, and parameter specifications. Some of these parameters are required and some are optional. A sample command list: **ic418.cmd** is included with the distribution and is shown in Figure D.3.

The command list is a simple ASCII text table, with each line setting

a file name or parameter. Each line in the list consists of a command (A,L,M,I,O,D,T,N,deplete,vel,icf) followed by various arguments. Each line may be no more than 60 characters in length, with individual arguments no longer than 15 characters, ended with a carriage return, one command per line. There may be up to 5 arguments depending upon the command. Commands may be placed in any order. A “Z” placed in the first column of any line will cause the code to skip that line. EMILI will warn before run time, if commands are repeated or if they conflict. The list is read in by the subroutine: **openall4.f**. A detailed description of each line in the example list (Figure D.3), and a description of every possible command perturbation is given below.

#### **Required:**

- “L ic418.in” This specifies the name of the file for the *Input Line List*.
- “T 10000” This sets the electron temperature to 10000 K. This is utilized in the calculation of *Template Flux* values.
- “N 10000” This sets the electron density to 10000 electrons/cm<sup>3</sup>. This is also utilized in *Template Flux* calculations.
- “I 10” This sets the instrumental resolution or natural line width, whichever is the largest, to 10 km/sec. This is utilized by the *Multiplet Check*, to determine if certain multiplet lines are too close to be fully resolved, and thus not searched for during that phase of the code’s calculations.
- “vel+” Commands starting with “vel” indicate how the velocity structure

```

A abund.dat
M ic418.match
O ic418.out
D ic418.dat
T 10000
N 10000
I 10
L ic418.in
vel+
icf+
Z deplete Fe 50 1 2

```

Figure D.3 A *Command/Parameter List* (ic418.cmd).

should be calculated. The calculation may be carried out in three different ways, reflected in these three options:

- “vel+” Calculate the velocity correction for each energy bin (see Table 1) from the data of the *Matched Line List*. In order to use this option you must specify the file name for the *Matched Line List* with the “M” command.
- vel-: Assume that the observed lines already have been corrected to the nebular rest frame, and that there is no ionization energy dependent ve-

locity flow. This essentially sets the velocity correction value to zero for each energy bin.

- “vel 99 99 99 89 89” Use the values specified as arguments as the velocity correction values (in km/sec) to apply to an ion residing in each of the five bins.
- “icf+” Commands beginning with “icf” specify how the ICF values for each bin should be specified and consequently used to calculate ionic abundances. These calculations may be performed in three different ways, specified here by three different formats:
  - “icf+” Calculate the ICF values for each bin from the data of the *Matched Line List*. If this option is used a *Matched Line List* must be specified with the “M” command.
  - “icf-” Use the default ICF values for each bin (see Table D.2).
  - “icf 0.1 0.2 0.3 0.3 0.1” Use the values specified as arguments as the ICF values to be applied to ions in each of the five energy bins. These must sum to one.

**Optional:**

- “M ic418.match” This specifies the name of the *Matched Line List*. If this command is not included, one must choose to use manual or default values for the velocity correction and ICF values for each bin.

- “O ic418.out” This specifies the name of the file to include the *Full Output List*. If the command is not included, an “.out” will be tacked onto the *Input Line List* name and used as the file name.
- “D ic418.dat” This specifies the name of the *Summary List*. If this command is not included, a “.dat” will be tacked onto the *Input Line List* name and used as the file name.
- “A abun.dat” This specifies the name for the *Abundance Table*. If not present in the *Command/Parameter List* the code will utilize the default table: **abun.dat**.
- “deplete Fe 50 1 2”

Lines beginning with “**deplete**” tell EMILI to reduce the abundance of certain ions, after the ionic abundances have been calculated using the ICF values. This command may have up to four arguments specified in the following order:

1. The element to deplete.
2. The factor by which to deplete (negative values enhance).
3. The lower end of the range of ionization states to deplete.
4. The upper end of the range of ionization states to deplete.

The following examples illustrate the options that EMILI will assume if specific arguments are missing:

- “deplete Fe 50 1 2” No arguments are missing. This example would ask EMILI to deplete the abundances of Fe I and Fe II by a factor of fifty.

- “**deplete Fe 50 1**” Argument four is not present in the command. EMILI will assume that only the ion indicated by argument three will be depleted. Thus in this example only Fe I would be depleted by a factor of fifty.
- “**deplete Fe 50**” Both arguments three and four are missing. EMILI will deplete all the ions of the indicated element. In this example all the ions of iron are depleted by a factor of fifty.

Arguments one and two must be present for a valid command.

## D.3 Installing and Running the Code

1. One should un-compress and un-archive the file: **em4.tar.gz** into an empty directory. All of the subroutines and data files will be placed in that directory after un-archiving. No additional sub-directories are created. Follow these commands:

```
>cd (name of the directory in which to place EMILI)

>gunzip em4.tar.gz

>tar -xvf em4.tar
```

2. In that directory, compile the code by executing the make file: **./em4.mak**. This is included as part of the distribution.

```
> ./em4.mak
```

The code should compile and run, although in differing Unix platforms the various compilers may complain. On my Red Hat distribution with the generic “f77” compiler, I receive no complaints. The make file assumes that a “f77” compiler exists on your machine.

3. Run the code from the command line:

```
> ./em4 cmdlist
```

where **cmdlist** is the name of the file containing the *Command/Parameter List*.

One should now see various things, starting with a welcome message, followed by a check of the *Command/Parameter List* for errors and proper format. If all is well, the program will echo to the screen the parameters you have entered, wait for a carriage return, then read in the transition and level information databases, before executing. If there are any “fatal” errors in the *Command/Parameter List*, you will need to correct them before the program will run. Don’t be alarmed if it takes a while to read in the transition database, as it includes 280,000 transitions in the specified optical range. EMILI will describe what it is doing every step of the way.

You will know the program is working on the data the user provided when long “block” lists of information begin scrolling on your screen, one for each line in your *Input Line List*. The screen output is echoed into the *Full Output List* (see



Sect. D.5.1) along with the ICF and velocity correction values, either specified in the *Command/Parameter List* or calculated by the code, as well as the other parameters specified in the *Command/Parameter List*.

When completed the program will drop you back to the shell, where you can look at the *Outputs* (see Sect. D.5) in your favorite text editor.

Try it with the included command/parameter and line lists: **ic418.cmd**, **ic418.match**, and **ic418.in**:

```
>./em4 ic418.cmd
```

**Yields:**

*Full Output List:*   **ic418.out**

*Summary List:*      **ic418.dat**

On my 700 MHz notebook it takes about 5-6 minutes to process the 805 lines in the list: **ic418.in**.

## D.4   The EMILI Process

The process begins by reading in the information about each unidentified line the user wishes to have EMILI identify from the *Input Line List*. If the user supplies a *Matched Line List*, and if the appropriate commands have been issued in the *Command/Parameter List*, the code will use the pre-identified lines to make *Ionic Abundance* calculations, and to determine if any *Velocity Structure* may be present, calculating any necessary correction values. If the *Matched Line List* is not sup-

plied, or if the ICF value and velocity structure commands have been set not to use the *Matched Line List*, the same calculations will be carried out with the default or manually specified values.

For each unidentified line, the code searches the transition database for all lines within 200 km/sec, to account for the largest possible systemic velocity for nearby emission-line regions. These comprise the first set of putative IDs for that line. The *Velocity Structure Correction* (manually specified or computed by the code), appropriate to each putative ID's source ion, is then applied to the observed wavelength of the line being identified in order to bring the observed value into the nebular "rest frame" for the region where that ion resides. Further consideration is given only those putative IDs for which the residual wavelength difference after correction is less than (currently) five sigma of the observed value's measurement error (transition wavelength uncertainties are currently **not** included in the error). For each surviving putative transition a *Template Flux* with respect to  $H\beta$  is calculated, which is a predicted, order-of-magnitude estimate of the strength of that line, under the specified nebular conditions (temperature and density supplied by the user). This estimate is based on makes several simplifying assumptions about each transition:

1. Each transition has both a collisionally excited and recombination component to its strength.
2. The collisionally excited portion of the flux uses order of magnitude estimates of collision strengths and transition probabilities according to the type of transition (electric dipole, magnetic dipole, electric quadrupole) it represents. The

collisional component assumes a simple two level atom, and allows for collisional de-excitation.

3. The recombination excited portion also uses a generic spontaneous transition coefficient, and is considered insensitive to either temperature or density, influenced mostly by the direct abundance of the source ion. It also assumes a two level atom and does not employ any branching ratios.

Only transitions which are within a factor of  $10^3$  of the highest calculated template flux among all putative IDs considered at this stage are retained. This assumes that the transitions predicted to be the strongest are the most likely to actually manifest themselves in the spectrum as an observed line.

Upon these remaining putative transitions a *Multiplet Check* is carried out. This involves looking for companion multiplet lines in the *Input Line List*, of the same or stronger transition type, which are approximately close both in wavelengths and expected observed flux. It is expected that the ratio of the products of the statistical weights and Einstein coefficients between the putative ID transition and another transition from the same multiplet, should be fairly close to the ratio of their associated lines' observed flux ratio, within a factor of three. If the Einstein coefficients are not available for these transitions, or when comparing different types of transitions (such as magnetic dipole versus electric quadrupole) the code assumes that the ratio of observed fluxes should at least be within a factor of ten (or  $10^{-4}$  when a weaker-type transition type is compared to a stronger type). Since multiplet lines arise from the same element and creation mechanism, they should also show the same residual

velocity differences between corrected observed values and laboratory wavelengths.

This check is **only** carried out for lines originating from pure LS coupling levels.

Finally, the code uses the residual wavelength difference between the corrected wavelength of observed line and the putative ID's laboratory transition, the relative strength of its *Template Flux* with respect to other putative IDs surviving to this stage, and the results of the *Multiplet Check* to rank the potential IDs. This is done by assigning a numeric Identification Index (*IDI*) value, derived from these criteria, to each putative ID. See Table D.3 for a detailed explanation of how this score is calculated.

## D.5 Outputs

EMILI generates two output files, whose names the user may specify in the *Command/Parameter List*:

**Outputs:**    *Full Output List*,  
                  *Summary List*

We describe the *Full Output List*, and *Individual Line Identification* within that list, and *Summary List* in the following sections.

### D.5.1 Full Output List

The distribution comes with a sample *Full Output List*: **ic418.out**, which will be regenerated if the code is run with an unaltered command list: **ic418.cmd**. The output consists of five parts (the first four depicted in Figure D.4) listed in the following

Table D.3 For each observed unidentified line, all putative IDs are ranked, by defining a “score” or IDI value for each transition. The IDI is awarded on the basis of the putative ID meeting the main criteria listed below. A lower score generally means a better ID.

### 1. Flux Basis ( $F$ )

Putative ID template flux satisfies the following condition:

$F$	Condition
0	Exceeds computed fluxes of all other putative IDs by factor $\geq 10$ .
1	Within a factor of 10 of the largest putative ID template flux.
2	Within a factor of 100 of the largest putative ID template flux.
3	Within a factor of 1000 of the largest putative ID template flux.

### 2. Wavelength Basis ( $W$ )

The residual wavelength difference (in km/s) between the corrected observed line’s wavelength and that for the putative ID is within a number of measurements sigmas ( $\sigma$ ) of the observed line’s corrected value:

$W$	Conditions
0	$\leq 0.5\sigma$
1	$\leq 1.0\sigma$
2	$\leq 1.5\sigma$
3	$\leq 2.0\sigma^{(a)}$

(a) code currently set to include only transitions  $\sigma \leq 5$

### 3. Multiplet Basis ( $M$ )

For a putative ID, the number of detected multiplet members,  $D$ , out of a possibly observable number,  $P$ :

$M$	Conditions
0	$P/D = 1/1, D > 2$
1	$P/D = 0/0, 2/1$
2	$P/D = 1/0, (> 2/1)$
3	$P/D = (> 1)/0$

$IDI = F + W + M$ , with equal weight to each factor.

```

EMILI Output File
-----
Input Line List: emili8.in
Input Matched List: emili8.match
Results List: emili9.out
Short Results List: emili9.dat
Abundance Table: abund.dat
Electron Temp: 10000.
Electron Density: 10000.
Inst. Resolution: 10.

ICF Values: Bin/%
ix 1: 0.00999999978
ix 2: 0.498415828
ix 3: 0.489584208
ix 4: 0.00100000005
ix 5: 0.00100000005

Velocity Structure: Bin/Vel (km/s)
irvcor 1: 4.26208973
irvcor 2: 4.08970976
irvcor 3: 1.74469769
irvcor 4: -0.0550202653
irvcor 5: -0.0550202653

```

Figure D.4 The header for the EMILI output file generated by its run on the included data. Information regarding the input/output files, specified temperature, density, and instrumental resolution, is contained here, as are the values for the ICFs (labeled here as “*ix* 1” – “*ix* 5”) and the velocity corrections (labeled here as “*irvcor* 1” – “*irvcor* 5”) for the five ionization energy bins. No elements were depleted in this run.

order:

1. *Parameter Summary:* This will echo those parameters specified in the *Command/Parameter List*, including file names, electron temperature or density, and the instrumental resolution/natural line width.
2. *ICF Values:* The value for each ionization energy bin is listed here.
3. *Elements Depleted:* The ions that were depleted or enhanced in the *Command/Parameter List*, and the amount by which they were depleted or en-

hanced.

4. *Velocity Structure*: The velocity correction in km/sec applied for all ions residing in each energy bin.
5. *Individual Line Identifications*: There then follow several “blocks” of information. The output contains one such block of information for each unidentified line in the *Input Line List*. This block includes an individual line’s potential identifications (up to 100 per each line), derived from the results of the checks carried out by the code. Following the first row, which reiterates the observed parameters of the line, each succeeding row lists a “putative” ID, drawn from the transition database, that the code has judged to be a possible ID. Each transition is listed in order of velocity residual between the corrected observed wavelength and the laboratory wavelength of the putative ID, starting with the greatest value to one side of the corrected observed wavelength, proceeding to the greatest value on the other side. An example of an identification of a line observed at  $6347.19\text{\AA}$  after correction to the nebular rest frame, from the included *Full Output List* **ic418.out** is given in Figure D.5. We detail the format of this figure in the following section.

## D.5.2 Sample Line Identification

Format of a sample *Individual Line Identification* from the *Full Output List* (see Figure D.5):

Observed Line: 6347.19 5.1E-04 S/N: 83.30 FWHM: 47.7									
6347.15	6346.860	N II	470862882	262	3.5E-04	13.8	5/0	8	
6347.19	6346.970	Mg II	806382603	262	1.0E-04	10.4	2/0	8	
6347.15	6347.030	Mn III	1680117006	6	1.3E-06	5.8	7/0	9	
6347.15	6347.030\$	Ni II	1880698124	6	5.9E-06	5.8	0/0	7D	
6347.10	6347.014	Ca I	1342797915	7	9.5E-07	4.0	1/0	7D	
+ 6347.15	6347.110	Si II	940585992	262	6.7E-04	2.0	1/1	2A	6371.370 0.6
+ 6347.15	6347.170*	Si II	940655642	6	1.2E-04	-0.8	0/0	2A	
+ 6347.15	6347.230	Cl II	1142065248	6	1.0E-06	-3.6	3/0	7D	
6347.10	6347.243	Ca I	1342715984	7	1.0E-06	-6.8	1/0	8	
6347.10	6347.250\$	Si I	940079130	6	2.8E-05	-6.9	0/0	6C	
6347.10	6347.330\$	Si I	940078106	6	2.8E-05	-10.7	0/0	7D	
6347.15	6347.380	Ni II	1880493233	6	6.0E-06	-10.7	1/0	9	
6347.10	6347.340 [V II]		1544610843	38	2.5E-05	-11.2	5/0	9	
6347.10	6347.346\$	Fe I	1745668264	7	3.6E-05	-11.5	0/0	7D	
6347.10	6347.346\$	Ni I	1879307325	7	2.0E-06	-11.5	0/0	8	
6347.10	6347.422	Ca I	1342798940	7	9.5E-07	-15.2	1/0	9	
6347.15	6347.543	Fe II	1746262248	7	2.7E-04	-18.4	6/0	8	
6347.15	> 6346.560	Si II	940680287	262	1.1E-04	28.0	1/0	0<	
<div style="display: flex; justify-content: space-around; font-weight: bold; font-size: 1.2em;"> <span>A</span> <span>B</span> <span>C</span> <span>D</span> <span>E</span> <span>F</span> <span>G</span> <span>H</span> <span>I</span> <span>J</span> </div>									

Figure D.5 An example of EMILI output from the *Full Output List* (ic418.out). This is an identification of a line observed at 6347.19Å (after correction to the nebular rest frame as established by the Balmer and Paschen series of H $\beta$ ). EMILI suggests that Si II  $\lambda$ 6347.100Å is the most likely ID. This ID has a small residual wavelength difference (indicated by small value in km/sec in column G). It also has a *Template Flux* (column F) nearly the same value as what was observed (top line, second numeric value). An additional multiplet line, Si II 6371.370Å (column J), was found to correspond with another line in the *Input Line List* and indeed the code found the only other multiplet line it expected to find (column H). Thus, this putative ID did well (column I) with a low score and a primary (“A”) ranking.

The first row contains the observed parameters of the particular line, including observed wavelength, flux with respect to H $\beta$ , signal to noise, and FWHM in km/sec, drawn from the *Input Line List*. There then follows a table of information, whose columns provide the following information:

#### Columns:

- **A.** The observed line’s wavelength corrected appropriately for the ion responsi-



ble for the putative ID transition in that row. A plus before the value indicates that the transition's laboratory wavelength and the corrected observed wavelength are less than one sigma of the observed value's measurement error apart.

- **B.** The putative ID's laboratory wavelength. A "\$" following the wavelength value indicates that the transition involves a non LS coupling level as either or both the origin and destination level. As mentioned, the *Multiplet Check* is not currently carried out for such putative IDs. An "\*" following the wavelength value indicates that all of the multiplet lines involving the particular putative ID, are unresolvable because they are all within the natural line width or instrumental resolution specified in the *Command/Parameter List*. These are collapsed into a statistically weighted single line of the wavelength proceeding the "\*". The *Multiplet Check* is not carried out for these lines. The code is currently limited to collapsing lines down if all of the multiplet lines are within the instrumental resolution/natural line width. Thus, if two of six lines of a particular multiplet, could be blended, the code considers each of those two as a separate ID. This will be a focus of continuing work in the next version of the code.
- **C.** The spectroscopic notation for the putative ID.
- **D.** An internal reference number for this transition in the Atomic Line List v2.04. This integer, along with the integer in column **E**, can be used with an auxiliary reader included with the EMILI distribution (see Sect. D.5.4) to obtain information about the electronic configuration, term notation, and angular

momentum  $j$  values belonging to the levels this transition traverses.

- **E.** A second internal reference number for the transition.
- **F.** The *Template Flux* calculated for the putative ID.
- **G.** The residual wavelength difference, measured in km/sec, between the corrected observed value of the line, and the laboratory wavelength of the putative ID.
- **H.** The *Multiplet Check* statistics, with the numbers of expected multiplet lines, followed after the slash by the number of lines found to have potential matches in the *Input Line List*, not including the putative line itself.
- **I.** The EMILI assigned **IDI** value (see Table D.3) which serves as a measure of the “goodness” of the match based upon the criteria mentioned above, with lower numbers indicating better IDs. EMILI also assigns a letter “A,B,C, or D” to indicate primary, secondary, tertiary, and fourth ranked identifications, based upon the relative numeric scores.
- **J.** Here is where supporting results from the *Multiplet Check* are noted. Additional multiplet lines’ laboratory wavelengths that were found to correspond with other lines in the *Input Line List* are listed here along with the residual velocity difference with those observed lines, for comparison with the same value in column **E**. Up to three lines, if they can be found, will be displayed here, listed in order of decreasing observed strength.

In the final row of each individual line identification, beginning with a “>” and ending with a “<”, in the location where a rank would go in the column **I**, is listed the transition with the strongest calculated *Template Flux* in the annulus between the initial EMILI acceptance radius and twice that radius away from the observed wavelength. As mentioned, EMILI is currently set to accept only those transitions within  $5\sigma$  of the observed wavelength for template flux calculations, where  $\sigma$  is the measurement uncertainty of the line being ID’d. Thus, this row includes the predicted strongest template flux transition in the region  $5 - 10\sigma$  away from the wavelength for that line in the *Input Line List*. The putative ID has no bearing on the rank of the other putative IDs (no *IDI* score is assigned), but the multiplet check is carried out. This was primarily put in to handle occurrences where the transition’s laboratory wavelength in the database appears to be highly suspect (such as is the case for [Ne III]  $\lambda 3868\text{\AA}$ ), and to allow them to be considered as additional alternative IDs.

### D.5.3 Summary List

This file contains a summary of the EMILI results (see Figure D.6 and the included file **ic418.dat**). For each unidentified line subjected to testing by the code, the corresponding primary ID or IDs, indicated by an “A” in column **G** in the *Full Output List* along with their laboratory wavelengths, are listed adjacent to that line’s measured attributes (observed wavelength and flux with respect to  $H\beta$ ).

4058.29	4.2E-05	N II	4058.16,
4065.23	5.5E-05	Fe III	4065.25,
4067.33	3.6E-05	[Fe III]	4067.30,
4068.67	1.8E-02	[S II]	4068.60,
4069.63	2.0E-04	O II	4069.62,
4069.89	2.0E-04	O II	4069.88,
4072.15	3.3E-04	O II	4072.15,
4074.51	1.0E-04	C II	4074.48,
4075.89	4.4E-04	O II	4075.86,
4076.37	7.6E-03	[S II]	4076.35,
4078.81	5.6E-05	O II	4078.84,
4079.64	2.5E-05	[Fe III]	4079.70,
4082.32	5.3E-05	N II	4082.27,
4083.87	4.8E-05	[Fe II]	4083.78, O II 4083.90,
4084.67	4.7E-05	[Co IV]	4084.59,
4085.10	7.6E-05	O II	4085.11,
4087.15	4.5E-05	O II	4087.15,
4089.29	1.1E-04	O II	4089.29,
4092.92	3.2E-05	O II	4092.93,
4093.92	4.9E-05	N III	4093.68, Na I 4093.88,
4095.65	4.2E-05	O II	4095.64,
4096.51	2.8E-05	[Fe III]	4096.61,

**A                      B                      C**

Figure D.6 A segment from a *Summary List* (ic418.dat). From left to right the columns are: **A**. a unidentified line's observed wavelength **B**. that line's measured flux with respect to H $\beta$  **C**. the EMILI primary IDs (labeled "A" in the *Full Output List*) associated with the line.

## D.5.4 Reader

A separate program is included with the distribution which reads the EMILI output and provides more detailed information regarding the transitions the user may choose as IDs then collating the information in an additional output file. Specifically, this reader will take a EMILI *Full Output List*, marked-up according to a simple scheme, and extract the information for user-chosen putative IDs, using the previously mentioned internal reference numbers found in the output, then tabulate it in a ASCII text file. These internal reference numbers provide information regarding the transition's atomic parameters and type. This allows for more rapid EMILI-derived

identifications, without generating gigantic lists of such information in the actual EMILI output files during run-time.

To use the reader, the user simply marks on the EMILI *Full Output List* an “\*” in the first space of the any row containing a putative ID of interest. This may be done for as many lines and for as many putative IDs for those lines as the user wishes. Entries will be generated in a user-named file. The routine will reference the transition database and provide information about these transitions in the same file.

For instance, suppose I were to mark an “\*” in the first space of the row containing the putative ID that begins with:

```
*+ 6347.15 |    6347.110  Si II      940585992    262 ...
```

The reader would generate a corresponding entry in the reader output file:

```
*+ 6347.19  47.7 5.1e-4  83.3 2A Si II 6347.11 2S 3s2.(1S).4s ...
```

where from left to right are observed wavelength, FWHM, flux, and S/N (as supplied in the *Input Line List*), then the ion, accepted rest (laboratory) wavelength, the upper and lower energy level terms and electron configurations, and finally the upper and lower total angular momentum  $j$  values for the levels traversed by the particular putative ID transition (entry is truncated here for space reasons). If additional IDs are marked for the same emission lines, these will align in the output file with the transition information for the first ID that the reader encounters in the individual line output lists.

To invoke the reader simply compile at the command prompt:

```
> ./emread.mak
```

then run at the command prompt:

```
>./emread arg1 arg2
```

where “arg1” is the name of the marked-up EMILI *Full Output List* and “arg2” is name chosen by the user for the results file.

## D.6 Future Improvements

In future editions of the code, we plan on making three major improvements.

1. **Broader Line List:** A still larger and more comprehensive transition database is currently being constructed (Atomic Line List v2.05), which will expand the transition list to include all elements  $Z \leq 36$  (up to all fourth row elements), and will include improved Coulomb calculations of transition probabilities.
2. **Cross Correlation:** Presently the code does not seek corroborating information about a particular putative ID, from the putative IDs of other unidentified lines, beyond those comparisons made during the *Multiplet Check*. Future editions of the code will compare the expected line strength ratio between different lines of differing multiplets with the observed value, and compare the velocity residuals between putative IDs of the same ion and creation mechanism.
3. **Multiple Iterations:** We plan on making the code iterative, using the best IDs from an initial run to re-calculate and improve the accuracy the ionic abundances and velocity structure corrections, for use in successive runs.

We will also be attempting to optimize the weighting given to each component (residual wavelength difference, relative template flux, and multiplet check results) used to construct the final score and subsequent rank for each putative ID for a particular unidentified line. This in order to ascribe more importance to those components which might be more or less appropriate for differing observing parameters (i.e. less emphasis on the residual wavelength difference for lower dispersion spectra etc.).

## D.7 Contact Information

This code is always evolving, and as such is still undergoing testing and revision as I write this, so please pardon the dust (a.k.a. numerous test comments scattered throughout its length). I cannot guarantee that the code is entirely “bug-free” yet (*caveat emptor*). However I hope you are able to use the code with as little trouble as possible, and that it provides you with interesting and accurate results. I am most happy to answer any questions and would appreciate reports of any errors you believe the code is making. Suggested improvements are always welcome.

**sharpee@pa.msu.edu**

For further details and updates please stop by the EMILI web page at:

**<http://www.pa.msu.edu/people/sharpee/emili.html>**

# Appendix E

## IC 418 Line List

Here is presented the IC 418 Line List. Columns are defined as follows:

- (1) The observed wavelength of the line corrected to the nebular rest frame for ionized hydrogen.
- (2) The full width at half maximum intensity (FWHM) of the line in  $\text{km s}^{-1}$ .
- (3) The observed intensity of the Line,  $F(\lambda)$ , with respect to the observed intensity of  $\text{H}\beta$  ( $F(\text{H}\beta) = 1.31 \times 10^{-11} \text{ erg cm}^{-3} \text{ s}^{-1}$ ) in units of  $F(\lambda) * 100/F(\text{H}\beta)$ .
- (4) The de-reddened intensity of the line,  $I(\lambda)$ , with respect to the de-reddened intensity of  $\text{H}\beta$  ( $I(\text{H}\beta) = 2.87 \times 10^{-11} \text{ erg cm}^{-3} \text{ s}^{-1}$ ) in units of  $I(\lambda) * 100/I(\text{H}\beta)$ .
- (5) The signal-to-noise (S/N) of the line. A value of 99999.0 indicates that no S/N was calculated for this line because it wasn't detected by RDGEN



initially, or was a member of a line blend for which S/N of the components were not calculated.

- (6) The EMILI IDI value and rank for the ID transition, where available.

An “\*” in this column indicates an IDI value greater than 9. A “<” in this column indicates that the ID was the strongest predicted transition outside of, but in the vicinity of, the initial EMILI search radius. IDs not chosen from the EMILI output have no data in this column.

- (7) The source ion of the ID transition.

- (8) The tabulated wavelength for the ID transition. All wavelengths are air

wavelengths, and are drawn primarily from the Atomic Line List v2.04.

Exceptions include non-EMILI ID’d He I lines, H I Balmer and Paschen lines above an upper level of  $n = 40$ , and an additional few cases noted by a “†”. A “\*” following the wavelength indicates that the line is a blend of all the closely spaced members of the same multiplet, and is a statistically weighted average of their wavelengths. A “?” after the wavelength indicates a questionable but possible ID based upon the EMILI results and the literature.

- (9) The velocity difference between the tabulated wavelength of the ID transition and the observed wavelength of the line. This value is determined from:

$$\delta V = c \frac{\lambda - \lambda_o}{\lambda} \text{ kms}^{-1} .$$

(10) The spectroscopic term notation and electron configuration of the lower level of the ID transition. Term notation is either in the LS or one of two intermediate coupling schemes:

- LS Coupling:  $(^{2S+1}L)$  where  $S$  is the spin of the valance electrons, and  $L$  the total orbital angular momentum of those electrons.

For example:  $^2P^o = 2Po$  in the table. An example of an ID transition with a lower level based on this coupling is O II  $\lambda 4393.483$ .

- LK Coupling:  $(^{2S_2+1}[K])$  where  $S_2$  is the spin of the external excited electron(s), and  $K$  the coupled value of the total orbital angular momenta of the core and external electron(s) ( $L$ ), in turn coupled with the total spin of the core electrons. This is distinguished from the  $J_1K$  coupling by the inclusion of the  $L$  value (in the usual LS spectroscopic notation a.k.a. P for  $L=1$ , D for  $L=2$  etc...) at the end of the electron configuration.

For example:  $^2[5/2] = 2[5/2]$  in the table. An example of an ID transition with an upper level based upon this coupling is N II  $\lambda 4432.735$

- $J_1K$  Coupling:  $(^{2S_2+1}[K])$  where  $S_2$  is the spin of the external excited electron(s), and  $K$  here is the value of the total angular momentum of the core term ( $J_1$ ) coupled with the orbital angular momentum of the external electron(s).

For example:  $^2[5]^o = 2[5]o$  in the table. An example of an ID transition with an upper level based on this scheme is Ne II  $\lambda 4391.991$ .

The electron configuration takes the form of, as an example,  $2s^2.2p^4$  in the table which is equivalent to  $2s^22p^4$ . Core electrons and external electrons may be separated in this scheme by a core term, in parenthesis and in LS coupling, followed by an external electron or term (also in LS coupling). Values enclosed in “<” and “>” in the core term indicate its total angular momentum  $J$  value.

Iron lines are all based on LS coupling and employ specific alphanumeric level identifiers in place of LS scheme notation.

- (11) The spectroscopic term notation and electron configuration of the upper level of the transition.
- (12) The total angular momentum  $j$  value for the lower state of the ID transition. A “\*\*\*\*” here indicates that the level is a blend of several closely spaced  $j$  values, or that the line was a blend of several transitions from the same level, such as a blended multiplet line indicated by an “\*” following the wavelength in column (7).
- (13) The total angular momentum  $j$  value for the upper state of the transition.
- (14) The EMILI multiplet check results, in the sense that if “5/1” appears in the table, 1 out of 5 lines expected to be present from the same multiplet in the line list, were matched by the code. EMILI did not carry out the check for transitions from Non-LS coupled levels, lines from blended levels, or lines judged by EMILI to blends of all multiplet transitions from the

same upper level. The check was also not done for non-EMILI IDs.

Table E.1 IC 418 Line List

$\lambda_o$ (Å) (1)	FWHM (km/s) (2)	$F(\lambda)/F(H\beta)$ (3)	$I(\lambda)/I(H\beta)$ (4)	S/N (5)	ID: (6)	Ion (7)	$\lambda$ (Å) (8)	$\delta V$ (km/s) (9)	Lower Term/Config (10)	Upper Term/Config (11)	$j_1$ (12)	$j_2$ (13)	Multi (14)
3512.511	22.9	0.1026	0.1365	37.6	2 A	He I	3512.505	-0.5	3Po 1s.2p	3D 1s.12d	2.0	****	0/0
3530.499	24.6	0.1509	0.2002	9990.0	3 A	He I	3530.482	-1.5	3Po 1s.2p	3D 1s.11d	2.0	****	1/0
3554.417	23.1	0.1771	0.2340	127.5	4 B	He I	3554.398	-1.6	3Po 1s.2p	3D 1s.10d	1.0	****	2/0
3560.616	20.3	0.0049	0.0065	7.3	...	...	...	...	...	...	...	...	...
3562.932	20.7	0.0138	0.0182	11.5	4 A	He I	3562.969	3.1	3Po 1s.2p	3S 1s.10s	2.0	1.0	1/0
3574.775	13.5	0.0036	0.0047	7.2	6 B	O II	3574.845 ?	5.9	2D 2s.2p.2.(3P).3d	2Po 2s.2p.2.(3P).5p	1.5	1.5	2/0
				8 D	N II	N II	3574.900 ?	10.5	3P 2s.2p.2.(4P).3d	3Do 2s.2p.2.(4P).3p	2.0	2.0	2/0
3579.402	23.4	0.0103	0.0135	8.1	...	...	...	...	...	...	...	...	...
3587.284	24.4	0.2549	0.3351	161.6	3 A	He I	3587.253	-2.6	3Po 1s.2p	3D 1s.9d	2.0	****	1/0
3590.815	25.3	0.0192	0.0252	21.9	5 A	C II	3590.757	-4.8	4D 2s.2p.(3Po).3p	4Po 2s.2p.(3Po).4s	1.5	0.5	7/0
				7 C	C II	C II	3590.876	5.1	4D 2s.2p.(3Po).3p	4Po 2s.2p.(3Po).4s	2.5	1.5	5/0
3601.327	14.8	0.0021	0.0027	7.2	...	...	...	...	...	...	...	...	...
3606.862	24.6	0.0053	0.0070	7.3	...	...	...	...	...	...	...	...	...
3613.634	21.7	0.4259	0.5577	293.5	2 A	He I	3613.642	0.6	1S 1s.2s	1Po 1s.5p	0.0	1.0	0/0
3616.798	20.7	0.0045	0.0059	11.0	3 A	S II	3616.767	-2.6	2Do 3s.2p.2.(3P).4p	2P 3s.2p.2.(3P).4d	2.5	1.5	1/0
3634.250	25.7	0.3883	0.5069	156.7	4 A	He I	3634.231	-1.6	3Po 1s.2p	3D 1s.8d	2.0	3.0	2/0
3649.872	32.6	0.0109	0.0141	7.5	...	...	...	...	...	...	...	...	...
3652.003	24.0	0.0254	0.0331	25.9	3 A	He I	3651.981	-1.8	3Po 1s.2p	3S 1s.8s	2.0	1.0	1/0
3654.256	9.3	0.0052	0.0067	7.7	...	H I	3654.266	0.8	2 2*	42 42*	****	****	...
3654.681	14.3	0.0107	0.0140	10.2	2 A	N II	3654.670 ?	-0.9	3F 2s.2p.2.(4P).3d	3Do 2s.2p.2.(2D).3p	4.0	3.0	2/1
				...	...	H I	3654.676	-0.4	2 2*	41 41*	****	****	...
3655.113	11.1	0.0114	0.0148	13.5	2 A	H I	3655.117	0.3	2 2*	40 40*	****	****	0/0
				...	...	N II	3655.030 ?	-5.2	3F 2s.2p.2.(4P).3d	3Do 2s.2p.2.(2D).3p	3.0	2.0	...
3655.588	11.6	0.0135	0.0176	19.0	2 A	H I	3655.593	0.4	2 2*	39 39*	****	****	0/0
				...	...	N II	3655.500 ?	-7.2	3F 2s.2p.2.(4P).3d	3Do 2s.2p.2.(2D).3p	1.0	1.0	...
3656.104	12.5	0.0231	0.0300	32.5	3 A	H I	3656.106	0.2	2 2*	38 38*	****	****	0/0
3656.667	13.5	0.0270	0.0352	44.9	2 A	H I	3656.663	-0.3	2 2*	37 37*	****	****	0/0
3657.276	16.2	0.0451	0.0586	54.9	2 A	H I	3657.267	-0.7	2 2*	36 36*	****	****	0/0
3657.936	18.1	0.0758	0.0986	96.0	2 A	H I	3657.923	-1.1	2 2*	35 35*	****	****	0/0
3658.647	19.9	0.0932	0.1212	102.1	2 A	H I	3658.639	-0.7	2 2*	34 34*	****	****	0/0
3659.428	23.5	0.1402	0.1823	126.5	2 A	H I	3659.421	-0.6	2 2*	33 33*	****	****	0/0
3660.286	26.3	0.1871	0.2433	152.8	2 A	H I	3660.277	-0.7	2 2*	32 32*	****	****	0/0
3661.230	27.9	0.2274	0.2956	193.0	2 A	H I	3661.218	-1.0	2 2*	31 31*	****	****	0/0
3662.262	29.1	0.2669	0.3470	266.4	2 A	H I	3662.256	-0.5	2 2*	30 30*	****	****	0/0
3663.406	30.7	0.3058	0.3975	267.6	2 A	H I	3663.404	-0.2	2 2*	29 29*	****	****	0/0
3664.683	31.3	0.3548	0.4610	353.9	2 A	H I	3664.676	-0.6	2 2*	28 28*	****	****	0/0
3666.098	31.4	0.3970	0.5158	364.1	2 A	H I	3666.095	-0.2	2 2*	27 27*	****	****	0/0

Table E.1 (continued) - IC 418 Line List

$\lambda_0$ (Å) (1)	FWHM (km/s) (2)	$F(\lambda)/F(H\beta)$ ( $F(H\beta) = 100$ ) (3)	$I(\lambda)/I(H\beta)$ ( $I(H\beta) = 100$ ) (4)	S/N (5)	ID: (6)	Ion (7)	$\lambda$ (Å) (8)	$\delta V$ (km/s) (9)	Lower Term/Config (10)	Upper Term/Config (11)	$j_1$ (12)	$j_2$ (13)	Multi (14)
3667.682	30.6	0.4353	0.5653	435.3	3 A	H I	3667.681	-0.1	2 2*	26 26*	****	****	0/0
3669.463	31.4	0.5017	0.6514	456.3	3 A	H I	3669.464	0.1	2 2*	25 25*	****	****	0/0
3671.475	31.4	0.5339	0.6930	557.6	2 A	H I	3671.475	0.0	2 2*	24 24*	****	****	0/0
3673.757	32.3	0.5922	0.7684	565.0	2 A	H I	3673.758	0.1	2 2*	23 23*	****	****	0/0
3676.361	32.8	0.6586	0.8542	486.9	3 A	H I	3676.362	0.1	2 2*	22 22*	****	****	0/0
3679.349	33.2	0.7847	1.0173	464.0	3 A	H I	3679.352	0.2	2 2*	21 21*	****	****	0/0
3682.806	34.3	0.8182	1.0602	256.7	2 A	H I	3682.808	0.2	2 2*	20 20*	****	****	0/0
3686.830	32.5	0.9390	1.2159	307.2	3 A	H I	3686.830	0.0	2 2*	19 19*	****	****	0/0
3691.556	32.6	1.1469	1.4841	289.2	2 A	H I	3691.554	-0.2	2 2*	18 18*	****	****	0/0
3697.156	33.5	1.2877	1.6649	436.3	2 A	H I	3697.152	-0.3	2 2*	17 17*	****	****	0/0
3703.852	31.8	1.4822	1.9143	455.8	3 A	H I	3703.852	0.0	2 2*	16 16*	****	****	0/0
3705.017	22.8	0.5795	0.7483	224.3	4 A	He I	3704.996	-1.7	3Po 1s.2p	3D 1s.7d	2.0	3.0	2/0
3711.968	32.0	1.7773	2.2926	726.1	3 A	H I	3711.971	0.2	2 2*	15 15*	****	****	0/0
3721.895	36.3	2.5687	3.3082	439.6	6 B	[S III]	3721.630	-21.4	3P 3s.2.3p.2	1S 3s.2.3p.2	1.0	0.0	0/0
					5 A	H I	3721.938	3.5	2 2*	14 14*	****	****	0/0
3726.035	41.9	96.1832	123.7908	8543.0	0 A	[O II]	3726.032	-0.2	4So 2s.2.2p.3	2Do 2s.2.2p.3	1.5	1.5	1/1
3728.785	43.2	40.6870	52.3426	4280.0	1 A	[O II]	3728.815	2.4	4So 2s.2.2p.3	2Do 2s.2.2p.3	1.5	2.5	1/1
3734.364	31.0	2.3876	3.0689	614.9	3 A	H I	3734.368	0.3	2 2*	13 13*	****	****	0/0
3735.506	38.9	0.0461	0.0593	35.1	8 C	O II	3735.722	17.3	2Po 2s.2.2p.2.(1D).3p	2D 2s.2.2p.2.(1D).4s	1.5	1.5	2/0
					0<	O II	3735.786	22.5	2Po 2s.2.2p.2.(1D).3p	2D 2s.2.2p.2.(1D).4s	1.5	2.5	2/0
3750.149	31.6	3.1656	4.0585	1262.0	3 A	H I	3750.151	0.2	2 2*	12 12*	****	****	0/0
3756.065	37.4	0.0610	0.0782	37.2	4 A	He I	3756.115	4.0	1Po 1s.2p	1D 1s.14d	1.0	2.0	0/0
3768.782	23.2	0.0238	0.0304	38.3	3 A	He I	3768.821	3.1	1Po 1s.2p	1D 1s.13d	1.0	2.0	0/0
3770.631	31.8	3.8028	4.8591	1284.0	3 A	H I	3770.630	-0.1	2 2*	11 11*	****	****	0/0
					7 B	He I	3770.750	9.5	1Po 1s.2p	1S 1s.13s	1.0	0.0	0/0
3777.164	41.5	0.0039	0.0050	9.4	5 A	Ne II	3777.134	-2.4	4P 2s.2.2p.4.(3P).3s	4Po 2s.2.2p.4.(3P).3p	0.5	1.5	6/0
3780.171	33.1	0.0035	0.0045	8.6	...	...	...	...	...	...	...	...	...
3784.851	22.5	0.0294	0.0374	71.6	3 A	He I	3784.895	3.5	1Po 1s.2p	1D 1s.12d	1.0	2.0	0/0
					9 B	O II	3784.990	11.0	2Po 2s.2.2p.2.(3P).4p	2D 2s.2.2p.2.(1D).4d	1.5	2.5	2/0
3795.635	30.0	0.0019	0.0025	6.6	...	...	...	...	...	...	...	...	...
3797.897	31.5	4.4534	5.6643	1187.0	2 A	H I	3797.898	0.1	2 2*	10 10*	****	****	0/0
3801.360	55.5	0.0055	0.0070	10.7	...	...	...	...	...	...	...	...	...
3802.720	37.6	0.0057	0.0073	11.9	8	S II	3802.604	-9.1	4Po 3s.2.3p.2.(3P).4p	4P 3s.2.3p.2.(3P).4d	1.5	0.5	6/0
3805.736	20.3	0.0331	0.0421	99.5	3 A	He I	3805.777	3.2	1Po 1s.2p	1D 1s.11d	1.0	2.0	0/0
3811.854	9.0	0.0015	0.0019	9.9	6 C	S II	3811.745	-8.6	2Po 3s.2.3p.2.(3P).4p	2D 3s.2.3p.2.(3P).4d	0.5	1.5	2/0
3813.451	26.5	0.0026	0.0033	7.6	...	...	...	...	...	...	...	...	...
3817.159	25.2	0.0027	0.0035	7.7	...	...	...	...	...	...	...	...	...
3819.628	23.9	0.8853	1.1218	525.4	4 A	He I	3819.603	-2.0	3Po 1s.2p	3D 1s.6d	2.0	2.0	4/0

Table E.1 (continued) - IC 418 Line List

$\lambda_0$ (Å) (1)	FWHM (km/s) (2)	$F(\lambda)/F(H\beta)$ ( $F(H\beta) = 100$ ) (3)	$I(\lambda)/I(H\beta)$ ( $I(H\beta) = 100$ ) (4)	S/N (5)	ID: (6)	Ion (7)	$\lambda$ (Å) (8)	$\delta V$ (km/s) (9)	Lower Term/Config (10)	Upper Term/Config (11)	$j_1$ (12)	$j_2$ (13)	Multi (14)
3821.849	26.8	0.0038	0.0049	18.3	...	...	...	...	...	...	...	...	...
3829.745	21.3	0.0184	0.0232	34.2	3 A	N II	3829.795	3.9	3P 2s2.2p.(2Po).3p	3Po 2s2.2p.(2Po).4s	1.0	2.0	4/2
3831.645	20.6	0.0237	0.0300	58.1	9	S II	3831.379	-20.8	2Po 3s2.3p2.(3P).4p	2D 3s2.3p2.(3P).4d	1.5	2.5	2/0
3833.550	20.0	0.0539	0.0681	105.7	7 C	C II	3831.726	6.3	2Po 2s2.4p	2D 2s.2p.(3Po).3p	1.5	2.5	2/0
3834.140	25.2	0.0024	0.0030	8.3	...	...	3833.584	2.7	1Po 1s.2p	1D 1s.10d	1.0	2.0	0/0
3835.387	32.0	7.5117	9.4921	2711.0	2 A	H I	...	...	...	...	...	...	...
3838.349	25.5	0.0581	0.0734	98.5	7 D	S III	3835.384	-0.2	2 2*	9 9*	****	****	0/0
3842.183	19.1	0.0100	0.0126	33.6	2 A	N II	3838.268	-6.3	3Po 3s2.3p.4s	3Po 3s2.3p.4p	2.0	2.0	3/1
3848.265	35.0	0.0217	0.0274	56.4	3 A	Mg II	3838.374	1.9	3P 2s2.2p.(2Po).3p	3Po 2s2.2p.(2Po).4s	2.0	2.0	3/1
3850.392	45.2	0.0183	0.0231	46.1	2 A	Mg II	3842.187	0.3	3P 2s2.2p.(2Po).3p	3Po 2s2.2p.(2Po).4s	0.0	1.0	5/3
3853.755	36.3	0.0046	0.0058	11.2	5 A	Si II	3848.212	-4.1	2D 3d	2Po 5p	2.5	1.5	2/1
3855.089	29.6	0.0078	0.0098	29.9	2 A	N II	3848.341	5.9	2D 3d	2Po 5p	1.5	1.5	2/0
3856.054	45.6	0.0805	0.1013	188.1	1 A	Si II	3850.386	-0.5	2D 3d	2Po 5p	1.5	0.5	2/1
3862.619	40.6	0.0337	0.0424	110.2	1 A	Si II	3853.664	-7.1	2D 3s.3p2	2Po 3s2.(1S).4p	1.5	1.5	2/0
3867.486	21.7	0.0677	0.0851	183.6	3 A	He I	3855.096	0.5	3P 2s2.2p.(2Po).3p	3Po 2s2.2p.(2Po).4s	1.0	0.0	5/3
3868.745	13.6	2.4614	3.0916	805.3	0<	[Ne III]	3856.018	-2.8	2D 3s.3p2	2Po 3s2.(1S).4p	2.5	1.5	2/2
3871.781	21.2	0.0606	0.0760	183.0	3 A	He I	3856.063	0.7	3P 2s2.2p.(2Po).3p	3Po 2s2.2p.(2Po).4s	2.0	1.0	4/3
3873.477	15.2	0.0014	0.0018	8.6	7	Fe I	3856.134	6.2	4Do 2s2.2p2.(3P).3p	4D 2s2.2p2.(3P).3d	1.5	0.5	9/1
3876.477	43.7	0.0055	0.0069	12.1	5 D	C II	3862.596	-1.8	2D 3s.3p2	2Po 3s2.(1S).4p	1.5	0.5	2/2
3882.178	13.7	0.0050	0.0063	27.4	3 A	O II	3867.472	-1.1	3Po 1s.2p	3S 1s.6s	2.0	1.0	1/0
3883.110	23.7	0.0022	0.0027	10.3	4 A	O II	3869.060	24.4	3P 2s2.2p4	1D 2s2.2p4	2.0	2.0	1/1
3884.008	16.9	0.0011	0.0014	8.8	6 A	C II	3871.830	3.8	1Po 1s.2p	1D 1s.9d	1.0	2.0	0/0
3888.939	66.4	12.8101	16.0294	3433.0	5 A	H I	3873.594 ?	9.0	z5Po 3d6.(5D).4s.4p.(3Po)	5D 3d6.4s.(6D).6s	3.0	3.0	4/1
3891.462	25.5	0.0027	0.0034	99990.0	6 A	Ar II	3876.392	-6.6	4Fo 2s.2p.(3Po).3d	4G 2s.2p.(3Po).4f	3.5	4.5	5/0
3892.335	14.0	0.0021	0.0027	8.0	5 B	S II	3876.653	13.6	4Fo 2s.2p.(3Po).3d	4G 2s.2p.(3Po).4f	2.5	3.5	8/0
3892.769	31.0	0.0020	0.0025	13.4	...	...	3876.186	-22.5	4Fo 2s.2p.(3Po).3d	4G 2s.2p.(3Po).4f	4.5	5.5	2/0
3895.096	32.9	0.0032	0.0040	7.4	8	Fe I	3882.194	1.2	4Do 2s2.2p2.(3P).3p	4D 2s2.2p2.(3P).3d	3.5	3.5	3/1
3896.201	27.7	0.0044	0.0055	13.7	6 A	O II	3882.446	-20.7	4Do 2s2.2p2.(3P).3p	4D 2s2.2p2.(3P).3d	1.5	1.5	7/0
							3883.137	2.1	4Do 2s2.2p2.(3P).3p	4D 2s2.2p2.(3P).3d	3.5	2.5	4/1
							3883.853	-12.0	4Fo 2s.2p.(3Po).3d	4G 2s.2p.(3Po).4f	4.5	3.5	5/1
							3889.049	8.5	2 2*	8 8*	****	****	0/0
							3888.605 *	-25.8	3S 1s.2s	3Po 1s.3p	****	****	...
							3891.401 ?	-4.7	4D 3s2.3p4.(3P).3d	4Do 3s2.3p4.(3P).4p	0.5	0.5	9/1
							3892.288	-3.6	4Po 3s2.3p2.(3P).4p	4P 3s2.3p2.(3P).4d	2.5	2.5	3/0
							...	...	...	...	...	...	...
							3895.232	10.5	z5Po 3d6.(5D).4s.4p.(3Po)	5D 3d6.4s.(6D).6s	2.0	2.0	7/1
							3896.303	7.9	4Do 2s2.2p2.(3P).3p	4P 2s2.2p2.(3P).3d	2.5	1.5	5/0
							3896.349	11.4	z5Po 3d6.(5D).4s.4p.(3Po)	5D 3d6.4s.(6D).6s	1.0	0.0	8/2

Table E.1 (continued) - IC 418 Line List

$\lambda_o$ (Å)	FWHM (km/s)	$F(\lambda)/F(H\beta)$ ( $F(H\beta) = 100$ )	$I(\lambda)/I(H\beta)$ ( $I(H\beta) = 100$ )	S/N	ID:	Ion	$\lambda$ (Å)	$\delta v$ (km/s)	Lower Term/Config	Upper Term/Config	$j_1$	$j_2$	Multi
(1)	(2)	(3)	(4)	(5)	(6)	(7)	(8)	(9)	(10)	(11)	(12)	(13)	(14)
3899.208	44.9	0.0064	0.0080	15.8	7	S III	3899.028	-13.8	3Po 3s2.3p.4s	3P 3s2.3p.4p	2.0	1.0	4/0
3907.470	21.9	0.0028	0.0035	13.5	3 A	O II	3907.455	-1.2	4Do 2s2.2p2.(3P).3p	4P 2s2.2p2.(3P).3d	2.5	2.5	4/0
3909.251	9.6	0.0015	0.0019	7.6	...	...	...	...	...	...	...	...	...
3918.930	18.7	0.0858	0.1068	226.4	4 A	C II	3918.967	2.8	2Po 2s2.3p	2S 2s2.4s	0.5	0.5	1/1
3920.640	18.3	0.1650	0.2052	372.8	3 A	C II	3920.682	3.2	2Po 2s2.3p	2S 2s2.4s	1.5	0.5	1/1
3923.200	36.9	0.0035	0.0043	14.6	...	...	...	...	...	...	...	...	...
3924.007	36.9	0.0029	0.0036	7.9	...	...	...	...	...	...	...	...	...
3926.544	21.8	0.1013	0.1258	247.6	3 A	He I	3926.544	0.0	1Po 1s.2p	1D 1s.8d	1.0	2.0	0/0
3929.127	18.5	0.0023	0.0028	5.8	5 A	O II	3926.581	2.8	4Do 2s2.2p2.(3P).3p	4P 2s2.2p2.(3P).3d	3.5	2.5	2/2
3935.956	22.3	0.0119	0.0147	43.8	1 A	He I	3928.970 *	-12.0	2Fo 2s2.4f	2G 2s2.14g	****	****	...
3962.513	44.8	0.0048	0.0059	9.6	...	...	3935.945	-0.8	1Po 1s.2p	1S 1s.8s	1.0	0.0	0/0
3963.797	17.1	0.0012	0.0014	7.7	...	...	...	...	...	...	...	...	...
3964.727	22.1	0.8384	1.0336	509.9	2 A	He I	3964.729	0.1	1S 1s.2s	1Po 1s.4p	0.0	1.0	0/0
3967.457	14.2	0.7914	0.9751	229.6	0<	[Ne III]	3967.790	25.2	3P 2s2.2p4	1D 2s2.2p4	1.0	2.0	1/1
3970.074	31.9	13.6820	16.8492	2775.0	3 A	H I	3970.072	-0.1	2 2*	7 7*	****	****	0/0
3977.342	25.5	0.0021	0.0026	9.6	6 A	C II	3977.250	-6.9	4Do 2s.2p.(3Po).3d	4D 2s.2p.(3Po).4f	2.5	2.5	6/0
3979.851	24.8	0.0016	0.0020	10.7	...	S II	3979.824	-2.0	4So 3s2.3p2.(3P).4p	4P 3s2.3p2.(3P).4d	1.5	0.5	...
3986.459	30.2	0.0027	0.0034	9.7	...	...	...	...	...	...	...	...	...
3988.516	25.8	0.0039	0.0048	9.9	...	...	...	...	...	...	...	...	...
3992.088	33.4	0.0007	0.0008	7.0	...	Ar II	3992.088 ?	0.0	4D 3s2.3p4.(3P).3d	4Do 3s2.3p4.(3P).4p	1.5	2.5	...
3998.781	32.7	0.0073	0.0089	19.9	8	N III	3998.630	-11.3	2D 2s2.4d	2Fo 2s2.5f	1.5	2.5	2/0
4004.939	33.7	0.0026	0.0032	8.2	7	Ni III	3998.759	-1.6	4So 3s2.3p2.(3P).4p	4P 3s2.3p2.(3P).4d	1.5	1.5	2/2
4009.256	21.7	0.1522	0.1860	367.9	1 A	He I	4005.180 ?	18.0	3F 3d7.(4F).4d	3Do 3d6.(5D).4s.4p	4.0	3.0	2/1
4015.931	20.1	0.0034	0.0041	15.3	...	...	4009.256	0.0	1Po 1s.2p	1D 1s.7d	1.0	2.0	0/0
4018.473	25.1	0.0009	0.0012	9.4	7 D	Ni III	4018.760 ?	21.4	3F 3d7.(4F).4d	3Do 3d6.(5D).4s.4p	3.0	2.0	5/2
4023.993	18.8	0.0176	0.0215	79.7	7 C	O II	4023.868	-9.3	2F 2s2.2p2.(1D).3d	2[2]o 2s2.2p2.(1D).4f.D	3.5	2.5	...
4026.207	22.9	1.7237	2.0978	412.4	8	He I	4023.980	-1.0	1Po 1s.2p	1S 1s.7s	1.0	0.0	0/0
4027.209	31.7	0.0280	0.0340	9999.0	3 A	Fe I	4026.078	-9.6	3Fo 2s2.2p.(2Po).3d	2[9/2] 2s2.2p.(2Po<3/2>).4f.G	3.0	4.0	...
4028.221	12.6	0.0045	0.0055	12.2	...	...	4026.186	-1.6	3Po 1s.2p	3D 1s.5d	2.0	2.0	4/0
4032.779	51.5	0.0080	0.0098	12.6	3 A	S II	4027.098 ?	-8.3	y5Fo 3d7.(4F).4p	g5G 3d6.4s.(4D).4d	5.0	4.0	5/2
4035.165	37.9	0.0059	0.0071	16.6	3 A	N II	4032.767	-0.9	4So 3s2.3p2.(3P).4p	4P 3s2.3p2.(3P).4d	1.5	2.5	1/1
4041.303	24.9	0.0100	0.0121	30.2	2 A	O II	4035.081	-6.2	3Fo 2s2.2p.(2Po).3d	2[7/2] 2s2.2p.(2Po<3/2>).4f.G	2.0	3.0	...
					4 B	O II	4035.073	-6.8	4F 2s2.2p2.(3P).3d	2[3]o 2s2.2p2.(3P).4f.F	2.5	2.5	...
					2 A	O II	4041.278	-1.9	4F 2s2.2p2.(3P).3d	2[2]o 2s2.2p2.(3P).4f.F	2.5	2.5	...
					3 B	N II	4041.310	0.5	3Fo 2s2.2p.(2Po).3d	2[9/2] 2s2.2p.(2Po<3/2>).4f.G	4.0	5.0	...



Table E.1 (continued) - IC 418 Line List

$\lambda_o$ (Å)	FWHM (km/s)	$F(\lambda)/F(H\beta)$ (3)	$I(\lambda)/I(H\beta)$ (4)	S/N	ID:	Ion	$\lambda$ (Å)	$\delta V$ (km/s)	Lower Term/Config	Upper Term/Config	$j_1$	$j_2$	Multi
(1)	(2)	(3)	(4)	(5)	(6)	(7)	(8)	(9)	(10)	(11)	(12)	(13)	(14)
4043.460	24.3	0.0033	0.0041	8.7	4 A	N II	4043.532	5.3	3Fo 2s2.2p.(2Po).3d	2[7/2] 2s2.2p.(2Po<3/2>).4f.G	3.0	4.0	...
4058.287	16.8	0.0035	0.0043	10.3	4 A	N II	4058.162	-9.2	3Fo 2s2.2p.(2Po).3d	2[7/2] 2s2.2p.(2Po<3/2>).4f.G	4.0	3.0	...
4065.230	25.5	0.0045	0.0055	23.4	4 A	Fe III	4065.253 ?	1.7	5Ho 3d5.(4G).5p	5G 3d5.(4G).6s	4.0	5.0	8/1
4067.329	22.2	0.0030	0.0036	6.2	...	...	...	...	...	...	...	...	...
4068.668	48.8	1.4822	1.7873	900.8	0 A	[S II]	4068.600	-5.0	4So 3s2.3p3	2Po 3s2.3p3	1.5	1.5	1/1
4069.626	18.9	0.0169	0.0204	9999.0	1 A	O II	4069.623	-0.2	4Do 2s2.2p2.(3P).3p	4F 2s2.2p2.(3P).3d	0.5	1.5	8/6
4069.888	13.0	0.0165	0.0199	9999.0	1 A	O II	4069.882	-0.4	4Do 2s2.2p2.(3P).3p	4F 2s2.2p2.(3P).3d	1.5	2.5	8/6
4072.149	15.2	0.0272	0.0327	100.3	1 A	O II	4072.153	0.3	4Do 2s2.2p2.(3P).3p	4F 2s2.2p2.(3P).3d	2.5	3.5	5/4
4074.505	35.9	0.0085	0.0102	19.2	5 B	N III	4074.460 ?	-3.3	4P 2p2.(3P).3d	4Po 2s.2p.(3Po).8d	1.5	****	2/0
					3 A	C II	4074.481	-1.8	4Do 2s.2p.(3Po).3d	4F 2s.2p.(3Po).4f	0.5	1.5	8/1
					5 B	C II	4074.544	2.9	4Do 2s.2p.(3Po).3d	4F 2s.2p.(3Po).4f	1.5	2.5	8/0
4075.889	17.0	0.0368	0.0442	9999.0	2 A	O II	4075.862	-2.0	4Do 2s2.2p2.(3P).3p	4F 2s2.2p2.(3P).3d	3.5	4.5	2/2
					5 C	C II	4075.940	3.8	4Do 2s.2p.(3Po).3d	4F 2s.2p.(3Po).4f	2.5	2.5	7/1
4076.374	46.7	0.6358	0.7653	352.0	1 A	[S II]	4076.349	-1.8	4So 3s2.3p3	2Po 3s2.3p3	1.5	0.5	1/1
4078.808	16.3	0.0047	0.0056	23.0	2 A	O II	4078.842	2.5	4Do 2s2.2p2.(3P).3p	4F 2s2.2p2.(3P).3d	1.5	1.5	8/5
4079.643	36.0	0.0021	0.0025	10.6	4 A	[Fe III]	4079.700	4.2	5D 3d6	3G 3d6	3.0	4.0	7/1
4082.319	36.0	0.0044	0.0053	13.3	9	Fe I	4082.107 ?	-15.6	z5Fo 3d6.(5D).4s.4p.(3Po)	g5D 3d6.4s.(4D).5s	2.0	2.0	*1
					4 A	N II	4082.271	-3.5	3Fo 2s2.2p.(2Po).3d	2[7/2] 2s2.2p.(2Po<1/2>).4f.F	3.0	4.0	...
4083.874	14.3	0.0040	0.0049	17.9	3 A	[Fe II]	4083.781	-6.8	a4F 3d7	b2H 3d6.(3H).4s	4.5	4.5	3/0
					3 A	O II	4083.899	1.8	4F 2s2.2p2.(3P).3d	2[4]o 2s2.2p2.(3P).4f.G	2.5	3.5	...
4084.670	20.5	0.0039	0.0047	22.5	*	Fe I	4084.492 ?	-13.1	z5Fo 3d6.(5D).4s.4p.(3Po)	g5D 3d6.4s.(4D).5s	5.0	4.0	2/0
4085.101	16.7	0.0064	0.0076	22.5	1 A	O II	4085.112	0.8	4Do 2s2.2p2.(3P).3p	4F 2s2.2p2.(3P).3d	2.5	2.5	7/5
4087.146	14.5	0.0037	0.0045	24.5	2 A	O II	4087.153	0.5	4F 2s2.2p2.(3P).3d	2[3]o 2s2.2p2.(3P).4f.G	1.5	2.5	...
4089.290	13.3	0.0095	0.0114	37.9	2 A	O II	4089.288	-0.2	4F 2s2.2p2.(3P).3d	2[5]o 2s2.2p2.(3P).4f.G	4.5	5.5	...
4092.920	10.8	0.0027	0.0032	16.8	1 A	O II	4092.929	0.6	4Do 2s2.2p2.(3P).3p	4F 2s2.2p2.(3P).3d	3.5	3.5	4/3
4093.921	39.5	0.0041	0.0049	11.0	6 C	Fe III	4093.645	-20.2	5Go 3d5.(4G).5p	5G 3d5.(4G).5d	3.0	2.0	*4
					5 A	N III	4093.680 ?	-17.7	2Do 2s.2p.(1Po).3d	2D 2s.2p.(3Po).6p	1.5	1.5	3/2
4095.648	19.4	0.0035	0.0042	10.5	7	N III	4095.340 ?	-22.6	2Do 2s.2p.(1Po).3d	2D 2s.2p.(3Po).6p	2.5	1.5	3/1
					2 A	O II	4095.644	-0.3	4F 2s2.2p2.(3P).3d	2[3]o 2s2.2p2.(3P).4f.G	2.0	3.5	...
4096.513	11.8	0.0024	0.0028	15.6	5 A	[Fe III]	4096.610 ?	7.1	5D 3d6	3G 3d6	2.0	3.0	8/1
4097.265	14.9	0.0096	0.0115	42.8	2 A	O II	4097.225	-2.9	4Po 2s2.2p2.(3P).3p	4D 2s2.2p2.(3P).3d	0.5	1.5	7/4
					2 A	O II	4097.257	-0.6	4F 2s2.2p2.(3P).3d	2[4]o 2s2.2p2.(3P).4f.G	3.5	4.5	...
4101.739	31.5	20.7242	24.8041	5729.0	2 A	H I	4101.734	-0.4	2 2*	6 6*	****	****	0/0
4104.747	55.1	0.0134	0.0160	18.1	1 A	O II	4104.724	-1.7	4Po 2s2.2p2.(3P).3p	4D 2s2.2p2.(3P).3d	1.5	2.5	5/4
4104.996	14.2	0.0038	0.0046	10.4	1 A	O II	4104.990	-0.4	4Po 2s2.2p2.(3P).3p	4D 2s2.2p2.(3P).3d	1.5	1.5	7/3
4108.454	33.4	0.0046	0.0055	7.8	...	...	...	...	...	...	...	...	...
4110.766	15.0	0.0063	0.0075	19.2	1 A	O II	4110.786	1.5	4Po 2s2.2p2.(3P).3p	4D 2s2.2p2.(3P).3d	1.5	0.5	7/4
4113.028	53.6	0.0068	0.0082	16.2	5 B	Fe I	4112.912 ?	-8.5	y5Do 3d7.(4F).4p	i5D 3d6.4s.(4D).4d	3.0	3.0	6/1

Table E.1 (continued) - IC 418 Line List

$\lambda_o$ (Å)	FWHM (km/s)	$F(\lambda)/F(H\beta)$ ( $F(H\beta) = 100$ )	$I(\lambda)/I(H\beta)$ ( $I(H\beta) = 100$ )	S/N	ID:	Ion	$\lambda$ (Å)	$\delta V$ (km/s)	Lower Term/Config (10)	Upper Term/Config (11)	$j_1$ (12)	$j_2$ (13)	Multi (14)
(1)	(2)	(3)	(4)	(5)	(6)	(7)	(8)	(9)	(10)	(11)	(12)	(13)	(14)
4119.214	17.3	0.0184	0.0219	61.2	1 A	O II	4119.216	0.2	4Po 2s2.2p2.(3P).3p	4D 2s2.2p2.(3P).3d	2.5	3.5	2/2
4120.312	17.4	0.0057	0.0068	99999.0	2 A	O II	4120.278	-2.5	4Po 2s2.2p2.(3P).3p	4D 2s2.2p2.(3P).3d	2.5	2.5	4/3
					0 <	O II	4120.547	17.1	4Po 2s2.2p2.(3P).3p	4D 2s2.2p2.(3P).3d	2.5	1.5	5/1
4120.829	22.8	0.1730	0.2062	351.8	3 A	He I	4120.811	-1.4	3Po 1s.2p	3S 1s.5s	2.0	1.0	1/0
4121.434	17.5	0.0140	0.0166	99999.0	2 A	O II	4121.462	2.1	4Po 2s2.2p2.(3P).3p	4P 2s2.2p2.(3P).3d	0.5	0.5	6/2
4123.658	15.5	0.0016	0.0019	7.8	...	...	...	...	...	...	...	...	...
4128.569	18.6	0.0136	0.0162	7.1	7 C	Fe II	4128.748	13.0	b4P 3d6.(3P4).4s	z4Do 3d6.(5D).4p	2.5	1.5	5/0
4131.757	19.8	0.0311	0.0370	92.4	8 B	Fe II	4131.870	8.2	z4Ho 3d6.(3H).4p	e4G 3d6.(5D).4d	4.5	4.5	7/1
4132.789	11.5	0.0070	0.0083	34.8	3 A	O II	4132.800	0.8	4Po 2s2.2p2.(3P).3p	4P 2s2.2p2.(3P).3d	0.5	1.5	6/1
4139.999	32.8	0.0024	0.0028	11.2	...	...	...	...	...	...	...	...	...
4143.758	23.1	0.2649	0.3140	226.1	4 B	O II	4143.739	-1.4	6P 2s.2p3.(5So).3p	6Do 2s.2p3.(5So).3d	2.5	3.5	5/1
					1 A	He I	4143.759	0.1	1Po 1s.2p	1D 1s.6d	1.0	2.0	0/0
4146.047	19.9	0.0050	0.0059	17.3	3 A	Ne II	4146.064	1.2	2P 2s2.2p4.(3P).4s	2So 2s2.2p4.(3P).5p	0.5	0.5	1/0
					4 B	O II	4146.076	2.1	6P 2s.2p3.(5So).3p	6Do 2s.2p3.(5So).3d	3.5	4.5	2/0
4153.287	15.1	0.0156	0.0184	75.7	3 A	O II	4153.298	0.8	4Po 2s2.2p2.(3P).3p	4P 2s2.2p2.(3P).3d	1.5	2.5	4/1
4156.328	30.3	0.0134	0.0159	48.5	4 A	N II	4156.358	2.1	3Do 2s2.2p.(2Po).3d	2[3/2] 2s2.2p.(2Po<3/2>).4f.D	1.0	2.0	...
					7 D	O II	4156.530	14.6	4Po 2s2.2p2.(3P).3p	4P 2s2.2p2.(3P).3d	2.5	1.5	4/1
4161.141	29.6	0.0018	0.0022	9.5	...	...	...	...	...	...	...	...	...
4167.285	31.6	0.0032	0.0038	10.9	...	...	...	...	...	...	...	...	...
4168.995	24.3	0.0393	0.0463	140.0	1 A	He I	4168.972	-1.7	1Po 1s.2p	1S 1s.6s	1.0	0.0	0/0
					8 C	O II	4169.224	16.4	4Po 2s2.2p2.(3P).3p	4P 2s2.2p2.(3P).3d	2.5	2.5	3/1
4176.145	27.3	0.0054	0.0064	13.0	3 A	N II	4176.159	1.0	1Do 2s2.2p.(2Po).3d	2[5/2] 2s2.2p.(2Po<1/2>).4f.F	2.0	3.0	...
4185.433	16.2	0.0069	0.0081	22.9	1 A	O II	4185.439	0.4	2Fo 2s2.2p2.(1D).3p	2G 2s2.2p2.(1D).3d	2.5	3.5	2/1
4187.368	33.6	0.0029	0.0034	7.4	8	Fe II	4187.493 ?	9.0	z4Ho 3d6.(3H).4p	e4G 3d6.(5D).4d	4.5	5.5	5/0
4188.379	11.5	0.0010	0.0011	8.2	...	...	...	...	...	...	...	...	...
4189.783	21.2	0.0106	0.0124	34.0	2 A	O II	4189.788	0.3	2Fo 2s2.2p2.(1D).3p	2G 2s2.2p2.(1D).3d	3.5	4.5	2/1
					8	O II	4189.581	-14.5	2Fo 2s2.2p2.(1D).3p	2G 2s2.2p2.(1D).3d	3.5	3.5	2/0
4192.167	48.9	0.0021	0.0024	9.8	8	O II	4192.512	24.7	2Do 2s2.2p2.(1D).3p	2P 2s2.2p2.(1D).3d	2.5	1.5	2/0
4196.805	36.1	0.0048	0.0056	13.5	7 D	O II	4196.698	-7.6	2Do 2s2.2p2.(1D).3p	2P 2s2.2p2.(1D).3d	1.5	0.5	2/0
4208.038	30.3	0.0053	0.0061	20.1	...	...	...	...	...	...	...	...	...
4211.316	24.5	0.0069	0.0081	32.8	7 C	[Fe II]	4211.099	-15.5	a4F 3d7	b2H 3d6.(3H).4s	3.5	5.5	4/0
4219.753	19.9	0.0013	0.0015	8.0	2 A	Ne II	4219.745	-0.6	4D 2s2.2p4.(3P).3d	2[4]o 2s2.2p4.(3P<2>).4f	3.5	4.5	...
					7	Ni III	4220.070 ?	22.5	3F 3d7.(4F).4d	3Do 3d6.(5D).4s.4p	2.0	3.0	4/2
4236.926	14.3	0.0026	0.0030	18.0	2 A	N II	4236.927	0.1	3Do 2s2.2p.(2Po).3d	2[5/2] 2s2.2p.(2Po<1/2>).4f.F	1.0	2.0	...
					6	N II	4237.047	8.6	3Do 2s2.2p.(2Po).3d	2[7/2] 2s2.2p.(2Po<1/2>).4f.F	2.0	3.0	...
4241.809	19.9	0.0060	0.0069	30.2	4 B	N II	4241.756	-3.8	3Do 2s2.2p.(2Po).3d	2[5/2] 2s2.2p.(2Po<1/2>).4f.F	2.0	3.0	...
					3 A	N II	4241.786	-1.6	3Do 2s2.2p.(2Po).3d	2[7/2] 2s2.2p.(2Po<1/2>).4f.F	3.0	4.0	...
4246.861	25.6	0.0027	0.0031	9.2	5 B	N II	4246.706	-10.9	3Do 2s2.2p.(2Po).3d	2[5/2] 2s2.2p.(2Po<1/2>).4f.F	3.0	2.0	...

Table E.1 (continued) - IC 418 Line List

$\lambda_o$ (Å) (1)	FWHM (km/s) (2)	$F(\lambda)/F(H\beta)$ ( $F(H\beta) = 100$ ) (3)	$I(\lambda)/I(H\beta)$ ( $I(H\beta) = 100$ ) (4)	S/N (5)	ID: (6)	Ion (7)	$\lambda$ (Å) (8)	$\delta V$ (km/s) (9)	Lower Term/Config (10)	Upper Term/Config (11)	$j_1$ (12)	$j_2$ (13)	Multi (14)
4253.919	38.7	0.0064	0.0074	15.8	2 A	O II	4253.894	-1.8	2G 2s2.2p2.(1D).3d	2[5]o 2s2.2p2.(1D).4f.H	4.5	5.5	...
4256.128	23.5	0.0037	0.0043	13.5	...	O II	4253.907	-0.8	2G 2s2.2p2.(1D).3d	2[5]o 2s2.2p2.(1D).4f.H	4.5	4.5	...
4259.506	19.4	0.0040	0.0046	15.9	...	...	...	...	...	...	...	...	...
4267.161	38.7	0.4963	0.5712	536.0	8 D	C II	4267.001	-11.3	2D 2s2.3d	2Fo 2s2.4f	1.5	2.5	2/0
					5 A	C II	4267.183	1.5	2D 2s2.3d	2Fo 2s2.4f	2.5	3.5	2/0
					8 D	C II	4267.261	7.0	2D 2s2.3d	2Fo 2s2.4f	2.5	2.5	2/0
4271.882	44.2	0.0050	0.0058	7.1	5 C	Fe I	4271.760 ?	-8.5	a3F 3d7.(4F).4s	z3Go 3d7.(4F).4p	4.0	5.0	2/0
4275.535	13.5	0.0056	0.0065	33.4	5 B	Fe II]	4275.492 ?	-3.0	z2Po 3d6.(3P4).4p	4P 3d6.(5D).4d	0.5	0.5	4/1
					2 A	O II	4275.551	1.1	4D 2s2.2p2.(3P).3d	2[4]o 2s2.2p2.(3P).4f.F	3.5	4.5	...
4276.820	44.0	0.0068	0.0079	23.5	6 B	O II	4276.749	-5.0	4D 2s2.2p2.(3P).3d	2[3]o 2s2.2p2.(3P).4f.F	2.5	3.5	...
					4 A	[Fe II]	4276.829	0.7	a4F 3d7	a4G 3d6.(3G).4s	3.5	4.5	5/1
4277.481	24.9	0.0029	0.0033	10.7	3 A	O II	4277.426	-3.9	4D 2s2.2p2.(3P).3d	2[3]o 2s2.2p2.(3P).4f.F	3.5	2.5	...
					3 A	O II	4277.427	-3.8	4D 2s2.2p2.(3P).3d	2[2]o 2s2.2p2.(3P).4f.F	0.5	1.5	...
4280.548	48.9	0.0022	0.0026	7.4	4 B	Fe II]	4280.542 ?	-0.4	z2Po 3d6.(3P4).4p	4P 3d6.(5D).4d	1.5	0.5	4/1
4281.246	20.9	0.0016	0.0019	9.1	3 B	O II	4281.313	4.7	4P 2s2.2p2.(3P).3d	2[2]o 2s2.2p2.(3P).4f.D	2.5	2.5	...
4282.957	16.1	0.0022	0.0026	13.4	2 A	O II	4282.961	0.3	4D 2s2.2p2.(3P).3d	2[2]o 2s2.2p2.(3P).4f.F	1.5	2.5	...
4285.699	13.2	0.0027	0.0031	16.5	2 A	O II	4285.684	-1.1	2F 2s2.2p2.(3P).3d	2[3]o 2s2.2p2.(3P).4f.F	2.5	3.5	...
					5 C	Fe II	4285.716 ?	1.2	x4Do 3d6.(3F4).4p	e4F 3d6.(5D).4d	2.5	2.5	7/1
4287.234	12.1	0.0048	0.0055	9999.0	7 B	[Fe II]	4287.394	11.2	a6D 3d6.(5D).4s	a6S 3d5.4s2	4.5	2.5	1/0
4287.551	15.1	0.0072	0.0083	9999.0	5 A	[Co II]	4287.499 ?	-3.6	a3F 3d8	b3P 3d7.(4P).4s	3.0	1.0	5/1
4292.406	21.2	0.0078	0.0089	35.2	6 B	O II	4287.727	12.3	2Po 2s2.2p2.(1D).3p	2D 2s2.2p2.(3P).4d	1.5	1.5	2/1
					6 B	O II	4292.214 ?	-13.4	2F 2s2.2p2.(3P).3d	2[2]o 2s2.2p2.(3P).4f.F	2.5	2.5	...
4294.777	27.8	0.0051	0.0059	21.1	2 A	O II	4292.250 *	-10.9	2Fo 2s2.2p.(3Po).3d	2G 2s2.10g	****	****	...
					6 B	O II	4294.919	9.9	4P 2s2.2p2.(3P).3d	2[2]o 2s2.2p2.(3P).4f.D	1.5	2.5	...
					...	...	...	...	...	...	...	...	...
4300.454	27.4	0.0030	0.0034	7.8	...	...	...	-4.0	2G 2s2.2p2.(1D).3d	2[4]o 2s2.2p2.(1D).4f.G	3.5	****	...
4303.129	16.9	0.0009	0.0010	7.9	4 A	O II	4303.072	0.3	4P 2s2.2p2.(3P).3d	2[3]o 2s2.2p2.(3P).4f.D	2.5	3.5	...
4303.819	14.6	0.0058	0.0066	34.1	2 A	O II	4303.823	-12.5	a4F 3d7	a4G 3d6.(3G).4s	2.5	2.5	8/0
4306.069	20.1	0.0061	0.0069	20.2	7 A	[Fe II]	4305.890 ?	-7.2	2D 2s2.2p2.(1D).3d	2[1]o 2s2.2p2.(1D).4f.P	1.5	****	...
					7 A	O II	4305.965	-2.6	4P 2s2.2p2.(3P).3d	2[2]o 2s2.2p2.(3P).4f.D	0.5	1.5	...
4307.269	19.5	0.0105	0.0119	45.3	3 A	O II	4307.232	1.4	4P 2s2.2p2.(3P).3s	4Po 2s2.2p2.(3P).3p	0.5	1.5	6/5
4317.119	16.4	0.0140	0.0159	57.8	1 A	O II	4317.139	10.1	4P 2s.2p.(3Po).3p	4Po 2s.2p.(3Po).4s	2.5	2.5	3/0
					8	C II	4317.265 ?	1.7	4P 2s.2p.(3Po).3p	4Po 2s.2p.(3Po).4s	0.5	1.5	6/1
4318.581	25.2	0.0076	0.0086	32.5	5 A	C II	4318.606	0.8	4P 2s2.2p2.(3P).3s	4Po 2s2.2p2.(3P).3p	1.5	2.5	4/4
4319.618	13.8	0.0073	0.0083	38.4	2 A	O II	4319.629	0.1	a4F 3d7	a4G 3d6.(3G).4s	2.5	3.5	8/1
					4 B	[Fe II]	4319.620 ?	4.3	x4Do 3d6.(3F4).4p	e4F 3d6.(5D).4d	2.5	3.5	5/1
					8 C	Fe II	4319.680 ?						

Table E.1 (continued) - IC 418 Line List

$\lambda_o$ (Å) (1)	FWHM (km/s) (2)	$F(\lambda)/F(H\beta)$ ( $F(H\beta) = 100$ ) (3)	$I(\lambda)/I(H\beta)$ ( $I(H\beta) = 100$ ) (4)	S/N (5)	ID: (6)	Ion (7)	$\lambda$ (Å) (8)	$\delta V$ (km/s) (9)	Lower Term/Config (10)	Upper Term/Config (11)	$j_1$ (12)	$j_2$ (13)	Multi (14)
4321.597	48.3	0.0070	0.0080	11.5	5 A	C II	4321.657	4.2	4P 2s.2p.(3P <sub>o</sub> ).3p	4P <sub>o</sub> 2s.2p.(3P <sub>o</sub> ).4s	1.5	1.5	6/1
4323.326	70.0	0.0082	0.0093	8.2	3 B	[Co II]	4323.278 ?	-3.4	a3F 3d8	b3P 3d7.(4P).4s	3.0	2.0	4/1
				8		C II	4323.106 ?	-15.3	4P 2s.2p.(3P <sub>o</sub> ).3p	4P <sub>o</sub> 2s.2p.(3P <sub>o</sub> ).4s	0.5	0.5	6/0
4325.866	45.0	0.0151	0.0171	49.4	8	O II	4325.761	-7.3	4P 2s.2p.2.(3P).3s	4P <sub>o</sub> 2s.2p.2.(3P).3p	0.5	0.5	6/0
				4 A		Fe I	4325.762 ?	-7.2	a3F 3d7.(4F).4s	z3Go 3d7.(4F).4p	2.0	3.0	5/1
				4 A		C II	4325.833 ?	-2.3	4P 2s.2p.(3P <sub>o</sub> ).3p	4P <sub>o</sub> 2s.2p.(3P <sub>o</sub> ).4s	2.5	1.5	4/0
4329.876	21.4	0.0062	0.0070	20.7	6 B	C II	4329.675 *	-13.9	2D 2s2.4d	2Fo 2s2.9f	****	****	...
4335.866	60.2	0.0082	0.0093	8.7	...	...	...	...	...	...	...	...	...
4336.830	11.5	0.0033	0.0037	12.2	1 A	O II	4336.859	2.0	4P 2s.2p.2.(3P).3s	4P <sub>o</sub> 2s.2p.2.(3P).3p	1.5	1.5	6/5
4340.465	31.6	39.6376	44.8053	6397.0	3 A	H I	4340.464	-0.1	2 2*	5 5*	****	****	0/0
4345.546	15.8	0.0170	0.0192	39.6	1 A	O II	4345.560	1.0	4P 2s.2p.2.(3P).3s	4P <sub>o</sub> 2s.2p.2.(3P).3p	1.5	0.5	6/5
4347.990	26.0	0.0046	0.0052	9.3	...	O II	4347.413 ?	-39.9	2D 2p2.(1D).3s	2D <sub>o</sub> 2s.2p.2.(1D).3p	1.5	1.5	...
				...		O II	4347.217 ?	-53.3	2D 2p2.(1D).3s	2D <sub>o</sub> 2s.2p.2.(1D).3p	2.5	1.5	...
4349.409	18.6	0.0292	0.0330	77.3	0 A	O II	4349.426	1.2	4P 2s.2p.2.(3P).3s	4P <sub>o</sub> 2s.2p.2.(3P).3p	2.5	2.5	3/3
4351.266	19.2	0.0071	0.0080	16.5	5 A	O II	4351.260	-0.4	2D 2s.2p.2.(1D).3s	2D <sub>o</sub> 2s.2p.2.(1D).3p	2.5	2.5	3/0
				9 C		O II	4351.457	13.2	2D 2s.2p.2.(1D).3s	2D <sub>o</sub> 2s.2p.2.(1D).3p	1.5	2.5	3/0
4359.380	42.0	0.0080	0.0090	27.9	3 A	[Fe II]	4359.333	-3.2	a6D 3d6.(5D).4s	a6S 3d5.4s2	3.5	2.5	2/0
				5 B		O II	4359.395	1.0	2D <sub>o</sub> 2s.2p.2.(3P).3p	2D 2s.2p.2.(3P).3d	1.5	2.5	3/0
4363.191	15.6	0.8321	0.9353	606.3	1 A	[O III]	4363.210	1.3	1D 2s2.2p2	1S 2s2.2p2	2.0	0.0	0/0
4366.875	13.4	0.0121	0.0136	53.0	1 A	O II	4366.895	1.3	4P 2s.2p.2.(3P).3s	4P <sub>o</sub> 2s.2p.2.(3P).3p	2.5	1.5	4/4
4368.264	54.9	0.0858	0.0964	291.3	2 A	O I	4368.193 *	-4.9	3S <sub>o</sub> 2s.2p.3.(4S <sub>o</sub> ).3s	3P 2s.2p.3.(4S <sub>o</sub> ).4p	****	****	...
4376.580	12.6	0.0014	0.0016	11.0	4 A	C II	4376.582	0.1	4P <sub>o</sub> 2s.2p.(3P <sub>o</sub> ).3d	4D 2s.2p.(3P <sub>o</sub> ).4f	1.5	2.5	5/0
4387.930	21.5	0.4889	0.5462	291.0	1 A	He I	4387.929	-0.1	1P <sub>o</sub> 1s.2p	1D 1s.5d	1.0	2.0	0/0
4390.550	47.1	0.0053	0.0059	32.0	...	...	...	...	...	...	...	...	...
4391.963	15.8	0.0020	0.0022	7.4	3 A	Ne II	4391.991	1.9	4F 2s2.2p4.(3P).3d	2[5]o 2s2.2p4.(3P<2>).4f	4.5	5.5	...
				3 A		Ne II	4391.995	2.2	4F 2s2.2p4.(3P).3d	2[5]o 2s2.2p4.(3P<2>).4f	4.5	4.5	...
4393.483	33.9	0.0041	0.0045	15.0	4 A	O II	4393.435	-3.3	2P <sub>o</sub> 2s2.2p2.(1D).3p	2P 2s2.2p2.(3P).4d	1.5	0.5	3/0
4396.586	20.4	0.0014	0.0016	7.7	4 A	O I	4396.560 ?	-1.8	3P 2s2.2p3.(4S <sub>o</sub> ).4p	3D <sub>o</sub> 2s2.2p3.(2D <sub>o</sub> ).4s	2.0	3.0	2/0
4411.172	13.3	0.0015	0.0016	12.5	4 A	C II	4411.152	-1.4	2D <sub>o</sub> 2s.2p.(3P <sub>o</sub> ).3d	2F 2s.2p.(3P <sub>o</sub> ).4f	1.5	2.5	2/0
4413.609	12.4	0.0025	0.0027	9999.0	...	...	...	...	...	...	...	...	...
4413.942	10.4	0.0019	0.0021	9999.0	3 A	[Fe II]	4413.781	-10.9	a6D 3d6.(5D).4s	a6S 3d5.4s2	2.5	2.5	3/2
4414.888	15.0	0.0273	0.0303	113.7	1 A	O II	4414.898	0.7	2P 2s2.2p2.(3P).3s	2D <sub>o</sub> 2s2.2p2.(3P).3p	1.5	2.5	2/1
4416.090	11.0	0.0015	0.0016	9999.0	6 A	[Fe II]	4416.266	12.0	a6D 3d6.(5D).4s	b4F 3d6.(3F4).4s	4.5	4.5	3/1
4416.515	17.4	0.0024	0.0026	9999.0	7 B	[Fe II]	4416.266	-16.9	a6D 3d6.(5D).4s	b4F 3d6.(3F4).4s	4.5	4.5	3/0
4416.969	15.5	0.0178	0.0197	92.2	3 A	O II	4416.975	0.4	2P 2s2.2p2.(3P).3s	2D <sub>o</sub> 2s2.2p2.(3P).3p	0.5	1.5	2/1
4418.945	35.3	0.0029	0.0032	11.1	5 C	O II	4418.870	-5.1	2P <sub>o</sub> 2s2.2p2.(1S).3p	2P 2s2.2p2.(1D).4d	0.5	1.5	1/0
				3 A		Fe II	4418.958 ?	0.9	y4Go 3d6.(3F4).4p	e4F 3d6.(5D).4d	2.5	1.5	8/1
4432.692	22.1	0.0032	0.0036	11.4	6 B	[Fe II]	4432.447	-16.6	a6D 3d6.(5D).4s	b4F 3d6.(3F4).4s	3.5	2.5	7/1

Table E.1 (continued) - IC 418 Line List

$\lambda_o$ (Å)	FWHM (km/s)	$F(\lambda)/F(H\beta)$ ( $F(H\beta) = 100$ )	$I(\lambda)/I(H\beta)$ ( $I(H\beta) = 100$ )	S/N	ID:	Ion	$\lambda$ (Å)	$\delta V$ (km/s)	Lower Term/Config	Upper Term/Config	$j_1$	$j_2$	Multi
(1)	(2)	(3)	(4)	(5)	(6)	(7)	(8)	(9)	(10)	(11)	(12)	(13)	(14)
4433.769	23.6	0.0025	0.0028	11.9	5 A	N II	4432.735	2.9	3Po 2s2.2p.(2Po).3d	2[5/2] 2s2.2p.(2Po<3/2>).4f.D	2.0	3.0	...
4437.552	22.0	0.0718	0.0792	211.5	6	N II	4433.475 ?	-19.9	3Po 2s2.2p.(2Po).3d	2[3/2] 2s2.2p.(2Po<3/2>).4f.D	0.0	1.0	...
4447.060	16.5	0.0035	0.0039	19.7	1 A	He I	4437.554	0.1	1Po 1s.2p	1S 1s.5s	1.0	0.0	0/0
4448.253	12.8	0.0008	0.0009	9.0	2 A	N II	4447.030	-2.0	1P 2s2.2p.(2Po).3p	1Do 2s2.2p.(2Po).3d	1.0	2.0	0/0
4448.825	9.5	0.0009	0.0010	9.2	5 A	O II	4448.191	-4.2	2Fo 2s2.2p2.(1D).3p	2F 2s2.2p2.(1D).3d	3.5	3.5	3/0
4452.262	43.9	0.0080	0.0088	34.1	2 A	O II	4448.850	1.7	2P 2s2.2p2.(1D).3d	2[1]o 2s2.2p2.(1D).4f.P	1.5	****	...
					4 A	[Fe II]	4452.098 ?	-11.1	a6D 3d6.(5D).4s	a6S 3d5.4s2	1.5	2.5	4/2
					8 C	O II	4452.378	7.8	2P 2s2.2p2.(3P).3s	2Do 2s2.2p2.(3P).3p	1.5	1.5	2/0
4453.475	16.3	0.0051	0.0056	29.1	7 D	Fe II	4453.205 ?	-18.2	y6Po 3d5.(6S).4s.4p.(3Po)	6P 3d6.(5D).4d	1.5	1.5	6/1
4454.107	21.5	0.0015	0.0017	6.5	8	O II	4453.966	-9.5	4P 2s2.2p2.(3P).3d	4So 2s.2p3.(5So).3s	1.5	1.5	2/0
4457.091	20.9	0.0122	0.0134	59.4	3 A	Ne II	4457.050	-2.8	2D 2s2.2p4.(3P).3d	2[2]o 2s2.2p4.(3P<2>).4f	1.5	2.5	...
					6 C	Ne II	4457.239	10.0	4P 2s2.2p4.(3P).3d	2[3]o 2s2.2p4.(3P<1>).4f	2.5	2.5	...
					6 C	Ne II	4457.265	11.7	2D 2s2.2p4.(3P).3d	2[2]o 2s2.2p4.(3P<2>).4f	1.5	1.5	...
4457.725	26.0	0.0026	0.0028	99999.0	6 A	[Fe II]	4457.945	14.8	a6D 3d6.(5D).4s	b4F 3d6.(3F4).4s	3.5	3.5	6/1
4459.898	17.2	0.0022	0.0025	14.3	6 A	N II	4459.937	2.6	3D 2s2.2p.(2Po).3p	3Po 2s2.2p.(2Po).3d	1.0	0.0	5/1
4465.404	14.8	0.0054	0.0059	32.4	1 A	O II	4465.408	0.3	6So 2s.2p3.(5So).3s	6P 2s.2p3.(5So).3p	2.5	3.5	1/1
					8	N II	4465.529	8.4	3D 2s2.2p.(2Po).3p	3Po 2s2.2p.(2Po).3d	1.0	1.0	5/0
4466.390	25.1	0.0027	0.0029	9.9	3 A	O II	4466.435	3.0	2P 2s2.2p2.(3P).3d	2[2]o 2s2.2p2.(3P).4f.D	1.5	2.5	...
					6 D	O II	4466.583	13.0	2P 2s2.2p2.(3P).3d	2[2]o 2s2.2p2.(3P).4f.D	1.5	1.5	...
4467.919	14.7	0.0038	0.0041	22.6	1 A	O II	4467.924	0.3	6So 2s.2p3.(5So).3s	6P 2s.2p3.(5So).3p	2.5	2.5	2/2
					5 B	Fe II	4467.931 ?	0.8	y4Go 3d6.(3F4).4p	e4F 3d6.(5D).4d	3.5	3.5	7/0
4469.375	13.5	0.0020	0.0022	12.1	1 A	O II	4469.378	0.2	6So 2s.2p3.(5So).3s	6P 2s.2p3.(5So).3p	2.5	1.5	2/2
					4 B	O II	4469.462	5.8	2P 2s2.2p2.(3P).3d	2[1]o 2s2.2p2.(3P).4f.D	0.5	0.5	...
4471.499	23.7	4.1046	4.4921	1935.0	4 A	He I	4471.474	-1.7	3Po 1s.2p	3D 1s.4d	2.0	3.0	2/0
4474.689	20.9	0.0024	0.0026	5.8	4 A	[Fe II]	4474.904	14.4	a6D 3d6.(5D).4s	a6S 3d5.4s2	0.5	2.5	4/2
4477.745	25.1	0.0055	0.0061	29.9	4 A	N II	4477.682	-4.2	3D 2s2.2p.(2Po).3p	3Po 2s2.2p.(2Po).3d	2.0	1.0	5/1
4481.213	30.6	0.0176	0.0193	81.2	7 A	Mg II	4481.126	-5.8	2D 3d	2Fo 4f	2.5	3.5	2/0
					7 A	Mg II	4481.150	-4.2	2D 3d	2Fo 4f	2.5	2.5	2/0
					8 C	Mg II	4481.325	7.5	2D 3d	2Fo 4f	1.5	2.5	2/0
4483.494	15.7	0.0018	0.0020	8.6	5 C	S II	4483.427	-4.5	4Do 3s2.3p2.(3P).4p	4P 3s2.3p2.(3P).5s	2.5	1.5	5/0
4485.231	34.2	0.0020	0.0021	10.5	7 B	Fe III	4485.575 ?	23.0	3G 3d5.(2G3).4s	3Fo 3d5.(a2F).4p	5.0	4.0	2/1
4487.744	17.4	0.0008	0.0009	99999.0	7	Fe II	4487.497 ?	-16.5	y6Po 3d5.(6S).4s.4p.(3Po)	6P 3d6.(5D).4d	2.5	2.5	6/1
					2 A	O II	4487.712	-2.2	2P 2s2.2p2.(1D).3d	2[2]o 2s2.2p2.(1D).4f.D	0.5	1.5	...
4488.194	18.9	0.0022	0.0024	9.7	4 D	N II	4488.095	-6.6	3D 2s2.2p.(2Po).3p	3Po 2s2.2p.(2Po).3d	2.0	2.0	4/1
					2 A	O II	4488.184	-0.7	2P 2s2.2p2.(1D).3d	2[2]o 2s2.2p2.(1D).4f.D	1.5	2.5	...
					2 A	O II	4488.198	0.3	2P 2s2.2p2.(1D).3d	2[2]o 2s2.2p2.(1D).4f.D	1.5	1.5	...
					3 C	S II	4488.188	-0.4	2D 3s2.3p2.(3P).4d	2[2]o 3s2.3p2.(1D<2>).5f	1.5	****	...
4489.468	23.0	0.0007	0.0007	7.0	3 A	O II	4489.461	-0.5	2P 2s2.2p2.(3P).3d	2[2]o 2s2.2p2.(3P).4f.D	0.5	1.5	...

Table E.1 (continued) - IC 418 Line List

$\lambda_o$ (Å) (1)	FWHM (km/s) (2)	$F(\lambda)/F(H\beta)$ ( $F(H\beta) = 100$ ) (3)	$I(\lambda)/I(H\beta)$ ( $I(H\beta) = 100$ ) (4)	S/N (5)	ID: (6)	Ion (7)	$\lambda$ (Å) (8)	$\delta V$ (km/s) (9)	Lower Term/Config (10)	Upper Term/Config (11)	$j_1$ (12)	$j_2$ (13)	Multi (14)
4491.278	19.6	0.0115	0.0125	56.5	5 B	C II	4491.130 *	-9.9	2Fo 2s2.4f	2G 2s2.9g	****	****	...
4503.289	17.4	0.0014	0.0015	10.3	4 A	O II	4491.222	-3.7	2P 2s2.2p2.(3P).3d	2[3]o 2s2.2p2.(3P).4f.D	1.5	2.5	...
4507.554	13.1	0.0047	0.0051	25.8	5 B	N II	4507.560	...	...	...	...	...	...
4530.404	16.7	0.0039	0.0042	21.6	3 A	N II	4530.410	0.4	3D 2s2.2p.(2Po).3p	3Po 2s2.2p.(2Po).3d	3.0	2.0	2/0
4545.218	23.6	0.0023	0.0024	11.8	...	...	...	0.4	1Fo 2s2.2p.(2Po).3d	2[9/2] 2s2.2p.(2Po<3/2>).4f.G	3.0	4.0	...
4552.505	22.1	0.0024	0.0026	11.3	3 A	N II	4552.522	...	...	...	...	...	...
4562.637	57.5	0.0387	0.0414	168.8	...	...	...	1.1	1Fo 2s2.2p.(2Po).3d	2[7/2] 2s2.2p.(2Po<3/2>).4f.G	3.0	4.0	...
4571.161	52.8	0.4017	0.4291	173.0	2 A	Mg I]	4571.096	...	...	...	...	...	...
4590.959	16.5	0.0135	0.0143	73.2	2 A	O II	4590.974	-4.3	1S 3s2	3Po 3s.3p	0.0	1.0	0/0
4596.171	15.5	0.0089	0.0094	37.8	8	O II	4595.957	1.0	2D 2s2.2p2.(1D).3s	2Fo 2s2.2p2.(1D).3p	2.5	3.5	2/1
4601.471	17.3	0.0248	0.0263	104.0	2 A	N II	4596.176	-14.0	2D 2s2.2p2.(1D).3s	2Fo 2s2.2p2.(1D).3p	2.5	2.5	2/0
4602.121	12.6	0.0020	0.0022	12.5	2 A	O II	4601.478	0.3	2D 2s2.2p2.(1D).3s	2Fo 2s2.2p2.(1D).3p	1.5	2.5	2/1
4607.140	17.5	0.0243	0.0257	96.0	4 A	[Fe III]	4602.129	0.4	3Po 2s2.2p.(2Po).3s	3P 2s2.2p.(2Po).3p	1.0	2.0	4/4
4609.436	15.3	0.0057	0.0060	23.7	2 A	O II	4607.153	0.5	2D 2s2.2p2.(3P).3d	2[3]o 2s2.2p2.(3P).4f.F	1.5	2.5	...
4611.738	41.4	0.0057	0.0061	8.1	5 B	O II	4611.582	-7.2	5D 3d6	3F4 3d6	4.0	3.0	4/1
4613.858	19.6	0.0172	0.0182	59.1	6 D	O II	4613.681	0.8	3Po 2s2.2p.(2Po).3s	3P 2s2.2p.(2Po).3p	0.0	1.0	...
4620.348	21.5	0.0101	0.0107	41.7	7 A	C II	4613.868	0.0	2D 2s2.2p2.(3P).3d	2[4]o 2s2.2p2.(3P).4f.F	2.5	3.5	...
4621.384	18.0	0.0250	0.0264	103.9	3 A	N II	4621.393	-10.1	4F 2s2.2p2.(3P).4d	2[2]o 2s2.2p2.(1D).4f.D	2.5	2.5	...
4627.940	16.0	0.0013	0.0013	7.0	8	[C I]	4621.570	-9.1	4F 2s2.2p2.(3P).4d	2[2]o 2s2.2p2.(1D).4f.D	2.5	1.5	...
4630.531	16.8	0.0765	0.0805	217.7	2 A	N II	4630.539	-11.5	2D 2s2.2p2.(3P).3d	2[3]o 2s2.2p2.(3P).4f.F	2.5	3.5	...
4634.079	18.8	0.0024	0.0026	16.6	2 A	N III	4634.120	0.7	3Po 2s2.2p.(2Po).3s	3P 2s2.2p.(2Po).3p	1.0	1.0	5/5
4637.456	23.2	0.0053	0.0056	19.5	8 C	C II	4637.630	-10.6	2D 2s2.4d	2Fo 2s2.8f	****	****	...
4638.816	18.4	0.0283	0.0297	125.4	2 A	O II	4638.856	0.6	3Po 2s2.2p.(2Po).3s	3P 2s2.2p.(2Po).3p	1.0	0.0	5/5
4640.604	15.4	0.0049	0.0052	23.4	3 A	N III	4640.640	2.3	2D 2s2.2p2.(3P).4d	2Fo 3s2.(1S).7f	1.5	2.5	2/0
4641.802	15.1	0.0407	0.0428	156.1	1 A	O II	4641.810	12.1	3P 2s2.2p2	1S 2s2.2p2	1.0	0.0	0/0
4643.078	17.0	0.0327	0.0344	140.5	2 B	N III	4641.850	6.9	2D 3d9	4P 3d8.(3P).4s	1.5	2.5	3/0
4649.128	15.6	0.0639	0.0670	210.8	1 A	O II	4649.135	0.5	3Po 2s2.2p.(2Po).3s	3P 2s2.2p.(2Po).3p	2.0	2.0	3/3
4650.826	15.5	0.0207	0.0217	99.3	1 A	O II	4650.838	2.7	2Po 2s2.3p	2D 2s2.3d	0.5	1.5	2/1
4651.559	24.6	0.0005	0.0005	6.0	6 A	O II	4651.326	11.2	2Po 2s2.4p	2D 2s2.6d	0.5	1.5	2/0
								2.6	4P 2s2.2p2.(3P).3s	4Do 2s2.2p2.(3P).3p	0.5	1.5	2/1
								2.3	2Po 2s2.3p	2D 2s2.3d	1.5	2.5	2/1
								0.5	4P 2s2.2p2.(3P).3s	4Do 2s2.2p2.(3P).3p	1.5	2.5	5/5
								3.1	2Po 2s2.3p	2D 2s2.3d	1.5	1.5	2/2
								0.5	3Po 2s2.2p.(2Po).3s	3P 2s2.2p.(2Po).3p	2.0	1.0	4/4
								0.4	4P 2s2.2p2.(3P).3s	4Do 2s2.2p2.(3P).3p	2.5	3.5	2/2
								0.8	4P 2s2.2p2.(3P).3s	4Do 2s2.2p2.(3P).3p	0.5	0.5	7/7
								-15.0	4F 2s2.2p2.(3P).4d	2[3]o 2s2.2p2.(1D).4f.F	2.5	****	...
								-5.5	3S 2s.3s	3Po 2s.3p	1.0	0.0	2/0

Table E.1 (continued) - IC 418 Line List

$\lambda_0$ (Å)	FWHM (km/s)	$F(\lambda)/F(H\beta)$ ( $F(H\beta) = 100$ )	$I(\lambda)/I(H\beta)$ ( $I(H\beta) = 100$ )	S/N	ID:	Ion	$\lambda$ (Å)	$\delta V$ (km/s)	Lower Term/Config (10)	Upper Term/Config (11)	$j_1$ (12)	$j_2$ (13)	Multi (14)
(1)	(2)	(3)	(4)	(5)	(6)	(7)	(8)	(9)	(10)	(11)	(12)	(13)	(14)
4634.475	19.6	0.0030	0.0031	14.7	6 A	O I	4654.556	5.2	5P 2s2.2p3.(4So).3p	5Do 2s2.2p3.(4So).8d	2.0	1.0	8/0
					6 A	O I	4654.557	5.3	5P 2s2.2p3.(4So).3p	5Do 2s2.2p3.(4So).8d	2.0	2.0	7/0
					6 A	O I	4654.559	5.4	5P 2s2.2p3.(4So).3p	5Do 2s2.2p3.(4So).8d	2.0	3.0	5/0
4658.174	31.1	0.0262	0.0274	116.9	5 A	[Fe III]	4658.050	-8.0	5D 3d6	3F4 3d6	4.0	4.0	3/1
4661.625	15.6	0.0221	0.0231	115.0	1 A	O II	4661.632	0.5	4P 2s2.2p2.(3P).3s	4Do 2s2.2p2.(3P).3p	1.5	1.5	7/7
4667.255	25.2	0.0027	0.0028	15.6	6 A	[Fe III]	4667.010	-15.8	5D 3d6	3F4 3d6	3.0	2.0	6/1
4669.227	57.3	0.0073	0.0076	34.3	2 A	O II	4669.260	2.1	2D 2s2.2p2.(3P).3d	2[2]o 2s2.2p2.(3P).4f.D	1.5	2.5	...
4673.725	16.4	0.0039	0.0041	22.8	1 A	O II	4673.733	0.5	4P 2s2.2p2.(3P).3s	4Do 2s2.2p2.(3P).3p	1.5	0.5	7/7
4674.903	16.7	0.0020	0.0021	16.1	...	...	...	...	...	...	...	...	...
4676.225	16.2	0.0152	0.0158	77.3	1 A	O II	4676.235	0.6	4P 2s2.2p2.(3P).3s	4Do 2s2.2p2.(3P).3p	2.5	2.5	4/4
4678.137	24.3	0.0013	0.0014	5.8	2 A	N II	4678.135	-0.2	1Po 2s2.2p.(2Po).3d	2[3/2] 2s2.2p.(2Po<3/2>).4f.D	1.0	2.0	...
4681.881	63.8	0.0021	0.0021	6.2	6 B	O II	4681.963	5.3	2P 2s2.2p2.(3P).4s	2Do 2s2.2p2.(3P).5p	1.5	2.5	2/0
4696.335	14.7	0.0026	0.0027	14.4	1 A	O II	4696.353	1.2	4P 2s2.2p2.(3P).3s	4Do 2s2.2p2.(3P).3p	2.5	1.5	5/5
4699.129	38.9	0.0128	0.0133	42.0	7	O II	4699.011	-7.5	2Do 2s2.2p2.(1D).3p	2F 2s2.2p2.(1D).3d	2.5	3.5	2/0
					6 B	O II	4699.218	5.7	2Do 2s2.2p2.(3P).3p	2F 2s2.2p2.(3P).3d	1.5	2.5	2/0
4703.145	16.4	0.0021	0.0021	7.1	4 A	O II	4703.161	1.0	2Do 2s2.2p2.(1D).3p	2F 2s2.2p2.(1D).3d	1.5	2.5	2/0
4705.344	14.6	0.0176	0.0183	61.4	4 A	O II	4705.346	0.1	2Do 2s2.2p2.(3P).3p	2F 2s2.2p2.(3P).3d	2.5	3.5	2/0
4710.015	20.7	0.0065	0.0067	21.7	...	...	...	...	...	...	...	...	...
4711.352	13.9	0.0029	0.0030	10.3	0 A	[Ar IV]	4711.370	1.2	4So 3s2.3p3	2Do 3s2.3p3	1.5	2.5	1/1
4713.174	24.2	0.5902	0.6098	233.5	3 A	He I	4713.139	-2.2	3Po 1s.2p	3S 1s.4s	2.0	1.0	1/0
4716.325	18.8	0.0036	0.0037	8.9	3 A	[Fe III]	4716.330	0.3	3F4 3d6	1F 3d6	3.0	3.0	2/0
4726.961	30.2	0.0026	0.0027	5.8	...	...	...	...	...	...	...	...	...
4733.956	34.5	0.0046	0.0048	18.6	0 A	[Fe III]	4733.910	-2.9	5D 3d6	3F4 3d6	2.0	2.0	7/2
4740.205	12.7	0.0035	0.0036	19.6	1 A	[Ar IV]	4740.160	-2.8	4So 3s2.3p3	2Do 3s2.3p3	1.5	1.5	1/1
4752.893	27.3	0.0168	0.0172	77.0	...	...	...	...	...	...	...	...	...
4754.741	35.8	0.0046	0.0047	23.3	3 A	[Fe III]	4754.690	-3.2	5D 3d6	3F4 3d6	3.0	4.0	4/0
4756.449	29.4	0.0233	0.0239	82.9	...	...	...	...	...	...	...	...	...
4757.232	17.1	0.0009	0.0010	8.6	...	...	...	...	...	...	...	...	...
4759.653	59.7	0.0061	0.0062	20.4	6 A	[Fe III]	4769.430	-14.0	5D 3d6	3F4 3d6	2.0	3.0	7/1
4772.109	33.6	0.0024	0.0025	14.0	4 A	[Fe II]	4772.062 ?	-2.9	a6D 3d6.(5D).4s	b4P 3d6.(3P4).4s	1.5	1.5	7/0
4774.263	13.5	0.0022	0.0022	15.0	1 A	N II	4774.244	-1.2	3D 2s2.2p.(2Po).3p	3Do 2s2.2p.(2Po).3d	1.0	2.0	6/3
4777.788	33.2	0.0032	0.0032	12.5	3 A	[Fe III]	4777.680	-6.8	5D 3d6	3F4 3d6	1.0	2.0	7/4
4779.715	17.8	0.0176	0.0179	88.9	2 A	N II	4779.723	0.5	3D 2s2.2p.(2Po).3p	3Do 2s2.2p.(2Po).3d	1.0	1.0	6/4
4781.311	28.9	0.0013	0.0013	7.9	6 A	N II	4781.190	-7.6	3D 2s2.2p.(2Po).3p	3Do 2s2.2p.(2Po).3d	2.0	3.0	4/0
4788.127	15.6	0.0192	0.0195	101.9	2 A	N II	4788.137	0.6	3D 2s2.2p.(2Po).3p	3Do 2s2.2p.(2Po).3d	2.0	2.0	6/3
4789.589	34.7	0.0268	0.0272	112.1	...	...	...	...	...	...	...	...	...
4792.040	19.2	0.0016	0.0017	7.8	5 C	S II	4792.007	-2.1	4Po 3s2.3p2.(3P).4p	4P 3s2.3p2.(3P).5s	2.5	2.5	3/0
					3 A	O II	4792.083 ?	2.7	4D 2s2.2p2.(3P).4d	2[3]o 2s2.2p2.(1D).4f.F	3.5	***	...

Table E.1 (continued) - IC 418 Line List

$\lambda_o$ (Å) (1)	FWHM (km/s) (2)	$F(\lambda)/F(H\beta)$ ( $F(H\beta) = 100$ ) (3)	$I(\lambda)/I(H\beta)$ ( $I(H\beta) = 100$ ) (4)	S/N (5)	ID: (6)	Ion (7)	$\lambda$ (Å) (8)	$\delta V$ (km/s) (9)	Lower Term/Config (10)	Upper Term/Config (11)	$j_i$ (12)	$j_f$ (13)	Multi (14)
4802.454	19.5	0.0181	0.0183	72.8	6 B	C II	4802.740 *	17.9	2Fo 2s2.4f	2G 2s2.8g	****	****	...
4803.276	16.9	0.0258	0.0261	76.5	4 A	N II	4803.286	0.6	3D 2s2.2p.(2Po).3p	3Do 2s2.2p.(2Po).3d	3.0	3.0	3/1
4810.209	49.2	0.0039	0.0040	12.9	4 A	Ne II	4810.214 ?	0.3	4Do 2s2.2p4.(3P).4p	4P 2s2.2p4.(3P).5d	1.5	0.5	7/0
					6	N II	4810.299	5.6	3D 2s2.2p.(2Po).3p	3Do 2s2.2p.(2Po).3d	3.0	2.0	4/0
4814.688	44.6	0.0079	0.0080	14.8	5 A	[Fe II]	4814.534	-9.6	4F 3d7	b4F 3d6.(3F4).4s	4.5	4.5	3/0
4815.483	60.5	0.0168	0.0170	13.7	6 B	S II	4815.552	4.3	4P 3s2.3p2.(3P).4s	4So 3s2.3p2.(3P).4p	2.5	1.5	1/0
				8	N II	N II	4815.617	8.4	5Do 2s2.2p2.(4P).3p	5P 2s2.2p2.(4P).3d	1.0	1.0	8/0
4861.327	32.5	100.0000	100.0000	13680.0	3 A	H I	4861.325	-0.1	2 2*	4 4*	****	****	0/0
4869.377	23.0	0.0052	0.0052	19.4	...	...	...	...	...	...	...	...	...
4881.140	33.4	0.0155	0.0154	56.9	...	[Fe III]	4881.000	-8.6	5D 3d6	3H 3d6	4.0	4.0	...
4890.905	33.5	0.0138	0.0137	50.5	5 A	O II	4890.856	-3.0	4So 2s2.2p2.(3P).3p	4P 2s2.2p2.(3P).3d	1.5	0.5	2/0
4906.809	13.1	0.0043	0.0042	22.5	3 A	O II	4906.830	1.3	4So 2s2.2p2.(3P).3p	4P 2s2.2p2.(3P).3d	1.5	1.5	2/1
4921.933	22.0	1.2341	1.2186	385.1	2 A	He I	4921.931	-0.1	1Po 1s.2p	1D 1s.4d	1.0	2.0	0/0
4924.524	16.4	0.0091	0.0089	25.1	1 A	O II	4924.529	0.3	4So 2s2.2p2.(3P).3p	4P 2s2.2p2.(3P).3d	1.5	2.5	1/1
				...	...	[Fe III]	4924.500 ?	-1.5	5D 3d6	3H 3d6	4.0	5.0	...
4931.229	18.8	0.0298	0.0294	85.6	0 A	[O III]	4931.226	-0.2	3P 2s2.2p2	1D 2s2.2p2	0.0	2.0	2/2
4953.007	16.8	0.0038	0.0037	14.0	3 A	O II	4952.940 ?	-4.1	2[4] 2s2.2p2.(3P<1>).5g	2[5]o 2s2.2p2.(1D).5f.H	3.5	****	...
				3 A	O II	O II	4952.950 ?	-3.4	2[4] 2s2.2p2.(3P<1>).5g	2[5]o 2s2.2p2.(1D).5f.H	4.5	****	...
4958.915	16.0	74.1985	72.7233	9084.0	0 A	[O III]	4958.911	-0.2	3P 2s2.2p2	1D 2s2.2p2	1.0	2.0	1/1
4964.751	32.7	0.0216	0.0211	29.6	3 A	C II	4964.736	-0.9	2P 2s.2p.(3Po).3p	2Po 2s.2p.(3Po).3d	1.5	1.5	3/0
4987.360	19.4	0.0170	0.0165	71.1	3 A	C II	4987.300 ?	-3.6	4P 2s.2p.(3Po).4p	4Do 2s.2p.(3Po).6d	2.5	3.5	0/0
				5 C	N II	N II	4987.377	1.0	3S 2s2.2p.(2Po).3p	3Po 2s2.2p.(2Po).3d	1.0	0.0	2/0
				...	...	[Fe III]	4987.200	-9.6	a5D	a3H	3.0	4.0	...
4994.374	18.6	0.0435	0.0423	146.2	...	N II	4994.371	-0.2	3S 2s2.2p.(2Po).3p	3Po 2s2.2p.(2Po).3d	1.0	1.0	...
5006.845	15.6	221.3740	214.9350	9892.0	0 A	[O III]	5006.843	-0.1	3P 2s2.2p2	1D 2s2.2p2	2.0	2.0	1/1
5015.679	21.3	2.4681	2.3922	651.7	1 A	He I	5015.678	-0.1	1S 1s.2s	1Po 1s.3p	0.0	1.0	0/0
5031.963	19.3	0.0449	0.0434	69.0	6 B	C II	5032.128	9.8	2Po 2p3	2D 2s.2p.(3Po).3p	1.5	2.5	2/1
5035.808	21.7	0.0577	0.0558	75.7	8 C	[Fe II]	5035.484 ?	-19.3	a6D 3d6.(5D).4s	b4P 3d6.(3P4).4s	0.5	1.5	8/0
				8 C	C II	C II	5035.923	8.0	2Po 2p3	2D 2s.2p.(3Po).3p	0.5	1.5	2/1
5041.022	44.7	0.0751	0.0725	199.7	4 A	Si II	5041.024	0.1	2Po 3s2.(1S).4p	2D 3s2.(1S).4d	0.5	1.5	2/0
5045.095	18.1	0.0300	0.0289	112.9	2 A	O II	5045.119 ?	1.4	2[4] 2s2.2p2.(3P<2>).5g	2[4]o 2s2.2p2.(1D).5f.G	****	4.5	...
				3 B	N II	N II	5045.099	0.2	3Po 2s2.2p.(2Po).3s	3S 2s2.2p.(2Po).3p	2.0	1.0	1/0
5047.741	23.1	0.1958	0.1887	167.0	1 A	He I	5047.738	-0.2	1Po 1s.2p	1S 1s.4s	1.0	0.0	0/0
5056.067	51.6	0.1247	0.1200	323.6	5 B	Si II	5055.984	-4.9	2Po 3s2.(1S).4p	2D 3s2.(1S).4d	1.5	2.5	2/0
				8	Si II	Si II	5056.316	14.8	2Po 3s2.(1S).4p	2D 3s2.(1S).4d	1.5	1.5	2/0
5080.619	43.0	0.0015	0.0014	7.1	...	...	...	...	...	...	...	...	...
5099.390	49.2	0.0009	0.0009	7.7	...	...	...	...	...	...	...	...	...
5121.850	20.8	0.0282	0.0268	103.7	1 A	C II	5121.828	-1.3	2Po 2s2.4p	2P 2s.2p.(3Po).3p	1.5	1.5	3/2



Table E.1 (continued) - IC 418 Line List

$\lambda_o$ (Å) (1)	FWHM (km/s) (2)	$F(\lambda)/F(H\beta)$ $(F(H\beta) = 100)$ (3)	$I(\lambda)/I(H\beta)$ $(I(H\beta) = 100)$ (4)	S/N (5)	ID: (6)	Ion (7)	$\lambda$ (Å) (8)	$\delta V$ (km/s) (9)	Lower Term/Config (10)	Upper Term/Config (11)	$j_1$ (12)	$j_2$ (13)	Multi (14)
5125.232	14.9	0.0061	0.0058	29.6	1 A	C II	5125.208	-1.4	2Po 2s2.4p	2P 2s.2p.(3Po).3p	0.5	0.5	3/2
5126.960	16.9	0.0032	0.0030	12.7	1 A	C II	5126.963	0.2	2Po 2s2.4p	2P 2s.2p.(3Po).3p	1.5	0.5	3/2
5131.705	57.3	0.0173	0.0164	47.1	...	...	...	...	...	...	...	...	...
5133.114	39.5	0.0047	0.0044	14.9	6 B	C II	5132.947	-9.8	4Po 2s.2p.(3Po).3s	4P 2s.2p.(3Po).3p	0.5	1.5	6/0
				8 D	C II	C II	5133.282	9.8	4Po 2s.2p.(3Po).3s	4P 2s.2p.(3Po).3p	1.5	2.5	4/0
5143.424	51.8	0.0100	0.0095	19.6	3 A	[Fe III]	5143.290 ?	-7.8	3D 3d6	3F2 3d6	3.0	3.0	4/1
				5 B	C II	C II	5143.494	4.1	4Po 2s.2p.(3Po).3s	4P 2s.2p.(3Po).3p	1.5	0.5	6/1
5145.165	14.8	0.0042	0.0040	12.3	3 B	C II	5145.165	0.0	4Po 2s.2p.(3Po).3s	4P 2s.2p.(3Po).3p	2.5	2.5	3/1
5146.692	54.1	0.0297	0.0281	90.1	8	O I	5146.462 ?	-13.4	3P 2s2.2p3.(4So).3p	3So 2s2.2p3.(4So).9s	1.0	1.0	2/0
				4 B	O I	O I	5146.610 ?	-4.8	3P 2s2.2p3.(4So).3p	3So 2s2.2p3.(4So).9s	2.0	1.0	1/0
				4 B	O I	O I	5146.652 ?	-2.3	3P 2s2.2p3.(4So).3p	3So 2s2.2p3.(4So).9s	0.0	1.0	2/0
				3 A	O I	O I	5146.700 ?	0.5	1F 2s2.2p3.(2Do).3p	1Do 2s2.2p3.(2Do<3/2>).7s	3.0	2.0	0/0
5151.117	20.5	0.0049	0.0046	16.4	2 A	C II	5151.085	-1.9	4Po 2s.2p.(3Po).3s	4P 2s.2p.(3Po).3p	2.5	1.5	4/2
5158.858	53.3	0.0108	0.0102	36.2	1 A	[Fe II]	5158.777	-4.7	a4F 3d7	a4H 3d6.(3H).4s	4.5	6.5	2/1
5167.180	40.6	0.0052	0.0049	9.9	5 A	O I	5167.300 ?	6.9	1D 2s2.2p3.(2Po).3p	1Po 2s2.2p3.(2Po).8s	2.0	1.0	0/0
5172.786	56.4	0.0052	0.0049	9999.0	6 A	[Fe III]	5172.640	-8.5	3D 3d6	3F2 3d6	3.0	2.0	4/1
				*	N II	N II	5172.973	10.8	5Do 2s.2p2.(4P).3p	5F 2s.2p2.(4P).3d	0.0	1.0	* /0
5173.564	30.7	0.0048	0.0045	9999.0	8 D	N II	5173.385	-10.4	5Do 2s.2p2.(4P).3p	5F 2s.2p2.(4P).3d	2.0	3.0	8/0
5175.862	14.0	0.0019	0.0018	8.1	5 C	N II	5175.889	1.6	5Do 2s.2p2.(4P).3p	5F 2s.2p2.(4P).3d	3.0	4.0	5/1
5179.521	18.6	0.0036	0.0033	18.4	7	N II	5179.344	-10.2	5Po 2s.2p2.(4P).3p	5D 2s.2p2.(4P).3d	3.0	4.0	2/0
				2 A	N II	N II	5179.520	-0.1	5Do 2s.2p2.(4P).3p	5F 2s.2p2.(4P).3d	4.0	5.0	2/1
5183.806	45.7	0.0053	0.0050	29.0	...	...	...	...	...	...	...	...	...
5191.702	18.8	0.0411	0.0386	186.5	5 A	[Ar III]	5191.820	6.8	1D 3s2.3p4	1S 3s2.3p4	2.0	0.0	0/0
5198.012	53.5	0.2145	0.2011	238.0	1 A	[N I]	5197.901	-6.4	4So 2s2.2p3	2Do 2s2.2p3	1.5	1.5	1/1
5200.329	53.2	0.1252	0.1173	238.8	0 A	[N I]	5200.257	-4.1	4So 2s2.2p3	2Do 2s2.2p3	1.5	2.5	1/1
5217.986	17.8	0.0011	0.0010	9.3	...	...	...	...	...	...	...	...	...
5258.999	24.3	0.0034	0.0031	7.6	4 B	C II	5259.055	3.2	4Fo 2s.2p.(3Po).3d	4D 2s.2p.(3Po).4p	3.5	2.5	5/1
5259.664	28.9	0.0034	0.0032	7.2	3 A	C II	5259.664	0.0	4Fo 2s.2p.(3Po).3d	4D 2s.2p.(3Po).4p	1.5	0.5	8/1
				5 C	C II	C II	5259.758	5.3	4Fo 2s.2p.(3Po).3d	4D 2s.2p.(3Po).4p	2.5	1.5	8/1
5261.726	49.0	0.0067	0.0062	25.6	3 A	[Fe II]	5261.621	-6.0	a4F 3d7	a4H 3d6.(3H).4s	3.5	5.5	5/1
5270.562	30.7	0.0163	0.0151	53.9	6 B	[Fe III]	5270.400	-9.2	5D 3d6	3P4 3d6	3.0	2.0	2/0
5273.346	49.8	0.0019	0.0018	8.1	4 A	[Fe II]	5273.346	0.0	a4F 3d7	b4P 3d6.(3P4).4s	4.5	2.5	2/0
5275.155	58.6	0.0201	0.0186	41.0	3 A	O I	5275.123	-1.8	3P 2s2.2p3.(4So).3p	3Do 2s2.2p3.(4So).7d	2.0	****	1/0
				5 B	O I	O I	5275.167	0.7	3P 2s2.2p3.(4So).3p	3Do 2s2.2p3.(4So).7d	0.0	****	2/0
5284.920	26.9	0.0020	0.0019	5.6	...	...	...	...	...	...	...	...	...
5299.059	53.3	0.0402	0.0371	180.2	9	O I	5298.887	-9.7	3P 2s2.2p3.(4So).3p	3So 2s2.2p3.(4So).8s	1.0	1.0	2/0
				4 A	O I	O I	5299.044	-0.8	3P 2s2.2p3.(4So).3p	3So 2s2.2p3.(4So).8s	2.0	1.0	1/0
				6 C	O I	O I	5299.088	1.7	3P 2s2.2p3.(4So).3p	3So 2s2.2p3.(4So).8s	0.0	1.0	2/0

Table E.1 (continued) - IC 418 Line List

$\lambda_0$ (Å)	FWHM (km/s)	$F(\lambda)/F(H\beta)$ ( $F(H\beta) = 100$ )	$I(\lambda)/I(H\beta)$ ( $I(H\beta) = 100$ )	S/N	ID:	Ion	$\lambda$ (Å)	$\delta V$ (km/s)	Lower Term/Config	Upper Term/Config	$j_1$	$j_2$	Multi
(1)	(2)	(3)	(4)	(5)	(6)	(7)	(8)	(9)	(10)	(11)	(12)	(13)	(14)
5330.516	33.1	0.0025	0.0023	8.2	8 D	O I	5330.726 ?	11.8	5P 2s2.2p3.(4So).3p	5Do 2s2.2p3.(4So).5d	3.0	2.0	5/0
					8 D	O I	5330.735 ?	12.3	5P 2s2.2p3.(4So).3p	5Do 2s2.2p3.(4So).5d	3.0	3.0	4/0
					8 D	O I	5330.741 ?	12.7	5P 2s2.2p3.(4So).3p	5Do 2s2.2p3.(4So).5d	3.0	4.0	2/0
5332.771	19.5	0.0061	0.0056	20.8	5 A	C II	5332.889	6.6	2Po 2s2.4p	2S 2s2.6s	0.5	0.5	1/1
5334.647	20.7	0.0069	0.0063	42.4	5 A	C II	5334.789	8.0	2Po 2s2.4p	2S 2s2.6s	1.5	0.5	1/1
5342.392	18.4	0.0302	0.0277	153.2	4 A	C II	5342.370 *	-1.2	2Fo 2s2.4f	2G 2s2.7g	****	****	...
5345.943	16.3	0.0038	0.0035	20.5	...	...	...	...	...	...	...	...	...
5368.205	20.7	0.0063	0.0057	27.9	6 D	C II	5368.340 ?	7.5	2D 2s2.4d	2Po 2s2.7p	1.5	1.5	2/0
				8	8	C II	5368.460 ?	14.2	2D 2s2.4d	2Po 2s2.7p	1.5	0.5	2/0
5374.845	14.8	0.0015	0.0014	7.3	...	...	...	...	...	...	...	...	...
5376.691	70.0	0.0058	0.0053	9.1	6 B	[Fe II]	5376.452	-13.3	a4F 3d7	a4H 3d6.(3H).4s	1.5	3.5	9/0
5380.882	78.3	0.0079	0.0072	13.6	8	O II	5380.640 ?	-13.5	4F 2s2.2p2.(3P).4d	4Do 2s2.2p2.(3P).7p	2.5	3.5	5/0
5400.553	50.4	0.0031	0.0029	9.6	...	...	...	...	...	...	...	...	...
5412.255	16.2	0.0006	0.0006	11.2	7 A	[Fe III]	5411.980	-15.2	5D 3d6	3P4 3d6	1.0	2.0	5/0
5432.799	24.8	0.0021	0.0019	12.9	7 A	[Fe II]	5433.129	18.3	a4F 3d7	b4P 3d6.(3P4).4s	3.5	2.5	4/0
				...	...	S II	5432.797	-0.1	4P 3s2.3p2.(3P).4s	4Do 3s2.3p2.(3P).4p	1.5	2.5	...
5452.063	20.2	0.0046	0.0042	25.9	3 A	N II	5452.071	0.4	3P 2s2.2p.(2Po).3p	3Po 2s2.2p.(2Po).3d	0.0	1.0	5/4
5454.035	43.2	0.0092	0.0083	46.8	8	S II	5453.855	-9.9	4P 3s2.3p2.(3P).4s	4Do 3s2.3p2.(3P).4p	2.5	3.5	2/0
				8	8	N II	5454.215	9.9	3P 2s2.2p.(2Po).3p	3Po 2s2.2p.(2Po).3d	1.0	0.0	5/0
5462.568	26.2	0.0050	0.0045	36.4	2 A	N II	5462.581	0.7	3P 2s2.2p.(2Po).3p	3Po 2s2.2p.(2Po).3d	1.0	1.0	5/4
5463.566	45.1	0.0018	0.0016	9.5	...	...	...	...	...	...	...	...	...
5473.624	42.0	0.0023	0.0021	17.3	3 B	S II	5473.614	-0.6	4P 3s2.3p2.(3P).4s	4Do 3s2.3p2.(3P).4p	0.5	0.5	7/1
5478.087	16.6	0.0033	0.0030	19.6	2 A	N II	5478.086	-0.1	3P 2s2.2p.(2Po).3p	3Po 2s2.2p.(2Po).3d	1.0	2.0	4/4
5480.050	17.0	0.0062	0.0056	34.9	1 A	N II	5480.050	0.0	3P 2s2.2p.(2Po).3p	3Po 2s2.2p.(2Po).3d	2.0	1.0	4/3
5495.655	19.1	0.0165	0.0148	87.5	3 A	N II	5495.655	0.0	3P 2s2.2p.(2Po).3p	3Po 2s2.2p.(2Po).3d	2.0	2.0	3/3
				7 C	7 C	[Fe II]	5495.824	9.2	a4F 3d7	a2D2 3d7	1.5	1.5	4/0
5512.790	60.9	0.0350	0.0313	95.3	8	O I	5512.602	-10.2	3P 2s2.2p3.(4So).3p	3Do 2s2.2p3.(4So).6d	1.0	****	2/0
				3 A	3 A	O I	5512.772	-1.0	3P 2s2.2p3.(4So).3p	3Do 2s2.2p3.(4So).6d	2.0	****	1/0
				5 B	5 B	O I	5512.820	1.6	3P 2s2.2p3.(4So).3p	3Do 2s2.2p3.(4So).6d	0.0	****	2/0
5517.686	24.3	0.2038	0.1819	313.3	2 A	[Cl III]	5517.720	1.9	4So 3s2.3p3	2Do 3s2.3p3	1.5	2.5	1/1
5526.212	25.8	0.0017	0.0015	7.1	2 A	N II	5526.234	1.2	5P 2s.2p2.(4P).3s	5Do 2s.2p2.(4P).3p	1.0	2.0	7/5
				2 A	2 A	S II	5526.243 ?	1.7	4F 3s2.3p2.(3P).3d	4Do 3s2.3p2.(3P).4p	3.5	3.5	4/2
5530.215	19.2	0.0023	0.0021	10.8	2 A	N II	5530.242	1.5	5P 2s.2p2.(4P).3s	5Do 2s.2p2.(4P).3p	2.0	3.0	5/3
5535.359	16.9	0.0056	0.0050	26.4	1 A	N II	5535.347	-0.6	5P 2s.2p2.(4P).3s	5Do 2s.2p2.(4P).3p	3.0	4.0	2/2
				3 C	3 C	C II	5535.353	-0.3	2S 2s2.4s	2Po 2s2.5p	0.5	1.5	1/0
				2 B	2 B	N II	5535.384	1.3	5P 2s.2p2.(4P).3s	5Do 2s.2p2.(4P).3p	1.0	1.0	8/4
5537.853	36.1	0.4000	0.3560	216.6	3 A	[Cl III]	5537.890	2.0	4So 3s2.3p3	2Do 3s2.3p3	1.5	1.5	1/1
5543.517	27.6	0.0050	0.0045	15.3	1 A	N II	5543.471	-2.5	5P 2s.2p2.(4P).3s	5Do 2s.2p2.(4P).3p	2.0	2.0	7/4

Table E.1 (continued) - IC 418 Line List

$\lambda_0$ (Å)	FWHM (km/s)	$F(\lambda)/F(H\beta)$ ( $F(H\beta) = 100$ )	$I(\lambda)/I(H\beta)$ ( $I(H\beta) = 100$ )	S/N	ID:	Ion	$\lambda$ (Å)	$\delta V$ (km/s)	Lower Term/Config	Upper Term/Config	$j_1$	$j_2$	Multi
(1)	(2)	(3)	(4)	(5)	(6)	(7)	(8)	(9)	(10)	(11)	(12)	(13)	(14)
5545.933	18.8	0.0017	0.0015	10.7	4 A	[Fe II]	5545.900 ?	-1.8	a4D 3d6.(5D).4s	a4G 3d6.(3G).4s	3.5	3.5	6/0
5547.994	36.1	0.0024	0.0022	7.7	...	...	...	...	...	...	...	...	...
5551.930	12.0	0.0007	0.0006	7.5	2 A	N II	5551.922	-0.4	5P 2s.2p2.(4P).3s	5Do 2s.2p2.(4P).3p	3.0	3.0	4/2
5554.983	56.0	0.0179	0.0159	84.5	7	O I	5554.832	-8.1	3P 2s2.2p3.(4So).3p	3So 2s2.2p3.(4So).7s	1.0	1.0	2/0
					4 B	O I	5555.004	1.2	3P 2s2.2p3.(4So).3p	3So 2s2.2p3.(4So).7s	2.0	1.0	1/0
					7	O I	5555.053	3.8	3P 2s2.2p3.(4So).3p	3So 2s2.2p3.(4So).7s	0.0	1.0	2/0
5567.469	19.8	0.0013	0.0012	7.2	...	...	...	...	...	...	...	...	...
5577.389	48.6	0.0297	0.0263	143.2	1 A	[O I]	5577.339	-2.7	1D 2s2.2p4	1S 2s2.2p4	2.0	0.0	0/0
5587.863	10.7	0.0013	0.0011	8.9	...	...	...	...	...	...	...	...	...
5595.511	35.5	0.0015	0.0014	8.7	7	Fe III	5595.329 ?	-9.8	5Fo 3d5.(4D).5p	5F 3d5.(4G).5d	1.0	2.0	*1
5606.134	34.0	0.0015	0.0013	10.4	7 A	[Fe II]	5606.246 ?	6.0	a4D 3d6.(5D).4s	b2P 3d6.(3P4).4s	3.5	1.5	2/0
					...	S II	5606.151	0.9	4F 3s2.3p2.(3P).3d	4Do 3s2.3p2.(3P).4p	4.5	3.5	...
5627.804	22.0	0.0021	0.0018	14.8	4 A	N II	5627.760	-2.4	3P 2s2.2p.(2Po).4p	3Po 2s2.2p.(2Po).5d	0.0	1.0	5/0
5640.188	24.4	0.0023	0.0020	10.5	6	S II	5640.345	8.4	4F 3s2.3p2.(3P).3d	4Do 3s2.3p2.(3P).4p	3.5	2.5	5/0
5648.066	24.5	0.0016	0.0014	10.1	4 A	C II	5648.070	0.2	4Po 2s.2p.(3Po).3s	4S 2s.2p.(3Po).3p	1.5	1.5	2/0
					5 B	N II	5648.137	3.8	3P 2s2.2p.(2Po).4p	3Po 2s2.2p.(2Po).5d	1.0	2.0	4/0
5662.337	27.3	0.0029	0.0025	8.3	...	...	...	...	...	...	...	...	...
5664.519	20.5	0.0017	0.0015	4.5	7 D	S II	5664.773	13.4	4F 3s2.3p2.(3P).3d	4Do 3s2.3p2.(3P).4p	1.5	0.5	8/1
5666.630	17.1	0.0473	0.0414	176.9	1 A	N II	5666.629	-0.1	3Po 2s2.2p.(2Po).3s	3D 2s2.2p.(2Po).3p	1.0	2.0	5/5
5676.023	17.6	0.0225	0.0197	123.4	1 A	N II	5676.017	-0.3	3Po 2s2.2p.(2Po).3s	3D 2s2.2p.(2Po).3p	0.0	1.0	5/5
5679.552	20.7	0.0771	0.0674	170.8	2 A	N II	5679.558	0.3	3Po 2s2.2p.(2Po).3s	3D 2s2.2p.(2Po).3p	2.0	3.0	2/2
5686.199	18.5	0.0145	0.0127	70.1	2 A	N II	5686.212	0.7	3Po 2s2.2p.(2Po).3s	3D 2s2.2p.(2Po).3p	1.0	1.0	5/5
5705.318	24.2	0.0020	0.0017	9.5	4 B	N II	5705.316	-0.1	3P 2s2.2p.(4P).3s	3Do 2s.2p2.(4P).3p	1.0	1.0	5/0
5708.910	43.1	0.0022	0.0019	3.7	...	...	...	...	...	...	...	...	...
5710.763	18.7	0.0156	0.0136	75.9	1 A	N II	5710.766	0.2	3Po 2s2.2p.(2Po).3s	3D 2s2.2p.(2Po).3p	2.0	2.0	4/4
5711.604	30.6	0.0009	0.0008	99999.0	*	Fe III	5711.414 ?	-10.0	5Fo 3d5.(4D).5p	5F 3d5.(4G).5d	5.0	5.0	3/0
					8 D	S II	5711.450	-8.1	4Po 3s2.3p2.(3P).5p	4P 3s2.3p2.(3P).6d	1.5	0.5	6/0
5724.956	32.9	0.0029	0.0025	10.9	9 D	Fe I	5711.849 ?	12.8	y5Fo 3d7.(4F).4p	g5D 3d6.4s.(4D).5s	2.0	2.0	*1
5730.637	17.5	0.0015	0.0013	8.9	2 A	N II	5724.752	-10.7	3D 2s2.2p.(2Po).4p	3Fo 2s2.2p.(2Po).5d	3.0	2.0	4/0
5739.757	18.7	0.0045	0.0039	21.8	2 A	N II	5730.656	1.0	3Po 2s2.2p.(2Po).3s	3D 2s2.2p.(2Po).3p	2.0	1.0	4/4
5744.476	46.3	0.0080	0.0069	20.4	...	Si III	5739.734	-1.2	1S 3s.4s	1Po 3s.4p	0.0	1.0	0/0
5747.287	17.1	0.0038	0.0033	29.3	7 B	[Fe II]	5746.966 ?	...	...	...	...	...	...
					3 A	O II	5747.330	-16.7	a4D 3d6.(5D).4s	b2P 3d6.(3P4).4s	2.5	1.5	2/0
5754.629	47.5	3.1908	2.7615	1907.0	2 A	[N II]	5754.644	0.8	1D 2s2.2p2	2F 2s2.2p2.(3P).5d	2.5	3.5	0/0
5759.785	48.3	0.0023	0.0020	7.0	...	...	...	...	...	1S 2s2.2p2	2.0	0.0	0/0
5764.485	59.9	0.0030	0.0026	16.2	6 B	S II	5764.596 ?	...	...	...	...	...	...
5766.223	25.1	0.0025	0.0022	10.4	...	...	...	5.8	4Po 3s2.3p2.(3P).5p	4P 3s2.3p2.(3P).6d	0.5	1.5	6/0
					...	...	...	...	...	...	...	...	...

Table E.1 (continued) - IC 418 Line List

$\lambda_0$ (Å)	FWHM (km/s)	$F(\lambda)/F(H\beta)$ ( $F(H\beta) = 100$ )	$I(\lambda)/I(H\beta)$ ( $I(H\beta) = 100$ )	S/N	ID:	Ion	$\lambda$ (Å)	$\delta V$ (km/s)	Lower Term/Config	Upper Term/Config	$j_1$ (12)	$j_2$ (13)	Multi (14)
(1)	(2)	(3)	(4)	(5)	(6)	(7)	(8)	(9)	(10)	(11)	(12)	(13)	(14)
5767.459	15.4	0.0015	0.0013	9.5	5 A	S II	5767.416 ?	-2.2	4Do 3s2.3p2.(3P).5p	4P 3s2.3p2.(3P).6d	3.5	2.5	2/0
				6 B	6 B	[Fe II]	5767.539 ?	4.1	b4P 3d6.(3P4).4s	c2D 3d6.(1D4).4s	2.5	2.5	3/0
5790.942	13.5	0.0012	0.0011	4.4	...	...	...	...	...	...	...	...	...
5793.201	16.7	0.0014	0.0012	4.9	6 B	C II	5793.300	5.1	4Fo 2s.2p.(3Po).4d	4G 2s.2p.(3Po).6f	1.5	2.5	8/0
5826.540	43.9	0.0022	0.0019	9.3	7 C	S II	5826.360 ?	-9.3	4Do 3s2.3p2.(3P).5p	4P 3s2.3p2.(3P).7s	1.5	2.5	5/0
5832.961	18.6	0.0033	0.0028	15.8	...	...	...	...	...	...	...	...	...
5846.704	20.6	0.0150	0.0129	75.2	...	...	...	...	...	...	...	...	...
5852.354	37.1	0.0031	0.0027	10.0	...	...	...	...	...	...	...	...	...
5855.143	61.6	0.0049	0.0042	12.3	...	...	...	...	...	...	...	...	...
5859.582	26.0	0.0015	0.0013	9.8	...	...	...	...	...	...	...	...	...
5867.726	16.4	0.0041	0.0035	22.3	6 D	Al II	5867.640 ?	-4.4	3D 3s.4d	3Fo 3s.6f	3.0	2.0	4/0
				7	7	Al II	5867.780 ?	2.7	3D 3s.4d	3Fo 3s.6f	2.0	2.0	5/0
				9	9	Al II	5867.890 ?	8.4	3D 3s.4d	3Fo 3s.6f	1.0	2.0	5/0
5875.650	25.9	16.0305	13.6746	5395.0	4 A	He I	5875.615	-1.8	3Po 1s.2p	3D 1s.3d	2.0	3.0	2/0
5879.032	23.3	0.0023	0.0020	8.5	3 A	N II	5879.080 ?	2.4	3Fo 2s2.2p.(2Po).4d	2[5/2] 2s2.2p.(2Po<3/2>).6f.G	2.0	2.0	...
5889.960	44.8	0.0931	0.0793	301.5	7	C II	5889.780	-9.2	2D 2s2.3d	2Po 2s2.4p	2.5	1.5	2/0
				4 B	4 B	Na I	5889.951 ?	-0.4	2S 3s	2Po 3p	0.5	1.5	1/0
5891.565	18.6	0.0213	0.0181	99.2	5 A	C II	5891.600	1.8	2D 2s2.3d	2Po 2s2.4p	1.5	0.5	2/0
5896.024	35.6	0.0405	0.0344	134.2	5 C	Na I	5895.924 ?	-5.1	2S 3s	2Po 3p	0.5	0.5	1/0
5915.611	56.5	0.0040	0.0034	16.0	...	...	...	...	...	...	...	...	...
5927.802	17.4	0.0225	0.0191	113.8	2 A	N II	5927.820	0.9	3P 2s2.2p.(2Po).3p	3Do 2s2.2p.(2Po).3d	0.0	1.0	5/4
5931.773	16.7	0.0322	0.0273	156.7	2 A	N II	5931.790	0.9	3P 2s2.2p.(2Po).3p	3Do 2s2.2p.(2Po).3d	1.0	2.0	5/4
5940.264	18.2	0.0164	0.0139	63.0	1 A	N II	5940.240	-1.2	3P 2s2.2p.(2Po).3p	3Do 2s2.2p.(2Po).3d	1.0	1.0	5/4
5941.663	16.0	0.0372	0.0315	137.3	1 A	N II	5941.650	-0.7	3P 2s2.2p.(2Po).3p	3Do 2s2.2p.(2Po).3d	2.0	3.0	2/2
5944.925	10.0	0.0009	0.0008	6.2	3 A	N II	5944.960 ?	1.8	3Fo 2s2.2p.(2Po).4d	2[7/2] 2s2.2p.(2Po<3/2>).6f.G	4.0	3.0	...
5952.385	13.8	0.0061	0.0052	33.7	2 A	N II	5952.390	0.3	3P 2s2.2p.(2Po).3p	3Do 2s2.2p.(2Po).3d	2.0	2.0	4/3
5957.653	34.0	0.0161	0.0136	99999.0	2 A	Si II	5957.560	-4.7	2Po 3s2.(1S).4p	2S 3s2.(1S).5s	0.5	0.5	1/1
5958.625	56.2	0.0563	0.0475	99999.0	8	O I	5958.385	-12.1	3P 2s2.2p3.(4So).3p	3Do 2s2.2p3.(4So).5d	1.0	***	2/0
				3 A	3 A	O I	5958.584	-2.1	3P 2s2.2p3.(4So).3p	3Do 2s2.2p3.(4So).5d	2.0	***	1/0
				5 C	5 C	O I	5958.640	0.8	3P 2s2.2p3.(4So).3p	3Do 2s2.2p3.(4So).5d	0.0	***	2/0
				2 A	2 A	Si II	5978.930	-4.4	2Po 3s2.(1S).4p	2S 3s2.(1S).5s	1.5	0.5	1/1
5979.018	49.5	0.0282	0.0238	182.4	2 A	Si II	5979.980 ?	-5.6	3D 2s2.2p.(2Po).3p	3Do 2s2.2p.(2Po).5d	2.0	3.0	4/0
5991.093	20.0	0.0011	0.0009	6.2	4 A	C I	5990.980 ?	7.5	3D 2s2.2p.(2Po).3p	3Po 2s2.2p.(2Po).6s	3.0	2.0	2/0
6013.010	35.7	0.0034	0.0028	13.4	8	C I	6013.160 ?	10.0	3D 2s2.2p.(2Po).3p	3Fo 2s2.2p.(2Po).5d	3.0	4.0	2/0
				8	8	C I	6013.210 ?	3.4	3D 2s2.2p.(2Po).3p	3Fo 2s2.2p.(2Po).5d	2.0	2.0	5/0
6019.822	40.3	0.0046	0.0039	19.4	7	C I	6019.890 ?	-11.8	3P 2s2.2p3.(4So).3p	3So 2s2.2p3.(4So).6s	1.0	1.0	2/0
6046.471	60.9	0.1053	0.0881	153.2	8	O I	6046.233	-1.6	3P 2s2.2p3.(4So).3p	3So 2s2.2p3.(4So).6s	2.0	1.0	1/0
				3 A	3 A	O I	6046.438	1.2	3P 2s2.2p3.(4So).3p	3So 2s2.2p3.(4So).6s	0.0	1.0	2/0
				5 B	5 B	O I	6046.495		3P 2s2.2p3.(4So).3p	3So 2s2.2p3.(4So).6s			

Table E.1 (continued) - IC 418 Line List

$\lambda_o$ (Å)	FWHM (km/s)	$F(\lambda)/F(H\beta)$ ( $F(H\beta) = 100$ )	$I(\lambda)/I(H\beta)$ ( $I(H\beta) = 100$ )	S/N	ID:	Ion	$\lambda$ (Å)	$\delta V$ (km/s)	Lower Term/Config	Upper Term/Config	$j_1$ (12)	$j_2$ (13)	Multi (14)
(1)	(2)	(3)	(4)	(5)	(6)	(7)	(8)	(9)	(10)	(11)	(12)	(13)	(14)
6074.324	19.0	0.0019	0.0015	12.0	...	...	...	...	...	...	...	...	...
6096.195	20.7	0.0017	0.0014	12.7	4 A	[Fe III]	6096.300 ?	5.2	3P4 3d6	1D4 3d6	2.0	2.0	1/0
6098.538	21.5	0.0014	0.0011	9.0	9 C	N II	6096.320	6.2	3Do 2s.2p2.(4P).3p	3F 2s.2p2.(4P).3d	3.0	4.0	2/0
6130.475	41.7	0.0034	0.0028	11.2	4 A	C II	6098.510	-1.4	2P 2s.2p.(3Po).3p	2Do 2s.2p.(3Po).3d	1.5	2.5	2/0
6147.234	17.7	0.0023	0.0019	12.1	...	...	...	...	...	...	...	...	...
6151.336	26.7	0.0306	0.0253	127.3	3 A	C II	6151.270	-3.2	2D 2s2.4d	2Fo 2s2.6f	1.5	****	1/0
6154.406	24.5	0.0040	0.0033	21.5	7 D	C II	6151.540	10.0	2D 2s2.4d	2Fo 2s2.6f	2.5	****	1/0
6155.983	18.9	0.0021	0.0018	7.0	1 A	O I	6155.961	...	...	...	...	...	...
6156.785	29.2	0.0043	0.0036	19.9	1 A	O I	6155.970	-1.1	5P 2s2.2p3.(4So).3p	5Do 2s2.2p3.(4So).4d	1.0	0.0	8/5
6158.143	35.3	0.0051	0.0042	19.9	1 A	O I	6155.989	-0.6	5P 2s2.2p3.(4So).3p	5Do 2s2.2p3.(4So).4d	1.0	1.0	8/4
6161.778	41.1	0.0048	0.0039	21.1	5 B	[Cl II]	6156.737	0.3	5P 2s2.2p3.(4So).3p	5Do 2s2.2p3.(4So).4d	1.0	2.0	7/4
6167.678	36.4	0.0030	0.0025	15.0	6 D	N II	6156.778	-2.4	5P 2s2.2p3.(4So).3p	5Do 2s2.2p3.(4So).4d	2.0	1.0	8/6
6170.170	15.5	0.0011	0.0009	8.7	1 A	N II	6156.778	-0.4	5P 2s2.2p3.(4So).3p	5Do 2s2.2p3.(4So).4d	2.0	3.0	5/3
6173.331	13.6	0.0027	0.0023	20.1	1 A	N II	6158.150	0.3	5P 2s2.2p3.(4So).3p	5Do 2s2.2p3.(4So).4d	3.0	2.0	5/3
6176.066	15.0	0.0014	0.0012	8.2	2 A	N II	6158.172	1.4	5P 2s2.2p3.(4So).3p	5Do 2s2.2p3.(4So).4d	3.0	3.0	4/2
6230.704	14.6	0.0018	0.0015	15.6	5 B	C II	6158.188	2.2	5P 2s2.2p3.(4So).3p	5Do 2s2.2p3.(4So).4d	3.0	4.0	2/1
6237.117	19.9	0.0063	0.0052	9999.0	4 A	C II	6161.830	2.5	1D 3s2.3p4	1S 3s2.3p4	2.0	0.0	0/0
6239.482	17.8	0.0102	0.0084	63.7	4 A	C II	6167.750	3.5	3Fo 2s2.2p.(2Po).3d	3D 2s2.2p.(2Po).4p	4.0	3.0	2/0
6300.405	56.2	2.6718	2.1753	1977.0	0 A	[O I]	6170.160	-0.5	3Fo 2s2.2p.(2Po).3d	3D 2s2.2p.(2Po).4p	2.0	1.0	5/2
6312.107	23.6	1.0534	0.8566	590.2	1 A	[S III]	6173.310	-1.0	3Fo 2s2.2p.(2Po).3d	3D 2s2.2p.(2Po).4p	3.0	2.0	5/2
6325.191	22.2	0.0032	0.0026	8.7	7 A	[Fe II]	6176.050 ?	-0.8	3Do 2s2.2p.(2Po).4d	2I[7/2] 2s2.2p.(2Po<1/2>).6f.F	3.0	3.0	...
6332.889	19.5	0.0047	0.0038	21.1	...	...	6250.760	2.7	2Do 2s.2p.(3Po).3d	2P 2s.2p.(3Po).4p	2.5	1.5	2/0
6334.480	22.0	0.0032	0.0026	14.4	...	...	6257.180	3.0	2Po 2s2.4p	2D 2s2.5d	0.5	1.5	2/1
6347.193	47.7	0.0634	0.0513	83.3	2 A	Si II	6259.560	3.7	2Po 2s2.4p	2D 2s2.5d	1.5	2.5	2/1
6363.886	56.7	0.9389	0.7594	485.2	0 A	[O I]	6300.304	-4.8	3P 2s2.2p4	1D 2s2.2p4	2.0	2.0	1/1
6371.418	31.0	0.0537	0.0434	198.3	1 A	Si II	6312.100	-0.3	1D 3s2.3p2	1S 3s2.3p2	2.0	0.0	0/0
6379.649	25.5	0.0011	0.0009	10.7	3 A	O II	6325.501 ?	14.7	b4P 3d6.(3P4).4s	c2D 3d6.(1D4).4s	0.5	1.5	4/0
6382.988	44.1	0.0024	0.0020	16.1	...	...	...	...	...	...	...	...	...
6392.496	17.6	0.0012	0.0009	6.2	7 A	[Fe II]	6325.501 ?	...	...	...	...	...	...
6402.269	21.9	0.0133	0.0107	75.5	3 A	Ne I	6392.698 ?	9.5	a2G 3d7	b4D 3d6.(3D).4s	4.5	3.5	3/0
					9 C	C II	6393.000	23.6	4D 2s.2p.(3Po).4p	4Fo 2s.2p.(3Po).5d	2.5	2.5	7/0
					3 A	Ne I	6402.249 ?	-1.0	2[3/2]o 2p5.(2Po<3/2>).3s	2[5/2] 2p5.(2Po<3/2>).3p	2.0	3.0	...

Table E.1 (continued) - IC 418 Line List

$\lambda_o$ (Å)	FWHM (km/s)	$F(\lambda)/F(H\beta)$ ( $F(H\beta) = 100$ )	$I(\lambda)/I(H\beta)$ ( $I(H\beta) = 100$ )	S/N	ID:	Ion	$\lambda$ (Å)	$\delta V$ (km/s)	Lower Term/Config	Upper Term/Config	$j_1$	$j_2$	Multi
(1)	(2)	(3)	(4)	(5)	(6)	(7)	(8)	(9)	(10)	(11)	(12)	(13)	(14)
6454.393	22.4	0.0013	0.0010	5.4	3 A	O I	6454.444	2.4	5P 2s2.2p3.(4So).3p	5So 2s2.2p3.(4So).5s	2.0	2.0	2/1
6455.997	19.3	0.0016	0.0013	8.7	2 A	O I	6455.977	-0.9	5P 2s2.2p3.(4So).3p	5So 2s2.2p3.(4So).5s	3.0	2.0	1/1
6461.848	18.6	0.0730	0.0584	93.5	6 C	C II	6461.950 *	4.7	2Fo 2s2.4f	2G 2s2.6g	***	***	...
6527.257	29.3	0.0358	0.0285	70.6	0 A	[N II]	6527.240	-0.8	3P 2s2.2p2	1D 2s2.2p2	0.0	2.0	2/2
6548.096	39.8	67.5573	53.6007	10430.0	0 A	[N II]	6548.040	-2.6	3P 2s2.2p2	1D 2s2.2p2	1.0	2.0	1/1
6562.804	31.3	393.8931	312.0430	14100.0	3 A	H I	6562.800	-0.2	2 2*	3 3*	***	***	0/0
6578.050	18.3	0.6794	0.5374	870.5	2 A	C II	6578.050	0.0	2S 2s2.3s	2Po 2s2.3p	0.5	1.5	1/0
6583.467	40.2	206.1069	162.9287	11370.0	0 A	[N II]	6583.460	-0.3	3P 2s2.2p2	1D 2s2.2p2	2.0	2.0	1/1
6610.650	25.0	0.0035	0.0028	11.7	2 A	N II	6610.560	-4.1	1D 2s2.2p.(2Po).3p	1Fo 2s2.2p.(2Po).3d	2.0	3.0	0/0
6678.153	21.6	4.9466	3.8721	2346.0	2 A	He I	6678.152	0.0	1Po 1s.2p	1D 1s.3d	1.0	2.0	0/0
6699.344	20.1	0.0016	0.0013	7.7	...	He I	6699.315	-1.3	3S 1s.3s	3Po 1s.27p	***	***	...
6704.604	43.8	0.0026	0.0020	7.8	...	He I	6704.653	2.2	3S 1s.3s	3Po 1s.26p	***	***	...
6710.658	54.0	0.0030	0.0023	9.0	...	He I	6710.656	-0.1	3S 1s.3s	3Po 1s.25p	***	***	...
6716.523	52.0	2.6718	2.0831	1437.0	0 A	[S II]	6716.440	-3.7	4So 3s2.3p3	2Do 3s2.3p3	1.5	2.5	1/1
6723.459	22.3	0.0092	0.0071	9999.0	8	C II	6723.130	-14.7	2D 2s2.4d	2Po 2s2.6p	1.5	1.5	2/0
					6 C	C II	6723.320	-6.2	2D 2s2.4d	2Po 2s2.6p	1.5	0.5	2/0
					4 A	C II	6723.450	-0.4	2D 2s2.4d	2Po 2s2.6p	2.5	1.5	2/0
6724.226	18.0	0.0040	0.0031	9999.0	6 A	C II	6724.300	3.3	4Do 2s.2p.(3Po).4d	4D 2s.2p.(3Po).6p	1.5	0.5	9/0
					8 D	C II	6724.560	14.9	4D 2s.2p.(3Po).3p	4Do 2s.2p.(3Po).3d	0.5	1.5	9/0
6725.248	17.2	0.0020	0.0015	9999.0	...	...	...	...	...	...	...	...	...
6730.893	52.7	5.6794	4.4215	2317.0	0 A	[S II]	6730.810	-3.7	4So 3s2.3p3	2Do 3s2.3p3	1.5	1.5	1/1
6744.386	52.3	0.0064	0.0050	27.0	...	He I	6744.098 ?	-12.8	3S 1s.3s	3Po 1s.21p	***	***	...
6755.955	18.2	0.0028	0.0022	16.5	...	He I	6755.847	-4.8	3S 1s.3s	3Po 1s.20p	***	***	...
6769.672	21.3	0.0033	0.0026	21.6	...	He I	6769.548	-5.5	3S 1s.3s	3Po 1s.19p	***	***	...
6779.954	17.9	0.0141	0.0109	9999.0	1 A	C II	6779.940	-0.6	4Po 2s.2p.(3Po).3s	4D 2s.2p.(3Po).3p	1.5	2.5	5/4
6780.626	17.7	0.0071	0.0055	9999.0	0 A	C II	6780.600	-1.1	4Po 2s.2p.(3Po).3s	4D 2s.2p.(3Po).3p	0.5	1.5	7/4
6783.937	19.1	0.0028	0.0022	12.4	4 A	C II	6783.910	-1.2	4Po 2s.2p.(3Po).3s	4D 2s.2p.(3Po).3p	2.5	3.5	2/0
6785.783	20.8	0.0047	0.0037	25.9	...	He I	6785.676	-4.7	3S 1s.3s	3Po 1s.18p	***	***	...
6787.361	46.1	0.0095	0.0073	45.5	6 D	C II	6787.210	-6.7	4Po 2s.2p.(3Po).3s	4D 2s.2p.(3Po).3p	0.5	0.5	7/0
6791.466	19.2	0.0085	0.0066	51.5	1 A	C II	6791.470	0.2	4Po 2s.2p.(3Po).3s	4D 2s.2p.(3Po).3p	1.5	1.5	7/4
6800.678	17.7	0.0065	0.0050	33.1	0 A	C II	6800.680	0.1	4Po 2s.2p.(3Po).3s	4D 2s.2p.(3Po).3p	2.5	2.5	4/3
6804.950	19.8	0.0043	0.0033	29.2	...	He I	6804.840	-4.9	3S 1s.3s	3Po 1s.17p	***	***	...
6809.953	24.6	0.0027	0.0021	12.6	4 A	N II	6809.970	0.8	3Po 2s2.2p.(2Po).3d	3S 2s2.2p.(2Po).4p	2.0	1.0	1/0
6821.403	22.5	0.0027	0.0021	13.9	3 A	N II	6821.410 ?	0.3	5Fo 2s.2p2.(4P).4f	5F 2s.2p2.(4P).6d	4.0	***	1/0
6826.875	21.1	0.0429	0.0331	9999.0	...	...	...	...	...	...	...	...	...
6829.900	16.6	0.0014	0.0010	3.4	7 A	[Fe II]	6830.033	5.9	a4D 3d6.(5D).4s	a6S 3d5.4s2	1.5	2.5	3/0
6834.197	31.9	0.0021	0.0016	6.5	5 B	N II	6834.090	-4.7	3Po 2s2.2p.(2Po).3d	3S 2s2.2p.(2Po).4p	1.0	1.0	2/0
6836.444	33.5	0.0014	0.0011	3.5	...	...	...	...	...	...	...	...	...

Table E.1 (continued) - IC 418 Line List

$\lambda_o$ (Å)	FWHM (km/s)	$F(\lambda)/F(H\beta)$ ( $F(H\beta) = 100$ )	$I(\lambda)/I(H\beta)$ ( $I(H\beta) = 100$ )	S/N	ID:	Ion	$\lambda$ (Å)	$\delta V$ (km/s)	Lower Term/Config	Upper Term/Config	$j_1$ (12)	$j_2$ (13)	Multi (14)
(1)	(2)	(3)	(4)	(5)	(6)	(7)	(8)	(9)	(10)	(11)	(12)	(13)	(14)
6856.005	20.0	0.0065	0.0050	46.7	2 A	He I	6855.883	-5.3	3S 1s.3s	3Po 1s.15p	1.0	***	0/0
6929.430	20.4	0.0024	0.0019	17.7	...	...	...	...	...	...	...	...	...
6930.769	18.0	0.0044	0.0034	25.8	...	...	...	...	...	...	...	...	...
6934.033	16.4	0.0095	0.0072	55.3	8 C	[Fe II]	6933.660	-16.1	a4D 3d6.(5D).4s	b4F 3d6.(3F4).4s	2.5	3.5	5/0
6989.531	21.9	0.0154	0.0117	72.5	1 A	He I	6933.890	-6.2	3S 1s.3s	3Po 1s.13p	1.0	***	0/0
7002.204	56.5	0.1122	0.0849	14.2	8	O I	6989.450	-3.5	3S 1s.3s	3Po 1s.12p	1.0	***	0/0
							7001.899	-13.1	3P 2s2.2p3.(4So).3p	3Do 2s2.2p3.(4So).4d	1.0	1.0	5/0
					7	O I	7001.922	-12.1	3P 2s2.2p3.(4So).3p	3Do 2s2.2p3.(4So).4d	1.0	2.0	5/0
					4 A	O I	7002.173	-1.3	3P 2s2.2p3.(4So).3p	3Do 2s2.2p3.(4So).4d	2.0	1.0	4/0
					4 A	O I	7002.196	-0.4	3P 2s2.2p3.(4So).3p	3Do 2s2.2p3.(4So).4d	2.0	2.0	4/0
					5 D	O I	7002.230	1.1	3P 2s2.2p3.(4So).3p	3Do 2s2.2p3.(4So).4d	2.0	3.0	2/0
					5 D	O I	7002.250	2.0	3P 2s2.2p3.(4So).3p	3Do 2s2.2p3.(4So).4d	0.0	1.0	5/0
7032.469	24.2	0.0048	0.0036	29.9	2 A	Ne I	7032.413 ?	-2.4	2[3/2]o 2p3.(2Po<3/2>).3s	2[1/2] 2p5.(2Po<3/2>).3p	2.0	1.0	...
7050.047	53.3	0.0064	0.0048	38.5	...	...	...	...	...	...	...	...	...
7062.334	19.2	0.0163	0.0123	63.3	1 A	He I	7062.260	-3.2	3S 1s.3s	3Po 1s.11p	1.0	***	0/0
7065.228	27.3	9.3893	7.0593	3291.0	3 A	He I	7065.179	-2.1	3Po 1s.2p	3S 1s.3s	2.0	1.0	1/0
					4 B	He I	7065.217	-0.5	3Po 1s.2p	3S 1s.3s	1.0	1.0	2/0
7080.387	42.4	0.0058	0.0043	31.4	...	...	...	...	...	...	...	...	...
7099.927	63.0	0.0033	0.0024	14.7	...	...	...	...	...	...	...	...	...
7102.675	21.2	0.0037	0.0028	16.4	3 A	[Ni II]	7102.650 ?	-1.1	2F 3d8.(3F).4s	2P 3d8.(3P).4s	2.5	1.5	1/0
7112.965	35.4	0.0069	0.0052	34.6	5 B	C II	7113.040	3.2	4D 2s.2p.(3Po).3p	4Fo 2s.2p.(3Po).3d	1.5	2.5	8/1
7115.642	21.1	0.0057	0.0043	30.8	3 B	C II	7115.630	-0.5	4D 2s.2p.(3Po).3p	4Fo 2s.2p.(3Po).3d	2.5	3.5	5/1
7120.052	42.1	0.0093	0.0070	41.5	8	C II	7119.760	-12.3	4D 2s.2p.(3Po).3p	4Fo 2s.2p.(3Po).3d	1.5	1.5	8/0
					5 B	C II	7119.910	-6.0	4D 2s.2p.(3Po).3p	4Fo 2s.2p.(3Po).3d	3.5	4.5	2/0
7135.744	28.9	11.0687	8.2608	2973.0	2 A	[Ar III]	7135.800	2.3	3P 3s2.3p4	1D 3s2.3p4	2.0	2.0	1/1
7155.557	27.9	0.0072	0.0054	9999.0	7 A	[Fe II]	7155.160	-16.6	a4F 3d7	a2G 3d7	4.5	4.5	3/0
7156.637	20.9	0.0045	0.0034	9999.0	3 A	O I	7156.701 ?	2.7	1Do 2s2.2p3.(2Do).3s	1D 2s2.2p3.(2Do).3p	2.0	2.0	0/0
7160.559	21.3	0.0295	0.0219	141.7	2 A	He I	7160.580	0.9	3S 1s.3s	3Po 1s.10p	1.0	***	0/0
7231.329	23.6	0.2290	0.1692	255.3	3 A	C II	7231.340	0.4	2Po 2s2.3p	2D 2s2.3d	0.5	1.5	2/1
7236.414	21.1	0.6328	0.4673	9999.0	2 A	C II	7236.420	0.2	2Po 2s2.3p	2D 2s2.3d	1.5	2.5	2/1
7237.145	16.6	0.0663	0.0489	15.5	...	C II	7237.170	1.0	2Po 2s2.3p	2D 2s2.3d	1.5	1.5	...
7252.759	31.3	0.0182	0.0135	9999.0	4 A	O II	7252.717	-1.7	4P 2s2.2p2.(3P).3d	4Po 2s2.2p2.(3P).4p	1.5	0.5	6/0
7254.380	69.3	0.2122	0.1564	15.0	7 D	O I	7254.154	-9.3	3P 2s2.2p3.(4So).3p	3So 2s2.2p3.(4So).5s	1.0	1.0	2/0
					4 B	O I	7254.448	2.8	3P 2s2.2p3.(4So).3p	3So 2s2.2p3.(4So).5s	2.0	1.0	1/0
					7 D	O I	7254.531	6.2	3P 2s2.2p3.(4So).3p	3So 2s2.2p3.(4So).5s	0.0	1.0	2/0
7281.348	26.1	1.0763	0.7911	323.1	2 A	He I	7281.351	0.1	1Po 1s.2p	1S 1s.3s	1.0	0.0	0/0
7291.573	34.6	0.0168	0.0123	77.8	2 A	[Ca II]	7291.470 ?	-4.2	2S 3p6.(1S).4s	2D 3p6.(1S).3d	0.5	2.5	1/0
7298.019	24.3	0.0288	0.0211	116.9	2 A	He I	7298.030	0.4	3S 1s.3s	3Po 1s.9p	1.0	***	0/0

Table E.1 (continued) - IC 418 Line List

$\lambda_0$ (Å) (1)	FWHM (km/s) (2)	$F(\lambda)/F(H\beta)$ ( $F(H\beta) = 100$ ) (3)	$I(\lambda)/I(H\beta)$ ( $I(H\beta) = 100$ ) (4)	S/N (5)	ID: (6)	Ion (7)	$\lambda$ (Å) (8)	$\delta V$ (km/s) (9)	Lower Term/Config (10)	Upper Term/Config (11)	$j_1$ (12)	$j_2$ (13)	Multi (14)
7319.087	34.7	5.0382	3.6886	2161.0	4 A	[O II]	7318.920	-6.8	2Do 2s2.2p3	2Po 2s2.2p3	2.5	0.5	3/1
7320.135	27.4	13.7405	10.0586	6483.0	4 A	[O II]	7319.990	-5.9	2Do 2s2.2p3	2Po 2s2.2p3	2.5	1.5	2/0
7329.679	28.9	8.0153	5.8617	3856.0	1 A	[O II]	7329.660	-0.8	2Do 2s2.2p3	2Po 2s2.2p3	1.5	0.5	2/1
7330.754	27.3	7.7099	5.6377	3856.0	1 A	[O II]	7330.730	-1.0	2Do 2s2.2p3	2Po 2s2.2p3	1.5	1.5	2/1
7378.035	66.3	0.0067	0.0049	21.5	3 A	[Ni II]	7377.830	-8.3	2D 3d9	2F 3d8.(3F).4s	2.5	3.5	1/0
7391.385	36.1	0.0018	0.0013	99999.0	...	...	...	...	...	...	...	...	...
7423.733	58.3	0.0215	0.0156	119.4	1 A	N I	7423.641	-3.7	4P 2s2.2p2.(3P).3s	4So 2s2.2p2.(3P).3p	0.5	1.5	2/2
7442.351	57.7	0.0502	0.0363	219.9	1 A	N I	7442.298	-2.1	4P 2s2.2p2.(3P).3s	4So 2s2.2p2.(3P).3p	1.5	1.5	2/2
7452.706	58.8	0.0041	0.0029	16.4	4 A	[Fe II]	7452.540	-6.7	a4F 3d7	a2G 3d7	3.5	4.5	4/0
7459.251	21.1	0.0065	0.0047	26.7	...	...	...	...	...	...	...	...	...
7468.457	59.2	0.0809	0.0583	99999.0	3 A	N I	7468.312	-5.8	4P 2s2.2p2.(3P).3s	4So 2s2.2p2.(3P).3p	2.5	1.5	1/1
7469.554	21.5	0.0114	0.0082	99999.0	2 A	O II	7469.530 ?	-1.0	2G 2s2.2p2.(1D).3d	2[3]o 2s2.2p2.(3P).5f.F	4.5	3.5	...
7499.977	21.7	0.0587	0.0422	38.7	2 A	He I	7499.846 *	-5.2	3S 1s.3s	3Po 1s.8p	***	***	...
7505.008	17.5	0.0066	0.0048	45.9	6 B	O II	7504.960 ?	-1.9	2G 2s2.2p2.(1D).3d	2[5] 2s2.2p2.(3P).5f.G	3.5	4.5	...
				6 C	C II	C II	7505.260 ?	10.1	2Po 2s2.5p	2D 2s.2p.(3Po).3p	1.5	2.5	2/1
7505.392	47.3	0.0311	0.0224	122.7	5 A	C II	7505.260 ?	-5.3	2Po 2s2.5p	2D 2s.2p.(3Po).3p	1.5	2.5	2/0
7507.456	43.2	0.0169	0.0122	41.5	5 A	[Ni I]	7507.380 ?	-3.0	3D 3d9.(2D).4s	1D 3d8.(1D).4s2	3.0	2.0	1/0
7509.767	16.6	0.0046	0.0033	23.9	...	...	...	...	...	...	...	...	...
7513.379	43.5	0.0076	0.0055	15.7	...	He I	7513.340 ?	-1.6	1S 1s.3s	1Po 1s.28p	***	***	...
7519.431	19.0	0.0144	0.0103	128.2	2 A	C II	7519.490	2.4	2Po 2p3	2P 2s.2p.(3Po).3p	1.5	1.5	3/2
				...	...	He I	7519.299 ?	-5.3	1S 1s.3s	1Po 1s.27p	***	***	...
7519.948	17.3	0.0129	0.0092	128.2	3 A	C II	7519.930	-0.7	2Po 2p3	2P 2s.2p.(3Po).3p	0.5	0.5	3/1
				5	C II	C II	7520.200	10.1	2Po 2s2.5p	2D 2s.2p.(3Po).3p	0.5	1.5	2/2
7524.101	17.8	0.0014	0.0010	7.5	4 A	C II	7524.370	10.7	2Po 2s2.5p	2D 2s.2p.(3Po).3p	1.5	1.5	2/2
7525.791	45.6	0.0020	0.0015	8.6	...	He I	7525.969	7.1	1S 1s.3s	1Po 1s.26p	***	***	...
7530.460	35.9	0.0053	0.0038	19.0	6 A	C II	7530.570	4.4	2Po 2p3	2P 2s.2p.(3Po).3p	1.5	0.5	3/1
7533.509	42.8	0.0037	0.0026	10.0	...	He I	7533.469	-1.6	1S 1s.3s	1Po 1s.25p	***	***	...
7542.126	44.1	0.0079	0.0057	36.6	...	He I	7541.944 ?	-7.2	1S 1s.3s	1Po 1s.24p	***	***	...
7551.525	42.1	0.0033	0.0024	18.2	...	He I	7551.571	1.8	1S 1s.3s	1Po 1s.23p	***	***	...
7562.471	31.9	0.0042	0.0030	17.2	...	He I	7562.569	3.9	1S 1s.3s	1Po 1s.22p	***	***	...
7569.057	40.5	0.0022	0.0015	99999.0	...	...	...	...	...	...	...	...	...
7574.071	15.3	0.0051	0.0036	40.7	...	...	...	...	...	...	...	...	...
7575.264	41.1	0.0036	0.0026	9.4	...	He I	7575.214	2.0	1S 1s.3s	1Po 1s.21p	***	***	...
7589.851	33.1	0.0047	0.0033	20.2	...	He I	7589.854	0.1	1S 1s.3s	1Po 1s.20p	***	***	...
7679.594	28.4	0.0036	0.0025	37.7	...	He I	7679.627	1.3	1S 1s.3s	1Po 1s.16p	***	***	...
7751.074	28.3	3.1374	2.1967	1789.0	1 A	[Ar III]	7751.100	1.0	3P 3s2.3p4	1D 3s2.3p4	1.0	2.0	1/1
7757.635	23.2	0.0096	0.0067	99999.0	1 A	He I	7757.620	-0.6	1S 1s.3s	1Po 1s.14p	0.0	1.0	0/0
7771.921	38.4	0.0504	0.0352	157.4	2 A	O I	7771.944	0.9	5So 2s2.2p3.(4So).3s	5P 2s2.2p3.(4So).3p	2.0	3.0	1/1



Table E.1 (continued) - IC 418 Line List

$\lambda_0$ (Å)	FWHM (km/s)	$F(\lambda)/F(H\beta)$ ( $F(H\beta) = 100$ )	$I(\lambda)/I(H\beta)$ ( $I(H\beta) = 100$ )	S/N	ID:	Ion	$\lambda$ (Å)	$\delta V$ (km/s)	Lower Term/Config	Upper Term/Config	$j_1$	$j_2$	Multi
(1)	(2)	(3)	(4)	(5)	(6)	(7)	(8)	(9)	(10)	(11)	(12)	(13)	(14)
7774.170	27.1	0.0308	0.0215	148.9	1 A	O I	7774.166	-0.2	5So 2s2.2p3.(4So).3s	5P 2s2.2p3.(4So).3p	2.0	2.0	2/2
7775.372	28.6	0.0185	0.0130	148.9	1 A	O I	7775.387	0.6	5So 2s2.2p3.(4So).3s	5P 2s2.2p3.(4So).3p	2.0	1.0	2/2
7811.659	23.1	0.0088	0.0061	45.3	2 A	He I	7811.680	0.8	1S 1s.3s	1Po 1s.13p	0.0	1.0	0/0
7816.122	20.1	0.0901	0.0627	80.5	2 A	He I	7816.122 *	0.0	3S 1s.3s	3Po 1s.7p	****	****	...
7860.551	54.2	0.0052	0.0036	28.7	3 A	C II	7860.500 ?	-1.9	2D 2s2.5d	2Fo 2s2.9f	2.5	****	1/0
7876.089	26.5	0.0418	0.0289	99999.0	1 A	[P II]	7875.990	-3.8	1D 3s2.3p2	1S 3s2.3p2	2.0	0.0	0/0
7877.066	53.8	0.0194	0.0134	99999.0	2 A	Mg II	7877.050	-0.6	2Po 4p	2D 4d	0.5	1.5	2/1
7880.901	21.0	0.0053	0.0037	21.8	1 A	He I	7880.890	-0.4	1S 1s.3s	1Po 1s.12p	0.0	1.0	0/0
7890.641	21.7	0.0013	0.0009	21.7	0 <	[Ni III]	7889.900	-28.2	3F 3d8	1D 3d8	3.0	2.0	1/0
7896.364	56.8	0.0324	0.0224	158.7	* C	Mg II	7896.040 ?	-12.3	2Po 4p	2D 4d	1.5	1.5	2/0
				3 A	Mg II	Mg II	7896.370	0.2	2Po 4p	2D 4d	1.5	2.5	2/1
7902.149	20.0	0.0019	0.0013	9.6	...	...	...	...	...	...	...	...	...
7906.002	29.5	0.0049	0.0034	11.2	...	...	...	...	...	...	...	...	...
7924.546	16.0	0.0019	0.0013	16.3	...	He I	7924.521	-0.9	3Po 1s.3p	3D 1s.29d	****	****	...
7932.977	22.8	0.0025	0.0017	7.7	...	...	...	...	...	...	...	...	...
7944.564	18.7	0.0033	0.0022	18.0	...	He I	7944.580	0.6	3Po 1s.3p	3D 1s.26d	****	****	...
7950.773	26.2	0.0052	0.0035	39.5	5 B	O I	7950.803 ?	1.1	3Do 2s2.2p3.(2Do).3s	3F 2s2.2p3.(2Do).3p	2.0	3.0	5/0
				6 D	Fe I	Fe I	7950.786 ?	0.5	w5Fo 3d6.(3F).4s.4p.(3Po)	5F 3d6.4s.(6D).5d	3.0	4.0	7/1
				6 D	Fe I	Fe I	7950.814 ?	1.5	w5Fo 3d6.(3F).4s.4p.(3Po)	5F 3d6.4s.(6D).5d	1.0	2.0	*1
7952.826	30.6	0.0039	0.0027	33.3	...	He I	7952.953	4.8	3Po 1s.3p	3D 1s.25d	****	****	...
7971.645	22.4	0.0047	0.0032	33.2	1 A	He I	7971.620	-0.9	1S 1s.3s	1Po 1s.11p	0.0	1.0	0/0
7973.190	26.1	0.0040	0.0028	22.2	...	He I	7973.166	-0.9	3Po 1s.3p	3D 1s.23d	****	****	...
7985.473	26.5	0.0057	0.0039	18.5	...	He I	7985.452	-0.8	3Po 1s.3p	3D 1s.22d	****	****	...
7995.554	39.8	0.0009	0.0006	9.1	...	...	...	...	...	...	...	...	...
7999.722	38.6	0.0079	0.0054	31.4	...	He I	7999.583 ?	-5.2	3Po 1s.3p	3D 1s.21d	****	****	...
8015.967	19.5	0.0063	0.0043	28.0	...	He I	8015.948	-0.7	3Po 1s.3p	3D 1s.20d	****	****	...
8035.090	17.6	0.0066	0.0045	34.5	...	He I	8035.047	-1.6	3Po 1s.3p	3D 1s.19d	****	****	...
8057.497	21.2	0.0086	0.0059	43.1	...	He I	8057.551	2.0	3Po 1s.3p	3D 1s.18d	****	****	...
8064.893	16.1	0.0011	0.0007	8.0	...	...	...	...	...	...	...	...	...
8084.272	22.6	0.0121	0.0082	56.7	...	He I	8084.292	0.7	3Po 1s.3p	3D 1s.17d	****	****	...
8093.881	67.6	0.0086	0.0058	36.9	5 A	He I	8094.080	7.4	1S 1s.3s	1Po 1s.10p	0.0	1.0	0/0
8115.313	37.0	0.0117	0.0079	99999.0	5 B	Mg II	8115.230	-3.1	2D 4d	2Po 6p	2.5	1.5	2/0
				6 D	Mg II	Mg II	8115.570	9.5	2D 4d	2Po 6p	1.5	1.5	2/1
8116.451	18.5	0.0098	0.0067	99999.0	4 A	O II	8116.490	1.4	2P 2s2.2p2.(3P).4d	2Po 2s2.2p2.(1D).4p	1.5	1.5	3/0
				...	...	He I	8116.426	-0.9	3Po 1s.3p	3D 1s.16d	****	****	...
8120.188	19.7	0.0039	0.0026	21.4	3 A	Fe I	8120.045 ?	-5.3	w5Fo 3d6.(3F).4s.4p.(3Po)	5F 3d6.4s.(6D).5d	4.0	3.0	7/1
				8	Mg II	Mg II	8120.440	9.3	2D 4d	2Po 6p	1.5	0.5	2/0
8140.560	13.0	0.0053	0.0036	36.2	...	...	...	...	...	...	...	...	...



Table E.1 (continued) - IC 418 Line List

$\lambda_0$ (Å) (1)	FWHM (km/s) (2)	$F(\lambda)/F(H\beta)$ ( $F(H\beta) = 100$ ) (3)	$I(\lambda)/I(H\beta)$ ( $I(H\beta) = 100$ ) (4)	S/N (5)	ID: (6)	Ion (7)	$\lambda$ (Å) (8)	$\delta V$ (km/s) (9)	Lower Term/Config (10)	Upper Term/Config (11)	$j_1$ (12)	$j_2$ (13)	Multi (14)
8155.505	19.3	0.0197	0.0133	82.9	4 A	He I	8155.590 *	3.1	3Po 1s.3p	3D 1s.15d	****	****	...
8185.270	20.8	0.0227	0.0152	168.0	7 D	N I	8184.862	-15.0	4P 2s2.2p2.(3P).3s	4Po 2s2.2p2.(3P).3p	1.5	2.5	4/1
8188.451	51.1	0.0567	0.0381	152.9	7 D	N I	8188.012	-16.1	4P 2s2.2p2.(3P).3s	4Po 2s2.2p2.(3P).3p	0.5	1.5	6/1
					4 A	O II	8188.520	2.5	2P 2s2.2p2.(3P).4d	2Po 2s2.2p2.(1D).4p	0.5	1.5	3/1
8200.503	51.5	0.0195	0.0131	138.6	2 A	N I	8200.357	-5.3	4P 2s2.2p2.(3P).3s	4Po 2s2.2p2.(3P).3p	0.5	0.5	6/3
8203.844	22.9	0.0204	0.0137	93.3	3 A	He I	8203.850 *	0.2	3Po 1s.3p	3D 1s.14d	****	****	...
8210.965	45.4	0.0295	0.0198	92.0	2 A	Fe I	8210.920 ?	-1.6	w5Fo 3d6.(3F).4s.4p.(3Po)	5F 3d6.4s.(6D).5d	3.0	3.0	8/2
					6	N I	8210.715	-9.1	4P 2s2.2p2.(3P).3s	4Po 2s2.2p2.(3P).3p	1.5	1.5	6/1
8213.890	47.3	0.0039	0.0026	37.9	4 A	[Fe III]	8213.900 ?	0.4	3D 3d6	1F 3d6	1.0	3.0	2/0
8216.298	62.2	0.0893	0.0598	304.1	5 B	N I	8216.336	1.4	4P 2s2.2p2.(3P).3s	4Po 2s2.2p2.(3P).3p	2.5	2.5	3/0
8223.218	50.4	0.0931	0.0623	347.8	1 A	N I	8223.128	-3.3	4P 2s2.2p2.(3P).3s	4Po 2s2.2p2.(3P).3p	1.5	0.5	6/2
8233.205	18.5	0.0175	0.0117	73.5	3 A	Mg II	8233.190 ?	-0.5	2G 5g	2Ho 9h	****	****	0/0
8234.505	27.7	0.0363	0.0243	143.6	4 B	C II	8234.300 ?	-7.5	2G 2s2.5g	2Fo 2s2.9f	****	****	0/0
					3 A	Mg II	8234.640 ?	4.9	2Po 4p	2S 5s	1.5	0.5	1/1
8235.769	18.2	0.0181	0.0121	67.5	...	...	...	...	...	...	...	...	...
8237.116	17.2	0.0221	0.0147	134.0	...	...	...	...	...	...	...	...	...
8238.620	15.6	0.0184	0.0123	116.1	4 B	S II	8238.590	-1.1	2D 3s2.3p2.(1D).3d	2Po 3s2.3p2.(1S).4p	1.5	1.5	2/0
8240.199	21.0	0.0337	0.0225	147.6	5 A	Fe III	8240.720 ?	18.9	5D 3d5.(6S).5d	5Do 3d5.(4D).5p	2.0	2.0	9/2
8241.366	6.5	0.0010	0.0006	9999.0	...	...	...	...	...	...	...	...	...
8242.031	8.1	0.0402	0.0269	9999.0	...	...	...	...	...	...	...	...	...
8242.508	53.9	0.0824	0.0551	9999.0	4 B	N I	8242.389	-4.3	4P 2s2.2p2.(3P).3s	4Po 2s2.2p2.(3P).3p	2.5	1.5	4/1
8243.704	12.6	0.0635	0.0424	9999.0	...	H I	8243.698	-0.2	3 3*	43 43*	****	****	...
8245.639	25.7	0.0643	0.0429	250.2	...	H I	8245.641	0.1	3 3*	42 42*	****	****	...
8247.727	26.8	0.0683	0.0456	266.5	...	H I	8247.730	0.1	3 3*	41 41*	****	****	...
8249.995	27.9	0.0779	0.0520	260.3	2 A	H I	8249.973	-0.8	3 3*	40 40*	****	****	0/0
8252.396	30.0	0.0947	0.0632	351.0	3 A	H I	8252.398	0.1	3 3*	39 39*	****	****	0/0
8254.352	7.7	0.0024	0.0016	9999.0	...	...	...	...	...	...	...	...	...
8255.102	22.5	0.0687	0.0458	372.5	1 A	H I	8255.018	-3.1	3 3*	38 38*	****	****	0/0
8256.551	13.4	0.0018	0.0012	9999.0	...	He I	8256.492 ?	-2.1	3D 1s.3d	3Fo 1s.33f	****	****	...
8257.581	18.9	0.0321	0.0214	9999.0	5 A	H I	8257.855	10.0	3 3*	37 37*	****	****	0/0
8258.116	20.6	0.0455	0.0303	9999.0	3 A	H I	8257.855	-9.5	3 3*	37 37*	****	****	0/0
8260.907	28.3	0.1061	0.0707	404.4	3 A	H I	8260.934	1.0	3 3*	36 36*	****	****	0/0
8264.339	32.8	0.1405	0.0936	22.6	2 A	H I	8264.284	-2.0	3 3*	35 35*	****	****	0/0
					7 B	He I	8264.530 *	6.9	3Po 1s.3p	3D 1s.13d	****	****	...
8265.723	18.0	0.0112	0.0075	67.0	1 A	He I	8265.710	-0.5	1S 1s.3s	1Po 1s.9p	0.0	1.0	0/0
8267.938	31.0	0.1176	0.0783	21.2	2 A	H I	8267.936	-0.1	3 3*	34 34*	****	****	0/0
8271.803	35.7	0.1130	0.0752	22.6	5 A	H I	8271.930	4.6	3 3*	33 33*	****	****	0/0
8276.325	44.5	0.1397	0.0930	26.4	2 A	H I	8276.308	-0.6	3 3*	32 32*	****	****	0/0

Table E.1 (continued) - IC 418 Line List

$\lambda_o$ (Å) (1)	FWHM (km/s) (2)	$F(\lambda)/F(H\beta)$ ( $F(H\beta) = 100$ ) (3)	$I(\lambda)/I(H\beta)$ ( $I(H\beta) = 100$ ) (4)	S/N (5)	ID: (6)	Ion (7)	$\lambda$ (Å) (8)	$\delta V$ (km/s) (9)	Lower Term/Config (10)	Upper Term/Config (11)	$j_1$ (12)	$j_2$ (13)	Multi (14)
8281.148	47.8	0.1336	0.0889	22.9	2 A	H I	8281.122	-1.0	3 3*	31 31*	***	***	0/0
8283.315	22.7	0.0061	0.0041	99999.0	...	He I	8283.306	-0.3	3D 1s.3d	3Fo 1s.28f	***	***	...
8285.688	22.2	0.0152	0.0101	99999.0	4 A	He I	8285.360 *	-11.9	3Po 1s.3p	3S 1s.13s	***	***	...
8286.579	34.7	0.1038	0.0691	99999.0	1 A	H I	8286.431	-5.4	3 3*	30 30*	***	***	0/0
8290.520	19.5	0.0046	0.0031	16.8	7 B	C II	8290.800 ?	10.1	2Po 2s2.5p	2D 2s2.7d	1.5	***	1/0
					...	He I	8290.559	1.4	3D 1s.3d	3Fo 1s.27f	***	***	...
8298.882	28.5	0.1916	0.1273	40.8	2 A	H I	8298.834	-1.7	3 3*	28 28*	***	***	0/0
					...	He I	8298.680	-7.3	3D 1s.3d	3Fo 1s.26f	***	***	...
8306.064	30.5	0.2481	0.1647	234.7	4 A	H I	8306.112	1.7	3 3*	27 27*	***	***	0/0
8307.803	18.5	0.0057	0.0038	99999.0	...	He I	8307.814	0.4	3D 1s.3d	3Fo 1s.25f	***	***	...
8314.233	34.0	0.2595	0.1722	292.4	3 A	H I	8314.260	1.0	3 3*	26 26*	***	***	0/0
8318.141	20.0	0.0075	0.0050	44.1	...	He I	8318.137	-0.1	3D 1s.3d	3Fo 1s.24f	***	***	...
8320.490	22.6	0.0031	0.0020	21.5	7 D	Fe I	8320.169 ?	-11.6	c3F 3d8	y3Go 3d6.(3H).4s.4p.(3Po)	3.0	4.0	4/1
8323.418	31.7	0.3053	0.2025	446.1	3 A	H I	8323.424	0.2	3 3*	25 25*	***	***	0/0
8329.838	21.1	0.0083	0.0055	51.4	...	He I	8329.867	1.0	3D 1s.3d	3Fo 1s.23f	***	***	...
8333.773	32.1	0.3183	0.2109	532.0	3 A	H I	8333.783	0.4	3 3*	24 24*	***	***	0/0
8339.344	25.7	0.0079	0.0052	27.0	4 A	Ca I	8339.210 ?	-4.8	1D 4s.4d	1Po 4s.77p	2.0	1.0	0/0
8342.203	21.3	0.0228	0.0151	99999.0	6 C	He I	8342.330 *	4.6	3Po 1s.3p	3D 1s.12d	***	***	...
8343.190	30.9	0.0108	0.0072	99999.0	...	He I	8343.273	3.0	3D 1s.3d	3Fo 1s.22f	***	***	...
8345.556	31.6	0.3710	0.2455	217.8	2 A	H I	8345.552	-0.1	3 3*	23 23*	***	***	0/0
8350.233	19.9	0.0090	0.0060	99999.0	...	...	...	...	...	...	...	...	...
8352.471	16.5	0.0015	0.0010	7.3	...	...	...	...	...	...	...	...	...
8358.975	32.0	0.4328	0.2861	101.2	3 A	H I	8359.003	1.0	3 3*	22 22*	***	***	0/0
					...	He I	8358.692 ?	-10.2	3D 1s.3d	3Fo 1s.21f	***	***	...
8361.738	27.8	0.1847	0.1221	405.4	1 A	He I	8361.711 *	-1.0	3S 1s.3s	3Po 1s.6p	***	***	...
8374.487	32.2	0.4359	0.2877	527.8	2 A	H I	8374.475	-0.5	3 3*	21 21*	***	***	0/0
8376.548	17.9	0.0100	0.0066	63.8	...	He I	8376.553	0.2	3D 1s.3d	3Fo 1s.20f	***	***	...
8382.927	21.1	0.0019	0.0012	10.3	...	He I	8382.921	-0.2	1Po 1s.3p	1D 1s.25d	***	***	...
8392.397	31.5	0.4863	0.3205	275.1	2 A	H I	8392.396	0.0	3 3*	20 20*	***	***	0/0
8399.830	19.6	0.0048	0.0031	36.8	...	He I	8399.811	-0.7	1D 1s.3d	1Fo 1s.19f	***	***	...
8405.417	28.5	0.0015	0.0010	10.8	...	He I	8405.379	-1.4	1Po 1s.3p	1D 1s.23d	***	***	...
8413.317	31.3	0.5649	0.3717	383.7	4 B	H I	8413.317	0.0	3 3*	19 19*	***	***	0/0
8419.009	24.3	0.0021	0.0014	9.4	...	He I	8419.032	0.8	1Po 1s.3p	1D 1s.22d	***	***	...
8421.969	21.4	0.0180	0.0118	94.5	...	He I	8421.959	-0.4	3D 1s.3d	3Fo 1s.18f	***	***	...
8424.347	24.4	0.0070	0.0046	43.6	...	He I	8424.379	1.1	1D 1s.3d	1Fo 1s.18f	***	***	...
8433.723	22.4	0.0095	0.0062	67.5	7 B	C II	8433.900	6.3	4Fo 2s.2p.(3Po).4d	4G 2s.2p.(3Po).5f	4.5	4.5	4/0
					6 A	[Cl III]	8434.000	9.9	2Do 3s2.3p3	2Po 3s2.3p3	1.5	1.5	2/1
8437.908	31.5	0.6618	0.4345	789.5	3 A	H I	8437.955	1.7	3 3*	18 18*	***	***	0/0

Table E.1 (continued) - IC 418 Line List

$\lambda_0$ (Å)	FWHM (km/s)	$F(\lambda)/F(H\beta)$ ( $F(H\beta) = 100$ )	$I(\lambda)/I(H\beta)$ ( $I(H\beta) = 100$ )	S/N	ID:	Ion	$\lambda$ (Å)	$\delta V$ (km/s)	Lower Term/Config	Upper Term/Config	$j_1$	$j_2$	Multi
(1)	(2)	(3)	(4)	(5)	(6)	(7)	(8)	(9)	(10)	(11)	(12)	(13)	(14)
8444.441	20.6	0.0353	0.0232	99999.0	3 A	He I	8444.440 *	0.0	3Po 1s.3p	3D 1s.11d	****	****	...
8446.549	68.1	1.7405	1.1419	99999.0	*	O I	8446.247	-10.7	3So 2s2.2p3.(4So).3s	3P 2s2.2p3.(4So).3p	1.0	0.0	2/0
					7 B	O I	8446.359	-6.7	3So 2s2.2p3.(4So).3s	3P 2s2.2p3.(4So).3p	1.0	2.0	1/0
					9 C	O I	8446.758	7.4	3So 2s2.2p3.(4So).3s	3P 2s2.2p3.(4So).3p	1.0	1.0	2/0
8451.153	21.0	0.0207	0.0136	99999.0	...	He I	8451.158	0.2	3D 1s.3d	3Fo 1s.17f	****	****	...
8453.496	25.8	0.0091	0.0060	38.8	...	He I	8453.596	3.5	1D 1s.3d	1Fo 1s.17f	****	****	...
8467.251	32.0	0.7710	0.5050	486.8	2 A	H I	8467.253	0.1	3 3*	17 17*	****	****	0/0
8474.190	19.4	0.0019	0.0013	11.6	...	He I	8474.172	-0.6	1Po 1s.3p	1D 1s.19d	****	****	...
8480.830	27.9	0.0165	0.0108	82.7	1 A	He I	8480.670 *	-5.7	3Po 1s.3p	3S 1s.11s	****	****	...
					7 B	[Cl III]	8481.200	13.1	2Do 3s2.3p3	2Po 3s2.3p3	2.5	1.5	2/1
8486.261	21.7	0.0247	0.0162	118.4	...	He I	8486.269	0.3	3D 1s.3d	3Fo 1s.16f	****	****	...
8488.736	21.4	0.0104	0.0068	49.9	...	He I	8488.727	-0.3	1D 1s.3d	1Fo 1s.16f	****	****	...
8495.350	27.5	0.0035	0.0023	15.2	...	...	...	...	...	...	...	...	...
8499.216	8.1	0.0028	0.0019	99999.0	...	He I	8499.187	-1.0	1Po 1s.3p	1D 1s.18d	****	****	...
8500.039	27.1	0.0068	0.0044	99999.0	8 C	[Cl III]	8500.200	5.7	2Do 3s2.3p3	2Po 3s2.3p3	1.5	0.5	2/0
8502.482	32.4	0.9160	0.5983	226.3	3 A	H I	8502.483	0.0	3 3*	16 16*	****	****	0/0
8518.027	19.1	0.0262	0.0171	147.4	2 A	He I	8518.036	0.3	1S 1s.3s	1Po 1s.8p	0.0	1.0	0/0
8529.022	21.0	0.0324	0.0211	195.2	...	He I	8528.967	-1.9	1Po 1s.3p	1D 1s.17d	****	****	...
					...	He I	8529.025	0.1	3D 1s.3d	3Fo 1s.15f	****	****	...
8531.522	24.1	0.0102	0.0066	66.5	5 A	He I	8530.930	-20.8	1D 1s.3d	1Po 1s.15p	2.0	1.0	0/0
					...	He I	8531.508	-0.5	1D 1s.3d	1Fo 1s.15f	****	****	...
8545.389	31.9	1.0458	0.6807	839.9	2 A	H I	8545.382	-0.2	3 3*	15 15*	****	****	0/0
8548.026	21.3	0.0019	0.0013	99999.0	3 A	[Cl III]	8548.200	6.1	2Do 3s2.3p3	2Po 3s2.3p3	2.5	0.5	3/2
8564.691	21.8	0.0041	0.0027	34.7	...	He I	8564.763	2.5	1Po 1s.3p	1D 1s.16d	****	****	...
8567.730	48.7	0.0019	0.0012	15.7	3 A	N I	8567.735	0.2	2P 2s2.2p2.(3P).3s	2Po 2s2.2p2.(3P).3p	0.5	1.5	3/1
8578.795	52.4	0.4382	0.2844	620.0	1 A	[Cl II]	8578.690	-3.7	3P 3s2.3p4	1D 3s2.3p4	2.0	2.0	1/1
8581.867	23.0	0.0405	0.0263	99999.0	...	He I	8581.856	-0.4	3D 1s.3d	3Fo 1s.14f	****	****	...
8582.627	21.3	0.0491	0.0319	99999.0	1 A	He I	8582.510 *	-4.1	3Po 1s.3p	3D 1s.10d	****	****	...
8584.378	21.1	0.0121	0.0078	65.8	...	He I	8584.369	0.3	1D 1s.3d	1Fo 1s.14f	****	****	...
8598.379	32.5	1.2901	0.8362	663.8	3 A	H I	8598.392	0.4	3 3*	14 14*	****	****	0/0
8608.294	25.3	0.0056	0.0036	29.8	...	He I	8608.312	0.6	1Po 1s.3p	1D 1s.15d	****	****	...
8617.062	54.2	0.0145	0.0094	84.3	3 A	[Fe II]	8616.952	-3.8	a4F 3d7	a4P 3d7	4.5	2.5	2/0
8629.244	34.0	0.0046	0.0030	99999.0	3 A	N I	8629.236	-0.3	2P 2s2.2p2.(3P).3s	2Po 2s2.2p2.(3P).3p	1.5	1.5	3/1
8632.937	40.7	0.0076	0.0049	99999.0	2 A	He I	8632.710 *	-7.9	3Po 1s.3p	3S 1s.10s	****	****	...
8648.270	20.7	0.0450	0.0291	271.6	...	He I	8648.258	-0.4	3D 1s.3d	3Fo 1s.13f	****	****	...
8650.793	20.7	0.0140	0.0091	83.9	6 A	O II	8650.920 ?	4.4	2Fo 2s2.2p2.(1D).4p	2D 2s2.2p2.(1D).5s	3.5	2.5	2/0
					...	He I	8650.811	0.6	1D 1s.3d	1Fo 1s.13f	****	****	...
8653.417	19.0	0.0026	0.0017	99999.0	3 A	He I	8653.240 *	-6.1	3D 1s.3d	3Po 1s.13p	****	****	...

Table E.1 (continued) - IC 418 Line List

$\lambda_0$ (Å)	FWHM (km/s)	$F(\lambda)/F(H\beta)$ ( $F(H\beta) = 100$ )	$I(\lambda)/I(H\beta)$ ( $I(H\beta) = 100$ )	S/N	ID:	Ion	$\lambda$ (Å)	$\delta V$ (km/s)	Lower Term/Config	Upper Term/Config	$j_1$ (12)	$j_2$ (13)	Multi (14)
(1)	(2)	(3)	(4)	(5)	(6)	(7)	(8)	(9)	(10)	(11)	(12)	(13)	(14)
8665.022	31.2	1.4733	0.9501	1255.0	3 A	H I	8665.018	-0.2	3 3*	13 13*	****	****	0/0
8675.887	32.3	0.0018	0.0012	4.9	5 A	N II	8676.090	7.0	3D 2s2.2p.(2Po).4p	3Po 2s2.2p.(2Po).5s	3.0	2.0	2/1
8680.370	56.8	0.0597	0.0385	396.1	1 A	N I	8680.282	-3.0	4P 2s2.2p2.(3P).3s	4Do 2s2.2p2.(3P).3p	2.5	3.5	2/2
8683.525	57.6	0.0647	0.0417	382.0	3 A	N I	8683.403	-4.2	4P 2s2.2p2.(3P).3s	4Do 2s2.2p2.(3P).3p	1.5	2.5	5/4
8686.267	52.3	0.0342	0.0220	9999.0	2 A	N I	8686.149	-4.0	4P 2s2.2p2.(3P).3s	4Do 2s2.2p2.(3P).3p	0.5	1.5	7/5
8698.894	18.4	0.0012	0.0008	11.3	5 D	N II	8698.990	3.3	3D 2s2.2p.(2Po).4p	3Po 2s2.2p.(2Po).5s	2.0	1.0	5/1
8703.334	54.0	0.0417	0.0268	254.2	1 A	N I	8703.247	-3.0	4P 2s2.2p2.(3P).3s	4Do 2s2.2p2.(3P).3p	0.5	0.5	7/5
8711.778	52.8	0.0425	0.0273	234.7	1 A	N I	8711.703	-2.6	4P 2s2.2p2.(3P).3s	4Do 2s2.2p2.(3P).3p	1.5	1.5	7/5
8718.959	53.4	0.0211	0.0135	143.9	2 A	N I	8718.837	-4.2	4P 2s2.2p2.(3P).3s	4Do 2s2.2p2.(3P).3p	2.5	2.5	4/3
8727.289	58.3	0.0521	0.0334	136.6	1 A	[C I]	8727.120	-5.8	1D 2s2.2p2	1S 2s2.2p2	2.0	0.0	0/0
8729.674	36.4	0.0079	0.0050	9999.0	5 A	He I	8730.090	14.3	1Po 1s.3p	1D 1s.13d	1.0	2.0	0/0
8733.415	22.1	0.0595	0.0382	263.2	...	He I	8733.434	0.7	3D 1s.3d	3Fo 1s.12f	****	****	...
8736.001	22.2	0.0212	0.0136	104.4	...	He I	8736.037	1.2	1D 1s.3d	1Fo 1s.12f	****	****	...
8740.119	25.2	0.0047	0.0030	15.2	3 A	He I	8739.960 *	-5.5	3D 1s.3d	3Po 1s.12p	****	****	...
8750.463	32.3	2.0458	1.3112	556.5	3 A	H I	8750.473	0.3	3 3*	12 12*	****	****	0/0
8776.749	19.7	0.0620	0.0397	9999.0	1 A	He I	8776.650 *	-3.4	3Po 1s.3p	3D 1s.9d	****	****	...
8780.667	19.5	0.0014	0.0009	11.7	...	...	...	...	...	...	...	...	...
8806.901	42.0	0.0064	0.0041	47.0	2 A	Mg I	8806.757 ?	-4.9	1Po 3s.3p	1D 3s.3d	1.0	2.0	0/0
8816.619	19.8	0.0092	0.0058	59.1	5 A	He I	8816.820	6.8	1Po 1s.3p	1D 1s.12d	1.0	2.0	0/0
					9 B	O II	8817.110	16.7	2F 2s2.2p2.(3P).4d	2Do 2s2.2p2.(1D).4p	2.5	2.5	2/0
8820.439	27.3	0.0037	0.0024	22.7	2 A	O I	8820.423	-0.6	1Do 2s2.2p3.(2Do).3s	1F 2s2.2p3.(2Do).3p	2.0	3.0	0/0
8829.753	24.2	0.0075	0.0048	9999.0	4 A	[S III]	8829.400	-12.0	3P 3s2.3p2	1D 3s2.3p2	0.0	2.0	1/1
8843.375	26.9	0.0009	0.0006	7.4	8	S II	8842.920	-15.4	2Po 3s2.3p2.(1S).4p	2D 3s2.3p2.(1D).4d	0.5	1.5	2/0
					4 A	[Ni I]	8843.374 ?	0.0	3F 3d8.(3F).4s2	1D 3d8.(1D).4s2	2.0	2.0	1/0
8845.337	21.7	0.0786	0.0501	311.6	5 A	He I	8845.000 *	-11.4	3D 1s.3d	3Fo 1s.11f	****	****	...
8847.902	26.2	0.0301	0.0191	9999.0	3 A	He I	8847.700	-6.9	1D 1s.3d	1Fo 1s.11f	2.0	3.0	0/0
8849.082	27.4	0.0112	0.0071	9999.0	4 A	He I	8849.145 *	2.1	3Po 1s.3p	3S 1s.9s	****	****	...
8853.998	26.0	0.0179	0.0114	38.7	3 A	He I	8854.100 *	3.4	3D 1s.3d	3Po 1s.11p	****	****	...
8862.752	32.6	2.5496	1.6217	464.6	3 A	H I	8862.783	1.1	3 3*	11 11*	****	****	0/0
8873.451	29.2	0.0051	0.0032	21.0	2 A	C I	8873.360 ?	-3.1	1D 2s2.2p.(2Po).3p	1Po 2s2.2p.(2Po).5s	2.0	1.0	0/0
8886.539	15.3	0.0011	0.0007	8.0	...	...	...	...	...	...	...	...	...
8892.237	49.0	0.0046	0.0030	26.6	5 A	[Fe II]	8891.913	-10.9	a4F 3d7	a4P 3d7	3.5	1.5	5/1
8914.751	21.3	0.0361	0.0229	131.9	2 A	He I	8914.771	0.7	1S 1s.3s	1Po 1s.7p	0.0	1.0	0/0
8930.778	24.2	0.0142	0.0090	51.2	5 A	He I	8930.970	6.4	1Po 1s.3p	1D 1s.11d	1.0	2.0	0/0
8949.241	15.3	0.0028	0.0017	16.5	1 A	He I	8949.200	-1.4	1Po 1s.3p	1S 1s.11s	1.0	0.0	0/0
8996.949	24.3	0.1260	0.0795	371.1	4 A	He I	8996.700 *	-8.3	3D 1s.3d	3Fo 1s.10f	****	****	...
8999.590	40.7	0.0435	0.0274	9999.0	3 A	He I	8999.400	-6.3	1D 1s.3d	1Fo 1s.10f	2.0	3.0	0/0
9009.026	19.9	0.0111	0.0070	36.5	4 A	He I	9009.180 *	5.1	3D 1s.3d	3Po 1s.10p	****	****	...

Table E.1 (continued) - IC 418 Line List

$\lambda_0$ (Å) (1)	FWHM (km/s) (2)	$F(\lambda)/F(H\beta)$ ( $F(H\beta) = 100$ ) (3)	$I(\lambda)/I(H\beta)$ ( $I(H\beta) = 100$ ) (4)	S/N (5)	ID: (6)	Ion (7)	$\lambda$ (Å) (8)	$\delta V$ (km/s) (9)	Lower Term/Config (10)	Upper Term/Config (11)	$j_1$ (12)	$j_2$ (13)	Multi (14)
9015.048	51.9	2.0076	1.2652	753.9	1 A	H I	9014.910	-4.6	3 3*	10 10*	****	****	0/0
9052.447	18.8	0.0027	0.0017	5.7	...	...	...	...	...	...	...	...	...
9063.275	21.5	0.0878	0.0552	144.4	2 A	He I	9063.282 *	0.2	3Po 1s.3p	3D 1s.8d	****	****	...
9068.905	31.2	28.3206	17.7936	3977.0	3 A	[S III]	9068.600	-10.1	3P 3s2.3p2	1D 3s2.3p2	1.0	2.0	1/1
9085.516	15.8	0.0132	0.0083	51.1	3 A	He I	9085.630	3.8	1Po 1s.3p	1D 1s.10d	1.0	2.0	0/0
9094.797	80.8	0.0165	0.0103	127.4	6 C	C I	9094.830	1.1	3Po 2s2.2p.(2Po).3s	3P 2s2.2p.(2Po).3p	2.0	2.0	3/0
9111.130	18.7	0.0014	0.0009	27.1	2 A	He I	9111.000	-4.3	1Po 1s.3p	1S 1s.10s	1.0	0.0	0/0
9123.737	40.4	0.1229	0.0770	441.8	0 A	[Cl II]	9123.600	-4.5	3P 3s2.3p4	1D 3s2.3p4	1.0	2.0	1/1
9143.128	27.1	0.0036	0.0022	7.5	...	...	...	...	...	...	...	...	...
9174.224	24.8	0.0108	0.0067	33.2	5 A	He I	9174.488 *	8.7	3Po 1s.3p	3S 1s.8s	****	****	...
9210.290	22.0	0.1412	0.0880	342.7	2 A	He I	9210.260 *	-1.0	3D 1s.3d	3Fo 1s.9f	****	****	...
9213.218	20.4	0.0438	0.0273	127.0	2 A	He I	9210.720 ?	14.0	c4F 3d6.(3F2).4s	z4Go 3d6.(3H).4p	3.5	2.5	7/1
9218.313	46.0	0.0718	0.0448	256.4	1 A	Mg II	9213.200	-0.6	1D 1s.3d	1Fo 1s.9f	2.0	3.0	0/0
9223.637	18.3	0.0102	0.0064	99990.0	...	...	...	-2.1	2S 4s	2Po 4p	0.5	1.5	1/1
9228.996	32.5	4.5115	2.8092	1894.0	2 A	H I	9229.014	0.6	3 3*	9 9*	****	****	0/0
9236.263	16.4	0.0219	0.0136	86.9	...	...	...	...	...	...	...	...	...
9244.407	50.0	0.0340	0.0211	150.2	3 A	Mg II	9244.260 ?	-4.8	2S 4s	2Po 4p	0.5	0.5	1/1
9250.959	22.5	0.0039	0.0024	17.9	5 B	Fe II	9244.739 ?	10.8	c4F 3d6.(3F2).4s	z4Go 3d6.(3H).4p	2.5	3.5	8/2
9260.917	43.8	0.0076	0.0047	99999.0	1 A	O I	9251.010	1.6	2Po 2s.2p.(3Po).3s	2D 2s.2p.(3Po).3p	0.5	1.5	2/0
					1 A	O I	9260.806	-3.6	5P 2s2.2p3.(4So).3p	5Do 2s2.2p3.(4So).3d	1.0	0.0	8/3
					1 A	O I	9260.848	-2.2	5P 2s2.2p3.(4So).3p	5Do 2s2.2p3.(4So).3d	1.0	1.0	8/2
					2 C	O I	9260.937	0.6	5P 2s2.2p3.(4So).3p	5Do 2s2.2p3.(4So).3d	1.0	2.0	7/4
9262.666	43.7	0.0156	0.0097	99999.0	1 A	O I	9262.382	-2.7	5P 2s2.2p3.(4So).3p	5Do 2s2.2p3.(4So).3d	2.0	1.0	8/5
					1 A	O I	9262.670	0.1	5P 2s2.2p3.(4So).3p	5Do 2s2.2p3.(4So).3d	2.0	2.0	7/4
					3 C	O I	9262.776	3.6	5P 2s2.2p3.(4So).3p	5Do 2s2.2p3.(4So).3d	2.0	3.0	5/3
9265.934	27.8	0.0202	0.0125	99.0	1 A	O I	9265.826	-3.5	5P 2s2.2p3.(4So).3p	5Do 2s2.2p3.(4So).3d	3.0	2.0	5/2
					1 A	O I	9265.932	-0.1	5P 2s2.2p3.(4So).3p	5Do 2s2.2p3.(4So).3d	3.0	3.0	4/2
					3 C	O I	9266.005	2.3	5P 2s2.2p3.(4So).3p	5Do 2s2.2p3.(4So).3d	3.0	4.0	2/1
9268.114	19.2	0.0012	0.0007	8.5	9 B	C II	9267.270 ?	-27.3	2Po 2s.2p.(3Po).3s	2D 2s.2p.(3Po).3p	1.5	1.5	2/0
					6 A	[Fe II]	9267.563 ?	-17.8	a4F 3d7	a4P 3d7	1.5	0.5	7/1
9303.057	20.0	0.0213	0.0132	99999.0	5 A	He I	9303.420	11.7	1Po 1s.3p	1D 1s.9d	1.0	2.0	0/0
9318.089	22.5	0.0184	0.0114	86.5	...	...	...	...	...	...	...	...	...
9387.009	55.1	0.0236	0.0146	135.5	7	N I	9386.805	-6.5	2P 2s2.2p2.(3P).3s	2Do 2s2.2p2.(3P).3p	0.5	1.5	2/0
					5 C	[Fe I]	9386.985 ?	-0.7	a5F 3d7.(4F).4s	a3P 3d6.4s2	3.0	2.0	2/0
9393.159	40.0	0.0086	0.0053	31.6	*	N I	9392.793	-11.7	2P 2s2.2p2.(3P).3s	2Do 2s2.2p2.(3P).3p	1.5	2.5	2/0
9463.585	23.3	0.2244	0.1380	473.9	1 A	He I	9463.534 *	-1.6	3S 1s.3s	3Po 1s.5p	****	****	...
9516.592	35.7	0.1321	0.0810	247.1	1 A	He I	9516.562 *	-0.9	3Po 1s.3p	3D 1s.7d	****	****	...

Table E.1 (continued) - IC 418 Line List

$\lambda_o$ (Å) (1)	FWHM (km/s) (2)	$F(\lambda)/F(H\beta)$ ( $F(H\beta) = 100$ ) (3)	$I(\lambda)/I(H\beta)$ ( $I(H\beta) = 100$ ) (4)	S/N (5)	ID: (6)	Ion (7)	$\lambda$ (Å) (8)	$\delta V$ (km/s) (9)	Lower Term/Config (10)	Upper Term/Config (11)	$j_1$ (12)	$j_2$ (13)	Multi (14)
9530.929	42.8	68.9313	42.2567	5092.0	3 A	[S III]	9530.600	-10.4	3P 3s2.3p2	1D 3s2.3p2	2.0	2.0	1/1
9545.854	32.6	5.8626	3.5913	1107.0	4 A	H I	9545.972	3.7	3 3*	8 8*	****	****	0/0
9552.904	24.7	0.0227	0.0139	66.5	2 A	He I	9552.890 *	-0.5	3D 1s.3d	3Po 1s.8p	****	****	...
9603.397	16.0	0.0277	0.0169	116.9	3 A	He I	9603.440	1.3	1S 1s.3s	1Po 1s.6p	0.0	1.0	0/0
9625.445	30.3	0.0374	0.0228	103.1	7	O I	9625.261	-5.8	3Do 2s2.2p3.(4So).4d	3D 2s2.2p3.(2Do).3p	3.0	2.0	4/0
					7	O I	9625.296	-4.7	3Do 2s2.2p3.(4So).4d	3D 2s2.2p3.(2Do).3p	3.0	3.0	3/0
					6 C	O I	9625.325	-3.7	3Do 2s2.2p3.(4So).4d	3D 2s2.2p3.(2Do).3p	2.0	2.0	6/0
					5 A	O I	9625.360	-2.6	3Do 2s2.2p3.(4So).4d	3D 2s2.2p3.(2Do).3p	2.0	3.0	4/0
					6 C	O I	9625.367	-2.4	3Do 2s2.2p3.(4So).4d	3D 2s2.2p3.(2Do).3p	1.0	2.0	6/0
					5 A	He I	9625.697	7.9	1Po 1s.3p	1D 1s.8d	1.0	2.0	0/0
9702.529	29.6	0.0198	0.0120	51.4	4 A	He I	9702.614 *	2.6	3Po 1s.3p	3S 1s.7s	****	****	...
9778.841	68.4	0.0072	0.0044	25.6	2 A	[Fe I]	9778.731 ?	-3.4	a5F 3d7 (4F).4s	a3P 3d6.4s2	1.0	2.0	2/1
9794.186	29.3	0.0027	0.0016	9.0	2 A	N II	9794.050 ?	-4.2	1Fo 2s2.2p.(2Po).4d	2[9/2] 2s2.2p.(2Po<3/2>).5f.G	3.0	4.0	...
9797.660	35.4	0.0177	0.0107	70.4	...	...	...	...	...	...	...	...	...
9805.383	71.6	0.0086	0.0052	22.6	...	...	...	...	...	...	...	...	...
9809.767	57.5	0.0136	0.0082	40.5	7	N I	9810.010	7.4	4Do 2s2.2p2.(3P).3p	4D 2s2.2p2.(3P).3d	1.5	0.5	7/0
9822.279	40.6	0.0126	0.0076	99999.0	9	N I	9822.750	14.4	4Do 2s2.2p2.(3P).3p	4D 2s2.2p2.(3P).3d	2.5	2.5	4/0
9824.092	56.2	0.0731	0.0442	99999.0	3 A	[C I]	9824.130	1.2	3P 2s2.2p2	1D 2s2.2p2	1.0	2.0	0/0
9834.627	51.5	0.0135	0.0082	14.7	5 C	N I	9834.610	-0.5	4Do 2s2.2p2.(3P).3p	4D 2s2.2p2.(3P).3d	2.5	1.5	5/0



# Bibliography

- [Acker et al. 1992] Acker, A., Marcout, J., Ochenbein, F., Stenholm, B., Tylanda, R., 1992, Strasbourg-ESO Catalog of Galactic Planetary Nebulae, <http://adc.gsfc.nasa.gov/cgi-bin/viewer/select.pl?catalog=5084>
- [Aller 1984] Aller, L.H., 1984, Physics of Thermal Gaseous Nebulae, Dordrecht, D., Reidel Publishing Company
- [Baldwin et al. 2000] Baldwin, J.A., Verner, E.M., Verner, D.A., Ferland, G.J., Martin, P.G., Korista, K.T., Rubin, R.H., 2000, ApJS, 129, 229
- [Balteau et al. 1995] Balteau, J.-P., Zavagno, A.; Morisset, C.; Péquignot, D., 1995 A&A, 303, 175
- [Barker 1991] Barker, T., 1991, ApJ, 371, 217
- [Bashkin & Stoner 1976] Bashkin, S., Stoner, J.A., 1976, Atomic Energy Levels & Grotrian Diagrams 1, North-Holland Publishing, Amsterdam
- [Bautista 1999] Bautista, M., 1999, ApJ, 527, 474
- [Bowen 1924] Bowen, I.S., 1924, ApJ, 67, 1
- [Brocklehurst 1972] Brocklehurst, M. 1972, MNRAS, 157, 211
- [Cardelli, Clayton, & Mathis 1989] Cardelli, J.A., Clayton, G.C., & Mathis, J.S., 1989, ApJ, 345, 245
- [Carswell et al. 2001] Carswell, R.F., Webb, J.K., Cooke, A.J., Irwin, M.J., 2001, VPFIT Manual, <http://www.ast.cam.ac.uk/~rfc/vpfit.html>
- [Capriotti 1998] Capriotti, E., 1998, RevMexAA, 7, 153
- [Cerruti-Sola & Perinotto 1989] Cerruti-Sola, M. & Perinotto, M., 1989, ApJ, 345, 339
- [Ciardullo et al. 1999] Ciardullo, R., Bond, H.E., Sipior, M.S., Fullton, L.K., Zhang, C.-Y., Schaefer, K.G., 1999, AJ, 118, 488
- [Copetti & Writzl 2002] Copetti, M.V.F. & Writzl, B.C., 2002, A&A, 382, 282

- [Davey et al. 2000] Davey, A.R., Storey, P.J., Kisieliu, R., 2000, A&AS, 142, 85
- [Dinerstein et al. 1995] Dinerstein, H.L., Sneed, C., Uglum, J., 1995, ApJ, 447, 262
- [Dinerstein et al. 1998] Dinerstein, H.L., Garnett, D.R., Pulliam Lafon C., 1998, AAS 193, 15.04
- [Escalante & Victor 1990] Escalante, V. & Victor, G.A., 1990, ApJ, 75, 513
- [Esteban et al. 1998] Esteban, C., Peimbert, M., Torres-Peimbert, S., Escalante, V., 1998, MNRAS, 295, 401
- [Esteban et al. 1999] Esteban, C., Peimbert, M., Torres-Peimbert, S., García-Rojas, J., Rodríguez, M., 1999, ApJS, 120, 113
- [Ferland 1992] Ferland, G.J., 1992, Astrophys. Lett., 389, L63
- [Ferland et al. 1998] Ferland, G.J., Korista, K.T., Verner, D.A., Ferguson, J.W., Kingdon, J.B., Verner, E.M., 1998, PASP, 110, 749
- [Flower 1969] Flower, D.R. 1969, MNRAS, 146, 243
- [Frank 1994] Frank, A., 1994, AJ, 107, 261
- [Garnett 1992] Garnett, D.R., 1992, AJ, 103, 1330
- [Garnett & Dinerstein 2001a] Garnett, D.R. & Dinerstein, H.L., 2001, RevMexAA 2000, 1
- [Garnett & Dinerstein 2001b] Garnett, D.R. & Dinerstein, H.L., 2001, ApJ, 558, 145
- [Gesicki, Acker, & Szczerba 1996] Gesicki, K., Acker, A., & Szczerba, R., 1996, A&A, 309, 907
- [Grandi 1975a] Grandi, S.A., 1975, ApJ, 196, 465
- [Grandi 1975b] Grandi, S.A., 1975, Astrophys. Lett., 199, 43
- [Grandi 1976] Grandi, S.A., 1976, ApJ, 206, 658
- [Hamuy et al. 1994] Hamuy, M., Suntzeff, N.B., Heathcote, S.R., Walker, A.R., Gigoux, P., Phillips, M., 1994, PASP, 106, 566
- [Harrington et al. 1980] Harrington, J.P., Lutz, J.H., Seaton, M.J., Stickland, D.J., 1980, MNRAS, 191, 13
- [Henry, Kwitter, & Bates 2000] Henry, R.B.C, Kwitter, K.B., Bates, J.A., 2000, ApJ, 531, 928 (HKB)
- [Hyung, Aller, & Feibelman 1994] Hyung, S., Aller, L.H., & Feibelman, W.A., 1994, PASP, 106, 745 (HAF)

- [Kaufman & Sugar 1986] Kaufman, V. & Sugar, J., 1986, JPCRD, 15, 321
- [Kingdon & Ferland 1995a] Kingdon, J.B. & Ferland, G.J., 1995, ApJ, 442, 714
- [Kingdon & Ferland 1995b] Kingdon, J.B. & Ferland, G.J., 1995, ApJ, 450, 691
- [Kisielius et al. 1998] Kisielius, R., Storey, P.J., Davey, A.R., Neale, L.T., 1998, A&AS, 133, 257
- [Kisielius & Storey] Kisielius, R. & Storey, P.J., 2002, A&A, 387, 1135
- [Kwok 2000] wok, S., 2000, The Origin and Evolution of Planetary Nebulae, Cambridge University Press, Cambridge, U.K.,
- [Kurucz & Bell 1995] Kurucz, R.L. & Bell, B., 1995, Atomic Line Data Kurucz CD-ROM No. 23,  
<http://cfa-www.harvard.edu/amdata/ampdata/kurucz23/sekur.html>
- [Liu & Danziger 1993] Liu, X.W. & Danziger, J., 1993, MNRAS, 263, 256
- [Liu et al. 1995a] Liu, X.W., Storey P.J., Barlow, M.J., Clegg, R.E.S., 1995, MNRAS, 272, 369
- [Liu et al. 1995b] Liu, X.W., Barlow, M.J., Danziger, I.J., Clegg, R.E.S., 1995, MNRAS, 273, 47
- [Liu et al. 2000] Liu, X.W., Storey, P.J., Barlow, M.J., Danziger, I.J., Cohen, M., Bryce, M., 2000, MNRAS, 312, 58
- [Liu 2001] Liu, X.W., 2001, ISA Symposium #209
- [Liu 2002] Liu, X.W., 2002, RevMexAA, 12, 70
- [Lucy 1995] Lucy, L.B., 1995, A&A, 294, 555
- [Luo, Liu, & Barlow 2001] Luo, S.-G., Liu, X.-W., Barlow, M.J., 2001, MNRAS, 326, 1049
- [Mendez 1989] Mendez, R.H., 1989, IAUS, 131, 261
- [Moore 1945] Moore, C.E., 1945, A Multiplet Table of Astrophysical Interest, NSRDS-NBS 40
- [Nahar 1995] Nahar, S., 1995, ApJS, 101, 423
- [Nussbaumer & Storey 1984] Nussbaumer, H., Storey, P.J., 1984, A&ASupp, 56, 293
- [Osterbrock 1989] Osterbrock, D.E., 1989, Astrophysics of Gaseous Nebulae & Active Galactic Nuclei. University Science Books, Mill Valley, CA
- [Osterbrock, Tran, & Veilleux 1992] Osterbrock, D.E., Tran, H.D., Veilleux, S., 1992, ApJ, 389, 305

- [Osterbrock et al. 1996] Osterbrock, D.E., Fulbright, J.P., Martel, A.R., Keane, M.J., & Trager, S.C. 1996, PASP, 108, 277
- [Osterbrock et al. 1997] Osterbrock, D.E., Fulbright, J.P., Bida, T.A., 1997, PASP, 109, 614
- [Peimbert 1967] Peimbert, M., 1967, ApJ, 150, 825
- [Peimbert, Sarmiento, & Fierro 1991] Peimbert, M., Sarmiento, A., Fierro, J., 1991, PASP, 103, 815
- [Peimbert et al. 1993] Peimbert, M., Storey, P.J., Torres-Peimbert, S., 1993, ApJ, 414, 626
- [Pequignot et al. 1991] Péquignot, D., Petitjean, P., & Boisson, C., 1991, A&A, 251, 680
- [Phillips, Riera, & Mampaso 1990] Phillips, J.P., Riera, A., & Mampaso, A., 1990, A&A, 234, 454
- [Rauch et al. 1990] Rauch, M., Carswell, R.F., Robertson, J.G., Shaver, P.A., & Webb, J.K., 1990, MNRAS, 242, 698
- [Reay & Worswick 1979] Reay, N.K. & Worswick, S.P., 1979, A&A, 72, 31
- [Rubin 1969] Rubin, R.H., 1969, AJ, 155, 169
- [Rubin et al. 2001] Rubin, R.H., Dufour, R.J., Martin, P.G., Ferland, G.J., Baldwin, J.A., Ortiz, C.O., Walter, D.K., 2001, RevMexAA, 10, 23
- [Shaw & Dufour 1995] Shaw, R.A., & Dufour R.J., 1995, PASP, 107, 896
- [Smits 1996] Smits, D.P., 1996, MNRAS, 278, 683
- [Stanghellini & Kaler 1989] Stanhellini, L.S. & Kaler, J.B, 1989, ApJ, 343, 811
- [Storey 1981] Storey, P.J., 1981, MNRAS, 195, 27
- [Storey 1994] Storey, P.J., 1994, A&A, 282, 999
- [Storey & Hummer 1995] Storey, P.J. & Hummer, D.G., 1995, MNRAS, 272, 41
- [van Hoof 1999] van Hoof, P.A.M, 1999, Atomic Line List v2.04, <http://www.pa.uky.edu/~peter/atomic/>, and private communication
- [Viegas & Clegg 1994] Viegas, S.M. & Clegg, R.E.S., 1994, MNRAS, 271, 993
- [Walsh et al. 2001] Walsh, J.R., Pequignot D., Sharpee B., Baldwin J., Morisset C., Storey, P.J., van Hoof, P.A.M., Williams R.E., 2001, ISA Symposium #209
- [Williams 1995] Williams, R., 1995, PASP, 107, 152

- [Williams et al. 2003] Williams, R., Jenkins, E.J., Baldwin, J.A., & Sharpee, B., 2003, PASP, 115, 178
- [Wilson 1953] Wilson, O.C., 1953, ApJ, 117, 264
- [Wilson & Bell 2002] Wilson, N.J. & Bell, K.L., 2002, MNRAS, 331, 389